

General Disclaimer

One or more of the Following Statements may affect this Document

- This document has been reproduced from the best copy furnished by the organizational source. It is being released in the interest of making available as much information as possible.
- This document may contain data, which exceeds the sheet parameters. It was furnished in this condition by the organizational source and is the best copy available.
- This document may contain tone-on-tone or color graphs, charts and/or pictures, which have been reproduced in black and white.
- This document is paginated as submitted by the original source.
- Portions of this document are not fully legible due to the historical nature of some of the material. However, it is the best reproduction available from the original submission.

SEP
E85-10078

NASA-CR-174405

THEMATIC MAPPER

(E85-10078 NASA-CR-174405) THEMATIC MAPPER:
DESIGN THROUGH FLIGHT EVALUATION Final
Report (Santa Barbara Research Center)
208 p HC A10/MF A01

N85-19492

CSCI 14B

G3/43 Unclass
00078

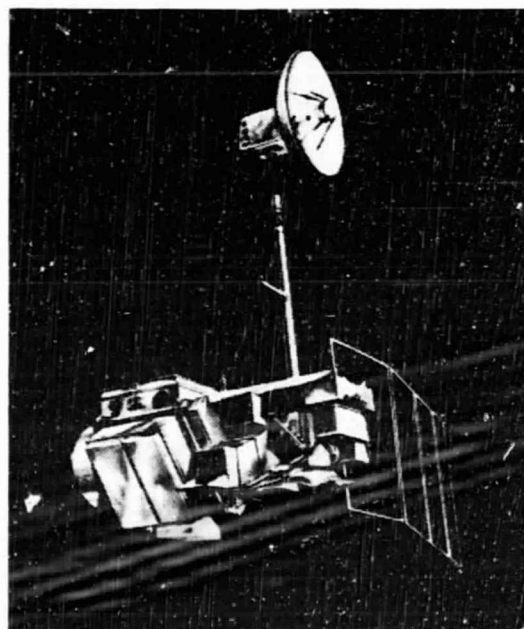


Original photography may be purchased
from EROS Data Center
Sioux Falls, SD 57198

THEMATIC MAPPER

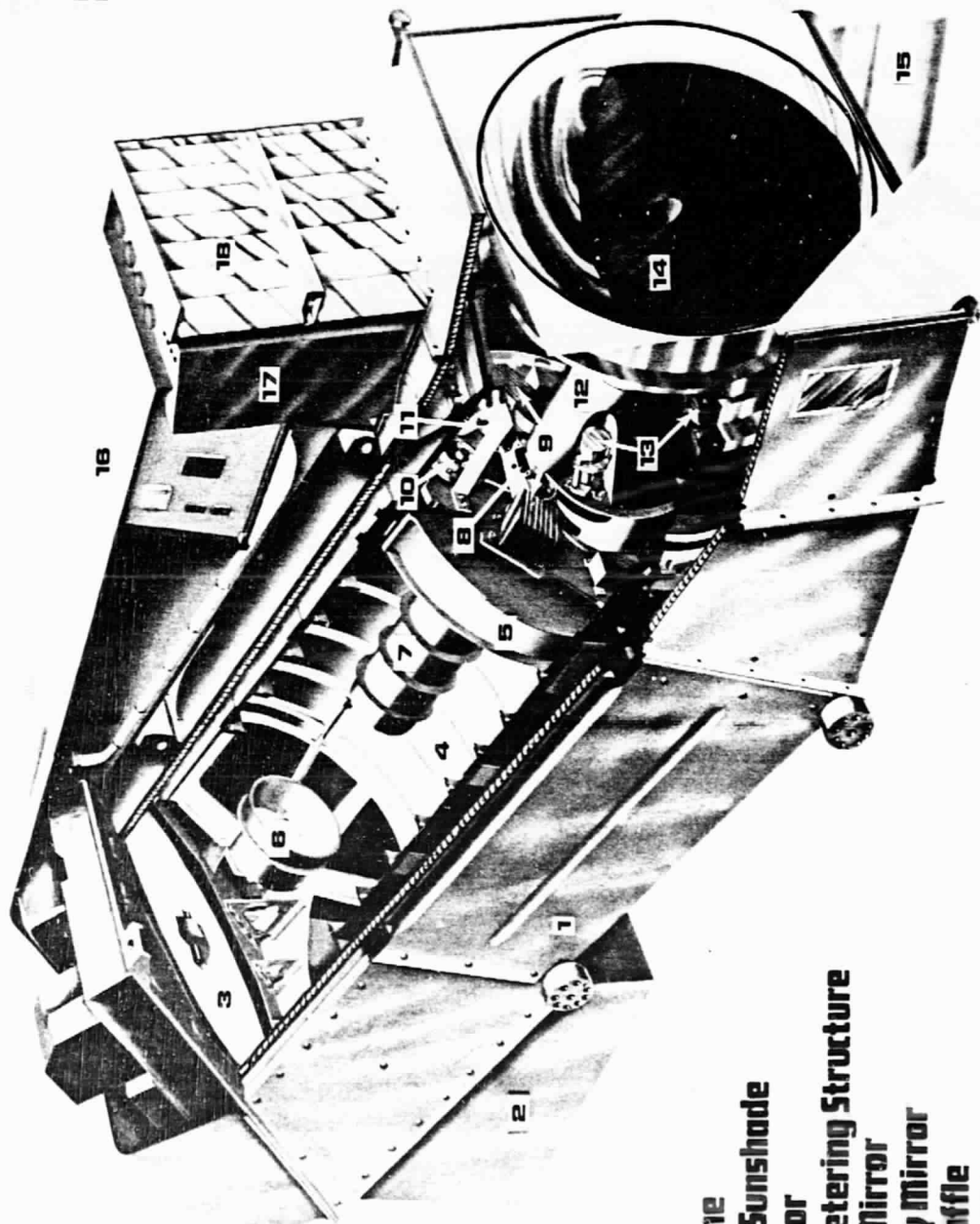
DESIGN THROUGH FLIGHT EVALUATION

FINAL REPORT



CONTRACT NO. NAS5-24200
OCTOBER 1984

THEMATIC MAPPER SCANNER



- 1 Mainframe
- 2 Aperture Sunshade
- 3 Scan Mirror
- 4 Optical Metering Structure
- 5 Primary Mirror
- 6 Secondary Mirror
- 7 Central Baffle
- 8 Prime Focal Plane
- 9 Hybrid Preamplifiers
- 10 Calibration Shutter
- 11 Black Body
- 12 Relay Optics Assembly
- 13 Alignment & Focus Mechanism(s)

- 14 Radiative Cooler
- 15 Earth Shield
- 16 Electronics Module
- 17 Multiplexer
- 18 Thermal Control Louvers

SANTA BARBARA RESEARCH CENTER

A Subsidiary of Hughes Aircraft Company

75 COROMAR DRIVE, GOLETA, CALIFORNIA

THEMATIC MAPPER

DESIGN THROUGH FLIGHT EVALUATION

FINAL REPORT

PREPARED FOR

**NATIONAL AERONAUTICS AND SPACE ADMINISTRATION
GODDARD SPACE FLIGHT CENTER
GREENBELT, MARYLAND**

**CONTRACT NO. NAS5-24200
TECHNICAL DIRECTION NO. 17**

OCTOBER 1984

REVISED DECEMBER 1984

CONTENTS

<u>Section</u>	<u>Page</u>
1 INTRODUCTION.....	1
2 HISTORICAL PERSPECTIVE.....	5
Design Requirements and Specifications.....	5
Hardware Development.....	7
3 THEMATIC MAPPER SYSTEM OVERVIEW.....	9
Design Details.....	14
Scan Mirror.....	14
Telescope.....	17
Scan-Line Corrector.....	18
Calibrator.....	18
Prime Focal Plane.....	20
Relay Optics.....	20
Cooled Focal Plane/Radiative Cooler.....	21
Signal Processing.....	22
4 PERFORMANCE AND USER REQUIREMENTS.....	25
Performance Parameters.....	25
Basic Limitations.....	25
Interrelationships Among Constraints.....	27
The Effect of Sensor Subsystems on Image Quality.....	28
Engineering Requirements.....	30
Radiometric Requirements.....	31
Spectral Requirements.....	31
Image Quality Requirements: MTF and Aliasing.....	33
Performance and User Requirements.....	37
5 MAJOR SYSTEM TRADE-OFFS LEADING TO THE INITIAL PROPOSAL.....	43
Image-Plane versus Object-Plane Scanning.....	43
Telescope Type.....	44
Scan-Mirror Mounting Angle and Size.....	44
Scan-Mirror Construction.....	46
Scan-Mirror Drive.....	46
Relay Optics.....	50
Registration Requirements.....	50
Scan-Line Correction.....	52
Detector Selection.....	53
Cooler Selection.....	53
Sampling Mode and Rate.....	55
Electrical Filter.....	56
Compression Amplifier.....	58
Multiplexer Design.....	58
Summary.....	59

CONTENTS (Cont)

<u>Section</u>	<u>Page</u>
6	RESOLUTION OF CRITICAL HARDWARE PROBLEMS..... 63
	Scan-Mirror Assembly..... 63
	Scan Mirror..... 63
	Scan-Angle Monitor..... 65
	Telescope Assembly..... 68
	Telescope Housing and Support Structures..... 69
	Primary-Mirror Mounting..... 70
	Telescope Mirror Materials..... 71
	Optical Finishing..... 73
	Aft-Optics Assembly..... 74
	Relay-Optics Assembly..... 74
	Relay-Optics Focus-Alignment Drive..... 77
	Focal Plane Assemblies..... 78
	Prime Focal-Plane Assembly..... 79
	Cables and First-Stage Preamplifier
	Substrate..... 80
	Electrical Crosstalk and Distributed
	Capacitance..... 79
	Assembly and Alignment..... 84
	Cold Focal-Plane Assembly..... 85
	Cold Focal-Plane Module..... 85
	Detector Arrays..... 87
	Cold Focal-Plane Cables..... 89
	Scan-Line Corrector..... 90
	On-Board Calibrator Assembly..... 90
	Fiber-Optics Assembly..... 95
	Calibrator Resonant Shutter..... 95
	Radiative Cooler..... 96
	Thermal Performance..... 100
	Structural Performance Development..... 101
	Contamination Control..... 103
	Electronics Module..... 104
	Housing and Heat Sink..... 104
	Printed Wiring Boards (PWB)..... 105
	Multiplexer Assembly..... 106
7	PRELAUNCH EVALUATION..... 109
	Bench Test and Calibration Equipment..... 109
	Prelaunch Testing..... 113
	Effective-Focal-Length Measurement..... 114
	Prime Focal-Plane Assembly Focus..... 117
	Scan-Mirror/Radiometer Alignment..... 117
	Cold Focal-Plane-Assembly Coarse Focus..... 118
	Cold Focal-Plane-Assembly Fine Focus and
	Band-to-Band Registration..... 118
	Electronic Module Integration..... 118
	Line-Spread Function (Optics and Detector)..... 118
	Radiometric and On-Board Calibrator
	Calibration..... 119

CONTENTS (Cont)

<u>Section</u>	<u>Page</u>
Spectral Response.....	120
TM Calibrator Calibration.....	121
Square-Wave Response.....	122
Geometric Accuracy and Band-to-Band Registration.....	125
Radiometric Calibration - Band 6.....	129
Coherent Noise.....	129
System-Readiness Test.....	130
Thermal-Vacuum Tests.....	130
 8 LANDSAT-4 IMAGE DATA QUALITY ANALYSIS.....	 131
Introduction.....	131
Landsat-4 LIDQA Objectives.....	131
Sensor Evaluation.....	132
Radiometry.....	132
Sensitivity.....	132
Dynamic Range.....	133
Ground Temperature Estimation from TM Band 6.....	135
Reflective-Band Calibration.....	138
Sensor Radiometric Stability and Anomalous Behavior.....	138
Resolution; Instantaneous Field of View (IFOV) and Blur.....	143
Sampling and Resampling Effects.....	143
Geometric Quality.....	144
Spectral Characteristics.....	146
Image Quality.....	146
Information Content.....	146
Image Utility Relative to MSS.....	147
Conclusion.....	153
 9 LANDSAT DATA ANALYSIS AT SANTA BARBARA RESEARCH CENTER.....	 155
Bright Target Recovery.....	155
Techniques for Detecting BTR Delays.....	155
Visual Detection of Simulated BTR Delays.....	156
Detection of Actual BTR Delays.....	158
Results and Discussion.....	158
Measurement of the Severity of BTR Delays.....	159
Cause of BTR Delays.....	163
Conclusions.....	166
Thematic Mapper Radiometric Performance.....	166
Landsat-5 Thermal Band.....	166
Effective Radiance.....	166
Calibration.....	168
Orbital Data Studies.....	169
Histogram Studies.....	169

CONTENTS (Cont)

<u>Section</u>		<u>Page</u>
	Gain and Offset.....	175
	Notations and Subscripts Used.....	175
	Notations.....	175
	Subscripts.....	175
<u>Appendix</u>		
A	HARD-COPY PRODUCTION.....	179
B	DESIGN CHANGES DURING HARDWARE DEVELOPMENT.....	183
	TM Critical Element Breadboard Program.....	183
	Conceptual Design Review.....	184
	Detail Design Review.....	184
	TM Engineering Model Preshipment Review.....	186
	Protoflight Preshipment Review.....	188
	Flight Model Preshipment Review.....	188
C	REFERENCES.....	191
	INDEX.....	199

ILLUSTRATIONS

<u>Figure</u>		<u>Page</u>
	Frontispiece	
1	Hardware Development Chronology.....	8
2	Single Detector Electromechanical Scanner Optical System.....	10
3	Single Detector Electromechanical Scanner System Block Diagram.....	11
4	Thematic Mapper Cutaway View.....	13
5	TM Optical System and Detector Arrays.....	15
6	Thematic Mapper System Block Diagram.....	6
7	Scan-Line Corrector Effect on Scan Pattern.....	19
8	IFOV Alignment.....	22
9	Fundamental Limitations on Sensor Design.....	26
10	Sensor Swath Coverage.....	27
11	Error Sources Affecting Image Quality.....	29
12	Relationship of Spectral Bandpass and Radiometric Uniformity.....	32
13	Detector Response to Sine-Wave Modulation.....	34
14	Functional Dependence of Modulation on Frequency...	35
15	"Aliasing" Error from Sampling.....	36
16	TM Ritchey-Chretien Telescope.....	45
17	Scan Mirror Geometry.....	45
18	Scan-Line Corrector.....	52
19	Configuration of Detector Arrays.....	54
20	Scan-Mirror Assembly.....	64
21	Representation of Scan-Mirror Assembly Kinematics..	66
22	SMA Scan Profiles and Nonlinearities.....	66
23	Functional Diagram of Scan-Angle Monitor.....	67
24	Scan-Angle Monitor (SAM).....	67
25	Optical Metering Structure.....	68
26	Telescope Assembly.....	70
27	Primary Mirror Mounted in Optical Metering Structure.....	71
28	Primary Mirror Blank.....	72
29	Aft-Optics Bulkhead.....	75
30	Aft-Optics Assembly.....	76
31	Aft-Optics Detail View.....	76
32	Relay-Optics Assembly.....	77
33	Inchworm.....	78
34	One of the Four Prime Focal Plane Assemblies.....	80
35	Bands 1 through 4 of the Prime Focal-Plane Assembly.....	80
36	Breakaway View of Band-Level Assemblies.....	81
37	Silicon FPA Detector/Frame Assembly.....	82
38	Enlarged View of a Prime Focal-Plane Substrate.....	83
39	Swamping Capacitors.....	84
40	Cold-Stage Detector/Dewar Exploded View.....	86
41	Cooled Focal-Plane Substrate Assembly with and without Spectral Filters.....	86

ILLUSTRATIONS (Cont)

<u>Figure</u>		<u>Page</u>
42	Cold Focal-Plane Detector Arrays:	
	Bands 7, 5, and 6.....	87
43	Spectral Filter Support Housing.....	88
44	Scan-Line Corrector.....	91
45	Scan-Line Correction Function.....	91
46	Internal Calibrator Flag Rotation.....	92
47	Internal Calibrator Flag Mechanism.....	93
48	Internal Calibrator Scheme.....	94
49	Radiative Cooler Exploded View.....	98
50	Radiative Cooler Layout.....	99
51	Electronics Module.....	104
52	Multiplexer Simplified Block Diagram.....	107
53	BTCE Functional Block Diagram.....	111
54	Test Setup Used to Measure Effective Focal Length.....	116
55	Optics Alignment Test Configuration.....	118
56	Radiometric Calibration Test Configuration.....	119
57	Typical Graph of Output Signal versus Input Radiance.....	120
58	Spectral Response Determination.....	121
59	TM Aligned to Calibrator.....	122
60	Full-Up Test Arrangement (Top View).....	123
61	Conventional Bar Reticle.....	123
62	Phased-Edge Reticle.....	124
63	Look-Up Table at Edge No. 2 = 50% Signal.....	125
64	Reassembled KER Data.....	125
65	Square-Wave-Response Test Sequence.....	126
66	GA/BBR Reticle Battlements.....	128
67	Comparison of Histograms Before and After Corrections for Unequal Bin Sizes (Los Angeles Scene).....	137
68	Relative Radiometric Stability; Bands 1 through 5 and 7.....	139
69	Initial Calibration Unchanged After Outgassing.....	142
70	Landsat-4 Thematic Mapper Geometric Correction System.....	145
71	Spectral Signatures Reveal Differences Among Crops.....	149
72	TM SWIR Capability Enhances Crop Discrimination....	150
73	Snow and Clouds: Similar in Visible Band, Separable in Shortwave Infrared.....	151
74	Cloud Rolloff, Simulated and Actual.....	157
75	Simulated Detector Rolloff, Including Delays.....	157
76	Detector Averages after Saturation (Delays).....	161
77	Detector Averages after Saturation (Successful Recoveries).....	162
78	Detector Averages, No Saturation.....	164
79	Detector Differences (16,14,12 vs 15,13,11).....	164

ILLUSTRATIONS (Cont)

<u>Figure</u>		<u>Page</u>
80	Detector Differences After Saturation, Maximum Duration (Detectors 16,14,12 vs 15,13,11).....	165
81	Alabama Scene: Raw Data Image and Corrected Image.....	170
82	Alabama Scene: Raw Data Frequency Histograms.....	173
83	Alabama Scene: Step-Size Correction from Multiplexer Unit Tests.....	73
84	Alabama Scene: Frequency Histograms, Hand-Adjusted for Quantizer Levels.....	173
85	Alabama Scene: Same Data as Figure 82; Channels Shifted Horizontally on Raw Data.....	174
86	Alabama Scene: Same Data as Figure 83; Channels Shifted Horizontally.....	174
87	Alabama Scene: Same Data as Figure 84; Channels Shifted Horizontally after Hand-Adjustment for Quantizer Levels.....	174
88	Alabama Scene Low-Level Frequency Histograms Adjusted by Multiplexer Unit-Test Data for Quantizer Levels.....	176
89	Alabama Scene Low-Level Frequency Histograms Hand-Adjusted for Quantizer Levels.....	176
90	Histogram from TM Band 2 Data of San Francisco, CA. Image Data is Clustered Between Grey Levels 16 and 90.....	180

<u>Plate</u>		<u>Following Page</u>
1	First True-Color Image Transmitted by Landsat-4 Four Days after Launch: Detroit, MI; Winsor, ON.....	2
2	Sierra Nevada Snow and Cloud Discrimination....	150
3	Density Slice of a Night Scene Over Buffalo, NY.....	152
4	Hue-Intensity-Saturation Transformation - Death Valley, CA.....	152
5	Bright Cloud Image.....	160
6	Linearly Stretched Images of San Francisco, CA.....	182
7	Color Film Generation Process.....	182
8	Full Scene Image of Las Vegas, NV.....	182
9	California Coastline - Point Conception to Santa Barbara.....	182
10	Full Scene Image of Salton Sea, CA.....	182
11	Subimage of Washington, DC (48 x 48 km).....	182

TABLES

<u>Table</u>		<u>Page</u>
1	TM Band Characteristics Summary.....	12
2	Required and Measured Spectral Coverage.....	37
3	Band Usage by Application Area.....	38
4	Line-Spread-Function Width (Optics and Detector Only).....	39
5	Measured Protoflight and Flight Radiometric Sensitivity	40
6	SWR Requirements and Measured Performance.....	40
7	Measured Protoflight Geometric Accuracy.....	41
8	Scan-Line Length.....	41
9	Measured Protoflight Dynamic Band-to-Band Registration (BBR).....	41
10	Scan-Mirror-Angle Trade-Offs.....	47
11	Scan-Mirror-Drive-Approach Trade-Offs.....	48
12	Methods for Meeting Registration of Band 5 with Bands 1 through 4.....	51
13	Butterworth Filter Characteristics.....	57
14	System Trade-Off Summary.....	59
15	Prelaunch Tests Performed on the Three TM Models...	113
16	Relationship of Required EFL Accuracy to Permissible Measurement Uncertainties.....	114
17	Reflective Band Radiance Parameters.....	134
18	Relative Gain and Offsets in Counts.....	136
19	Average Temperature Data (°C).....	138
20	Scenes Used to Measure Relative Gains for Bands 1 through 5 and 7.....	140
21	TM Protoflight Model (Landsat 4) Reflective Band...	140
22	Pixels from Saturation (Reverse Scan).....	160
23	Coefficients for Evaluating Effective Radiance Equations.....	167
24	Thermal Band Calibration at Launch.....	168
25	Evaluation Coefficients for Later Calibration Items.....	169
26	Coefficients for Evaluating Empirical Corrections.....	171
27	Quantizer Step-Size Corrections from Histogram Overlay Method and from Multiplexer Unit- Test Data.....	172
28	Gain and Offset Calculations for Alabama Scene.....	177
29	TM Power Supply Changes Documented at the Engineering Model Preshipment Review.....	189

Section 1

INTRODUCTION

The earth-remote-sensing research program at the National Aeronautics and Space Administration (NASA), Goddard Space Flight Center (GSFC), has matured substantially since the launch of the Landsat-3 spacecraft in 1978. Since that time a new sensor has emerged, known as the Thematic Mapper (TM). Taking its name from its mission to produce radiometrically and geometrically accurate maps of crops, forests, urban and rural areas, and other land use "themes," the TM has improved data-acquisition capability over the Multispectral Scanner (MSS), the chief imaging sensor on the first three Landsat spacecrafts. The first full-color imagery obtained from Landsat-4 is shown in Plate 1.

Landsats 4 and 5, launched in 1982 and 1984, not only carried the advanced sensor, but were redesigned to handle the increased data rates associated with it, and to communicate that data to earth via geosynchronous orbiting Tracking and Data Relay Satellites (TDRS). This report summarizes the TM development program at Hughes Aircraft Company and its Santa Barbara Research Center (SBRC) subsidiary. The entire Landsat 4 and 5 system development also entailed the spacecraft and ground systems; however, a description of these systems is beyond the scope of this report.

Section 2 presents a brief historical perspective of the evolution of design requirements and hardware development.

Section 3 comprises an overview description of the final design configuration of the Thematic Mapper, so the detailed discussions that follow can be understood in proper context. A more detailed description of the operation of the Thematic Mapper is contained in its Operation and Maintenance Manual [SBRC 1982a]. Following the design description, Section 4 contains a tutorial on the basic performance parameters that serve as sensor design guidelines to introduce a summary of system performance and user requirements, contained in Section 4.

Two major development phases led to the TM system. The first was the proposal design phase prior to contract award, and the second was the actual hardware phase leading to three TMs, including an engineering model (EM) to evaluate design decisions and hardware procedures, and the protoflight (PF) and flight (F) models that were launched on Landsats 4 and 5.

Section 5 provides a description of the initial engineering trade-offs that led to the 1976 Hughes TM proposal to GSFC, and Section 6 describes the hardware development program that began in 1977. One aspect of the TM program that requires emphasis is the extensive use of proven technology from prior programs to reduce costs and to improve performance. One example is the use

of radiative-cooler technology from the Visible-Infrared Spin-Scan Radiometer (VISSR) that provides imaging for global weather satellites, producing the images used by meteorologists, newspapers, and television networks to illustrate weather patterns.

As in any complicated system development, many problems occurred during the actual hardware phase that resulted in modifications to the original proposal design to meet the sensor specifications. For example, in some cases a proposed design technique was not found appropriate to fabricate a given assembly, and changes were required in areas of design or implementation procedures. However, ultimately almost all the original GSFC performance specifications were either met or exceeded, so that both the PF- and F-model TMs have performed well.

A major facet of the TM hardware program, not always appreciated for its complexity and difficulty, is the prelaunch performance evaluation. In fact, the design and development of adequate test equipment to examine data quality on the ground and to emulate orbital operating conditions was, by itself, a program rivaling sensor development in difficulty, since, to ensure data integrity, the calibration and test system had to perform better than the TM. Section 7 describes this test equipment and the tests performed to obtain the performance measurements summarized in Section 4.

It is clear from the images generated since the launch of Landsat 4 that the data quality of the TM is superior to that of the MSS. However, it remains to be seen if the NASA GSFC remote-sensing experiment will pass a final test of successful technology transfer to a commercially profitable system, as appears to be a goal of current United States national policy. Regardless of the degree to which Landsat becomes commercially successful, scientifically a strong case can be made that Landsat is highly successful. The key scientific results of Landsat 4 data studies, obtained by some fifty government, university, and industry investigative teams are summarized in Section 8. These studies verified that the TM sensor performed as well on-orbit as it did in the ground tests and that TM data is significantly more robust for applications than MSS data.

Landsat-5 was launched in March, 1984, and investigations are in progress to evaluate the performance of the flight model. Since these investigations have not yet been completed, Section 9 of this report summarizes only the flight-model evaluations performed at Hughes SBRC since August, 1984, when adequate data was available from Landsat-5. Two evaluation efforts are described: reflective-band bright-scene-recovery studies and thermal band radiometry.

Appendix A summarizes the methods and procedures used to produce color composite "hard-copy" image prints from computer-compatible tapes (CCTs) generated by the Thematic Mapper Image

Processing System (TIPS). The equipment and software are described, and some examples of TM image products generated at Hughes SBRC are included. Appendix B provides a calendar of the key events of the TM hardware program, including dates and the significance of major design reviews at GSFC. References are listed in Appendix C.



ORIGINAL PAGE
BLACK AND WHITE PHOTOGRAPH

Plate 1. First True-Color Image Transmitted by
Landsat-4 Four Days after Launch: Detroit, MI; Windsor, ON.

Section 2

HISTORICAL PERSPECTIVE

DESIGN REQUIREMENTS AND SPECIFICATIONS

Although the request for proposal (RFP) for the Thematic Mapper instrument was issued in July of 1976, the development of requirements for an advanced multispectral scanning instrument had begun several years earlier. In January 1970, the final report for the Multispectral Point Scanner Study, presented to Goddard Space Flight Center, suggested an advanced 7-band scanner with up to 12 detectors per band, providing a 37-meter instantaneous field of view (IFOV) [HAC 1970]. The Earth Observatory Satellite Mission Review Group, in November of 1971, suggested a 50-meter IFOV for a TM instrument [EOSMRG 1971]. These reports preceded the launch of the first Multispectral Scanner (MSS) instrument into polar orbit in July 1972 as the Earth Resources Technology Satellite (ERTS-A), later to become Landsat 1.

Prior to ERTS-A, research had been oriented toward proof-of-concept and feasibility studies on the need for remote sensing from an orbiting spacecraft. However, after the first MSS instrument was launched, research community attitudes shifted. Once remote collection of earth-resource data from space became a reality, it also quickly became a necessity. What was originally conceived as a research tool was accepted as a necessary and routine source for land-management data. Research efforts were re-oriented toward the many potential uses of MSS data as the number of actual data users increased dramatically. The operating MSS system became the foundation on which future requirements for remote sensing needs would be based. Investigations based on actual MSS data were performed by an expanded user community including NASA-sponsored principal investigators; federal, state, and local government agencies; foreign governments; universities, and private institutions. In addition, NASA sponsored a number of working groups whose charters were to review user needs and the status of current technology in order to make recommendations on the performance capabilities required on future remote-sensing instruments. The requirements established by these working groups were the basis for further advanced scanner development programs, ultimately leading to the TM design.

One such group met in Cocoa Beach, Florida, in December of 1972, and evaluated a wide range of future data requirements and the technological means to satisfy them [Cocoa Beach Working Group 1973]. Part of their recommendations included the use of electromechanical scanners, increased numbers of detectors, and larger collecting optics to provide a factor of 2 to 3 increase in spatial and spectral resolution.

Another, and perhaps the most important of these working groups, was the Landsat-D TM Technical Working Group, which met

at Purdue University in the spring of 1975 [Harnege and Landgrebe 1975]. This group of over 40 scientists and engineers from government, industry, and universities met to make final technical recommendations on the specifications for the instrument that would become the second-generation earth-resource scanner. The purpose of this group was to combine the knowledge gained from previous years of research by many individuals and groups into a specific set of suggested specifications for the TM.

The group recommended using seven spectral bands, covering spectral regions where research indicated the greatest amount of earth-resource information could be obtained. It was noted that perhaps three or four bands would be sufficient to provide good classification accuracy for any one application. However, a minimum of six bands were recommended since the same set of three or four bands would not be optimum for all times, places, or applications. The seven bands actually specified by this group were in close agreement with the final TM bands. TM Band 1 (0.45 to 0.52 μm), Band 2 (0.52 to 0.60 μm), Band 3 (0.63 to 0.69 μm), Band 5 (1.55 to 1.75 μm), and Band 6 (10.4 to 12.5 μm) were exactly as defined by this group. Band 4 (0.76 to 0.90 μm) of the TM was suggested as two separate bands in the working group report. Although TM Band 7 (2.08 to 2.35 μm) was discussed in the report, it was not specified. The original RFP (in 1976) asked that the TM be designed to provide for a seventh band, but it was not actually defined as a requirement until early 1978.

The need to keep the spectral bands within narrow ranges was recognized by the report as being necessary to avoid the atmospheric water absorption region as well as the ozone and carbon dioxide absorption regions, while providing better resource classification. The radiometric sensitivity was recommended at 0.5% noise equivalent reflectance variation ($\text{NE}\Delta\rho$) for all reflective bands and 0.5K ($\text{NE}\Delta T$) for the thermal band. These values were used in the final TM design requirements except for Band 1 ($\text{NE}\Delta\rho$ specified as 0.8%) and Band 5 ($\text{NE}\Delta\rho$ specified as 1%). The report also recommended a 30- to 40-meter instantaneous field of view (IFOV) with a design goal of 30 meters (which became the TM requirement), distinguishing agricultural plots of less than 20 acres. The 120-meter IFOV recommended for the thermal band was the same as the final TM design requirement.

The group was not convinced that the spatial sampling rate of 1.4 samples per IFOV, being considered at the time, was appropriate or necessary and recommended further study to consider not only the effects on the data, but also on the ground-processing capabilities. In the final design, the TM incorporated a once-per-IFOV sampling rate.

HARDWARE DEVELOPMENT

An overview of hardware development from the time of the precursor design effort through the delivery of the TM Flight 1 model is shown in Figure 1. The purpose of the precursor study was to design a class of scanners suitable for mapping the entire earth in 3- to 4-week intervals with a spatial resolution in the range of 30 to 60 meters and a spectral range from the visible into the thermal infrared band. The design recommended in the study included a 40.6-cm (diameter) aperture, object-space scan mirror, 7 spectral bands, and fields of view from 37 to 111 meters for a 556 km sun-synchronous orbit.

The Multispectral Scanner (MSS) design study started in 1969 prior to completion of the Precursor Study and, using its results, evolved a similar design, but reduced in power and weight to fit the constraints of a Thor Delta launch vehicle and a Nimbus type of spacecraft.

Another precursor of the TM design was the Scanning Spectroradiometer Point Design, an 8-week study started in June 1973, which led to a design intended to satisfy performance requirements similar to those of the TM. This study marked the first detailed consideration by SBRC (for this application) of a two-way scanning mirror motion with a scan-line corrector (an image-motion compensator), detector arrays at the focal plane, a 40.6-cm telescope with axis tilted up, and a brazed beryllium scan mirror.

Breadboard work was started on the TM in June 1974, first on the two-way scan mirror and then on the scan-line corrector and a silicon photodiode array and preamplifier. The TM proposal was submitted in August 1976. Hughes was announced the winner of the competition in February 1977, and the TM development program was started in April 1977.

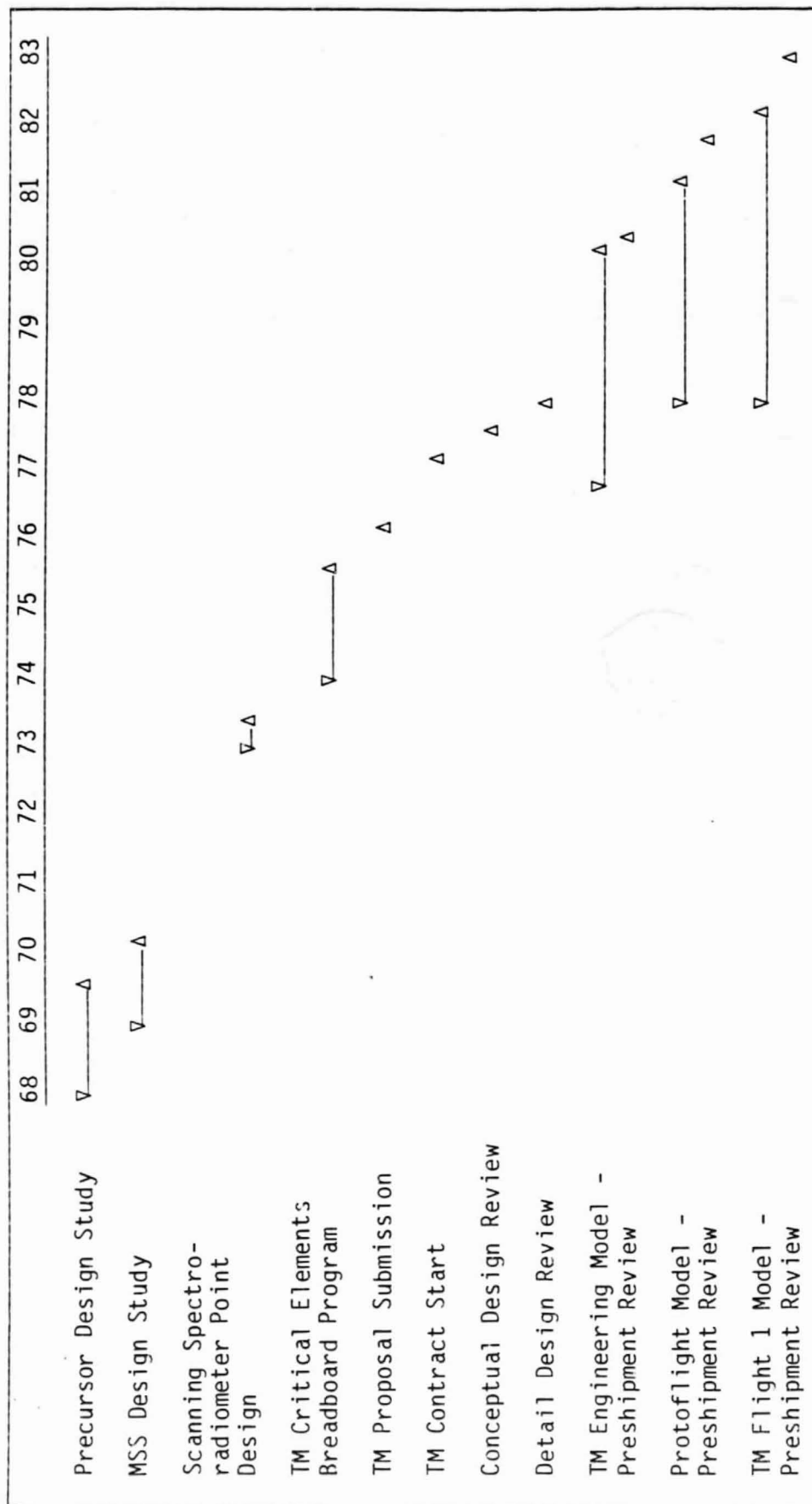


Figure 1. Hardware Development Chronology

Section 3

THEMATIC MAPPER SYSTEM OVERVIEW

DESIGN OVERVIEW

The Thematic Mapper (TM) is a remote-sensing instrument in a configuration known as an object-plane electromechanical scanner. Its purpose is to make resource images of the earth from a remote (orbital) position. As shown in Figure 2, this instrument travels around the earth in a polar orbit and uses a flat scan mirror, placed in front of a telescope (object plane), to view the earth. The geometry of the scan-mirror/telescope system is designed so the line of sight from the mirror to the earth's surface is scanned back and forth (cross track) across the ground path (along track) of the orbiting spacecraft. Although the TM employs a set of 16 detectors in each of 6 reflection bands and 4 detectors in a thermal band, Figure 2 illustrates the fundamental detector scanning concept with a single detector for simplicity. The detector is sampled in such a way that a single sweep of the scan mirror is divided into a row of square picture elements (pixels) each having an instantaneous field of view (IFOV) corresponding to the area of the detector projected onto the ground. The final image, consisting of a large number of individual pixels, is produced by continuous cross-track scanning of the earth scene.

As illustrated in block-diagram form in Figure 3, the detector converts the viewed scene energy (photons) from each pixel into a weak electrical analog signal. This signal is amplified, sampled, and then quantized into a digital (binary) word. The many separate digital words generated during the scanning process are combined into a digitized data stream, transmitted by the spacecraft, received at ground terminals, and subsequently reconstructed into images of the earth's surface.

The portion of the electromagnetic spectrum (spectral band) within which the instrument is sensitive is determined by the detector material and a spectral filter placed in front of the detector. This design requires that a separate detector and filter be used for each spectral band the instrument is designed to sense. The principal characteristics of the spectral bands covered by the TM are listed in Table 1.

The basic elements of the TM instrument are shown in the frontispiece and in Figure 4. Scene energy from earth is first reflected off the scan mirror, which is protected from stray radiation by the sun shade. The scene energy is then focused by the telescope onto the detectors of Bands 1, 2, 3, and 4 at the prime focal plane and via the relay optics onto the detectors of Bands 5, 6, and 7 at the cold focal plane, which is cooled by the radiative cooler. A scan-line corrector behind the telescope keeps the scan lines parallel. The scan-line corrector is

followed by a calibrator that provides known reference sources to the detectors. The detectors convert the scene energy into analog electrical signals, which are amplified and sent to the processing electronics where the signals are further amplified and filtered.

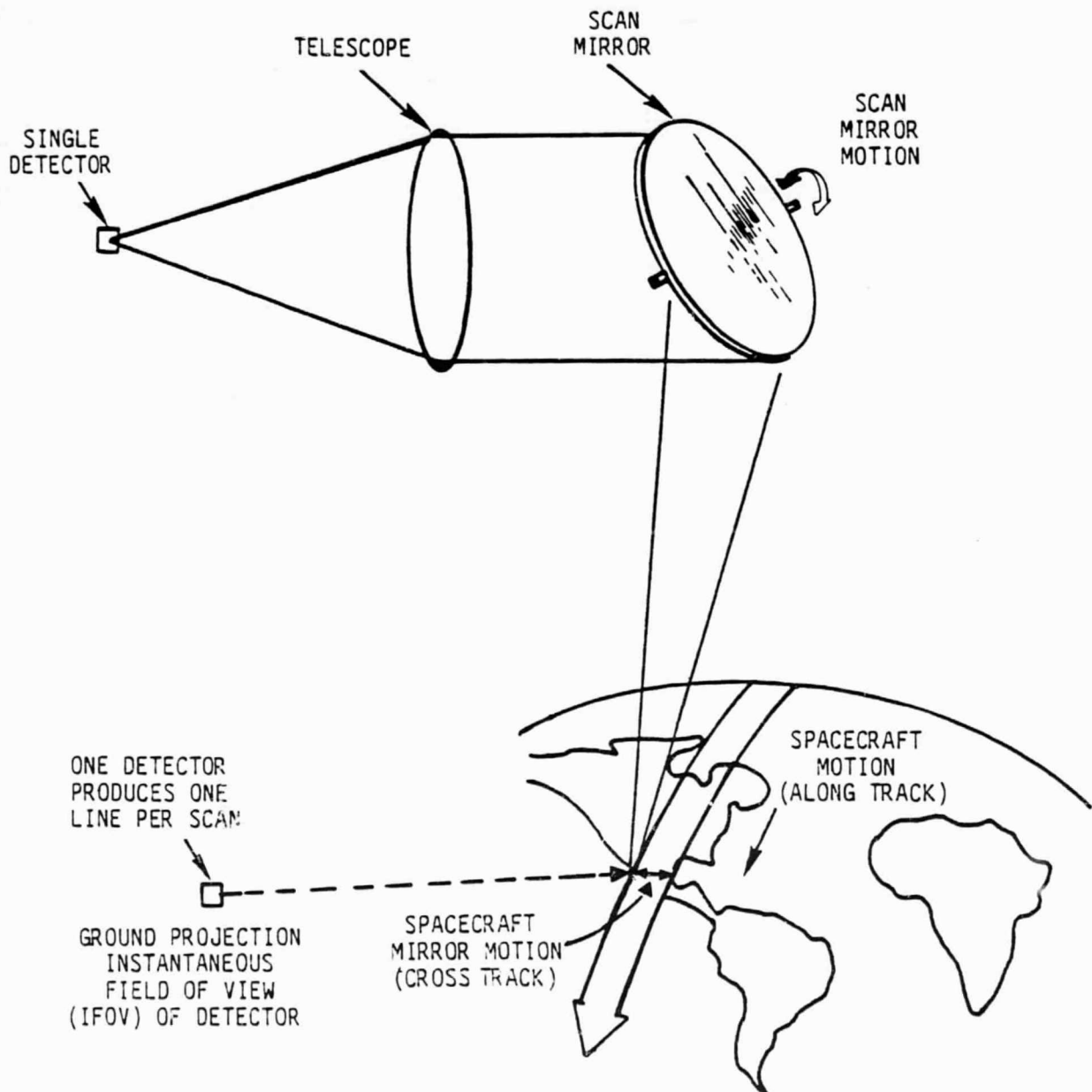


Figure 2. Single Detector Electromechanical Scanner Optical System

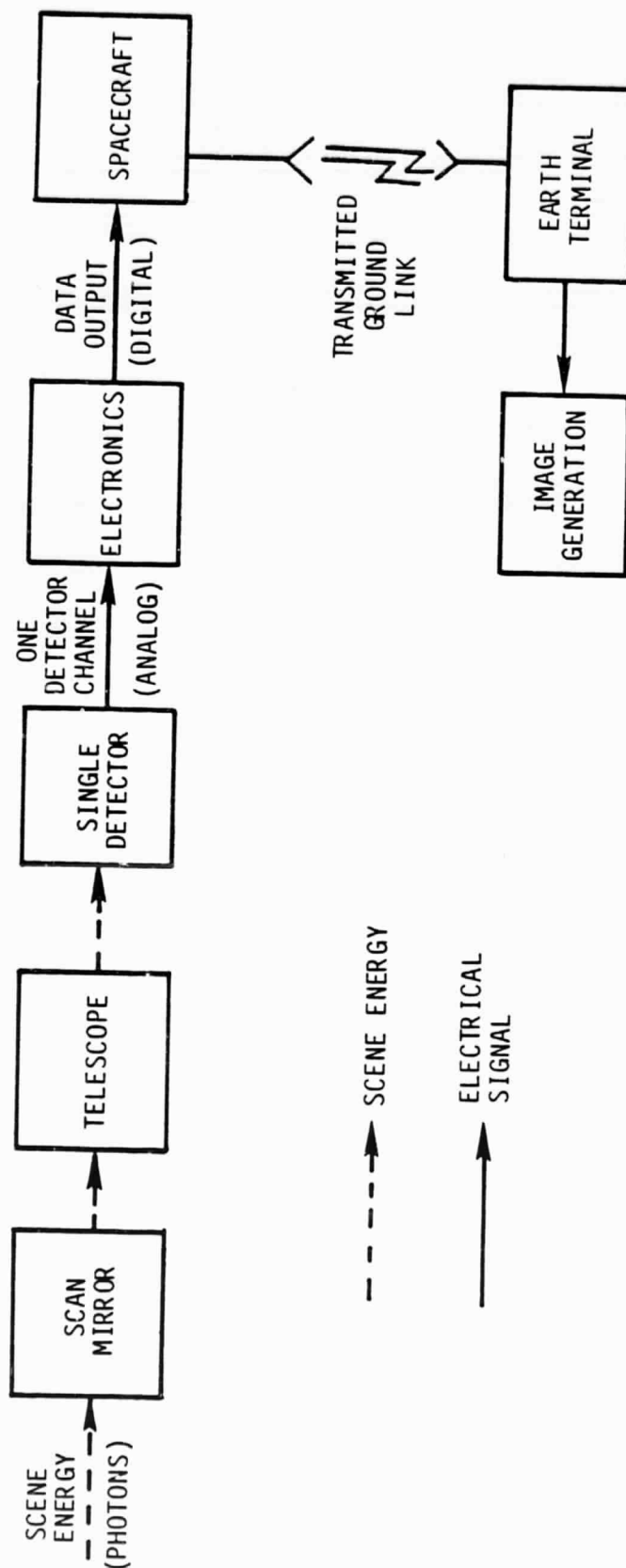


Figure 3. Single Detector Electromechanical Scanner System Block Diagram

Table 1. TM Band Characteristics Summary
 (Original Design Specifications)

Band	Spectral Range (μm)	Detectors (All Monolithic)		Spatial Resolution (m)	Radiometric Resolution	IGFOV* (μr) Nominal
		Type	Number			
1	0.45 to 0.52	Si	16	30	0.8% $\text{NE}\Delta\rho$	42.5
2	0.52 to 0.60	Si	16	30	0.5% $\text{NE}\Delta\rho$	42.5
3	0.63 to 0.69	Si	16	30	0.5% $\text{NE}\Delta\rho$	42.5
4	0.76 to 0.90	Si	16	30	0.5% $\text{NE}\Delta\rho$	42.5
5	1.55 to 1.75	InSb	16	31	1.0% $\text{NE}\Delta\rho$	43.75
6	10.4 to 12.5	HgCdTe	4	120	0.5K $\text{NE}\Delta\text{T}$	170
7	2.08 to 2.35	InSb	16	31	2.4% $\text{NE}\Delta\rho$	43.75
		Total	100			

*Instantaneous geometric field of view

The multiplexer then samples these parallel signals in sequence, converts them into digital words, and combines all the individual digital words into a serial-digital data stream to be transmitted back to earth.

The visible portion of the spectrum is covered by Band 1 (blue), Band 2 (green), and Band 3 (red). Band 4 covers the near infrared (IR), just beyond the visible red band. Band 5 and Band 7 are in the short wavelength infrared (SWIR) region. These bands sense the sun's energy that is reflected from the earth's surface. Band 6 responds to infrared energy emitted from the earth's surface (thermal infrared or TIR). The detectors of Bands 5, 6 and 7 must be cooled, because at these relatively long wavelengths high noise signals result from the internal thermal excitation of the detector materials. Cooling minimizes the noise signals and allows detection of the scene energy. As a result, Bands 5, 6, and 7 had to be located at a cooled focal plane, separate from the prime focal plane of Bands 1 through 4. The actual spectral coverage of each band is documented in the subsection on Performance and User Requirements in Section 4.

It should be understood that detectors in Bands 4 through 7 are sensitive to IR energy in spectral regions invisible to the human eye. To portray the images from these bands, they are displayed in visible colored pictures referred to as "false color" images. The images from these IR bands can be superimposed using different false colors or can be combined with images from any of the visible bands to produce a false-color, composite image. The particular kind of information desired determines which bands are used to make an image. Appendix A summarizes the process of creating color images from TM data and provides some examples.

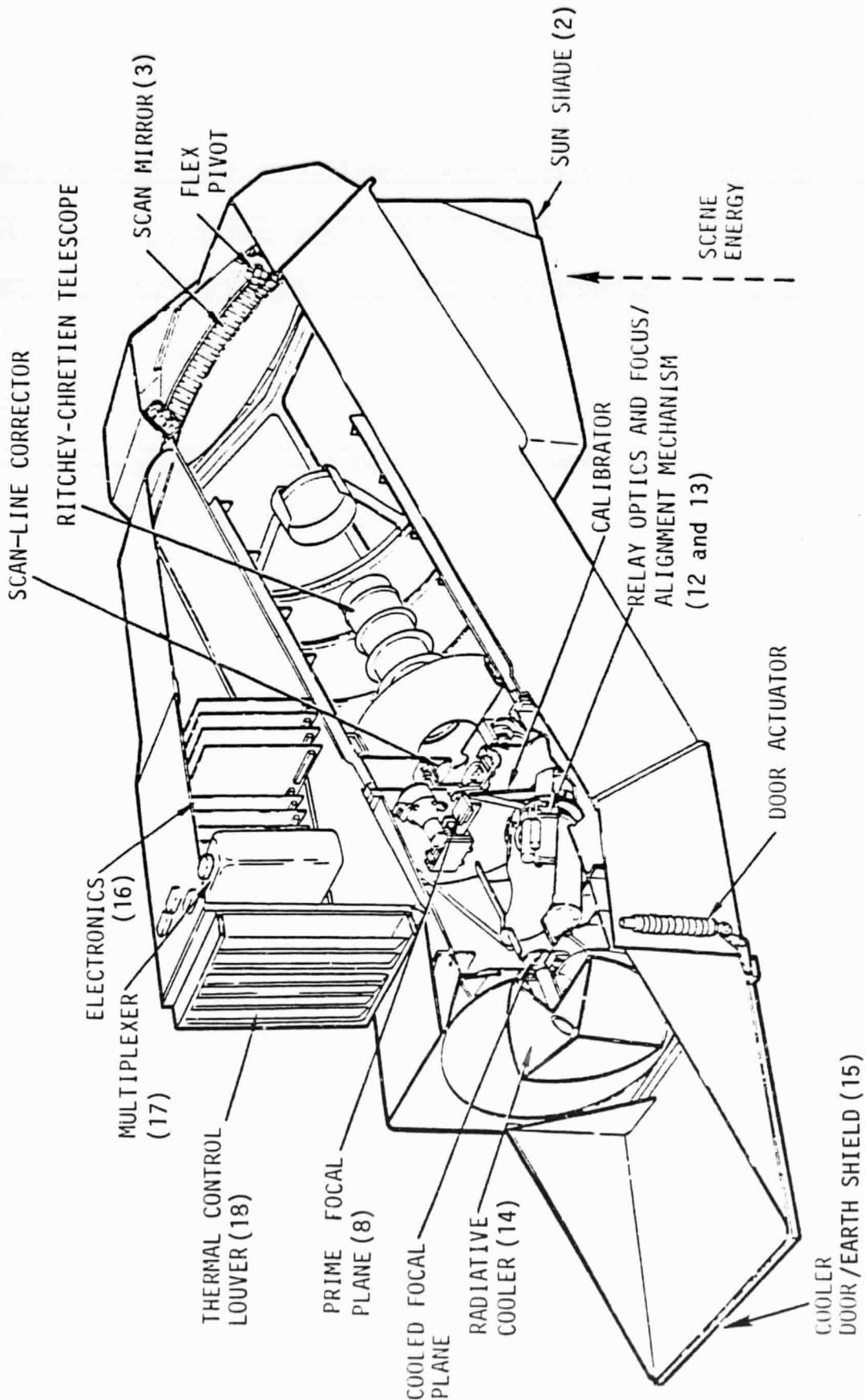


Figure 4. Thematic Mapper Cutaway View
[Numbers refer to the same assemblies in the Frontispiece.]

As shown in Figure 5, there are 16 detectors per band for Bands 1 through 5 and 7, providing a 30-meter ground IFOV for Bands 1 through 4, and a 31-meter ground IFOV for Bands 5 and 7. There are four detectors for Band 6, providing a 120-meter ground IFOV. A single active scan of the object-plane scan mirror sweeps a ground swath 185 kilometers by 480 meters across these detectors, collecting 16 lines of data at a time for Bands 1 through 5 and 7, and 4 lines at a time for Band 6. Each line of data (except for Band 6) is converted into 6176 pixels. One image, consisting of 5792 lines, takes 362 scans (16 lines per scan) to complete and produces over 35 million (6176×5792) pixels in just under 26 seconds.

The analog signal of each individual detector sample is quantized into an 8-bit binary word giving an encoding resolution of 256. This means that the total (dynamic) range of the detector signal is divided up into 256 steps. The data from all 100 signal channels is combined into an 84.9 Mbps (megabits per second) data stream.

DESIGN DETAILS

The details of the TM design are presented in this subsection by tracing the path of the scene energy from the earth as it enters the TM until it comes out as a digitized data stream. The basic elements of the design along this path are shown in Figure 6. This block diagram, the TM cutaway view shown in Figure 4, and the optical system shown in Figure 5 are germane to the following discussion.

Scan Mirror

As indicated in Figure 6, the radiant scene energy first enters through the sunshade. The sunshade was designed to prevent stray radiation from the sun, earth, or moon from entering the optical field of view. The first optical surface the energy contacts is the scan mirror. The scan mirror is a flat 21 inch by 16 inch (clear aperture) ellipse that provides the 185 km scan motion at a 7 Hz (cycles per second) scan frequency.

To attain the required control accuracy, a microprocessor is used as part of a digital controller to drive the scan mirror, and the scan mirror is torqued only during its turnaround periods in conjunction with low-loss leaf-spring mirror-reversal bumpers. The mirror is mounted on flex pivots (Figure 4), eliminating the friction and lubrication problems associated with bearing surfaces. The spring rate of the flex pivots is compensated for by a specially shaped permanent magnet assembly (flex-pivot compensator). This allows the active scan period, during which data is collected, to be free floating and, therefore, very linear.

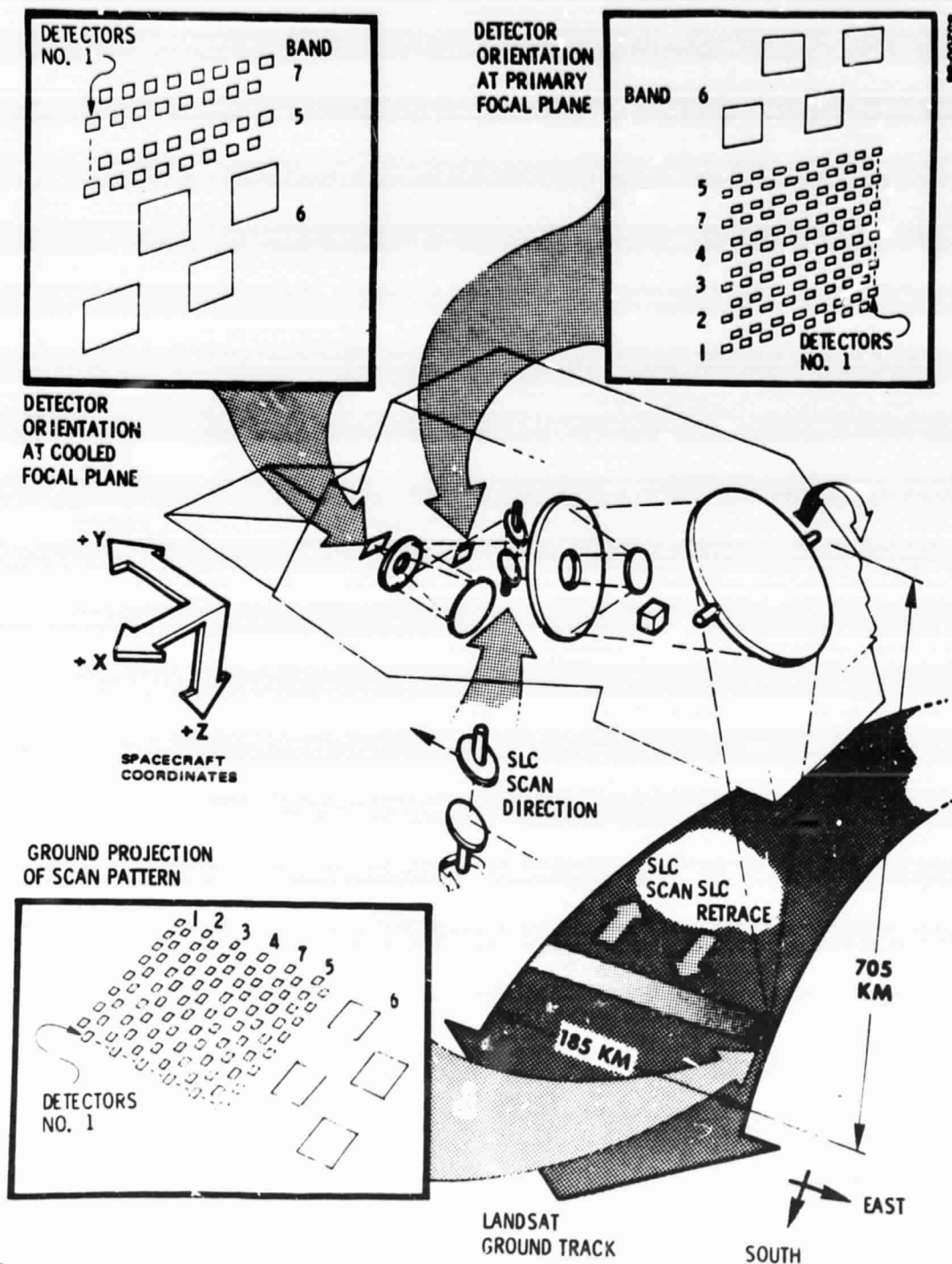


Figure 5. TM Optical System and Detector Arrays

ORIGINAL PAGE
BLACK AND WHITE PHOTOGRAPH

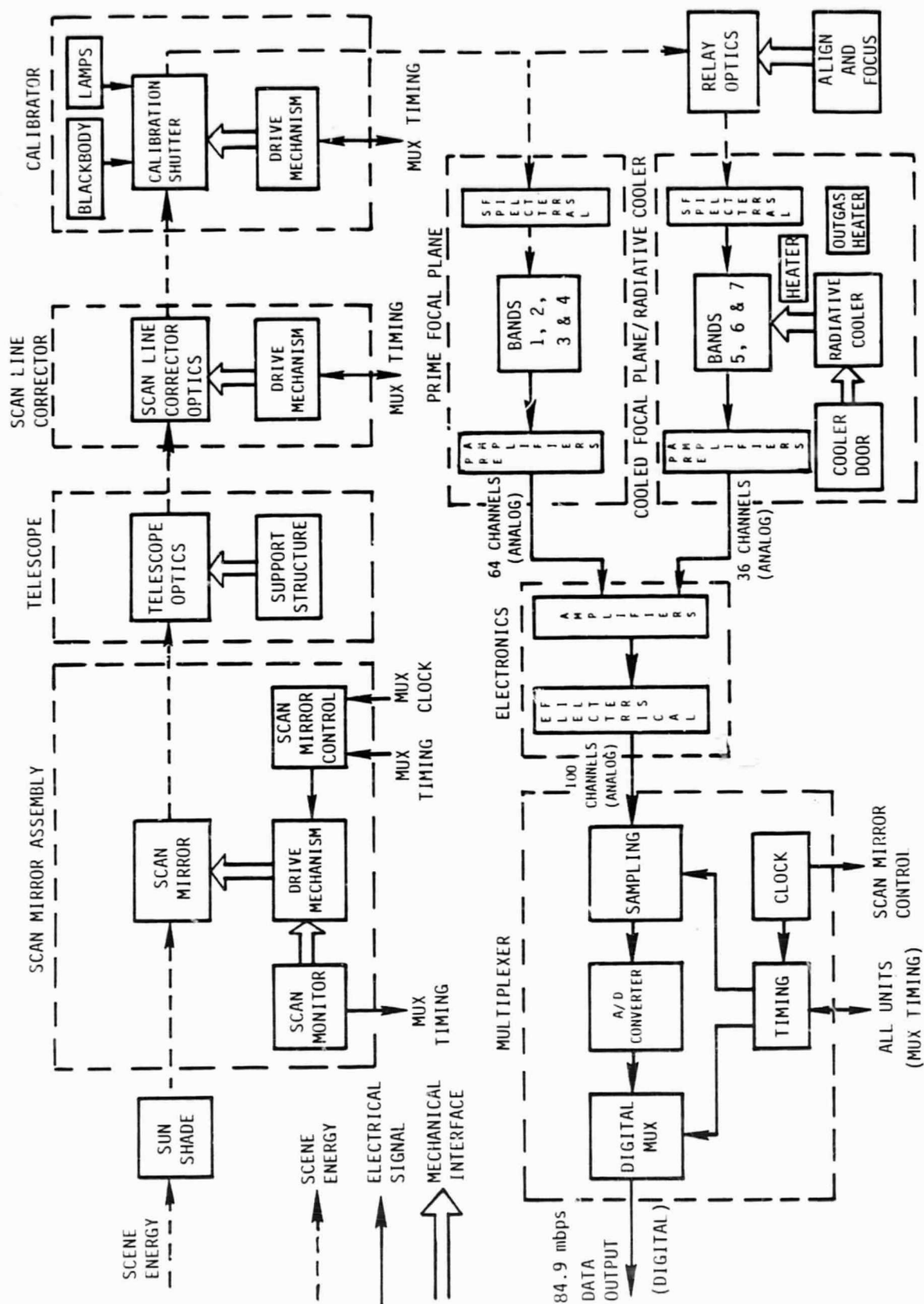


Figure 6. Thematic Mapper System Block Diagram

The size of the mirror was minimized by tilting the telescope's optical axis with respect to the scan mirror to give an angle of 70° between the telescope's optical axis and the line of sight from the mirror to the earth.

The scan-mirror assembly had to have a high stiffness-to-weight ratio to give it a low inertia while maintaining a high degree of mirror surface flatness. The requirements were met by utilizing a beryllium eggcrate design for the scan mirror and mounting it to a beryllium frame. The mirror surface is nickel plated and silver coated to give high reflectance with low scattering over all the TM spectral bands. A final coat of silicon dioxide (SiO_2) was applied to protect the silver coating.

The scan-mirror assembly generates pulses at the start, middle, and end of each scan line. The scan mirror's start and end-of-scan pulses are the pulses to which all other elements of the system are synchronized. The proper synchronization of all the elements of an electromechanical scanner is very important to ensure that the millions of individual pixels required to make an image are properly placed to maintain geometric accuracy. Due to the importance of this feature, a backup scan-monitor system is provided by electric pickoff coils located in each bumper assembly.

Telescope

The scene energy reflected from the scan mirror enters a telescope consisting of a primary and secondary mirror configuration often referred to as a Ritchey-Chretien design. Both telescope mirrors are constructed of ultra-low-expansion (ULE) titanium glass, coated with silver and protected with a SiO_2 overcoat. The telescope has a clear aperture of 40.6 cm (16 inches) and a 243.8 cm (96 inches) effective focal length (EFL).

The large size of this telescope required that the support structure be as light as possible while still giving the required stiffness and low thermal expansion. Graphite-epoxy composite material meets these requirements and was chosen as the material for the telescope support tube. However, the tendency of graphite-epoxy composite material to absorb water from the air complicated the handling of the instrument and required that the TM be kept in an environment with strict humidity control during all assembly, test, and shipping operations.

A second and more complex problem resulted from the need to place the detectors at the proper focus. Special measurement techniques were developed to determine the effective focal length (EFL) of the telescope to within the very small tolerance dictated by the registration requirements.

Scan-Line Corrector

The telescope images the scene through a scan-line corrector (SLC) onto the focal plane. The SLC is a two-mirror device with an axis of rotation perpendicular to the axis of rotation of the scan mirror.

The TM collects data in both scan directions. If no corrections were made, the TM scan pattern would be as shown in Figure 7a. Without the SLC there would be gaps where no scene data would be collected (underlap) and areas where the scene data would be collected twice (overlap). The SLC steps the line of sight in the direction of spacecraft travel at the end of each scan and then moves the line of sight in a direction opposite to the spacecraft travel during the active scan at a rate exactly matching the ground-track movement during the scan period (Figure 7b). As a result, the forward and reverse scans become parallel to each other and perpendicular to the ground track without over- or underlap, as shown in Figure 7c.

This corrected scan geometry allows the TM to collect data in both scan directions and yields 85% scan efficiency, compared to the MSS value of less than 50%. Therefore, each individual detector views the scene for a longer period of time (increased dwell time) compared to a lower scan-efficiency system. This increases the signal to the detector, and provides improved radio-metric sensitivity for the data user.

Calibrator

The calibrator is an oscillating shutter mechanism located between the SLC and the prime focal plane. It is used to provide calibration sources for all 100 detector channels.

The calibrator is synchronized with the scan mirror in such a way that it brings the calibration sources sequentially in view of the detectors during each scan mirror turnaround (when no scene data is being taken). The calibration source consists of three tungsten lamps, which, in combination provide eight known radiant levels for Bands 1 through 5 and 7, and a blackbody (standard thermal radiator), which can be set to any of three known temperatures for Band 6. A black surface of a known temperature also provides a source for a dc-restoration of all bands. The dc-restore function provides Bands 1 through 5 and 7 with a zero radiance reference and provides Band 6 with an ambient temperature reference. Should a problem occur in the drive mechanism of the calibration shutter, it can be commanded aside, and a backup shutter can be used to provide the essential dc-restore function.

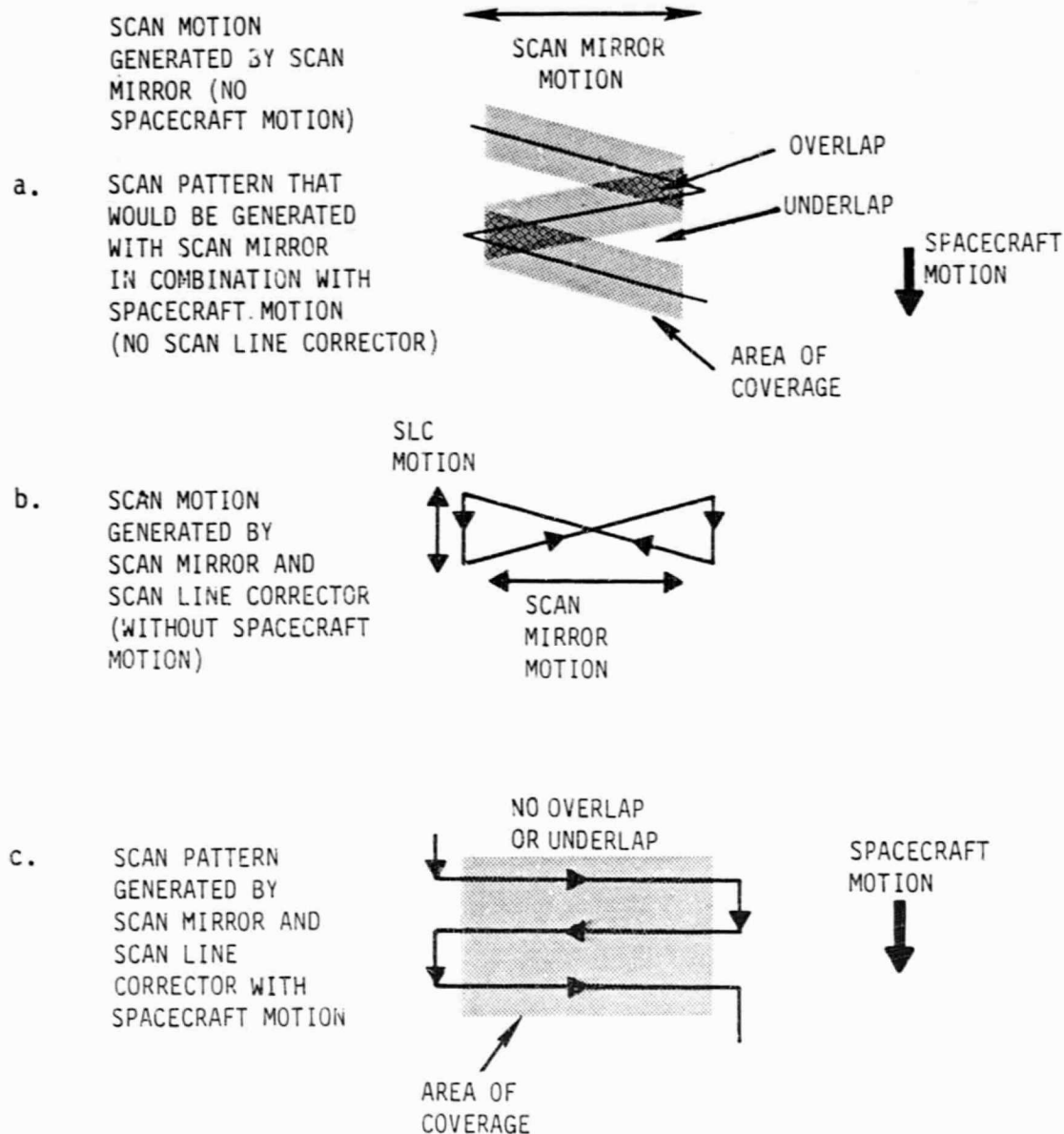


Figure 7. Scan-Line Corrector Effect on Scan Pattern

Prime Focal Plane

The scene radiant energy, after passing through individual spectral filters for each band, reaches the detectors of Bands 1 through 4 located at the prime (uncooled) focal plane. Each individual spectral filter, in combination with the detector material, determines the frequency or spectral range of radiant scene energy (band) over which the detectors will respond. Each band consists of a 16-detector array, within a single silicon crystal (monolithic). Each of these monolithic silicon detector arrays is located at the prime focal plane.

Each of the 16 detectors is approximately $0.01 \text{ cm} \times 0.1 \text{ cm}$ and provides a 30-meter IFOV. The array of each band is configured as two parallel columns of 8 detectors, staggered to provide 16 side-by-side lines per scan-mirror sweep (one column of 8 contains the even-numbered detectors, the other contains the odd). Each band is registered to all others so that the 16 lines of each band will overlap precisely. This allows the data from separate bands to be combined to produce a correctly registered composite image.

The arrays are placed close together to keep them near the telescope's optical axis where image quality is best and to reduce the time-delay between data collects for each band. This minimizes registration errors that might result due to slight changes in scan-mirror velocity.

The detectors convert the scene radiant energy (photons) into very low level analog electrical signals, requiring that the preamplifiers be located near the prime focal plane and as close as possible to the detectors to minimize unwanted noise. Low-noise current-mode preamplifiers were designed to provide the initial amplification of the small detector signals. A boost amplifier further amplifies the signal over the system bandwidth and interfaces with the multiplexer electronics.

Relay Optics

Part of the scene radiant energy at the prime focal plane is refocused with 0.5 magnification through a relay optical system to the Bands 5 through 7 detectors at the cooled focal plane.

The relay optics consist of a folding mirror and a spherical mirror made of the same ULE glass used for the telescope mirrors and mounted in a graphite-epoxy structure. The mirrors are coated with aluminum and a protective SiO_2 overcoat, which efficiently reflects the scene radiant energy of Bands 5, 6, and 7. Aluminum was not used for the other optical surfaces ahead of the relay optics because aluminum absorbs scene energy in Band 4.

A unique feature of the relay optics is the ability to move the spherical mirror with respect to the optical axis in small linear steps using piezoceramic "inchworms." The piezoelectric

property causes a small dimensional change to occur when an electric field is applied. Three of these devices, located at equally spaced suspension points around the spherical mirror, can be commanded to provide on-orbit focus (when moved together) and registration corrections (when moved differentially) of the cooled focal plane (Bands 5 through 7) with respect to the prime focal plane (Bands 1 through 4). This capability was provided as a safeguard. However, to date, no post-launch corrections have been implemented.

Cooled Focal Plane/Radiative Cooler

The scene energy coming from the relay optics passes through spectral filters and then contacts the detectors of Bands 5 through 7. Bands 5 and 7 each consist of a monolithic 16 detector array made from indium antimonide (InSb). The layout of these detectors is the same as the arrays of the prime focal plane, except the detectors are half the size. Band 6 consists of a monolithic four-detector array made from mercury cadmium telluride (HgCdTe). These detectors provide a 120-meter IFOV. The four detectors are configured into two columns of two detectors, staggered to provide four side-by-side lines per scan.

Since the InSb detectors used for Bands 5 and 7 are similar in operation to the silicon detectors of the prime focal plane bands (high impedance), a combination current-mode preamplifier with boost amplifier was also used to provide the necessary low-noise amplification. The HgCdTe detectors of Band 6 are low-impedance devices. Their noise characteristics allowed the use of bipolar preamplifiers without boost amplifiers.

The detector arrays of Bands 5, 6, and 7 are mounted on the radiative cooler. The radiative cooler is designed to provide the required cooling of these arrays by radiating heat into deep space. It also has provisions for cooling the arrays during bench testing. The arrays can be controlled to any of three temperatures (90K, 95K or 105K) by means of a thin-film heater on the back of the cold focal-plane substrate. The arrays of the cold focal plane must be kept cold to function properly; and the temperature must be held constant to get predictable detector responses.

The radiative cooler is protected by a door in the launch configuration to prevent contamination. The door is commandable to an intermediate outgassing position after launch to allow contaminants to vent out prior to cool-down (door fully opened). This action, combined with turning the heaters on during the outgassing process, prevents contaminants from settling on and degrading the specular surfaces of the radiative cooler, thus degrading the performance of the cooled detectors.

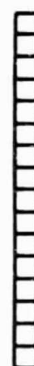
Signal Processing

After amplification and filtering in the analog electronics, the signals from the 100 detector channels (64 plus 36) are fed to the multiplexer, which determines the sequence in which the detector channels are sampled and sequentially converts each held sample into an 8-bit digital (binary) word. This 8-bit binary word gives an encoding resolution of 256 levels.

Each detector channel has its own track-and-hold circuit. These circuits allow the detectors to continuously track the scene energy and then hold the analog signal level each detector has when it is sampled. The detectors are sampled at a frequency that places the centers of each projected detector one IFOV apart on the ground. Each band has one analog-to-digital (A/D) converter which converts the analog signal of the track-and-hold circuits for all the detectors within a band into 8-bit digital words. All detectors in one column of a detector array are sampled simultaneously and then converted to digital words. The next column is sampled later such that an integral number of IFOVs separates the two columns in the raw data transmitted to ground. This integral IFOV spacing is then removed in ground processing. The result is a single, straight column perpendicular to the scan direction and composed of all the detectors of a band, placed side-by-side as shown in Figure 8.



Before Ground Processing



After Ground Processing

Figure 8. IFOV Alignment

During mirror turnaround, the detector channels are dc-restored and calibration data is collected. Additional scans are made with each scan parallel to, and placed next to, the previous scan by the combined action of the scan mirror, scan-line corrector, and spacecraft motion.

To correctly perform the above process, the multiplexer provides a time base (clock) for a digital system that controls the scan mirror motion. The multiplexer is synchronized to the "line

start" and "line stop" optical pickoffs on the scan mirror that occur at the beginning and end of the active scan period. The multiplexer then uses this information to synchronize the motion of the scan-line corrector, calibrator, and data-processing electronics to the scan mirror.

The final function of the multiplexer is to combine the individual digital words into an 84.9 Mbps data stream, which is sent to the spacecraft for transmittal to the earth ground-processing equipment, either directly or via a tracking and data-relay satellite (TDRS).

The multiplexer, in combination with the other electronics, dissipates most of the power the TM uses. Potential heating problems are prevented by cooling these systems with a louver assembly that faces in the same direction as the radiative cooler. The amount of cooling is controlled by bimetallic actuators that control the angle of the louver blades, thereby controlling the effective emissivity of the radiating area.

Section 4

PERFORMANCE AND USER REQUIREMENTS

PERFORMANCE PARAMETERS

The basic design goal of a sensor instrument such as the TM is to create a system that provides radiometrically accurate and spatially detailed spectral signature maps of the earth's surface from orbit. The requirements established by the earth-resource scientists for the TM system take into account both the quality of data needed and the technical limitations imposed on attaining that quality of data. The limitations result partly from the technology available and partly from some fundamental physical limitations. A brief review of these limitations is presented here to introduce the key performance parameters that define TM image quality. More can be found in Short [1982], Slater [1980], and Schueler [1983].

Basic Limitations

Figure 9 illustrates the three fundamental limitations that prevent a perfect sensor from being designed: radiometric, spatial, and spectral resolution (and coverage).

Radiometric resolution is constrained by uncertainties in the exact value of a signal received by the sensor. These uncertainties are created by noise in the received radiance and in the sensor electronics. Radiometric coverage is limited by the maximum signal anticipated, and in principle, the sensor can be designed to measure signals to the very peak of the reflected or emitted radiance from the earth's surface.

Spatial coverage is controlled by the swath over which the sensor scanning system is designed to image. The sensor may be designed to cover a wide swath in two basic ways, as depicted in Figure 10. The scanning sensor on the left is called a whiskbroom sensor, because the image is acquired by a single detector that is rapidly scanned back and forth across the orbital track as the sensor moves along its polar orbit. The concept on the right is known as a pushbroom sensor, because the image is acquired by a line array of detectors covering the entire cross-track field of view. The scan is accomplished by the orbital motion of the sensor, and no scanning mirrors are needed to obtain the image.

The whiskbroom concept allows a wide swath to be created with only a single detector and narrow field-of-view optics. The difficulty with the whiskbroom concept is that the detector must be moved rapidly, and it cannot spend much time sampling individual spots on the ground. Each of these individual spots on the ground, equal in area to the geometrical projection of the detector onto the ground, is referred to as the instantaneous field of view (IFOV) of the detector.

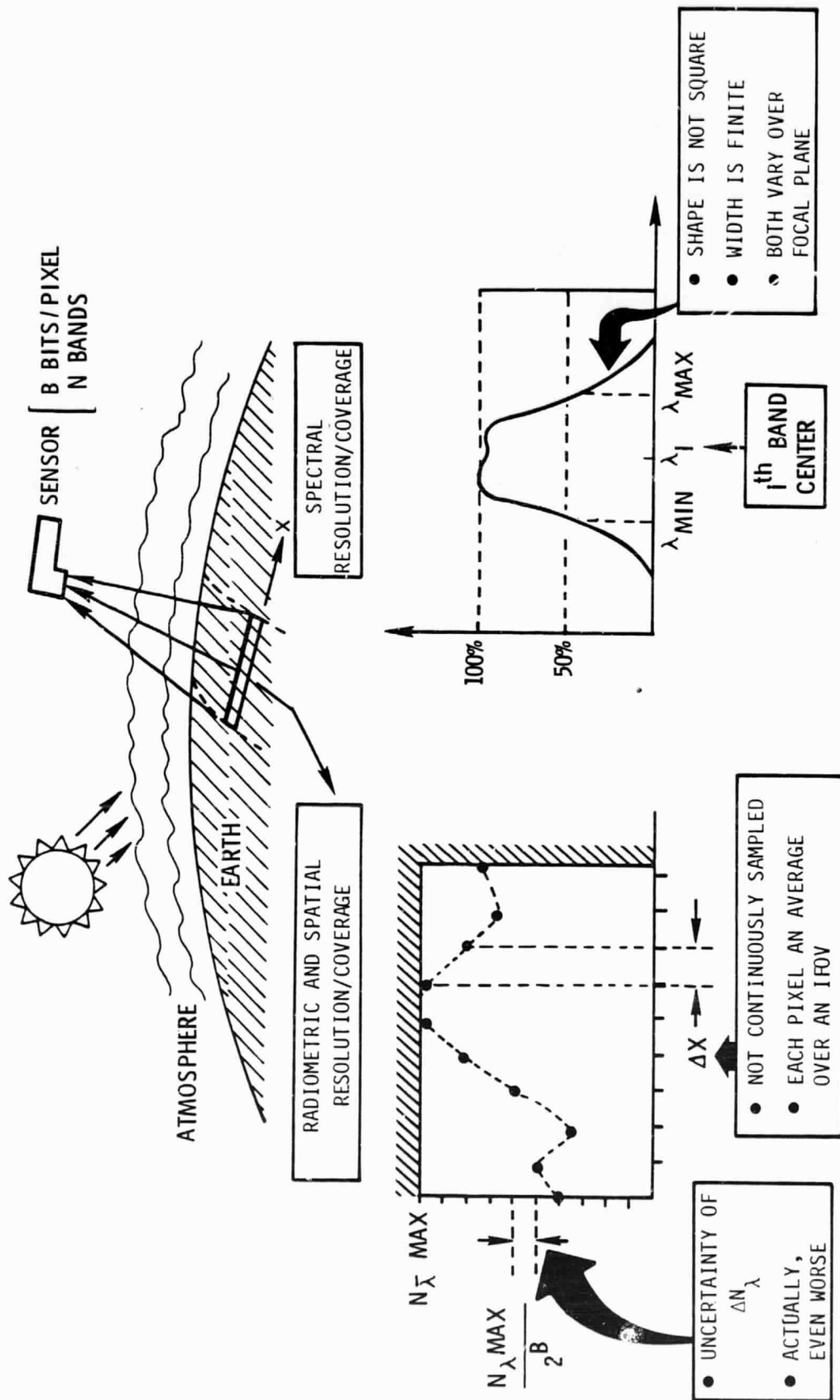


Figure 9. Fundamental Limitations on Sensor Design

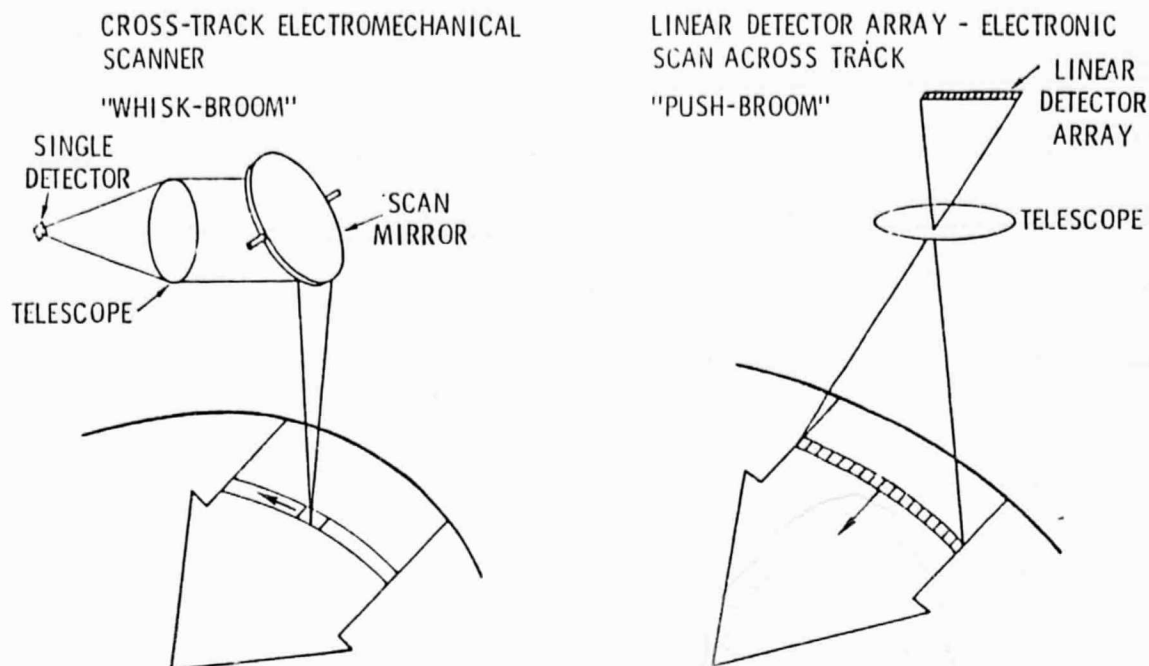


Figure 10. Sensor Swath Coverage

The pushbroom concept uses a line array of detectors extending across the orbital track, so no cross-track scanning is required. In this case, no scan-mirror system (such as used in the TM) would be required, and the detectors would each be able to spend a much longer time sampling the ground IFOV. This configuration increases the amount of signal the detectors receive and improves radiometric resolution by improving the signal-to-noise ratio (SNR) of the sensor. However, the concept requires a wide field-of-view optical system and thousands of detectors.

A compromise approach is to use a hybrid of the pure whisk-broom approach and the pure pushbroom approach; i.e., to place a line array of detectors parallel to the orbital motion of the sensor and to scan the line array across-track more slowly than would be necessary with a single detector. This hybrid approach offers improved SNR over the pure whiskbroom scanning concept and was selected for the TM.

Interrelationship Among Constraints

The advantages and disadvantages of the basic scanning mechanisms just described illustrate the intimate relationship between radiometry and spatial coverage. Instantaneous, wide spatial coverage offers improved SNR, and, therefore, improved radiometric accuracy leading to development efforts to produce line arrays as long as the state of technology allows. In the case of the TM, line arrays consisting of 16 detectors were used.

The instantaneous field of view, or IFOV, referred to above, plays a critical role in spatial resolution. The smaller the IFOV, the better the spatial resolution of detail on the ground. However, there is a relationship between the radiometry and spatial-image quality that must be considered. As the IFOV is reduced, the detector size is reduced, and the amount of radiant energy seen by the detector is reduced. Therefore, a smaller IFOV leads to reduced signal, and the SNR is degraded.

Finally, the spectral coverage and resolution define how well the sensor will provide spectral signature information. Again, there is a connection between spectral integrity and radiometric quality. As the spectral bandpass associated with a given detector's sensitivity is made finer, so as to provide more definitive spectral information, the radiant energy absorbed by the detector is reduced, and SNR is degraded.

In addition to the three basic limitations imposed on the sensor as depicted in Figure 9, the designer also attempts to minimize radiometric calibration errors and geometric errors. Radiometric calibration errors include absolute radiance measurement errors as well as relative errors between spectral bands and within bands, from detector-channel-to-detector-channel in a multidetector sensor such as the TM. Geometric errors include pointing errors, band-to-band registration errors, and errors caused by nonuniform motion of the scanning mechanism.

The Effect of Sensor Subsystems on Image Quality

The diagram of Figure 11 tabulates the principal error sources contributing to inaccuracies in each of the categories of image quality previously discussed. At the top of the diagram is a block-sequence representation of the sensor. This block representation is general enough that it does not suggest any specific design, nor does it limit the design to any specific set of requirements, such as those imposed by NASA on the TM. Therefore, Figure 11 can be regarded as a generic chart of items to consider when designing any electro-optical imaging sensor system. For example, any sensor must have optics to focus an image to be detected, a spectral separation system to define spectral bands, and detectors to convert the detected light into electrical signals to be processed into video by an electronics system. To enhance transmission of signal to the ground, the analog signals must be digitized, and the remaining electronics blocks are provided to illustrate that process.

Each sensor subsystem is subject to errors that will affect one or more of the image-quality categories of Figure 9. These image-quality measures are listed in the left column of Figure 11. The way in which each subsystem affects each measure is indicated by an entry in the appropriate box underneath the subsystem of interest. For example, as the optical system's transmission drops, SNR drops, and this degrades radiometric resolution, as indicated by the entry in the top left box under the

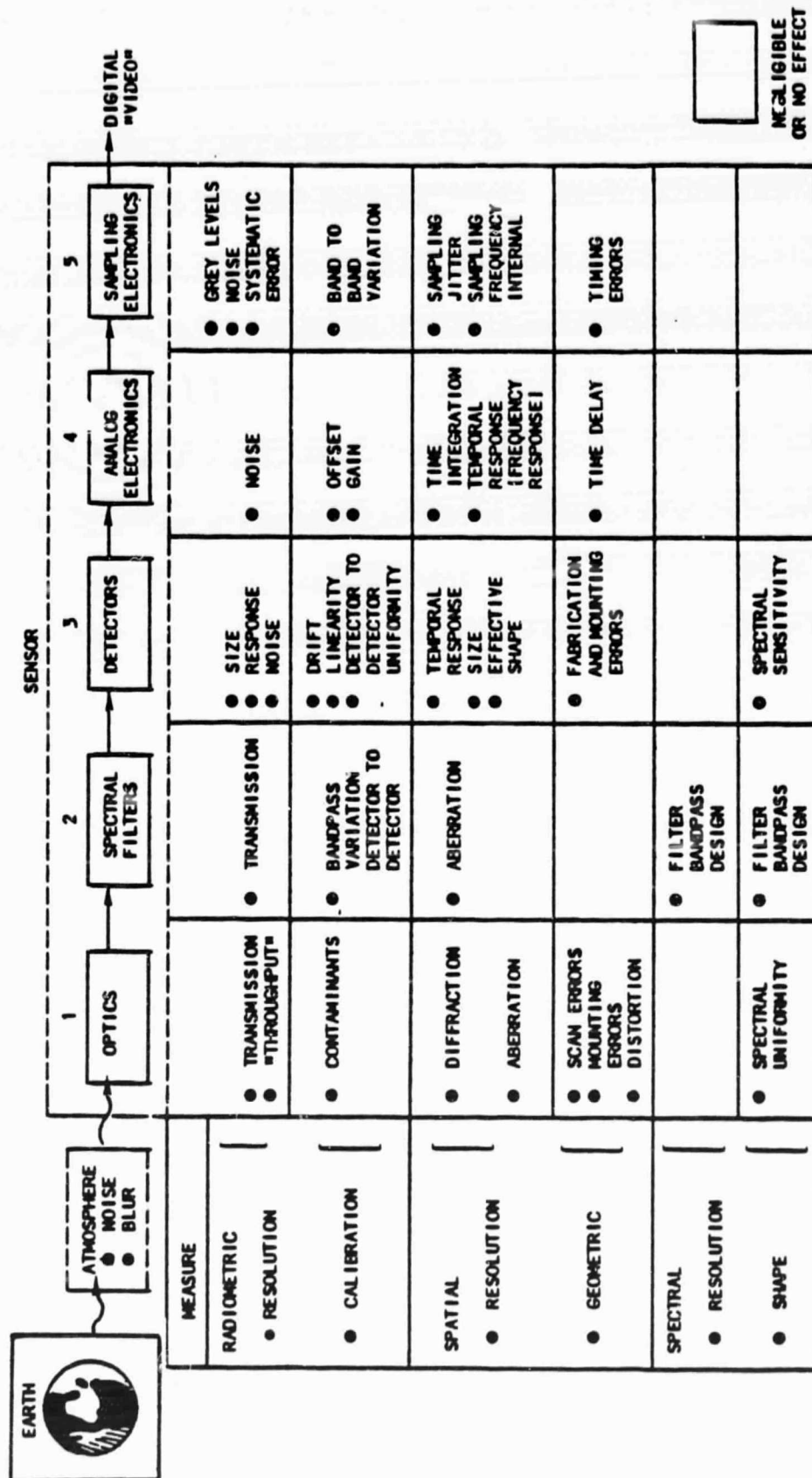


Figure 11. Error Sources Affecting Image Quality

optics block of the sensor block diagram. In general, anything that reduces signal or adds noise will reduce radiometric resolution. The chief sources of signal reduction and noise are listed from block to block in Figure 11. In general, radiometric calibration is degraded by anything that causes uncontrollable signal variations to occur between calibration checks. The major sources are listed in the row beside the calibration entry in the left column of the figure.

Spatial resolution is degraded by sensor subsystems that tend to blur the image. These include optical diffraction and aberration, detector IFOV, and temporal frequency response. Temporal frequency response is important because the detectors are usually sampled while scanning rapidly over the scene. If the sample rate is fast, little time is available for a detector to respond to radiance changes from scene location to location, and slow response will blur the image. By the same token, the electronics' temporal response is also a factor in spatial resolution.

Geometric errors result primarily from sensor pointing and scanning errors. If the sensor wobbles in orbit and the wobble is not accounted for, error will result; the scan mechanism can give the same sort of error. Band-to-band registration error results mainly from errors in fabrication and alignment of the detectors in the focal plane, although electronic timing errors and sampling errors can also contribute to degradation.

Spectral resolution is affected almost exclusively by the design of the spectral filtering system. However, spectral bandpass shape can be affected by several factors throughout the imaging chain. The optical system may consist of reflective mirrors whose surfaces have wavelength-dependent reflectivity. The filters may exhibit nonuniformity along the spatial dimension of the line detector array, so that spectral bandpass nonuniformities will occur in a given spectral band for different detectors. Finally, the detectors themselves have a characteristic spectral response, which is generally not flat. The uniformity of this response from detector to detector within a given spectral band also affects spectral bandpass uniformity.

Engineering Requirements

The TM requirements gave the designer the radiometric, spatial, and spectral performance goals the instrument had to meet to match user needs. These requirements were stated in terms of engineering requirements or specifications that allowed the designers to test each design approach by calculating the theoretical performance of a design and comparing that prediction against the specification. Moreover, the requirements were stated in terms of laboratory-measurable quantities to allow the performance of the sensor to be checked against the specifications as the sensor was being constructed and tested. The engineering requirements are stated in different terms from the usual user

requirements. In the following subsections, each of the principal radiometric, spectral, and spatial image quality requirements is discussed in turn. Design of electro-optical sensors is covered in more detail in Seyrafi [1973].

Radiometric Requirements

The data user is accustomed to quantifying radiometric resolution in terms of "noise-equivalent ground reflectance variation" ($NE\Delta\rho$) or "noise-equivalent temperature difference" ($NE\Delta T$) in the thermal regions. This reflectance, or emittance, variation produces a signal change at the sensor, equal to the sensor noise level and is translated to the resulting SNR for engineering design and measurement purposes. (The process for performing this translation is explained in the Manual of Remote Sensing [Colwell 1983, chap. 12].) Measurement of the sensor's SNR is a straightforward process, and is described in Section 7 of this report. Radiometric accuracy requirements are stated in terms of a percentage relative to the full-scale radiance the sensor must measure, and the engineering requirements are stated in these same terms. Although radiometric accuracy is conceptually simple to specify and to appreciate, it is extremely difficult to attain excellent accuracies and even more difficult to verify radiometric-accuracy performance. For example, the TM requirements for radiometric accuracy were stringent (10% of full-scale signal), and to verify this performance required a calibration sensor of even better accuracy. As a result, the radiometric calibration program to test the TM, described in Section 7, was extremely difficult and expensive.

Spectral Requirements

The spectral data-quality requirements are conceptually simple, but in practice are also difficult to attain and to verify. The major requirement of interest is the spectral bandpass center and width. In general, the goal is to have a sensor with an exactly uniform spectral response over some wavelength interval with sharp cutoffs on either end. In practice, it is difficult to obtain either uniformity or very sharp spectral cutoffs. Therefore, the sensor designer needs some quantified requirements on the allowable uniformity errors and on the sharpness of the spectral cutoffs.

In this regard, it is possible to relate the spectral bandpass uniformity to radiometric uniformity. Figure 12 illustrates this concept. Figure 12a shows the spectral responses of two detectors, labeled detector A and detector B. Both detectors are members of the same spectral band, and both are illuminated through the same spectral filter. However, the detectors do not share the same spatial location underneath the spectral filter, and the spectral response of the filter may vary from point to point along its length. As a result, even after radiometric calibration, the two detectors may have different spectral responses over the bandpass illustrated in the diagram. The detectors have

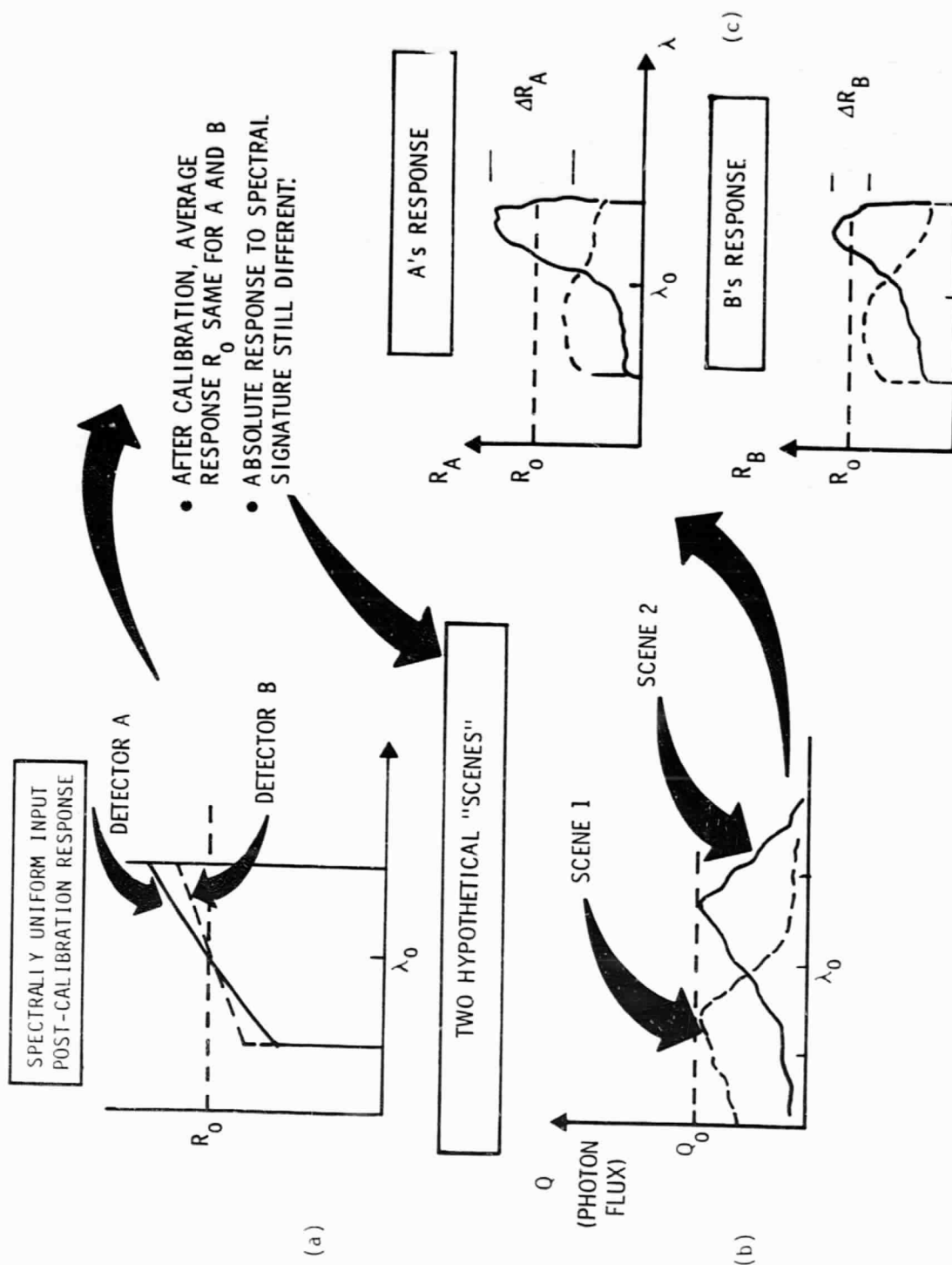


Figure 12. Relationship of Spectral Bandpass and Radiometric Uniformity

the same average response to light after calibration, but the calibration cannot correct for variations in spectral response within a bandpass. In Figure 12b, two hypothetical scenes are illustrated, each with different spectral content. Finally, Figure 12c shows the response of each detector of Figure 12a to the scene spectral radiance of Figure 12b. Both detectors respond more strongly to scene 2 than to scene 1, because both detectors have a nonuniform spectral bandpass. Therefore, the non-uniform spectral bandpass causes radiometric error in measuring radiance of a scene input. Moreover, since the slopes of the bandpasses for the two detectors are not equal, the responses of the detectors do not agree, even though the detectors are calibrated so that the average response to a flat input spectrum is the same for both.

Therefore, there is a relationship between radiometry and the spectral bandpass shape (slope and cutoff sharpness) and detector-to-detector bandpass uniformity. This relationship can be exploited to derive sensor spectral performance requirements. In principle, once the sensor is built it is possible to test the sensor's spectral response from channel to channel to verify performance. The tests that were performed in this regard are discussed in Section 7 of this report.

Image Quality Requirements: MTF and Aliasing

The user requirement for spatial image quality, usually referred to in terms of IFOV, is more complicated in concept than either the radiometric resolution or spectral resolution requirements, but in practice is simple to specify. However, the actual measurement program required to verify performance is complicated and difficult.

Spatial resolution is affected by several sensor subsystems, as generally discussed in reference to Figure 11 above. Detector IFOV is only one element of the spatial resolution parameter. In fact, by itself, it falls quite short of describing the actual spatial resolution of the sensor. In addition to IFOV, optical blur, detector-motion blur, and the electronics' temporal-response blur must also be specified. The total system blur may be characterized by the width of the image of a perfect line source. This image is called the system line-spread-function (LSF) and is described by Schueler [1983a]. Spatial resolution is conceptually complex because of the apparent dissimilarity among the many factors contributing to blur. However, these factors can be combined into a single parameter that describes the total system blur. This parameter is the modulation-transfer function, or MTF, which is the Fourier transform of the LSF [Schueler 1983a]. As the name implies, the MTF describes how image modulation is transferred through the system. To understand the utility and power of the MTF parameter, the basic concept of image modulation must be understood.

As a detector scans across the image provided by the optics, the intensity of the light falling on the detector changes due to the variation in light intensity reflected from different points on the ground scene the sensor is imaging. These variations are modulations, and, depending on the rapidity with which the detector scans and on the sharpness of edges within the scene, the modulation can be slow or fast. Slow modulations are generally imaged fairly well, but faster modulations, corresponding to sharp edges in the scene, may be blurred.

Any complicated image-modulation pattern can be constructed mathematically by combining simple sinusoidal-wave patterns of different frequency and amplitude. Sharp edges would contain high proportions of high-frequency sine waves, and slow gradations in brightness would contain larger amounts of lower frequency sine waves. The response of a detector to a sine-wave modulation input is illustrated in Figure 13. The input sine-wave amplitude is larger than the output sine-wave amplitude because the detector has a finite IFOV that averages the sine wave over a distance denoted by the Greek letter "alpha" in the diagram. The reduction in the amplitude of the sine-wave modulation is a function of the frequency of the sine wave. A sine wave with a low frequency would not be affected much, whereas a high-frequency sine wave might be considerably reduced in amplitude.

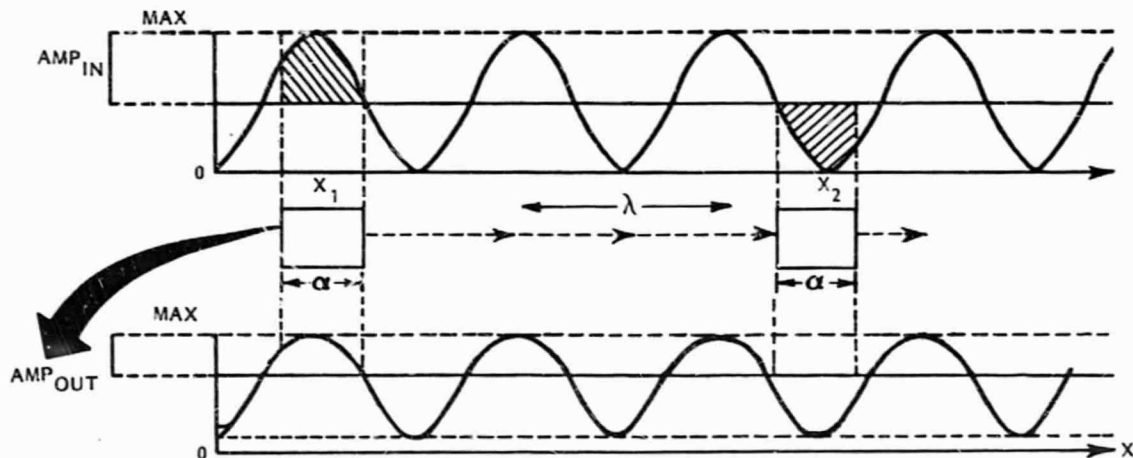


Figure 13. Detector Response to Sine-Wave Modulation

A plot of the functional dependence of the modulation on the frequency of the sine wave for the square-detector IFOV is depicted in Figure 14. As shown, the modulation of high frequencies is considerably reduced. In fact, for some frequencies whose periods fit perfectly within the detector IFOV, the MTF is zero, and the detector will sense no image variation at all. Not only the detector IFOV has this effect. The MTF associated with any other part of the imaging chain can be computed theoretically, or measured experimentally, in at least an approximate fashion with input sine-wave or square-bar light patterns of different frequencies. When a square-bar pattern is used, the resulting

sensor response is called square-wave response (SWR). SWR and MTF are closely related and one can be approximated from the other. A more detailed description of the use of SWR in the TM testing program is given in Section 7.

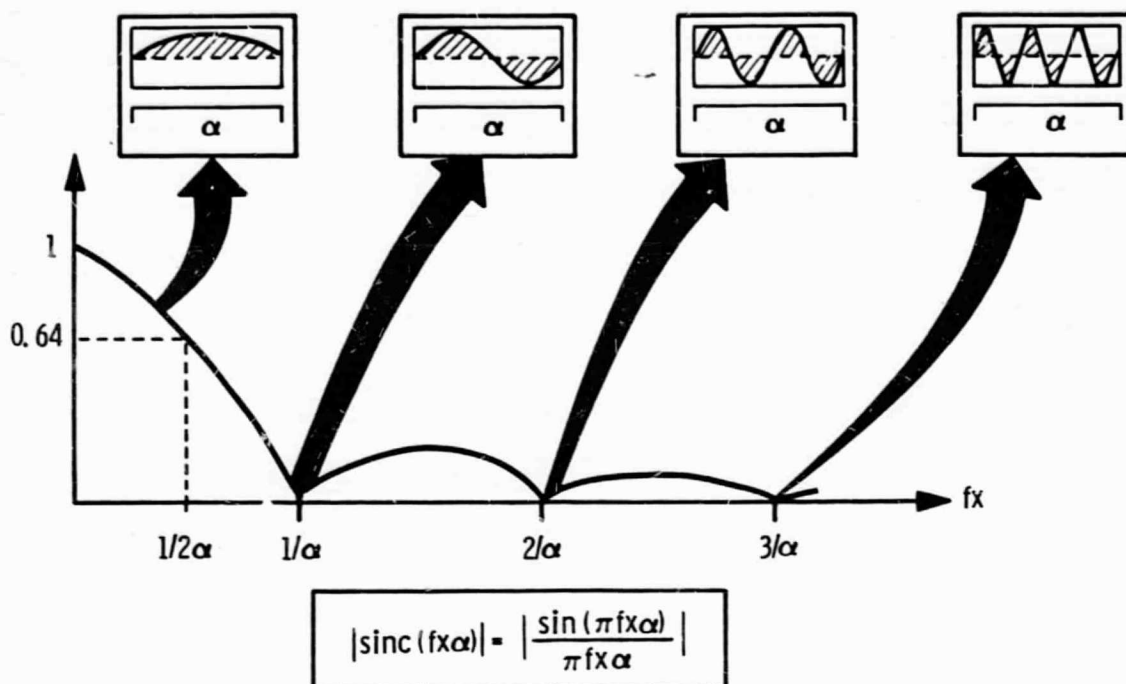


Figure 14. Functional Dependence of Modulation on Frequency

Finally, the reduction in total-system modulation is the product of the reduction in modulation due to each component MTF, from the optics to the detector to the electronics. The convenience of being able to separately compute the MTF (or SWR) for each component and then simply multiply the component MTFs (or SWRs) to get the net system value is an important design feature of the MTF concept. Therefore, the sensor specification for spatial resolution is often provided by specifying the net system MTF or SWR at several spatial frequencies.

The discrete sampling interval is an additional consideration that affects image quality. Because the optics system passes a detector, or several detectors, over the ground quite rapidly, it is impossible to continuously sample the ground scene. Instead, the scene is sampled at discrete intervals. In most cases, discrete sampling produces a very good approximate representation of the information in the scene, because very little change occurs between samples. However, it is conceivable that rapid variations in scene intensity could occur between samples, and, in this case, the sensor would miss some information in the scene. The effect of this sampling error can be quantified with the spatial-frequency sine-wave concept already used to describe MTF.

Figure 15 shows an analog sine wave of period 1.5α that is sampled at the points indicated by the arrows, spaced a distance α apart. The samples provide the image information from which a representation of the analog information that was sampled can be reconstructed. If this is done, the result is a sine wave of lower frequency, shown in the bottom graph. In effect, the sampled high-frequency sine wave has been reduced in frequency because the samples were not close enough together to accurately represent it. The new, lower-frequency sine wave is called an "alias" of the correct, original sine wave. This new sine wave represents incorrect image information, which degrades the accuracy of the sensor in its measurement of any signal containing frequencies too high to be accurately sampled.

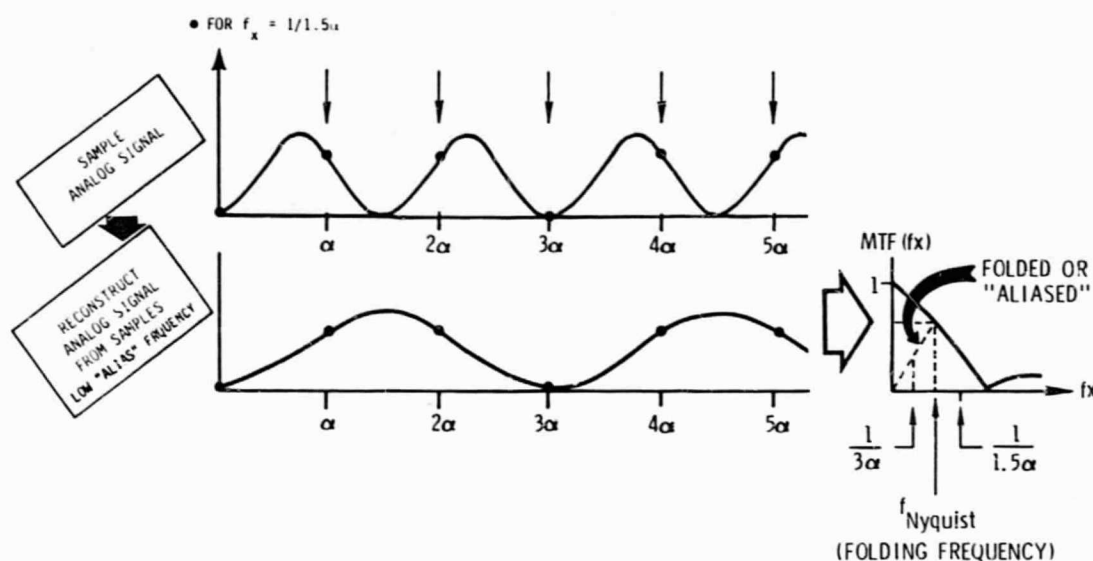


Figure 15. "Aliasing" Error from Sampling

A graph of the MTF associated with a sampled-data sensor might appear as shown on the far right of Figure 15. The frequency of the input sine wave is $1/1.5\alpha$, and this frequency is "aliased" to $1/3\alpha$ by the sensor samples that are spaced by the distance α . In fact, any input sine wave with a frequency exceeding $1/2\alpha$ (or a period less than 2α) will be aliased. The frequency $1/2\alpha$ is the frequency about which all higher frequencies are "folded" to lower frequency aliases. This frequency of $1/2\alpha$ is also known as the Nyquist frequency.

To avoid this aliasing phenomenon, either the samples have to be spaced more closely together, or the input analog information must be filtered to remove the high-frequency information (above the Nyquist frequency) so that it will not be aliased to lower frequencies and added to the low-frequency information that actually exists in the scene. Because it is impossible to sample fast enough to eliminate aliasing, generally the latter tactic is used. Analog electronic prefiltering of the detector signals

prior to sampling is one way to remove the high frequencies from the scene information so that aliasing errors do not occur. The disadvantage of prefiltering is that the electronics filter usually rolls off gradually starting at low frequencies, and some loss of MTF at the lower frequencies will occur. To combat this, filtering is designed to provide as sharp a cutoff as practicable. A detailed treatment of the aliasing and prefiltering problem can be found in Barbe and Campana [1977].

PERFORMANCE AND USER REQUIREMENTS

The quality of the three TM instruments was demonstrated during prelaunch testing, during which virtually all specifications were met with margin. This section discusses the results of these tests and their relationship to user requirements, using, where possible, quantitative comparisons. Only the results considered to be of prime importance to the user community are discussed here. These results include spectral coverage, spatial coverage, radiometry, square-wave response, geometric accuracy, and band-to-band registration.

The results of the analysis of spectral response of the protoflight (PF) and flight (F) models of the TM are given in Table 2. The design requirements for lower and upper band edge are shown in the first columns. These requirements match the specific needs for several application areas very well. Table 3 shows general areas of interest for each of the TM bands [GSFC 1973].

As the results show, the band responses meet the design criteria, except for the upper edge of Band 6 for the PF model. However, this failure is not critical, as long as sufficient energy is gathered to satisfy the NEAT requirements, which, as discussed below, were met.

Table 2. Measured Spectral Coverage (50% Response Band Edge, μm)

Band	Requirement		PF Performance		F Performance	
	Lower	Upper	Lower	Upper	Lower	Upper
1	0.45 \pm 0.01	0.52 \pm 0.01	0.45	0.52	0.45	0.52
2	0.52 \pm 0.01	0.60 \pm 0.01	0.53	0.61	0.53	0.61
3	0.63 \pm 0.02	0.69 \pm 0.01	0.62	0.69	0.63	0.69
4	0.76 \pm 0.02	0.90 \pm 0.01	0.78	0.91	0.78	0.90
5	1.55 \pm 0.02	1.75 \pm 0.02	1.57	1.78	1.57	1.78
6	10.4 \pm 0.10	12.5 \pm 0.10	10.42	11.66	10.45	12.42
7	2.08 \pm 0.03	2.35 \pm 0.03	2.10	2.35	2.10	2.35

Table 3. Band Usage by Application Area (X means useful band)

	Band 1	Band 2	Band 3	Band 4	Band 5	Band 6	Band 7
Agriculture			X		X	X	X
Forestry		X	X		X	X	X
Geography			X		X	X	X
Geology	X			X		X	X
Hydrology	X	X	X	X		X	
Meteorology	X	X	X	X		X	
Oceanography	X	X	X	X		X	

User requirements for spatial coverage were quite varied. IFOV sizes from less than 10 meters to greater than 1,000 meters were specified by users from various application areas. The 30-meter (42.5 μ r) IFOV size chosen represents a compromise between user needs and available technology.

Spatial coverage test results are shown in Table 4. (Note: Band 6 was not remeasured for the F model due to the difficulty of the measurement, the fact that the detector size and effective focal length were known, and because the square-wave response exceeded the specification with significant margin.)

The test data indicates that many of the IFOVs for Bands 1 through 5 and 7 may be slightly larger than specified. For example, a measured line-spread-function (LSF) width of 46.3 μ rad (Band 1, Channel 1, F model) is equivalent to approximately a 32.4-meter IFOV. Part of the measured overshoot may be due to a measurement problem. The detector size was accurately known and the telescope EFL was also well known, and MTF (SWR) measurements were met with considerable margin, making the question of IFOV size relatively unimportant.

User requirements in the area of radiometry were not formally specified (i.e., quantitatively) by the user community. The TM design specifications offer the best set of criteria by which to judge the requirements users have. Table 5 presents the specified scene radiance, the corresponding SNR and $NE\Delta\rho/NE\Delta T$ requirements, and the measured prelaunch SNR and $NE\Delta\rho/NE\Delta T$ values for the protoflight and flight models. As can be seen, all measurements passed the specification.

Table 6 shows the results of the square-wave response (SWR) tests at a single frequency (Nyquist). All bands show a SWR better than the specification. This requirement, like radiometry, is best judged by the design criteria specified for TM. Qualitatively, it can be said that TM's SWR is good enough to allow accurate mapping of edges and linear features for many users.

Table 4. Line-Spread-Function Width, μrad
 (Optics and Detector Only)

Band	Channel	Track		Scan		Specified Maximum
		PF	F	PF	F	
1	1		44.8		46.3	< 43.2
	2	44.4	45.1	44.0	45.3	
	15		43.4		46.0	
	16	43.4	43.2	42.3	44.3	
2	1	44.8	45.9	44.9	44.5	< 43.2
	2		45.6		44.6	
	15		44.1		44.7	
	16		42.9		44.7	
3	1		44.2		44.7	< 43.2
	2	45.5	43.3	45.1	43.6	
	15		44.1		43.6	
	16	43.9	42.7	44.9	43.7	
4	1		45.7		44.4	< 43.2
	2	44.0	43.8	44.1	45.9	
	15		44.3		45.3	
	16	43.1	42.9	44.5	44.3	
5	1		51.4		44.8	< 46.35
	2	47.5	50.5	42.6	44.5	
	15		51.0		44.7	
	16	46.9	50.0	42.5	44.5	
7	1		46.7		45.8	< 46.35
	2	47.8	46.4	45.5	45.4	
	15		46.8		45.4	
	16	49.6	46.9	44.8	45.0	
6	1	172.2		173.0		< 174.4
	2	173.8		170.2		
	3	177.5		178.3		
	4	175.3		174.0		

Table 5. Measured Protoflight and Flight Radiometric Sensitivity

Band	Scene Radiance (mW/cm ² -sr)		SNR (Band Average)						NEΔρ (%)		
	Specified		Minimum Scene			Maximum Scene					
	Min	Max	Measured		Spec	Measured		Spec	Measured		Spec
			PF	F		PF	F		PF	F	
1	0.28	1.00	52.0	60.3	32	143.9	143.2	75	0.16	0.16	0.8
2	0.24	2.33	60.0	59.7	35	279.0	234.9	170	0.18	0.21	0.5
3	0.13	1.35	48.0	46.25	26	248.0	215.1	143	0.20	0.23	0.5
4	0.19	3.00	35.0	46.2	32	342.0	298.7	240	0.19	0.22	0.5
5	0.08	0.60	40.0	35.8	13	194.0	175.4	75	0.23	0.25	1.0
7	0.046	0.43	21.0	28.3	5	164.0	180.6	45	0.41	0.37	2.4
6	300K	320K	NEΔT=0.12K	NEΔT=0.13	NEΔT=0.5K	NEΔT=0.10K	NEΔT=0.11	NEΔT=0.42K			

Table 6. SWR Requirements and Measured Performance

Band	Square-Wave Response at Nyquist Frequency (Band Average)		
	Specified	Measured PF	Measured F
1	0.35	0.46	0.42
2	0.35	0.44	0.41
3	0.35	0.41	0.39
4	0.35	0.43	0.40
5	0.35	0.42	0.44
7	0.35	0.44	0.42
6	0.35	0.44	0.43

Table 7 shows measurements for protoflight geometric accuracy. Table 8 shows F model scan-line length. Statistics for the PF model are similar to the F model.

Table 9 shows the PF band-to-band registration. All measurements are within specification.

Table 7. Measured Protoflight Geometric Accuracy

<u>Scan Rate</u>
<ul style="list-style-type: none"> Average rate within 0.5% of nominal rate (2.21095 rad/sec)
<u>Overlap/Underlap</u>
<ul style="list-style-type: none"> Mission requirements will be met on-orbit (less than 6 meters, neglecting bowtie effect)
<u>Scan-Line Length</u>
<ul style="list-style-type: none"> 400 scan statistics (typical) <ul style="list-style-type: none"> Average = 60742.89 μs Maximum = 60747.35 μs Minimum = 60738.30 μs σ = 1.71 μs (one IFOV dwell time = 9.61 μs)
<u>Scan-Profile Linearity</u>
<ul style="list-style-type: none"> Peak nonlinearity <ul style="list-style-type: none"> <25 μrad forward scan <40 μrad reverse scan
<u>Scan Profile Repeatability</u>
<ul style="list-style-type: none"> Both forward and reverse profiles are repeatable to within 3 μr after application of midscan correction

Table 8. Scan-Line Length [400 scan statistics (typical)]

Forward	SME 1*(μ s)	SME 2 (μ s)	Reverse	SME 1 (μ s)	SME 2 (μ s)
Average	60741.9	60742.9	Average	60742.9	60741.9
Maximum	60748.7	60751.1	Maximum	60749.8	60751.1
Minimum	60737.2	60734.9	Minimum	60735.6	60738.1
σ	2.4	2.6	σ	2.5	2.6

*Scan-mirror electronics, 1 set.

Table 9. Measured Protoflight Dynamic Band-To-Band Registration (BBR)

	Measured	Specified
Along-Scan Registration		
Within PFPA*	<0.1 IFOV	<0.2 IFOV (6 meters)
Within CFPA**	<0.08 IFOV	<0.2 IFOV (6 meters)
CFPA to PFPA	<0.19 IFOV	<0.3 IFOV (9 meters)
Cross-Scan Registration		
Within PFPA	<0.13 IFOV	<0.2 IFOV (6 meters)
Within CFPA	<0.10 IFOV	<0.2 IFOV (6 meters)
CFPA to PFPA	<0.27 IFOV	<0.3 IFOV (9 meters)

*Prime focal-plane assembly

**Cold focal-plane assembly

Section 5

MAJOR SYSTEM TRADE-OFFS LEADING TO THE INITIAL PROPOSAL

At the proposal phase, the design concepts and system parameters of the TM were optimized by extensive trade-off analyses, utilizing, whenever possible, military and civilian flight program experience, especially the multispectral scanner (MSS) and Visible-Infrared Spin-Scan Radiometer (VISSR) instrument developments. Beginning with the basic scanning and optical design and progressing through more detailed optical and mechanical considerations to the types of electrical filters and amplifiers needed to optimize the system performance, trade-offs were performed that led to a proposed design meeting mission requirements while minimizing weight, power, and cost.

Using the trade-off parameters discussed in Section 4 as well as considering complexity, design risk, and cost, a total of 14 major system trade-offs were performed. Although the proposed design met all mission requirements, problems occurred in the hardware phase that required modification of the initial design. These changes are documented in Sections 6 and 7 and Appendix B.

IMAGE-PLANE VERSUS OBJECT-PLANE SCANNING

For an image-plane scanner, the entire field of view must be imaged simultaneously through the entrance aperture; only a portion of the optics is used for any one scan position, and the portion of the optics used is different as the scan angle changes. This has the effect of varying the apparent radiance with angle and also changing the optical square-wave response with scan angle. The amplitude modulation can be corrected by calibration throughout the scan, but the result places a substantial burden on ground processing. The changes in square-wave response may be acceptable if the response for the central part of the field is overdesigned.

The object-plane scan system images through high-precision, symmetrical telescopes and uses the complete aperture throughout the scan for high optical efficiency and negligible scan modulation. Having a constant aperture utilization across scan makes it feasible to use one set of calibration corrections throughout the scan and, in addition, the uniformity across scan makes it feasible to depend on an internal calibration light for operational calibration. Since the light cannot indicate changes in telescope transmissivities, the integrity of the internal light must be verified from time to time by measuring a sample of sunlight. This sun sample will enter from a different scan angle throughout the year; therefore, amplitude uniformity throughout scan is necessary to ensure a stable calibration.

The object-plane design also permits a simple arrangement of detectors in the focal plane with a minimum number of optical elements so that transmissivities are high and the optical path

is relatively short. As a result, thermal-expansion problems are minimized, and the optical support structure is small and, therefore, lighter. Also, since the scan mirror is not in the focal path, the focus is insensitive to relative motions between the mirror mechanism and the optical support structure.

Based on prior experience, an oscillating scan mechanism was selected for the TM. This concept had been shown to provide precise linear scan with imaging performed as the mirror swings from east to west as well as from west to east. Thus, the TM design provided for object-plane scanning with an oscillating mirror giving uniform aperture geometry across scan, precision on-axis optics, and high scan accuracy.

TELESCOPE TYPE

Both refractive and reflective telescope designs were considered. Refractive optical systems are not suited for operation over the spectral range demanded of the TM, since the only materials transparent over this spectral range (0.45 to 12.5 μm) are halogen salts, which are hygroscopic. In addition, adequate color correction could have been accomplished only with a multi-element lens, which would degrade optical transmittance. Thus, reflective optical designs were the only practical approach available.

Numerous reflective designs have been developed, using one, two, three, or more mirrors. Typically, the single-mirror systems are long and awkward to package and have only a small on-axis zone that yields good image quality. However, a large number of optical surfaces should be avoided, if possible, since surface loss and complexity increase quickly with each additional mirror surface. For two-mirror telescope designs, image quality depends greatly on the surface shape of the design. A comparison of the better-known two-mirror telescope configurations showed clearly that the Ritchey-Chretien design provided an image that was more than adequate for TM requirements. The Ritchey-Chretien design uses an aspheric figure on both the primary mirror and the secondary mirror. The rotational symmetry of a Ritchey-Chretien telescope permits conventional optical finishing and testing techniques to be used throughout fabrication. The specific design adopted for the TM is illustrated in Figure 16. Low-expansion materials are used throughout to ensure that thermal changes and gradients will not affect system performance.

SCAN-MIRROR MOUNTING ANGLE AND SIZE

Once the object-plane scan method and telescope type (optical system) had been selected, the next important trade-off was selection of the scan-mirror mounting angle (θ in Figure 17). This angle determines the size and moment of inertia of the mirror and the configuration of the entire instrument. Scan-mirror

moment of inertia should be minimized to reduce the spacecraft's rotation by momentum exchange and to reduce the amplitudes of the mirror's reversal shock spectrum.

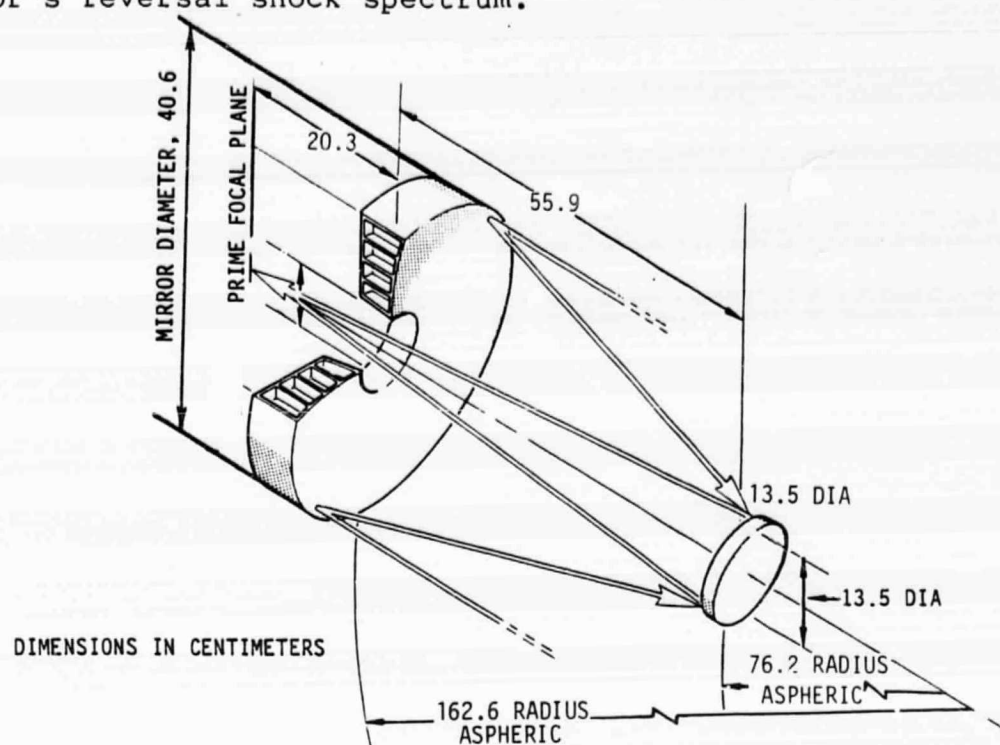


Figure 16. TM Ritchey-Chretien Telescope

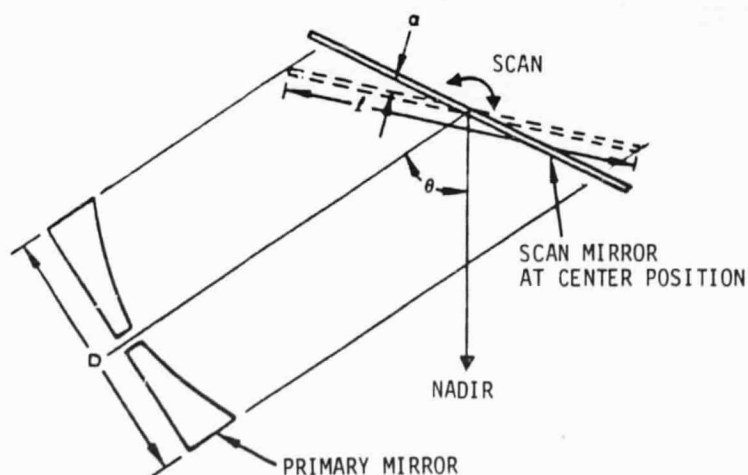


Figure 17. Scan Mirror Geometry

The spacecraft will rotate opposite to the scan mirror by an amount proportional to the ratio of their moments of inertia. However, this spacecraft motion only shortens the scan lines by a slight amount and can be fully compensated for by appropriately increasing the scan angle α in Figure 17. The major restriction on mirror-angle selection (θ in Figure 17) was the baffling of

the secondary mirror. If a 60° angle were used, the secondary mirror would require a 4.6-cm baffle, which would increase the diameter of the secondary mirror assembly and result in a 4 percent increase in obscuration and some loss of SNR. In addition, such an angle would present a difficult interface with the radiative cooler and would require a more unsymmetrical cooler housing structure. Finally, the amount of cross-axis jitter that is produced for a given amount of actual mirror cross-axis motion increases with decreasing mirror angle. Table 10 summarizes these trade-offs. On the basis of these results, an angle of 70° was selected as the optimum angle. This angle resulted in a 53.1-cm (21-inch) scan mirror (see Figure 17). with a $0.352 \text{ cm-kg-sec}^2$ ($0.305 \text{ in-lb-sec}^2$) moment of inertia. The 70° angle results in a mirror 9.6 cm (about 4 inches) shorter than one with an MSS-style 90° mirror angle and a 36-percent lower moment of inertia.

SCAN-MIRROR CONSTRUCTION

The scan-mirror structure had to meet stringent requirements for optical quality, low dynamic distortion, low thermal distortion and low moment of inertia. Graphite-epoxy, Cervit, and beryllium were considered for the application. Beryllium, because of its high stiffness-to-weight ratio, was selected.

Analysis of various structural forms, including machined-block, machined-eggcrate and brazed-eggcrate designs showed that a brazed-eggcrate configuration best satisfied the requirements. The brazed-eggcrate design is fabricated from individual web sheets, slotted to permit assembly into an eggcrate core structure. The assembled core structure is sandwiched between two beryllium face sheets. The entire assembly is held together by brazing at approximately 590°C (1100°F) in a furnace. This design had the lowest moment of inertia, and the natural symmetry of the construction made it the best choice from the point of view of thermal considerations. However, it was changed to a machined eggcrate construction early in the development program (see page 63).

SCAN-MIRROR DRIVE

Trade-off selections in the scan-mirror-drive approach were made to achieve high performance, simplicity, and to minimize momentum transfer between the mirror and the supporting structure.

Table 11 lists the scan-mirror-drive-approach trade-offs that led to the TM design selection. The trade-offs are grouped by major areas: general approach, suspension, drive, and bumpers. Under each area the trade-offs are listed, selected approach is stated, and the major reasons for selecting the approach are given.

Table 10. Scan-Mirror-Angle Trade-Offs

Item	Mirror Angle			
	60°	70°	75°	90°
TM instrument size (cm) Delta launch-vehicle size constraints	163.8x108x71.1 108 cm height exceeds GSFC spec, but will fit delta	165.1x101.6x71.1 OK	167.6x94x71.1 OK	177.8x76.2x71.1 OK
Mirror size, length (cm) Moment of inertia (cm-k _g -sec ²)	50.0 0.300	53.1 0.352	55.1 0.387	62.7 0.554
Spacecraft motion/line (μrad peak to peak) (Fraction of TM IFOV)	6.2 0.15	7.3 0.17	8.0 0.19	11.4 0.27
Baffling of secondary mirror Baffle length (cm) Percent additional obscuration Design complexity	4.6 4.0 May be difficult	Not required N/A OK	1.8 1.5 OK	Not required N/A OK
Cooler interface (deg) Angle between optical axis and center of curvature cooler	79 (OK)	89 (OK)	94 (OK)	109 (requires larger relay mirror)
Angle between optical axis and cooler (180° desired)	143 (Unsymmetrical mounting interface)	153 (OK)	158 (OK)	173 (Best)
Scan monitor location	Back of mirror	Back of mirror	Back of mirror	Corner or back of mirror
Cross-axis jitter angle multiplier (object-space motion to mirror motion)	1.73	1.64	1.59	1.41
Mounting at center of gravity	May be difficult	OK	OK	Best

Table 11. Scan-Mirror-Drive-Approach Trade-Offs

Area	Trade-Off	Selection	Reasons for Selection
General Approach	One-way versus two-way scan	Two-way scan	<ol style="list-style-type: none"> 1. Achievable scan efficiency is higher; more efficient use of data bandwidth 2. Lower forces on mirror; lower reactions on structure; less excitation of mirror and structure
	Free flight versus rate control during active scan	Free flight	<ol style="list-style-type: none"> 1. Simpler control electronics 2. Residual flex pivot torques can be satisfactorily compensated
Suspension	Flex pivots versus bearings	Flex pivots	<ol style="list-style-type: none"> 1. No lubrication required 2. No friction - minimizes unpredicted along-scan velocity variations (residual flex pivot torques can be compensated)
	Bendix design versus Hughes design	Bendix design	<ol style="list-style-type: none"> 1. Proven life characteristics 2. Shear stiffness adequate (Hughes design three times stiffer)
Drive	Permanent magnet versus torquer compensation of flex-pivot torques	Permanent magnet	<ol style="list-style-type: none"> 1. Simplicity (torquer compensation requires additional control electronics)
	Torquer with bumpers versus torquer alone	Torquer with bumpers	<ol style="list-style-type: none"> 1. Bumpers reduce the electrical energy required to ~0.1 of the torque-only energy
	Center-drive moving magnets versus loud-speaker on mushroom bumpers	Center-drive moving magnets	<p>Alternative implications:</p> <ol style="list-style-type: none"> 1. Large addition to mirror moment of inertia 2. Large energy loss in bumpers 3. No passive bumper damping possible 4. Cannot be used for starting mirror
	Center-drive moving magnets versus coils on flex pivot compensator	Center-drive moving magnets	<p>Alternative implications:</p> <ol style="list-style-type: none"> 1. Time constants too long (~10 ms) 2. Poor electrical-to-torque conversion efficiency (five times more power)
	Center-drive moving magnets versus moving magnets at end of mirror, fixed coils	Center-drive moving magnets	<p>Alternative implications:</p> <ol style="list-style-type: none"> 1. Poor electrical-to-torque conversion efficiency 2. Cannot be used for starting mirror

Table 11. Scan-Mirror-Drive-Approach Trade-Offs (Cont)

Area	Trade-Off	Selection	Reasons for Selection
Bumpers	Center-drive moving magnets versus two tractive magnets below mirror	Center-drive moving magnets	Alternative implications: 1. Time constants too long (~44 ms) 2. Poor electrical-to-torque conversion efficiency (four times more power)
	Iron versus no iron in coils	No iron in coils	1. Fast response time, at a cost of more electrical energy to produce torque 2. Zero torque during active scan
	Coils versus magnets on mirror	Magnets on mirror	1. No flexing of leads to coils; no commutator 2. Higher mass (moment of inertia) of magnets is acceptable
	Single-leaf spring versus double-leaf wishbone	Single-leaf spring	1. Lower mass; lower momentum transfer to structure; lower excitation of mirror modes 2. Contact traversal, wear characteristics adequate (wishbone has less traversal, less wear)
	Single-leaf spring versus coil spring	Single-leaf spring	1. Lower mass; lower momentum transfer to structure; lower excitation of mirror modes 2. Contact traversal, wear characteristics adequate (coil has zero traversal)
	Tapered versus other shapes	Tapered (triangular)	1. Peak stress is approximately constant along length, therefore, minimum mass, minimum momentum transfer, minimum excitation of mirror modes
	Contact point at ends versus center of percussion	Ends	1. Little effect on mirror stresses, no difference in absorbed energy. 2. End mounting allows direct mounting of bumpers to assembly structure; minimum mass added to assembly
			3. Minimum turnaround force a. Minimum frictional energy loss b. Minimum mirror excitation

RELAY OPTICS

Two relay-optics design concepts were considered. Early design efforts generated a four-mirror concept with excellent image quality, but the concept was unattractive from the point of view of fabrication, assembly, and alignment. In an effort to alleviate these problem areas, an alternate two-mirror design was developed, resulting in an image with a slight loss in sharpness compared to the four-mirror design. However, the geometric image was still sufficiently small that diffraction effects overwhelmed the geometric blur disadvantage. The advantages of the two-mirror design, resulting in its selection, were:

1. Fewer elements facilitated assembly, alignment, and maintenance of alignment.
2. Rotational symmetry simplified fabrication and alignment.
3. The less complex shapes resulted in reduced fabrication cost.
4. 45° mirrors were eliminated, and polarization effects reduced.
5. The reduction in optical elements allowed greater throughput.

REGISTRATION REQUIREMENTS

The difficult system requirement to register points imaged in Band 5 to the same points imaged in Bands 1 through 4 to within 8.5 μ r required a thorough trade-off study. Small shifts occur in the cold stage of the radiative cooler when it cools down from 300K ambient temperature to its operating temperature of approximately 95K. There were limitations on how accurately the focal-plane arrays could be manufactured and aligned, and any change in scan velocity from nominal would produce a slight sampling registration error.

To determine the best design approach for meeting the registration requirement, a trade-off study of seven different design concepts was performed. Table 12 presents the results of the study.

The selected method was one that combined a thermally stable mirror-relay design with a backup, in-flight alignment mechanism for a one-time alignment after initial cooldown. The design makes use of extra lateral stiffeners in the cooler support structure and ultra-low-expansion optical support materials, such as graphite-epoxy. The alignment mechanism selected was a piezoelectric inchworm device with 1×10^{-6} meter positioning resolution. The advantages of this design are that it can drive

Table 12. Methods for Meeting Registration of Band 5 with Bands 1 through 4

Methods	Advantages	Disadvantages	Relative Risk
Mirror relay	--	<ul style="list-style-type: none"> • Difficult to meet 0.2 IFOV requirement 	None
Enlarge cooled detectors (Magnification > 0.5)	<ul style="list-style-type: none"> • No impact on design 	<ul style="list-style-type: none"> • Only reduces effect of absolute displacement errors • Reduces performance in all cooled bands 	None
Mirror relay with one-time in-orbit alignment (Selected)	<ul style="list-style-type: none"> • Straightforward • Can also provide focus adjustment 	<ul style="list-style-type: none"> • Requires measurement and ground command 	Minimal
Field-stop image-relay into cooler	<ul style="list-style-type: none"> • Simplest • Exact registration 	<ul style="list-style-type: none"> • 36% SNR degradation • Maximum shifts ± 2 mil • f/1.5 relay difficult • Possible catastrophic loss of image 	None up to catastrophic failure modes
Coldfinger (flexible)	<ul style="list-style-type: none"> • Eliminates cooler misregistration • 20 to 50% of problem will still remain 	<ul style="list-style-type: none"> • Spec still may not be met • 2 suspensions required • 10 to 30% increase in heat loads 	Minimal
Heat pipe	<ul style="list-style-type: none"> • Not significant over coldfinger except in heat loss 	<ul style="list-style-type: none"> • Complex; requires development 	Moderate
IR fiber-optics relay	<ul style="list-style-type: none"> • Exact registration 	<ul style="list-style-type: none"> • Requires tapered fiber development • Dewar packaging 	<ul style="list-style-type: none"> • High development risk • Low flight risk

large loads with no backlash, resolution is excellent, and it has the built-in, fail-safe feature of remaining clamped when power is removed. This approach has an additional feature that provides focus adjustment when equal movement of all three inchworms is commanded.

SCAN-LINE CORRECTION

Scan-line correction requires two mirrors that move to create image displacement while remaining parallel to each other. (The use of a single moving mirror introduces changes in the direction of the incident cone of light, resulting in scan modulation.) With two mirrors, the emerging optical beam is always parallel to the entering beam, the apparent exit pupil is unchanged, and scan modulation is eliminated.

An initial design included a pair of mirrors moving about separate pivot axes in the converging beam ahead of the first focus. Subsequent ray-tracing analysis of this design indicated that the defocusing produced was at least an order of magnitude better than needed. This raised the possibility that the two mirrors might be moved about a single-pivot axis without exceeding an acceptable defocusing limit. Subsequent analysis showed that a scan-line corrector (SLC) moving about a single-pivot axis would be acceptable. Figure 18 shows the SLC design that resulted.

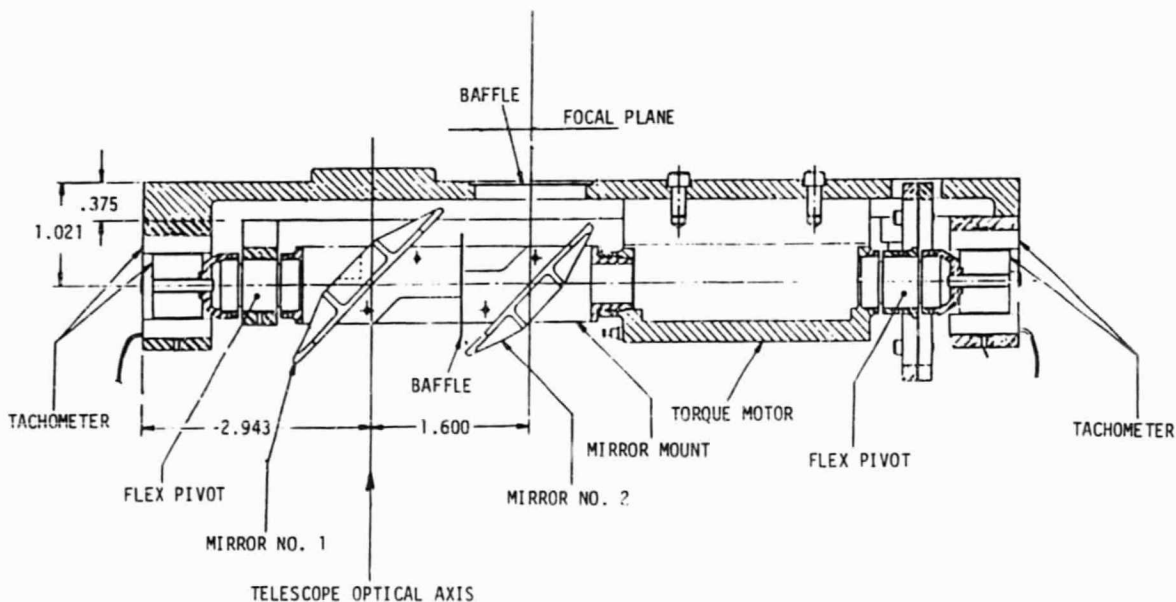


Figure 18. Scan-Line Corrector

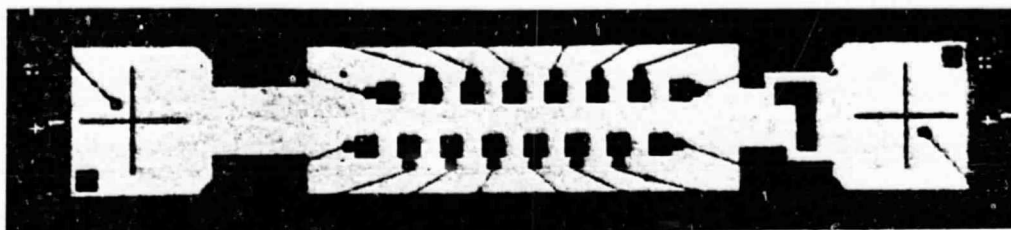
DETECTOR SELECTION

Monolithic arrays of detectors were selected after carefully considering the candidates for detector configuration. Figure 19 shows the detector configuration at the prime and cooled focal planes. The other candidates were: discrete detectors, monolithic detectors with hybrid preamplifier input stages, a monolithic array of detectors and input circuits, and a monolithic array of charge-coupled devices (CCDs). All of these configurations, except the discrete detectors, could have been located in the focal plane, if suitably arranged. The discrete detectors could not be packed closely enough to cover the scene at that location with reasonable scan-mechanism rates, electronic bandwidths, and high-quality focal-plane area. Fiber-optic relays, used with the discrete detectors were a feasible option, but the transmittance loss penalized SNR unacceptably. The expected performance of the CCDs was promising due to their special ability to transfer, delay, and integrate (TDI) signals in a low-noise manner, increasing the SNR by the square root of the number of elements per channel. However, their early level of development precluded them from use. Monolithic arrays of detectors and input circuits could form fairly compact arrangements, but without the transfer-integration advantage of the CCDs, there was no clear SNR advantage.

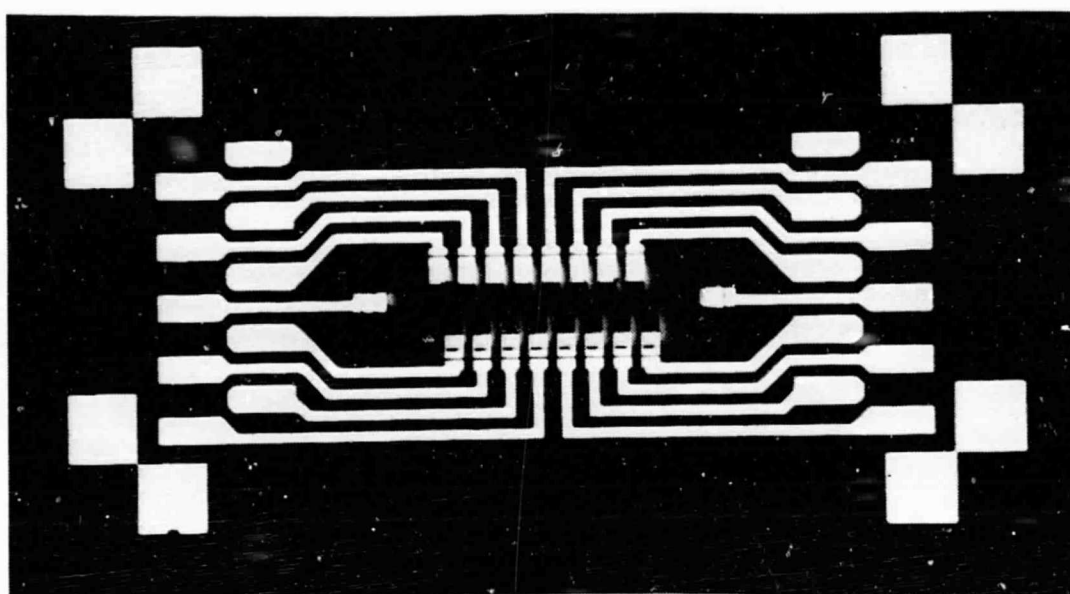
Input devices are limited to those that can be formed directly on the same substrate. Some compromise in material selection and special processing was required to produce photodiodes and field-effect transistors (FETs) on the same substrate. A monolithic detector array with short connections to input circuits was deemed to provide the best performance of the individual components, optimized for each function. For example, the FETs selected for use with the silicon detector arrays demonstrated outstanding noise and capacitance characteristics. Close spacing of the arrays for different bands could be achieved with this technique because the preamplifier input stage did not have to occupy space in the focal plane. In addition, considerations for the InSb and HgCdTe detectors added support for the choice of monolithic detector arrays at the cooled focal plane. To reach the low operating temperatures, the focal-plane area should be minimized, as should the apertures through which thermal radiation enters, and close spacing of the arrays facilitates both requirements.

COOLER SELECTION

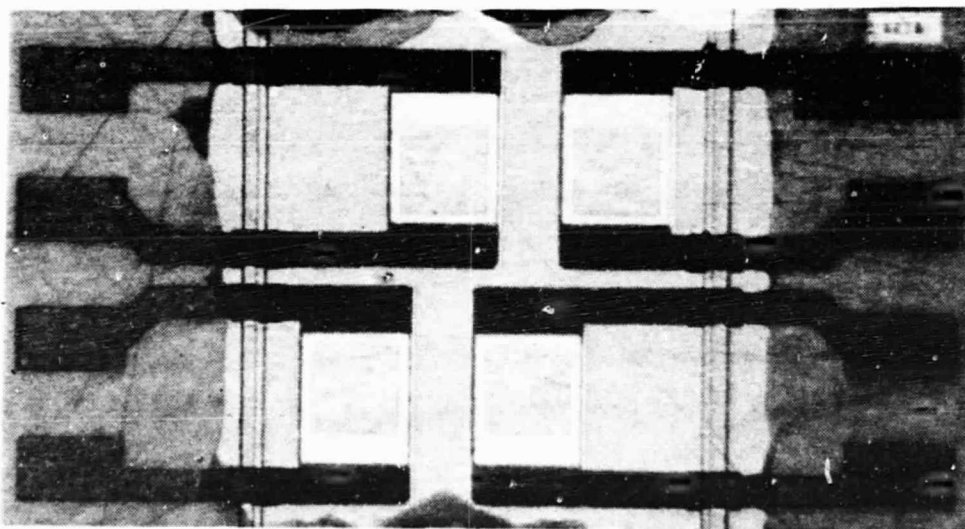
The radiative cooler design evolved from experience with visible and near IR spin-scan radiometer (VISSR) coolers and resulted in a design that satisfied mission requirements within the spacecraft and environmental constraints. The performance-critical areas of internal thermal isolation and external space radiation were made the subjects of trade-off studies.



SILICON PHOTODIODE ARRAY (BANDS 1 - 4)



INDIUM ANTIMONIDE (InSb) PHOTODIODE DETECTOR ARRAY (BANDS 5 AND 7)



MERCURY CADMIUM TELLURIDE (HgCdTe) DETECTOR ARRAY (BAND 6)

Figure 19. Configuration of Detector Arrays

The thermal properties of candidate high-emittance surfaces for use on the TM cooler radiators were first evaluated. The 30-minute solar impingement requirement led to the use of white paint on open honeycomb for the radiators, because this surface presented the highest thermal emittance consistent with an acceptable solar absorptance.

The next study involved selection of low-thermal-emittance coatings and surfaces with low solar diffuseness for use on the specular shields. Vacuum-deposited aluminum on polished nickel was the obvious choice, since this surface presented exceptionally low values for these properties. Successful use of this surface on the VISSR radiative coolers also made its use on the TM cooler a low-risk option. Similarly, a review of low-thermal-emittance surfaces for use in controlling interstage radiation led to the choice of surfaces identical to those used on the VISSR coolers. For the cold-to-intermediate stage cavity, the choice was electroplated-gold-to-electroplated-gold. The intermediate-to-ambient-stage cavity surfaces were multilayer-insulation-to-electroplated-gold. Again, this design was selected because of its exceptionally low radiation coupling value and because previous use made its application a low-risk option.

The cooler interstage support members must satisfy several dissimilar design requirements: interstage heat transfer (radiation, conduction) must be reduced to very low levels, a rigid and stable structure is needed, and large thermal gradients between stages must be accommodated. An analytical performance comparison was made of three candidate support member materials; i.e., titanium-tube truss members, a polycarbonate resin cone, as used on the MSS cooler, and the filament-wound fiberglass members used on the VISSR cooler. This trade-off led to selection of filament-wound fiberglass as the highest performance interstage support material. Its successful history on the VISSR cooler also made its use on the TM cooler a low-risk approach.

SAMPLING MODE AND RATE

The TM photodiode detectors issue a continuous signal stream with a zero level referenced to dark once every 71 ms. This type of signal output offered the option of using either track-and-hold or integrate-and-dump sampling. Sampling rates could be selected at any frequency consistent with performance. The transfer functions for the two methods differ primarily in that the integration-and-dump operation has the effect of a sinc function filter (Figure 14), whereas the track-and-hold operation permits the designer to insert a presampling filter, tailored to the needs of the application. The track-and-hold method was selected because the filter could be shaped to give better noise bandwidth and a 10 percent higher response at one-half the cutoff frequency.

The need to reduce the amount of data to be processed, reflected in the RFP's request for data compaction, influenced adopting the recommendation that the lowest rate consistent with an IFOV of 30 meters be used. The effect of sampling once per IFOV rather than 1.4 times per IFOV (as on the MSS) was evaluated numerically. The latter rate represents the maximum that could be used for seven bands while remaining within the RFP's 120 Mbps constraint. The two factors to be considered in choosing the lower sampling rate were increased aliasing noise and reduced resolution for reconstructed images. Aliasing, as discussed earlier, occurs during sampling and has the effect of folding back the high-frequency content of the scene into the passband of the presampling filter. The fold line occurs at the sampling frequency. Therefore, the lower sampling rate causes the image to be situated with more overlap into the filter passband than would be the case for the higher sampling rate. The actual rms voltage level that folds into the frequencies corresponding to 200-, 100- and 40-meter fields in the scene was calculated to determine the severity of the problem. This analysis showed that aliasing errors are smaller than those caused by the square-wave response and would not have a degrading effect on required performance.

ELECTRICAL FILTER

The electrical filter requirements included an MTF response of 0.99 for bar charts of 200 meters and at least 0.7 for bar charts of 30 meters, a noise bandwidth narrow enough to protect the signal-to-noise ratio, and a falloff sharp enough to reject the frequencies that produce aliasing. The phase shift had to be smooth enough that the response time was fast, and the overshoot had to be limited to 1 percent of the step size. These qualities had to be obtained with a filter network having a matched response over all 100 signal channels. The difficulty in satisfying these requirements simultaneously can be demonstrated by examining the characteristics of the entire range of Butterworth-Thomson filters shown in Table 13. The m parameter has the effect of varying the filter from the original Butterworth filter ($m = 0$), which has maximally flat amplitude response with poor phase flatness, to the Bessel filter ($m = 1$), which has maximally flat delay with poor amplitude flatness. The intermediate values of m combine the delay with poor amplitude flatness. The intermediate values of m combine the good qualities of two extremes in varying degrees. Table 13 shows several of these gradations for two-, three-, and four-pole networks, identified under "order." For generality, the bandwidths are normalized to the half-power, corresponding to bar charts of not more than 30 meters.

The filter selected was a modified Butterworth, designed at GSFC by Larry Goldberg, and it has become known as a 3-pole Goldberg filter. The filter provides amplitude response that very closely approaches that of the $m = 0$ Butterworth, while providing a decrease in overshoot from 8 to 1 percent.

Table 13. Butterworth Filter Characteristics

Filter Type ($n =$)	Order	Overshoot (%)	Noise Bandwidth Factor	Rise/Fall Times 1% (μ s)	Frequency with Respect to 3 dB Bandwidth for MTF =			Percent Aliasing Noise (Scene -6 dB/Octave)	
					0.94	0.89	0.79	1 Sample/IFOV	1.5 Sample/IFOV
0.2	2	3.05	1.11	6.9/5.7	0.22	0.66	0.87	8.5	5.0
0.4	2	1.89	1.12	6.9/4.6	0.17	0.66	0.84	11.1	6.7
1.0	2	0.43	1.15	6.9					
0	3	8.15	1.05	7.2/14.4	0.48	0.81	0.93	3.3	1.5
0.3	3	4.75	1.04	7.2/5.1	0.23	0.72	0.87	4.4	2.1
0.4	3	3.87	1.04	7.2/4.8	0.18	0.67	0.87	4.9	2.3
1.0	3	0.75	1.07	6.9	0.14	0.60	0.84	7.5	3.8
0.4	4	5.04	1.00	7.5/4.5	0.17	0.66	0.87		
0.5	4	4.01	1.00	7.5/4.2	0.17	0.66	0.37	3.2	1.2
0.6	4	3.13	1.01	7.5/3.6	0.17	0.66	0.85		
1.0	4	0.84	1.05	7.5	0.14	0.60	0.84	5.7	2.7
					Selected Modified Butterworth				
0	3	1.0	1.0	16.4/	0.42	0.61	0.86	5.2	2.5

COMPRESSION AMPLIFIER

Analysis of SNR ratios for each band showed that all but Band 4 met requirements. To bring Band 4 within specification, it was necessary to include a compression amplifier. Trade-offs were performed among linear, segmented linear, and logarithmic amplifiers. The amplifier selected was a two-segment linear amplifier that could be shaped to exceed the required SNR levels at both ends with only a single break point. After the initial design trade-offs, this amplifier was found to be unnecessary, allowing the use of similar amplifiers in all bands.

MULTIPLEXER DESIGN

Of the many TM multiplexer trade-offs performed, four were of critical importance to the final design. The first of these trade-offs determined the sensor data-path configuration; i.e., how many A/D converters would be used. Six A/D converters, with Bands 5 and 6 sharing one, were chosen because the choice provided modular growth, graceful degradation in the event of failures, and acceptable power and weight requirements.

The second major trade-off involved the data-output configuration. As originally proposed, the multiplexer utilized two NRZ output streams, each operating at half the total data rate. This approach was chosen because it offered enhanced design margins and lower multiplexer development cost. However, it was later found that these cost savings were more than offset by higher costs for the spacecraft to interface with dual data streams, so a single 85 megabit output was adopted during the course of the program.

The third major choice involved high-speed-logic trade-offs. The Schottky TTL was considered to be too slow, the MECL III had high power dissipation and required transmission-line interconnects, and the custom LSI was not only expensive, but also was not amenable to easy modification. The ECL 10,000 was selected because it represented the best compromise among the options while satisfying the performance requirements. Low-power Schottky was used for those circuits not requiring extremely high speeds.

Component packaging concepts were the fourth critical trade-off area. This trade-off study resulted in selecting hybrid microcircuits, which combined miniaturization for optimum analog-circuit performance and very low weight with the capability to rather easily make changes during the design phase.

SUMMARY

The major trade-offs discussed in this section are summarized in Table 14.

Table 14. System Trade-Offs Summary

System Trade-Offs	Trade-Off Factors	Result
<u>Scanning and Optics</u>		
Object-plane versus image-plane scanning	<ul style="list-style-type: none"> •Optical throughput •Optical quality over field of view •Complexity and reliability •Alignment and stability •Scan modulation and polarization •Cost 	Object-plane scanning
Primary optical system type	<ul style="list-style-type: none"> •Transmittance •Optical quality over field of view •Complexity and size •Manufacturing cost 	Ritchey-Chretien
Scan-mirror mounting angle and size	<ul style="list-style-type: none"> •Mirror length and moment of inertia •Overall instrument size and mounting •Baffling of secondary mirror •Cooler interface •Scan-monitor location •Cross-axis jitter 	70° angle, 53.1-cm (21-inch) mirror, scan monitor mounted on scan-mirror assembly
Scan-mirror construction methods and materials	<ul style="list-style-type: none"> •Weight and momentum •Stiffness •Surface flatness •Manufacturing complexity •Cost 	Brazed beryllium eggcrate construction
Scan-mirror drive concept	<ul style="list-style-type: none"> •Scan efficiency and linearity •Complexity •Reliability •Torque and momentum 	Free-flight scan with flex pivots, moving magnets, and single-leaf springs
Four-mirror versus two-mirror relay optics	<ul style="list-style-type: none"> •Image quality •Size and packaging constraints •Fabrication and alignment •Transmittance and polarization •Fabrication cost 	Two-mirror relay

Table 14. System Trade-Offs Summary (Cont)

System Trade-Offs	Trade-Off Factors	Result
<u>Subsystem Design Concepts</u>		
Design methods to meet registration requirements	<ul style="list-style-type: none"> •Quality of registration achieved •Complexity and risk •Effects on radiometric performance •Cost 	Stable design; flex pivot compensator; in-flight alignment mechanism
Detector array selection	<ul style="list-style-type: none"> •Radiometric performance •Maturity of CCD processes •Packaging considerations (including stray capacitance and crosstalk) 	Monolithic arrays
Cooler selection	<ul style="list-style-type: none"> •Cryogenic performance •Structural stability •Past experience •Size and weight •Cost •Ease of alignment and bench-test cooling 	Improved VISSR design
SLC selection	<ul style="list-style-type: none"> •Scan linearity and repeatability •Moment of inertia •Defocusing and scan modulation 	Two mirrors rotated together about a single axis
<u>Signal Processing and Data Handling</u>		
Sampling mode and rate		
Track-and-hold versus integrate-and-dump	<ul style="list-style-type: none"> •Frequency response •Noise bandwidth •Aliasing •Flexibility 	Track-and-hold
Sample rate (1.0 to 1.4 IFOV)	<ul style="list-style-type: none"> •MTF of analog-reconstructed data •Data rate •Aliasing and image reconstruction 	1.0 sample/IFOV

Table 14. System Trade-Offs Summary (Cont)

System Trade-Offs	Trade-Off Factors	Result
Electrical filter selection	<ul style="list-style-type: none"> •Frequency response •Response to step input •Noise bandwidth •Rejection of aliasing noise 	Modified Butterworth (Goldberg)
Multiplexer design and components		
Configuration	<ul style="list-style-type: none"> •A/D converter speed required •Weight and power •Design risk •Cost 	One A/D converter per band; two NRZ data outputs (later changed to one)
Logic family	<ul style="list-style-type: none"> •Speed-power product •Packaging simplicity 	Mix of ECL 10,000 and 54LS
DC-restore for Band 6 (ambient versus cold-level restore)	<ul style="list-style-type: none"> •Stray light baffling •Sensitivity to gain changes •Reference level accuracy •Initial calibration 	Ambient reference (Temperature-controlled central baffle)

Section 6

RESOLUTION OF CRITICAL HARDWARE PROBLEMS

The translation of mission requirements into sensor design, discussed in Sections 4 and 5, resulted in the configuration shown in the frontispiece. Implementation of the design requirements presented an opportunity to utilize novel design solutions. The most significant challenges and solutions to the hardware problems of the TM are summarized here.

SCAN-MIRROR ASSEMBLY

The major elements of the scan-mirror assembly (SMA) consist of the scan mirror and associated drive subsystem, and the scan-angle monitor (SAM). Figure 20 depicts the SMA configuration, showing the location of the SAM within the assembly.

A number of problems were experienced with the scan-mirror assembly during its development and fabrication. Had these not been corrected, the system performance of the TM would have been seriously degraded.

Scan Mirror

As originally designed, the scan mirror consisted of an eggcrate structure sandwiched between two flat, bare beryllium plates. The entire structure was elliptical with face dimensions for major and minor axes of 53.8 cm (21.2 in.) and 41.4 cm (16.3 in.), respectively. Nominal thickness was 4.14 cm (1.63 in.) and nominal weight 1.71 kg (3.76 lb).

Problems were encountered with print-through of the internal eggcrate structure onto the optical surface. The print-through problem was caused by thermally induced bimetallic stress changes (thermal cycling). A 0.1°C thermal gradient across the mirror produces ±2.9 microinches in nonflatness. The 0.1°C gradient is consistent with specification; however, the resulting nonflatness causes a 6% degradation in MTF at ±10°C while the specification allows only a 4% degradation. To control these effects, the TM scan mirror is held at a nominal operating temperature of 22°C. This controlled-temperature operation required the use of on-board heaters.

Because of the print-through problem, after the Conceptual Design Review the construction of the scan mirror was changed from an eggcrate with facesheets brazed on each side to two half-mirror slabs with an eggcrate machined on one side of each half. These were then brazed together. This design change reduced the print-through caused by the bimetallic and thermal-stress effects at the brazed-eggcrate-facesheet interface.

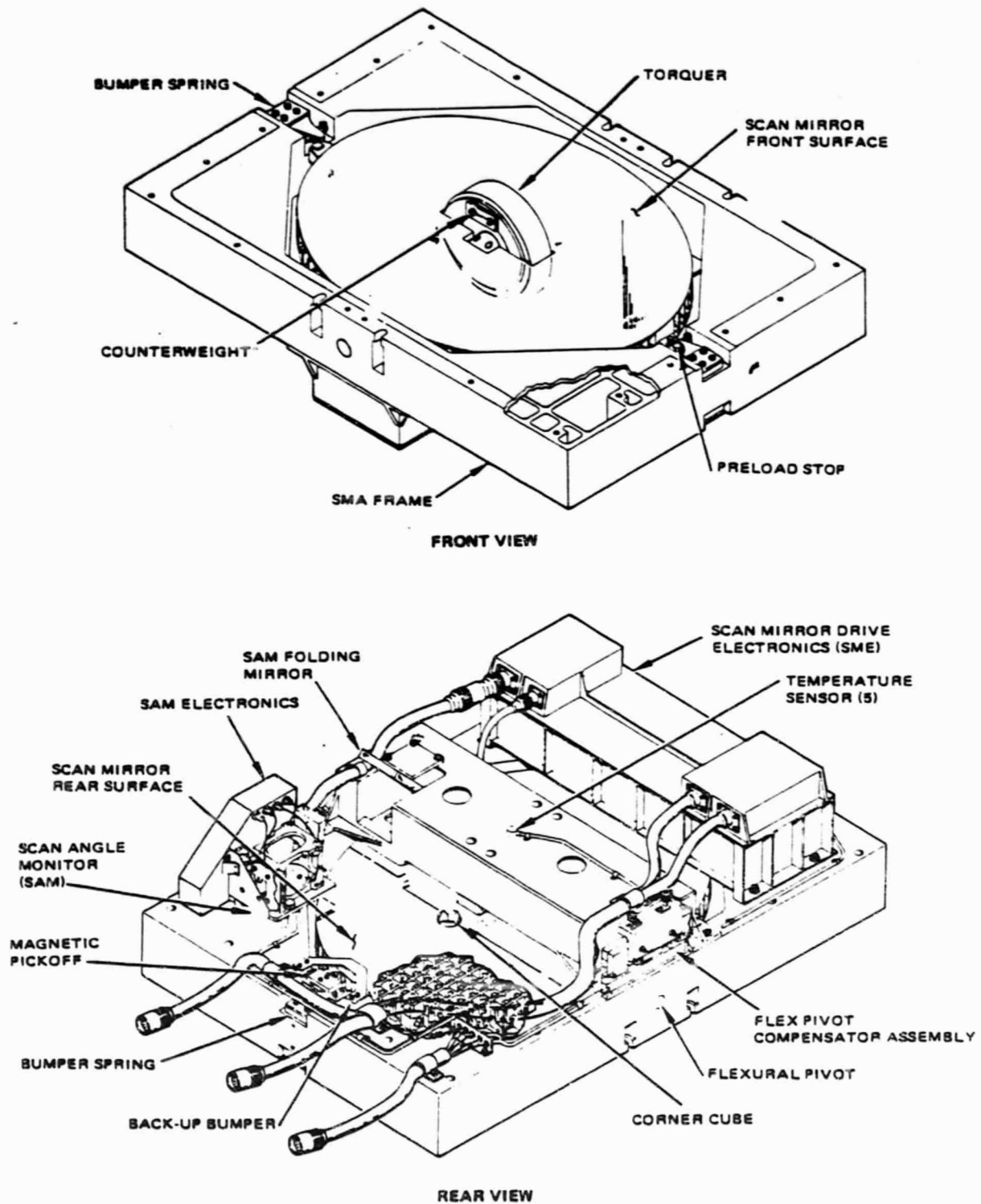


Figure 20. Scan-Mirror Assembly

Six-inch square samples of beryllium were fabricated and subjected to various simulated performance tests. During a surface scattering test, the bare beryllium scattered in excess of its allowable contribution to the overall system requirement. To rectify the scattering problem, the bare beryllium optical surfaces were plated with 0.005 inch of nickel.

Plating the optical surfaces with nickel solved the scattering problem, but during the plating process the nickel built up asymmetrically inside the eggcrate structure. The asymmetrical buildup of material caused a balance problem, adversely affecting timing and vibration. This problem was solved by plating both halves of the scan mirror and masking off the inner machined eggcrate structure. Plating both sides of the scan mirror also helped balance thermal stresses between the front and rear, resulting from the differences in the coefficients of thermal expansion of beryllium and nickel. Unplated areas were passivated for protection.

Following the Engineering Model Review, a vibration absorber was added to the scan mirror to damp out vibrations induced by the bumper impacts during mirror turnaround. This provided an acceptable mirror figure at scan start and throughout the active scan. Further, a ground-commandable correction to the scan profile, based on the location of the midscan pulse from the SAM, was allowed for, and the magnetic compensator was redesigned to enable position adjustment. Representations of the assembly's kinetics and motion profiles are presented in Figures 21 and 22, respectively.

Scan-Angle Monitor

A functional diagram of the SAM is presented in Figure 23, illustrating the operational aspects of the SAM assembly shown in Figure 24.

Following the Detailed Design Review, the scan-angle monitor (SAM) was redesigned to improve mirror startup. First, the frame material was changed from aluminum to beryllium to increase rigidity so that relative motion between the SAM and the mirror pivots would not cause a variation in the active scan amplitude. A controlled heater was also added at the SMA interface to provide constant temperature so thermal expansion would not affect the scan amplitude.

Following the Engineering Model Review, the SAM was further redesigned to provide two, instead of four, bounces of its optical path at the back of the scan mirror to reduce cross-axis sensitivity.

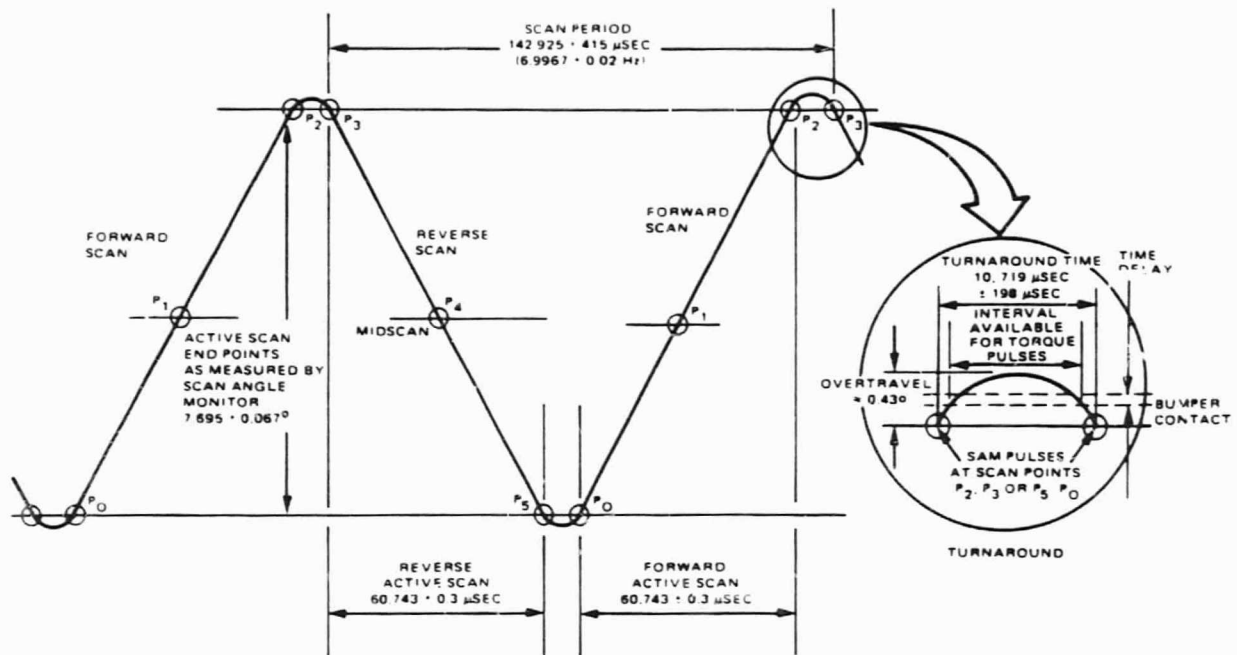


Figure 21. Representation of Scan-Mirror Assembly Kinematics

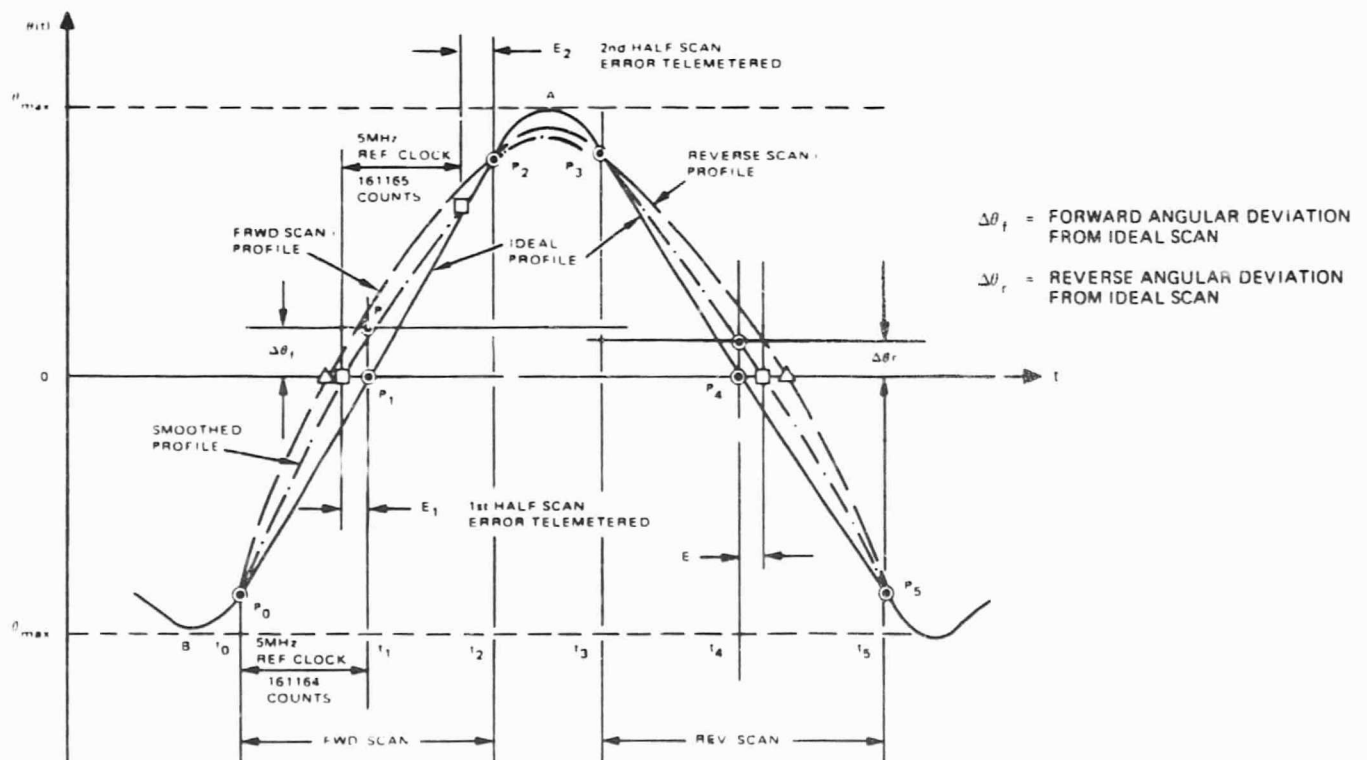


Figure 22. SMA Scan Profiles and Nonlinearities

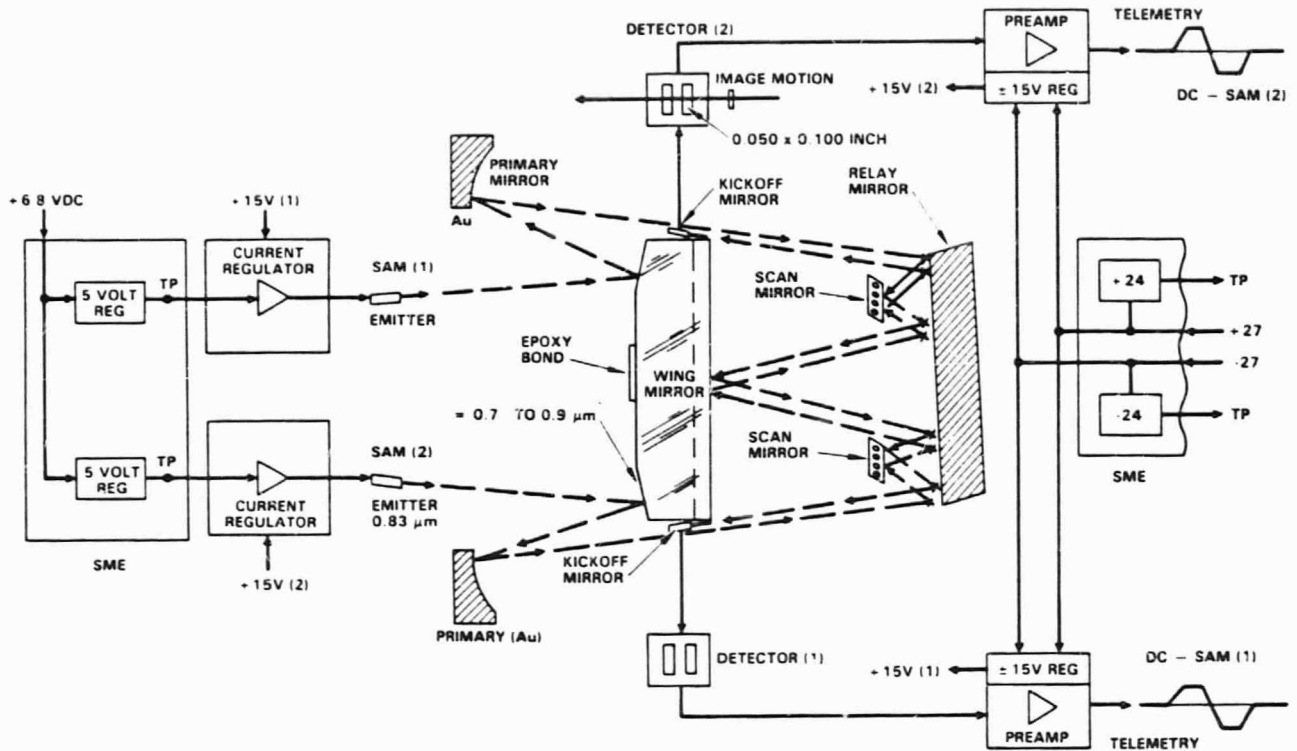


Figure 23. Functional Diagram of Scan-Angle Monitor

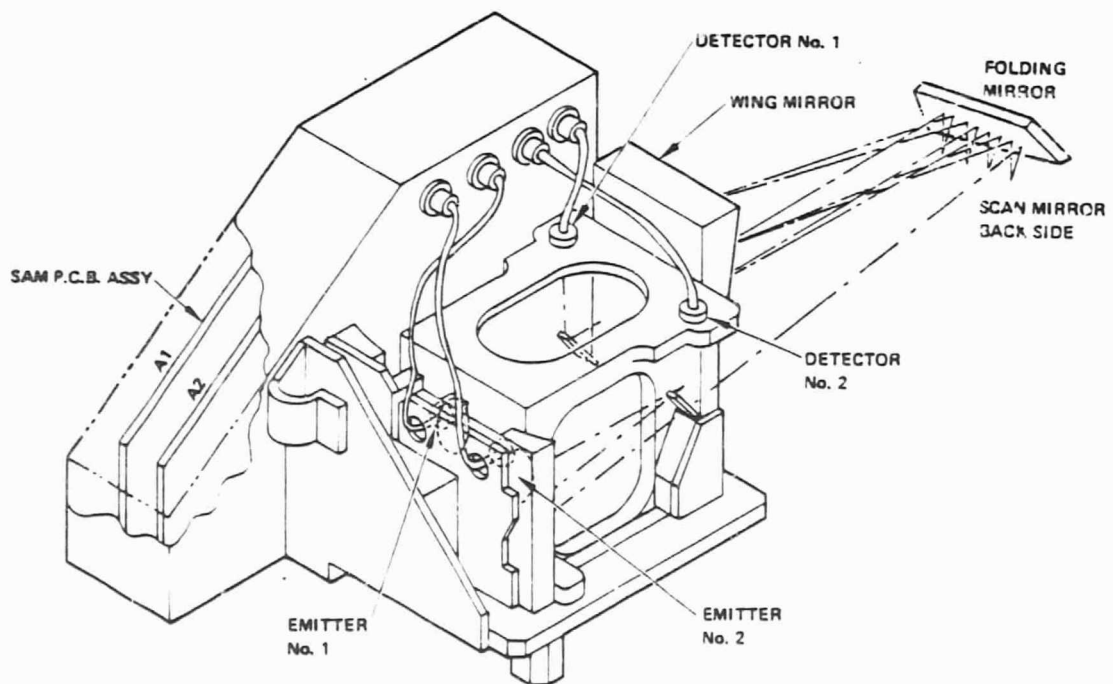


Figure 24. Scan-Angle Monitor (SAM)

TELESCOPE ASSEMBLY

A significant design challenge was encountered in the optical metering structure (OMS), as depicted in Figure 25. The optical metering structure consists primarily of the graphite-epoxy and Invar components that serve as a metering structure, or support, for optical mirrors, detectors, and electronics. This structure consists of a telescope housing and support cone, an aft-optics assembly, comprising an aft-optics plate, a relay-optics base, a spherical-mirror mount, and relay-optics housing, and a radiative cooler adapter.

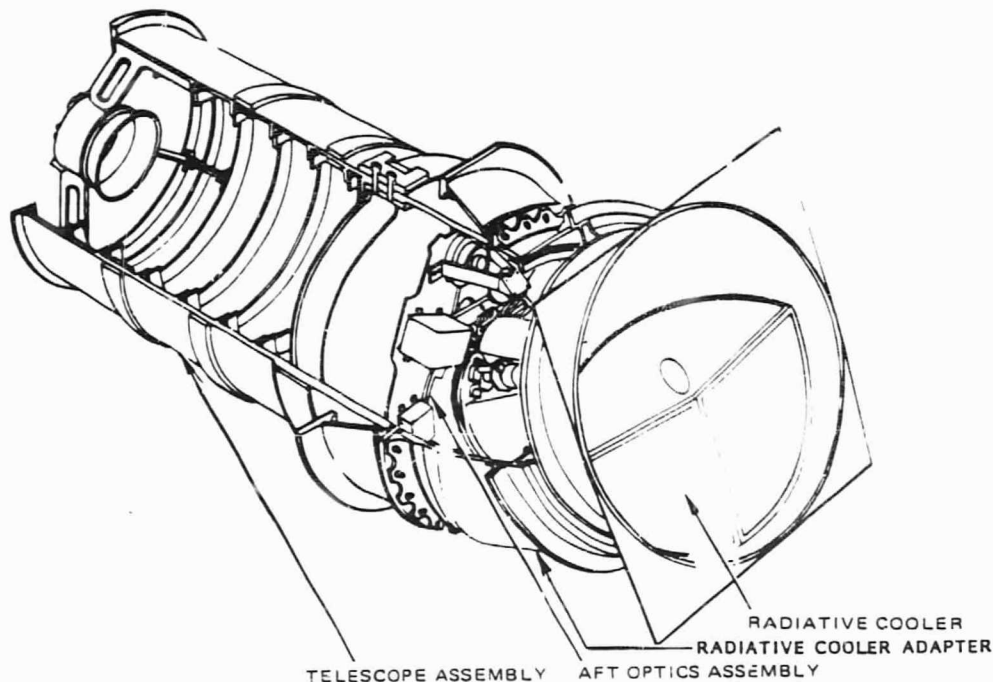


Figure 25. Optical Metering Structure

Each component has distinct functional and/or dimensional requirements and, when assembled, must satisfy the overall dynamic and thermal stability performance requirements. Because of temperature variations in the TM's orbital environment and duty cycle, the OMS had to be thermally stable across its temperature operating range. In effect, it had to be built from a material that would have a near-zero thermal-expansion coefficient over that range. Graphite-epoxy GY-70/X-30 quasi-isotropic laminate was characterized as the best candidate material. Other advantages were the material's low density, excellent stiffness-to-weight and strength-to-weight ratios, and nonmagnetic properties. General Dynamics was selected to develop the OMS because of their experience in the design and fabrication of thermally stable structures and in the use of GY-70/X-30.

The advanced technology required to utilize the graphite-epoxy was complicated by the material's moisture absorption properties. Absorbed moisture causes graphite-epoxy to expand, resulting in a shift in focus and possible misregistration in the case of the relay optics. The resolution of the handling problem was to maintain the OMS in an environment of 20-percent relative humidity when not in use and at 40 percent when testing or assembly activities were under way. Special graphite-epoxy witness samples were kept in the same environment as the OMS, and monthly length and weight measurements were made of these samples to ensure dimensional stability was maintained.

Telescope Housing and Support Structures

The telescope housing, as diagrammed in Figure 26, is the largest component of the OMS. It supports the entire OMS assembly on its outer support cone. The only aluminum (2024-T851) and high-strength graphite-epoxy (T300/934) in the entire structure is in the support cone. (T300/934 was used here because strength and mounting interface considerations were more important than thermal stability and stiffness.) The rest of the structure is fabricated from GY-70/X-30 graphite-epoxy and/or low-expansion Invar LR-35. The straight cylindrical portion of the telescope housing is approximately 45 cm (18 in.) in diameter and 94 cm (37 in.) long. This cylinder has internal provisions for mounting the secondary-mirror support spider, the primary mirror, and aft-optics plate. The aft flange is used to mount the radiative cooler adapter.

Designing the secondary-mirror support spider required optimizing stiffness, weight, and envelope constraints and minimizing obscuration. Satisfying these requirements accounts for the complexity of the Invar LR-35 secondary-mirror mount design.

Several important functional requirements dictated the design of the primary-mirror support. It is necessary to limit the radial load acting on the mirror; provide axial, lateral, and torsional stiffness; perfectly register (0.001 inch perpendicular to the optical axis) and support a bonded-in mirror; provide for the mirror to be removed; and limit the axial-distortion effect.

Special bonding techniques and tooling were used to accurately and adequately bond all Invar LR-35 parts in place. An epoxy adhesive (Hysol 934) was used for bonding, although lockbolts were also employed to supplement the bonds in order to obviate destructive inspection of the bond joints.

Eight light baffles were required inside the telescope's cylinder. These annular, blade-like baffles were edge-bonded to the cylinder's inner skin using Hysol 934 adhesive. The baffles were equally spaced down the cylinder. The last baffle was located just in front of the primary mirror to define the aperture. This baffle was precision machined to within a few thousandths of an inch of its desired diameter and was concentric with the optical axis within 0.001 inch.

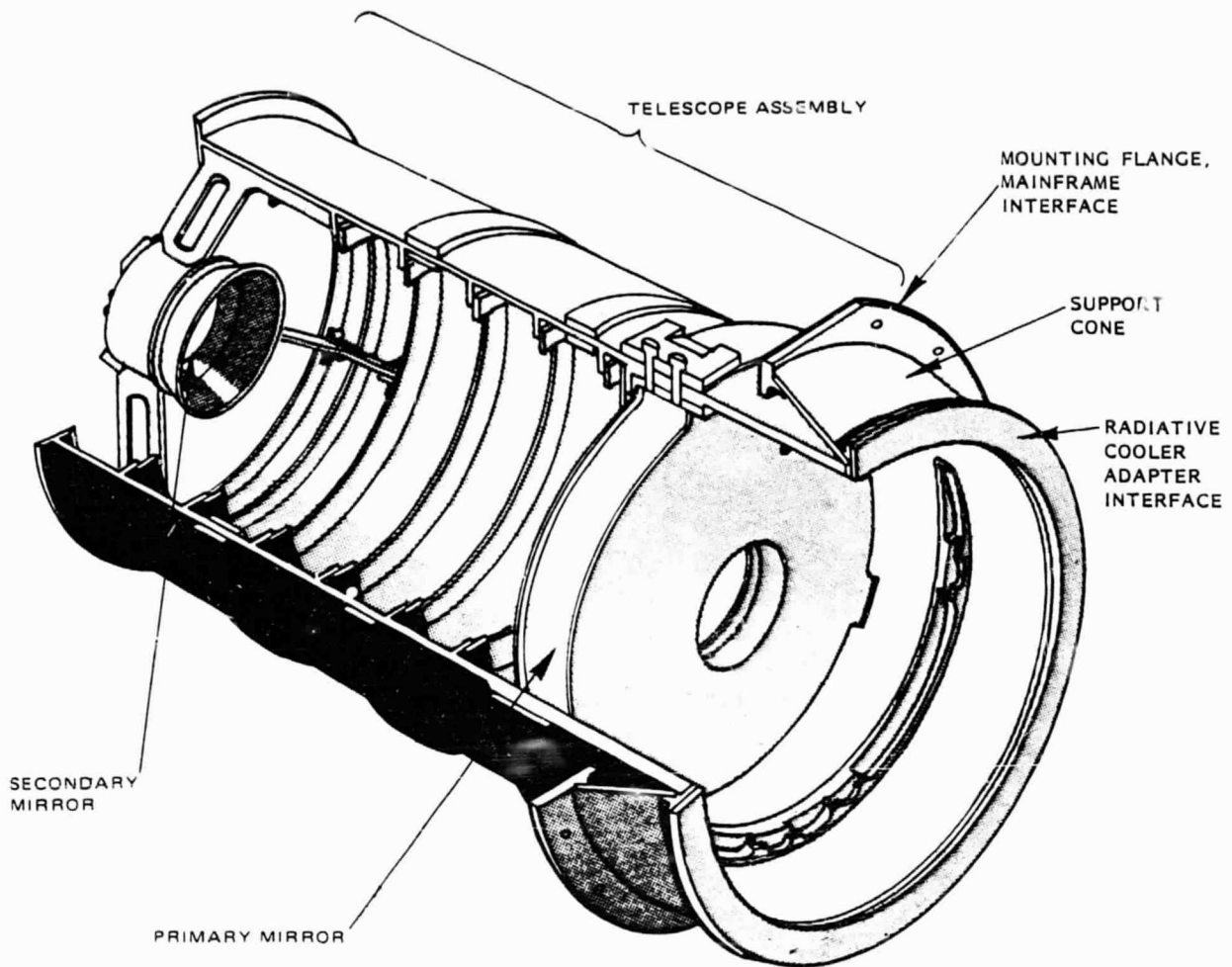


Figure 26. Telescope Assembly

Primary-Mirror Mounting

Mounting the telescope's primary mirror without inducing distortions to the figure proved difficult. Whereas the secondary mirror was mounted in a strain-free manner in a cell, adjustable for tilt, decenter, and focus, the primary mirror was rigidly fastened to the telescope tube. Figure 27 shows the primary mirror mounted in the optical metering structure.

Problems arose in the process of attaching the mirror to the mounting ring. The mirror was epoxy-bonded to Invar supports at three mounting feet, equally spaced around the mounting ring. In one case the epoxy was put on too thick and in the wrong places, making the primary mirror impossible to remove without breaking the glass. This deficiency was corrected by a change in bonding procedures. For Flight Model 1, the mirror was under size on the mounting diameter. The condition was corrected by inserting a

0.018-inch shim behind each of the three mirror mounting pads. The housing itself was not modified.

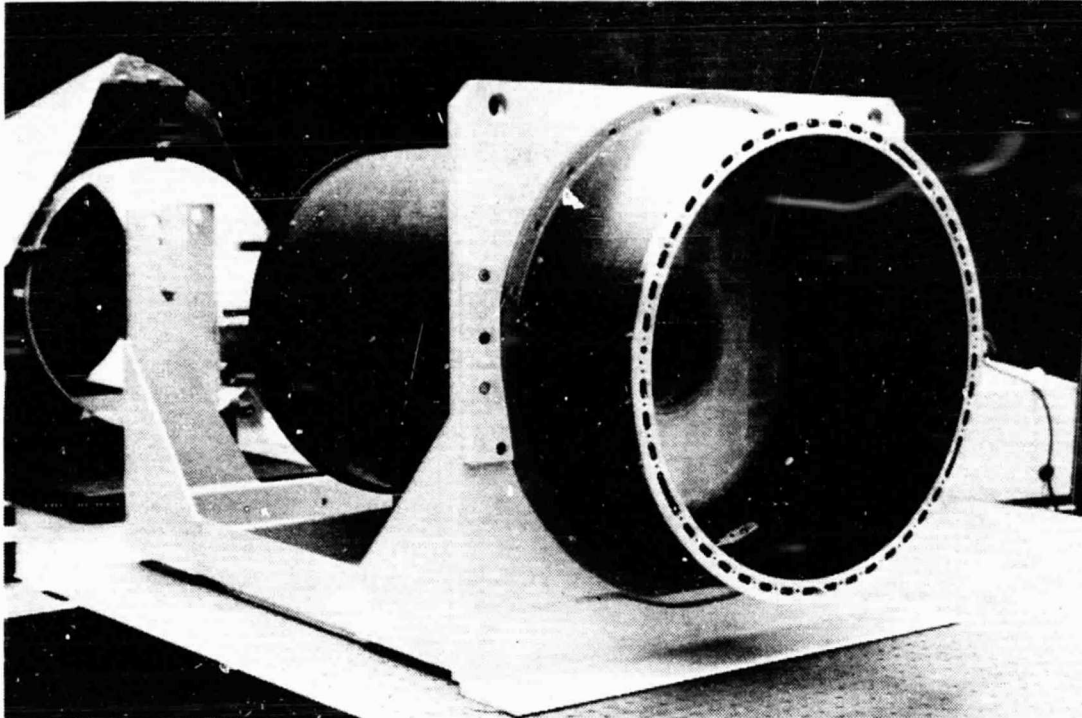


Figure 27. Primary Mirror Mounted in Optical Metering Structure

A more fundamental problem existed with regard to strain-induced distortion of the figure of the primary mirror. It was demonstrated both analytically and experimentally that mirror distortions were a result of deformations in the mounting flange of the optical metering structure. With the mirror initially installed in the telescope tube, the process of attaching the optical metering structure to the mainframe caused deformation of the flange, which transmitted strain through the graphite-epoxy support cone, resulting in a torque on one of the three mounting feet. The solution to the problem was to first attach the metering structure to the mainframe before bonding the primary mirror in place. This approach proved effective in keeping strain and distortion at acceptable levels.

Telescope Mirror Materials

The telescope materials were selected for strength, mechanical rigidity, and thermal properties at spacecraft temperatures. Both mirror substrates are made of ULE material (titanium silicate), which is formed by adding a controlled amount of titanium powder to the fused silica melt. The result is a glass-like material with a coefficient of thermal expansion near zero at spacecraft operating temperatures. The secondary mirror blank

is a simple round shape, machined from a solid piece of ULE, and it posed no special fabrication problems. On the other hand, the primary mirror blank is a much more complicated structure, having been designed specifically to achieve minimum weight. The primary mirror blank is built up as an eggcrated core with a circular mounting ring sandwiched between two flat faceplates, as shown in Figure 28. The components are machined separately and then fitted together in the proper orientation. The mirror blank is formed in a gas-fired oven at very high temperatures. The parts are fused together through successive steps of heat sealing and slumping and then annealed.

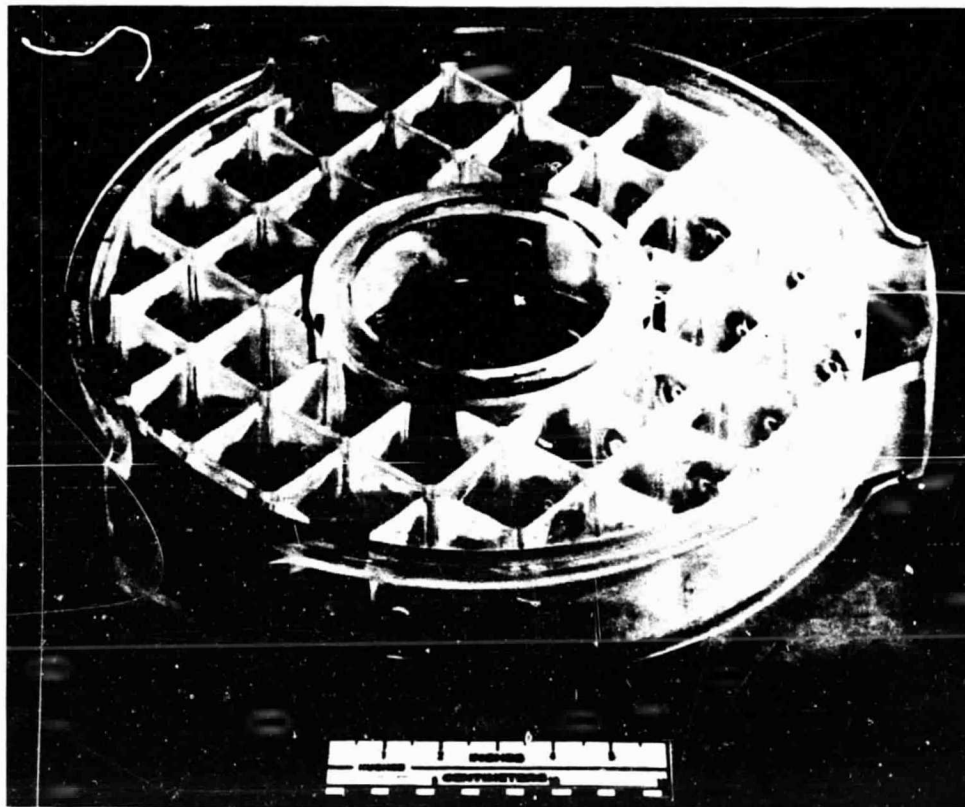


Figure 28. Primary Mirror Blank

Several problems were encountered during the manufacture of the lightweight primary-mirror blank. Dimensional discrepancies were encountered due to the relatively rough machining practices of the glass manufacturer (compared to the optical finishing house) and the fact that dimensions always change during the heat-sealing and slumping operations. Mechanical stresses also caused problems that were attributed to mounting during the machining and grinding operations; incomplete fusion and the appearance of small cracks or strut-end checks (an actual separation of a faceplate from a strut) within the core. These types of problems were corrected by a "refusing" operation in which the damaged areas were heated in a high-temperature furnace. In addition, improved vendor procedures were implemented for grinding

the surfaces. It was decided that the final edge grinding could be done best by the optical finishing house, and this alternative was implemented for the later blanks.

Optical Finishing

Inadvertent chipping of mirror edges by hard contact with metal surfaces and improper use of support fixturing was a recurring difficulty. This problem was encountered first at the glass vendor, then at the optical finishing house, later at the coater, and finally at SBRC. This damage occurred despite the fact the personnel involved were trained optical technicians, familiar with proper glass-handling procedures and techniques. The situation was improved by cautioning the persons involved as to the fragile nature of large glass mirror structures and by having them tape or otherwise protect any metal edges likely to come into contact with the mirrors. As a corrective action, the damaged surfaces were carefully inspected and tested using birefringence and dye penetrant tests to verify there were no cracks that were likely to run. The affected areas were then carefully stained and painted black.

Durability of the reflective silver coatings was another problem area. Coatings initially failed during tape testing following humidity exposure, and the mirrors had to be recoated. After delivery to SBRC, other mirrors, including the scan-line corrector mirrors, showed signs of mirror degradation; e.g., spots in the coating, which grew with time, and color change with time. After these coating problems were discovered, a study was conducted to find the cause of the degradation. The study lasted approximately four months and resulted in recommendations for storage, handling, and continuous monitoring of the coated parts.

As an outgrowth of this study, a contamination-monitoring program was initiated using witness samples from the coating lots of each of the actual mirrors used in each instrument. The purpose of this program was twofold: (1) to continuously monitor the witness samples for signs of coating degradation or failure, and (2) to assess the cumulative effects of handling and environment on the quality of the optical coatings (i.e., reflectance and scatter). The results of this program and the study show the problem of silver-mirror durability still exists, but certain measures, such as proper and thorough cleaning of the substrates prior to coating, storage in a nitrogen-purged environment, and proper handling to prevent contamination can reduce long-term degradation of the silver coating.

Two coating vendors were originally used, one coating the primary optics, the other coating the scan-line corrector and scan mirrors. Following the study, only the vendor who had coated the scan-line corrector and scan mirrors was used because this vendor had a lower frequency of outright failures and showed a decrease in the frequency and degree of degradation in later coating runs. The mirrors used in the protoflight and flight models were from this vendor and have performed well.

Aft-Optics Assembly

The aft optics support plate, diagramed in Figure 29, is multifunctional. It is the only all-Invar component in the optical metering structure and is the heart of the aft-optics assembly shown in Figure 30. The plate supports the relay optics inside the telescope and the radiative-cooler adapter, supports the central light baffle inside the telescope, and serves as a mount for the prime focal-plane assembly, the scan-line corrector, primary and redundant shutters, transformers, and numerous other electrical and optical components comprising the aft optics, as shown in greater detail in Figure 31. This plate is second only to the telescope in weight, even though the design was modified several times in an attempt to minimize its weight while maximizing its stiffness.

An all-composite (graphite-epoxy) design was initially proposed but, because of the number of holes and mounting provisions required, this design was discontinued in favor of the all-Invar design. The Invar design offered more flexibility in mounting arrangements, and the material's inherent isotropic properties (thermal conductivity and expansion) simplified the thermal-design requirements. These benefits offset the weight-saving potential of the composite design.

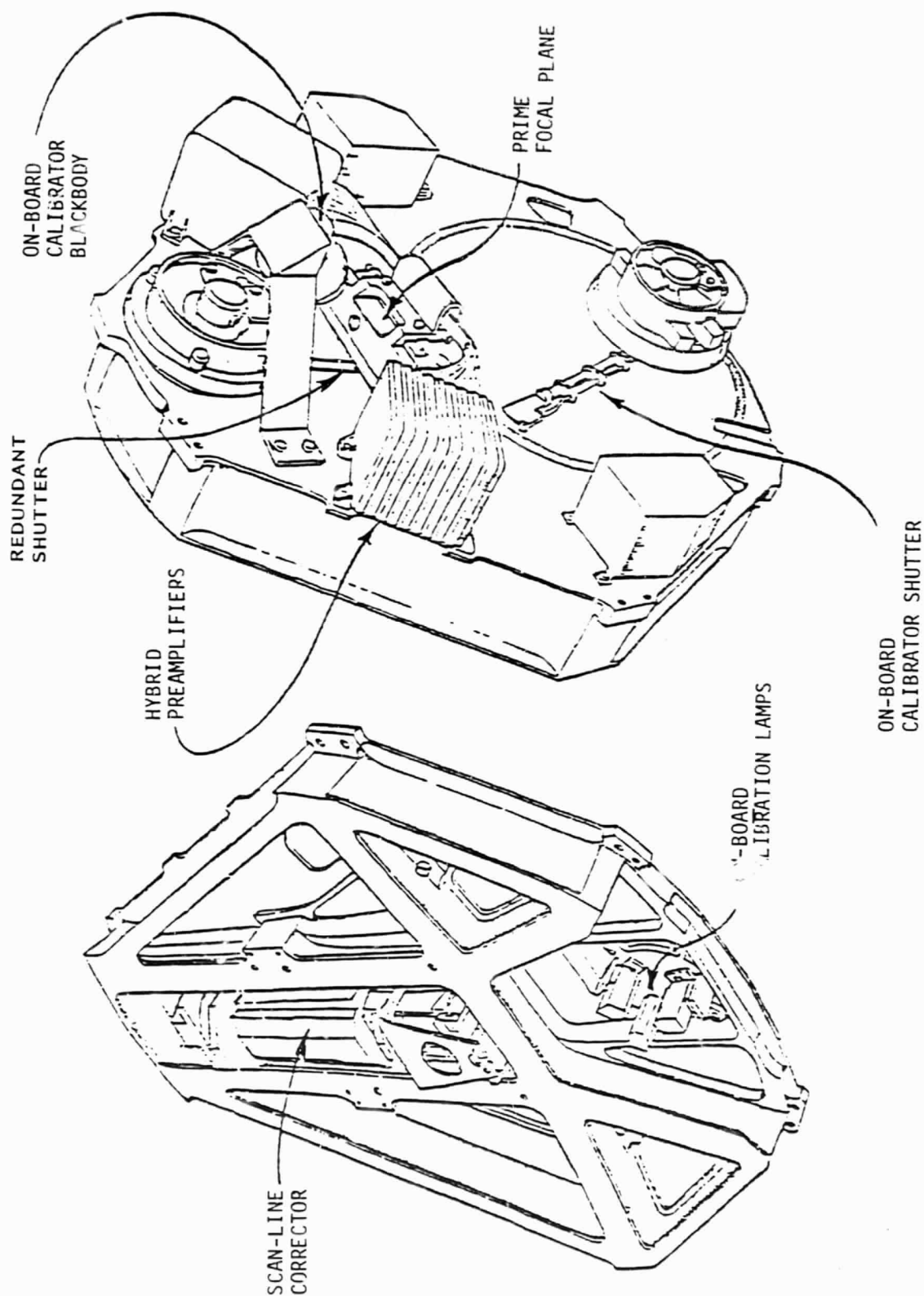
In spite of the complexity of the assembly as a whole, no design problems were experienced. However, several alignment difficulties were encountered with the associated subassemblies, such as the calibration/restore shutter and the prime focal-plane detector arrays. These problems and their solutions are discussed in appropriate subsections.

Relay-Optics Assembly

The relay-optics housing and base and the spherical-mirror mount were complex hardware components to design. Load, stiffness, and interface and functional requirements dictated the structural geometry. Figure 32 shows the housing and assembly.

Since accessibility was an essential design requirement, it became necessary to use Invar in the make-and-break joints. The low-expansion flanges that can be fabricated from Invar and its simple pin-and-fastener registration capability facilitated the fabrication.

The base structure of the relay-optics assembly contains a circular graphite-epoxy diaphragm that provides lateral support for the spherical mirror mount. The diaphragm was sized with specific stiffness limitations to make it compatible with the inchworm-adjuster load limitations. These adjusters attach to the three ears on the spherical mirror mount. Since Invar tangent bars inside the spherical mirror mount are determinant mounts for the mirror, they limit mirror distortion caused by thermal and dynamic disturbances.



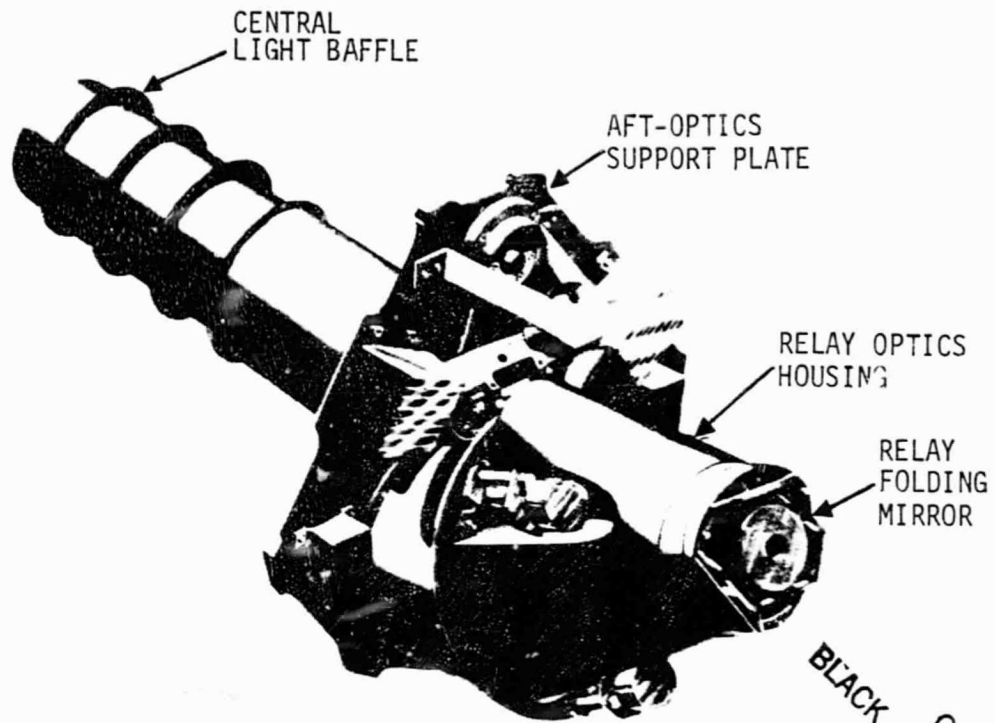


Figure 30. Aft-Optics Assembly

ORIGINAL PAGE
BLACK AND WHITE PHOTOGRAPH

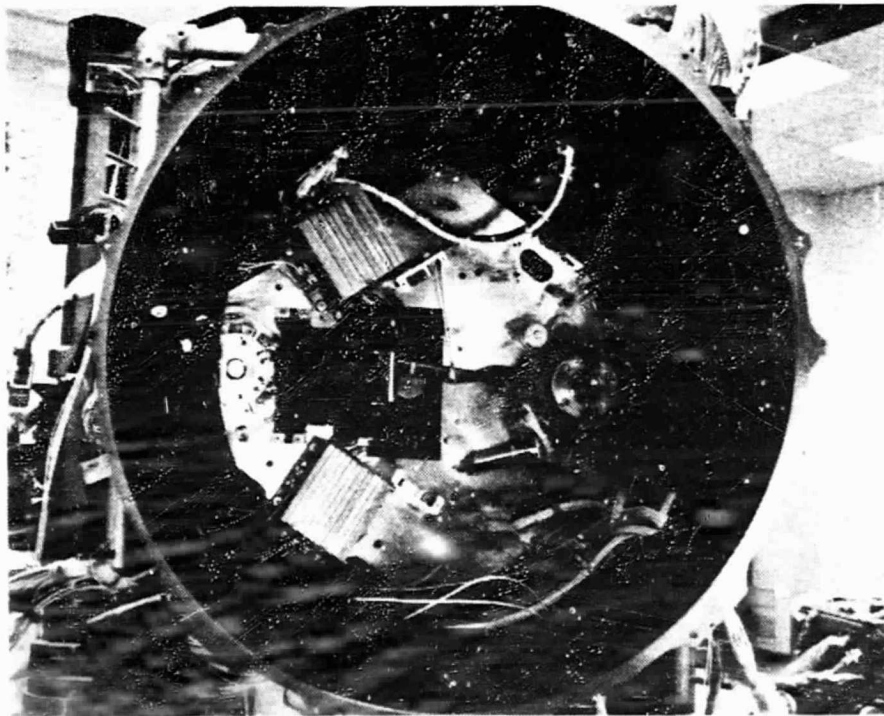


Figure 31. Aft-Optics Detail View

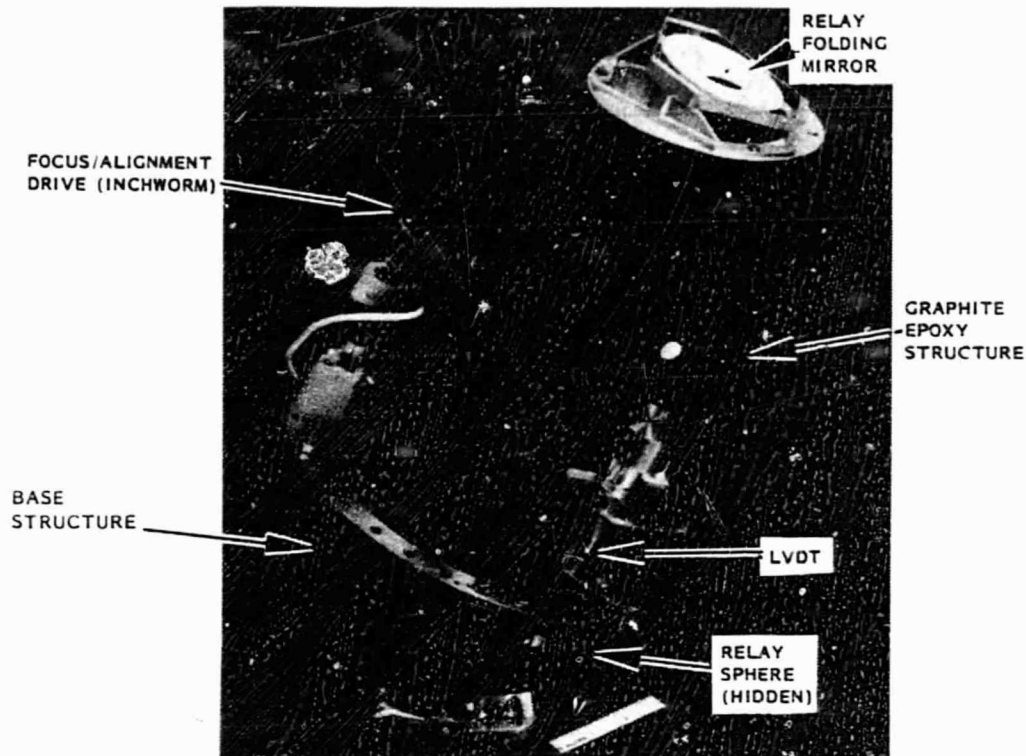


Figure 32. Relay-Optics Assembly

The relay-optics housing bolts to the base and contains provisions for attaching the inchworms. The three holes in the larger bottom flange allow the inchworms to pass through and attach to the spherical mirror mount. The smaller end of this graphite-epoxy cone-like structure supports the relay-optics flat mirror. Inside the relay-optics housing is an arrangement of light baffles, also made from graphite-epoxy, with pressed fiberglass tips.

Relay-Optics Focus-Alignment Drive

To allow for the possibility of realignment of the relay optics following a launch and cool-down and to assure correct focus at the cooled detector bands, a set of three piezoceramic devices, equally spaced around the periphery of the mirror, was employed to move the mirror to a corrected position. These actuators, or inchworms (an example of one is shown in Figure 33), had the following operational problems associated with them, but all were eventually solved:

1. One unit failed with a locked up brake during a temperature test. This was due to a very slight misalignment of the brake clamp with the other two clamps that operate on a common shaft. Rather than continuing to rely upon very precise clamp alignments to preclude binding, the shaft was redesigned to allow compliance between the

shaft section at the brake clamp and the shaft section through the other two clamps.

2. A unit failed to operate because of excessive play in a swivel jaw of a clamp assembly. The swivel jaw was deleted from the clamp design after it was determined to be unnecessary for proper clamp operation. No further problems due to clamps were experienced.
3. A conductive-epoxy joint failed during a vibration test due to loads in the cable being transmitted to the joint. Redesign of the cable termination provided better mechanical anchoring of the cable, eliminating stress at the conductive joint.
4. Improper installation of a setscrew caused some deformation of a shaft. The function of the tapered setscrew was to prevent shaft rotation by engaging a keyway in the shaft, but over-tightening resulted in keyway deformation. The setscrew was redesigned to eliminate this possibility.

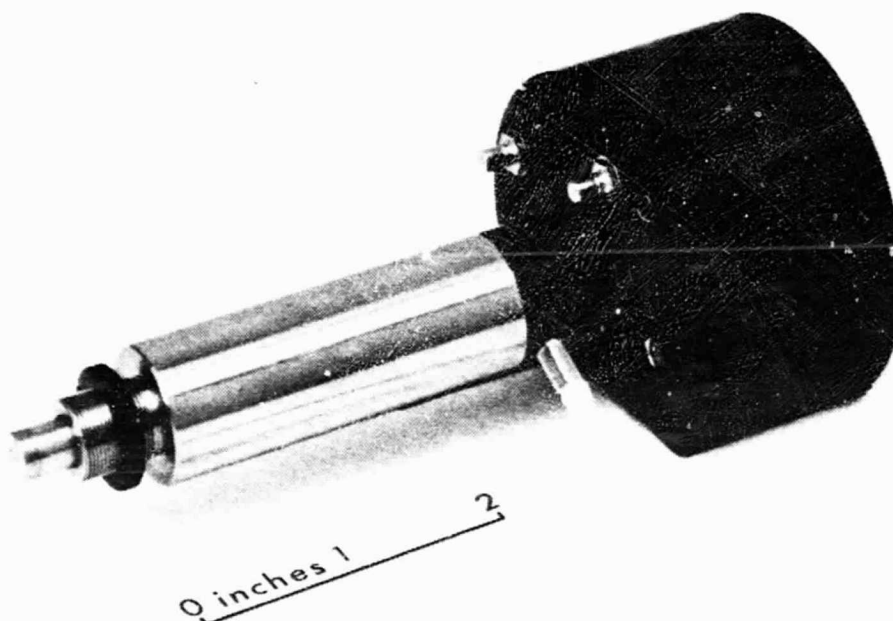


Figure 33. Inchworm

ORIGINAL PAGE
 BLACK AND WHITE PHOTOGRAPH

FOCAL PLANE ASSEMBLIES

The challenge for the prime focal plane and the cold focal plane was twofold: developing the focal plane assemblies and developing the detector arrays. The crux of the problem was the establishment of the dimensions of the arrays and detectors. They had to be small enough to result in an acceptable image

quality at the array extremities (large field angles for the telescope) but, at the same time, large enough to provide electrical and optical isolation between adjacent detectors in a given band. Further, extremely accurate dimensional alignment of each band was essential to satisfying the band-to-band registration requirements. The detectors had to be large enough to fabricate to close tolerances, but small enough to have low capacitance for noise containment. Consequently, all detector-input circuit-capacitance effects had to be minimized, so the detector circuitry was mounted close to the individual detectors.

The visible and near-IR detector arrays for each spectral band were each made from a single crystal (monolith) of silicon. The fabrication steps included ion implantation to form the sensitive photodiode-junction region, a metal mask for precise delineation of the sensitive area, deposited leads from wire-bond pads to the sensitive areas, and silicon monoxide layers under the metal mask and between the mask and the leads. The requirements of Bands 5 through 7 were met by using InSb photodiodes for Bands 5 and 7 and by using HgCdTe for Band 6.

Prime Focal-Plane Assembly

Figure 34 shows one of the four prime focal-plane subassemblies in a test configuration, consisting of a flat cable, substrate, and a single array of detectors. Figure 35 shows the four arrays at the prime focal plane. The band-level subassemblies shown in Figure 36 are mounted perpendicular to the focal plane with detector leads connecting to the traces visible at the top of the substrate (Figure 35).

Problems in fabricating the prime focal-plane assembly occurred with the cables and substrates, electrical crosstalk and distributed capacitance, and its assembly and alignment.

Cables and First-Stage Preamplifier Substrate

The silicon detector first-stage preamplifier electronics were fabricated on a fused quartz substrate approximately 0.020 inch thick. Quartz was chosen as the substrate material because of its superior dielectric properties. Flat, laminated cable was bonded to the substrate, which was fastened in a detector/frame assembly as shown in Figure 37. The shielded, polyimide, flat cables had been designed with a thickness that allowed maximum flexibility for a low-radius bend, just as the cable leaves the detector/frame assembly. However, the cables, as delivered, had been fabricated with a thicker adhesive layer than specified, resulting in a stiffer cable. This ultimately caused bending stress fractures in the quartz substrates. Since the program schedule did not allow for refabrication of the cables, the frame assembly was successfully modified to reduce the bend radius required.

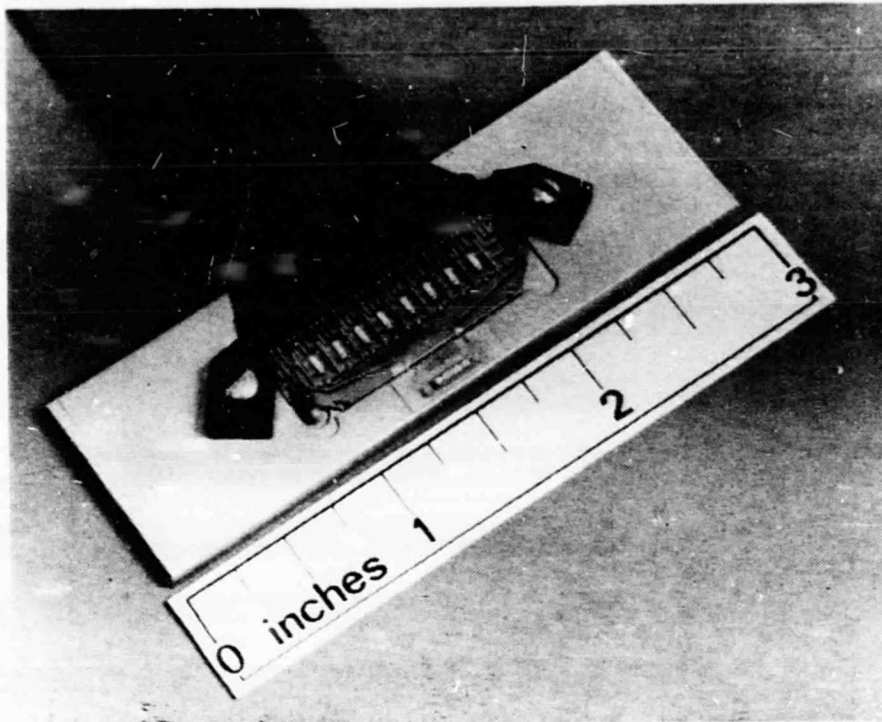


Figure 34. One of the Four Prime Focal Plane Assemblies

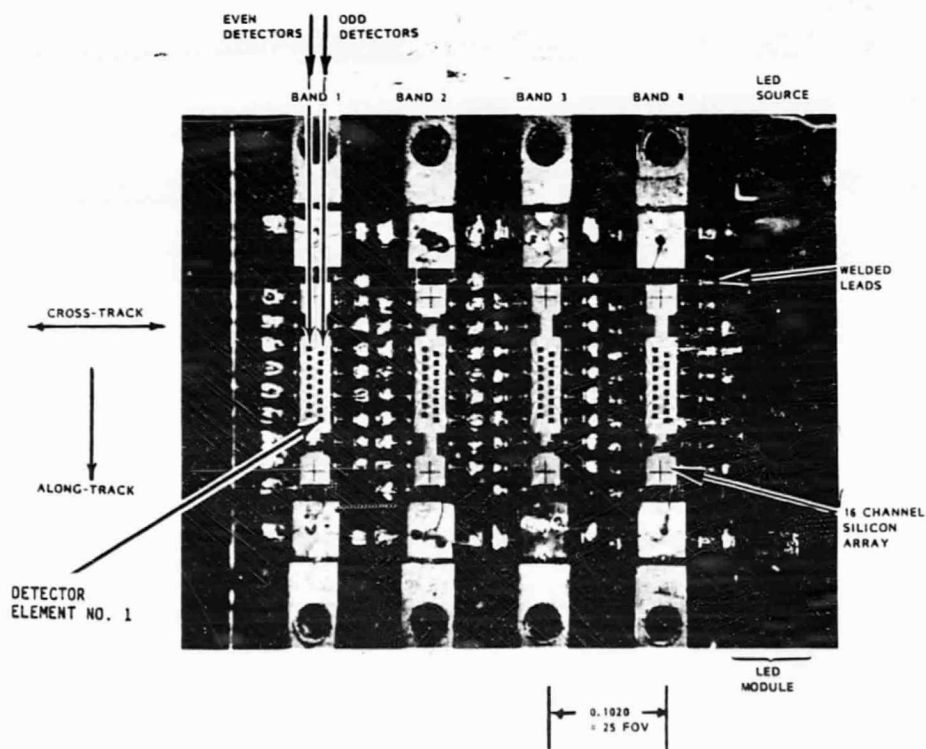


Figure 35. Bands 1 through 4 of the Prime Focal-Plane Assembly

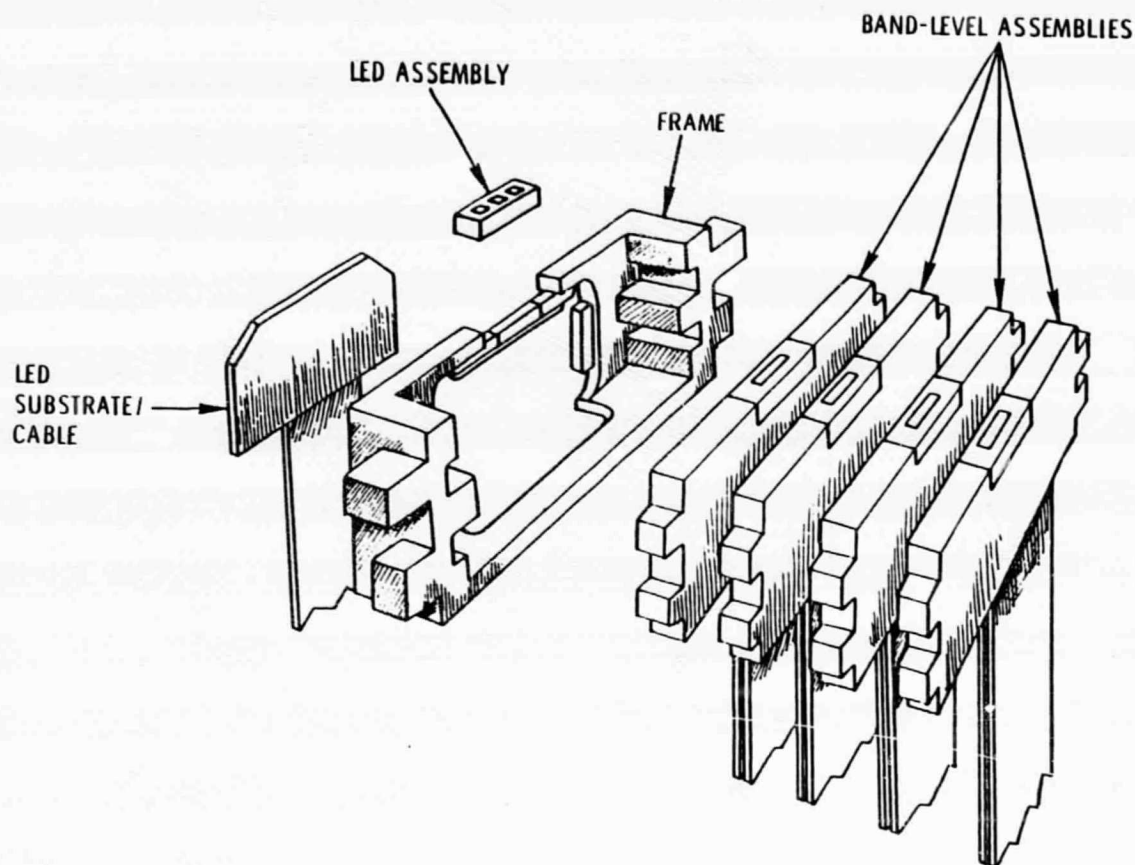


Figure 36. Breakaway View of Band-Level Assemblies

Electrical Crosstalk and Distributed Capacitance

A significant problem encountered in the design of the prime and cold focal planes was associated with attaining the desired signal-processing frequency response (flat bandpass to 52 kHz) while using very large feedback resistors ($10^9\Omega$ for Bands 1 through 4 and $2 \times 10^8\Omega$ for Bands 5 and 7) in the current-mode preamplifiers. These very high valued feedback resistors were

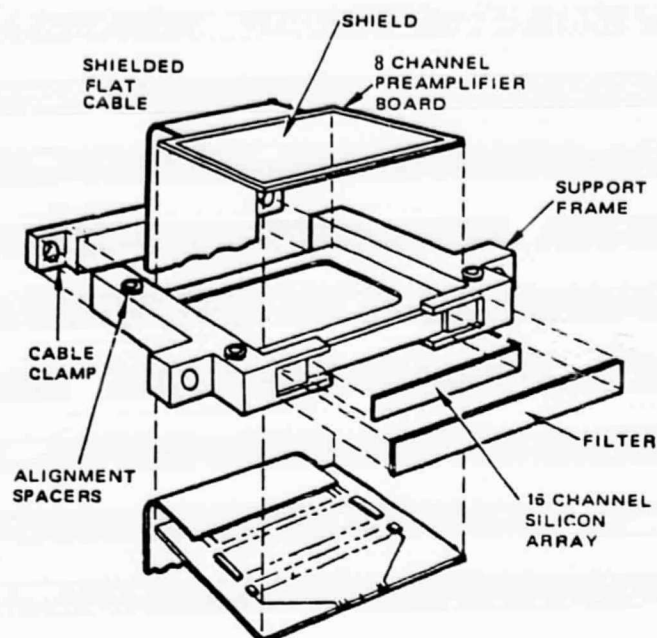


Figure 37. Silicon FPA Detector/Frame Assembly

chosen to optimize the amount of Johnson noise contributed by this source. Making the resistors larger than the values chosen would not have reduced the overall noise significantly because other noise sources would become dominant. Lowering the value of the resistors would rapidly degrade the system noise because the Johnson noise would become the dominant noise source.

The large-valued feedback resistors (which are mounted as close as possible to the detector elements and preamplifier input JFETs to minimize input node capacitance and, thereby, minimize system noise) have associated with them parasitic capacitances in shunt and to ground. These stray capacitances would limit the frequency response of the preamplifier to approximately 10 kHz, and the shape of the response would not be a simple 6 dB per octave rolloff, but would be quite complex due to the nature of the distributed stray capacitance to ground. The limited frequency response of the preamplifier thus requires subsequent "boosting" to attain the overall flat system response to 52 kHz. (To obtain the 52 kHz response in the preamplifier without subsequent boosting would require that the parasitic capacitances of the feedback resistor be significantly less than 0.003 pF.)

To allow subsequent boosting in the postamplifiers with a simple zero, the rolloff of the preamplifier had to be that of a well-behaved simple pole. To accomplish this, a shunt swamping capacitor of approximately 0.03 pF was implemented in parallel with the feedback resistor to roll off the preamplifier response at about 3 kHz. One plate of the capacitor was the circuit trace under the end of the resistor. The dielectric utilized was the

ceramic substrate material of the resistor. The other plate was the resistor contact pad, which was trimmed to an appropriate size.

This design worked out very well, and the overall boosted response of the system could readily be trimmed to be flat from dc to 52 kHz with deviations in flatness held to ± 0.2 dB. To minimize crosstalk between channels and to provide a means for trimming the residual effects of the stray capacitances associated with the feedback resistor, aluminum shields were implemented adjacent to each resistor. Figure 38 is an enlarged view of a prime focal-plane substrate showing one FET, one feedback resistor, and two crosstalk shields. Also evident are the circuit trace and wirebond that implement the 0.03 pF "swamping" capacitors.

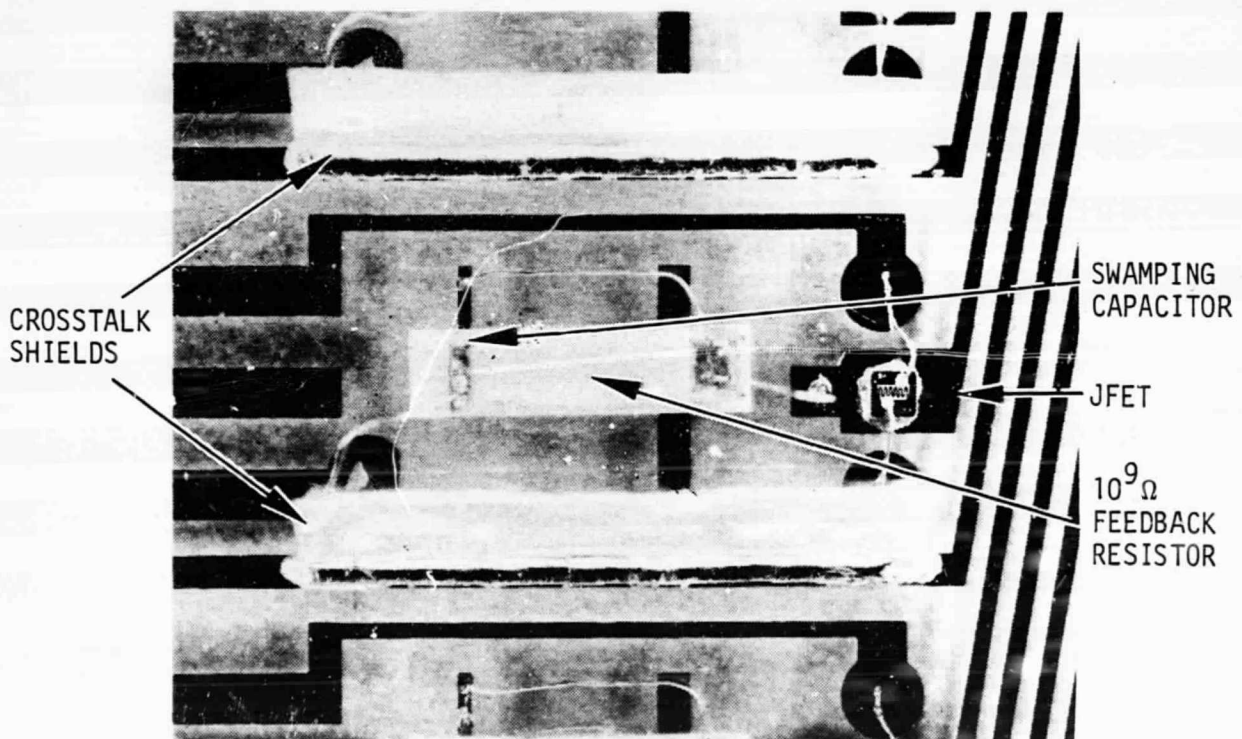


Figure 38. Enlarged View of a Prime Focal-Plane Substrate

The frequency response problems of spectral Bands 5 and 7 were solved in a similar manner on the cold focal plane. However, in this case, because of the lower value feedback resistors, a larger value capacitor was used. It was decided to fabricate a discrete capacitor using thin-film technology. The resulting capacitors can be seen in Figure 39 mounted on the out-board contact pad of the feedback resistor.

ORIGINAL PAGE
 BLACK AND WHITE PHOTOGRAPH



Figure 39. Swamping Capacitors

Assembly and Alignment

ORIGINAL PAGE
BLACK AND WHITE PHOTOGRAPH

The prime focal-plane assembly was designed to provide a full six-axis (ΔX , ΔY , ΔZ , $\Delta \theta_x$, $\Delta \theta_y$, $\Delta \theta_z$) independent alignment adjustment of each of the four arrays. Structural support for each array was provided by a beryllium frame. The detector array and filter are mounted on the top edge of the frame (see Figure 37), and two fused-quartz preamplifier boards are bonded into the frame, one on each side, with components inward. Connections are made to the electronics modules by flexible cables bonded to the preamplifier boards. Interconnections are made by wire bonds.

The beryllium frames, as received, were slightly warped. The assembly tooling flattened them while the fused-silica preamplifier substrates were bonded in place. This resulted in residual stress in the preamplifier substrates after the tooling was removed. This initial residual stress, combined with stresses introduced during alignment adjustments, caused several preamplifier substrates to crack and resulted in loss of several channel connections.

Since the frame assemblies of the arrays were complete when the substrate stress problem was discovered, an alternate assembly method was adopted to prevent any additional stresses from being introduced during alignment. Fully independent adjustment

was abandoned, and the frame assemblies were installed, aligned, and bonded onto the focal-plane bracket one at a time.* Stresses in the preamplifier substrates were monitored during alignment and bonding by an optical technique to prevent stresses beyond a predetermined level.

Also, the flex cables were stiffer than expected, so the focal-plane bracket was modified to reduce the bend radius of the cables to prevent additional stressing of the preamplifier substrates.

Cold Focal-Plane Assembly

Figure 40 is an exploded view of the cold-stage assembly, showing the location and orientation of the cold focal-plane assembly. Figure 41 is a photograph of the cold-stage assembly, with and without the spectral filters, where the detector arrays are located in the center of the disk, and the preamplifier first-stage FETs and feedback resistors are radially distributed about them.

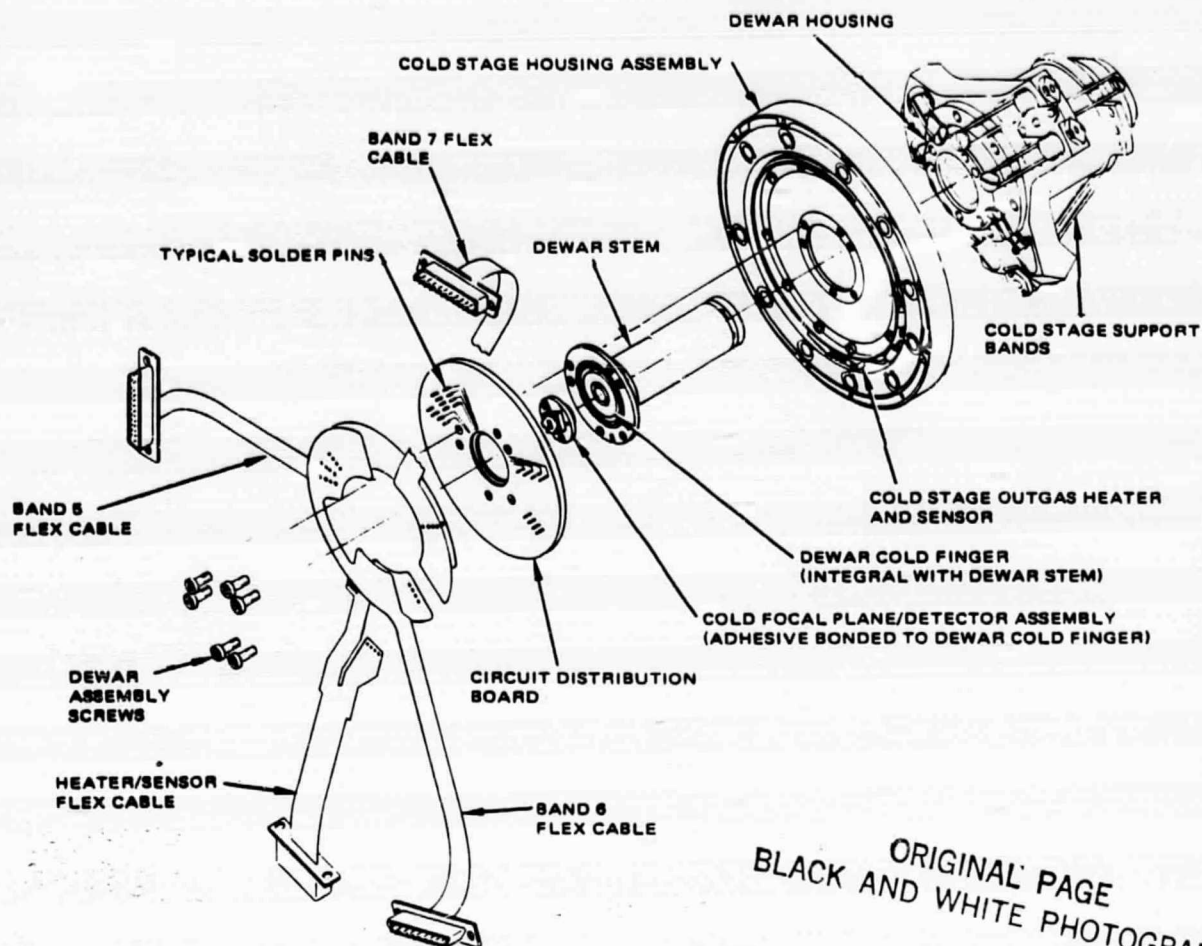
Cold Focal-Plane Module

The detector arrays of Bands 5, 6, and 7 are located under the spectral filters associated with each band and are bonded to a flat, circular, multilayer ceramic board, which is adhesive-bonded to the face of the Dewar coldfinger. The connections from the 36 individual detectors lead to the preamplifier electronics, oriented in a circular pattern on the board. Wire bond pads, concentrically positioned around the outer edge of the disk, allow the electronics to be connected to the annular-shaped circuit-distribution board.

Crosstalk between adjacent preamplifier channels was minimized by adding electrostatic shields over the feedback resistors. Additionally, the high value of the feedback resistors' stray capacitance caused poor frequency response. This was improved by placing the resistors on sapphire standoffs, reducing capacitance to ground. Also, the stray capacitance was swamped out by adding a parallel capacitor to each resistor as described on page 83.

Due to temperature cycling of the cold focal-plane assembly, fatigue cracks developed in the platinum wire bonds between the ceramic board and the circuit-distribution board. This was corrected by replacing the platinum wire bonds with gold wire bonds.

*The independent adjustment capability could be regained on future TM instruments by redesigning the preamplifier substrates using less stress-sensitive materials, such as polyimide/glass laminates.



ORIGINAL PAGE
BLACK AND WHITE PHOTOGRAPH

Figure 40. Cold-Stage Detector/Dewar Exploded View

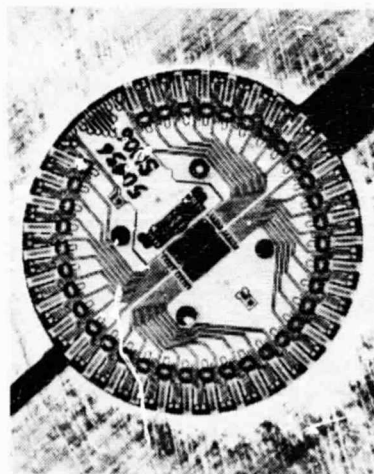
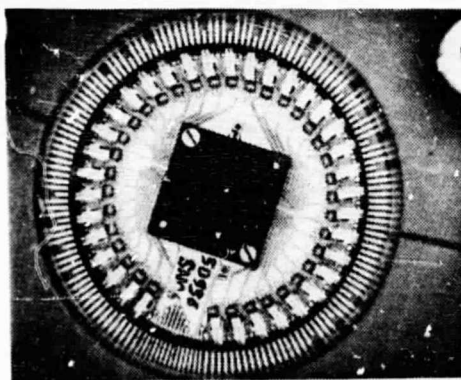


Figure 41. Cooled Focal-Plane Substrate Assembly with and without Spectral Filters

Detector Arrays

A photograph of the detector portion of the cooled focal-plane assembly comprising Bands 5, 6, and 7 is presented in Figure 42. The detectors, consisting of two 16-channel InSb subarrays and a 4-channel HgCdTe subarray, are epoxy-bonded to the ceramic substrate with a spectral filter support housing located above them, as shown in Figure 43. Reference to Figure 5 also will help in locating the cooled array with respect to the TM system's optical train.

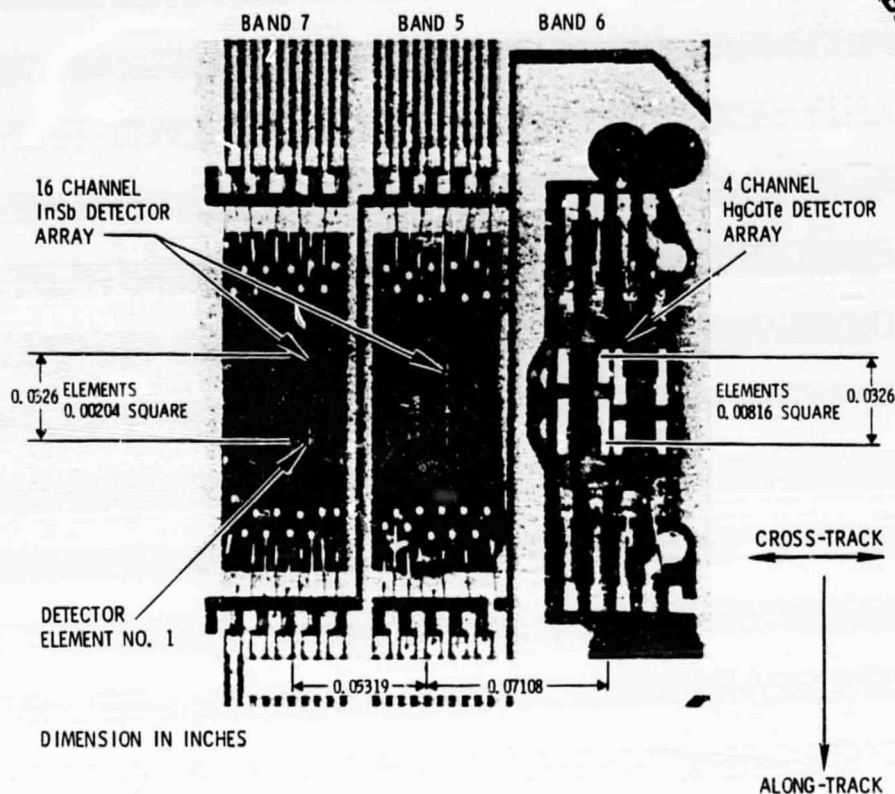


Figure 42. Cold Focal-Plane Detector Arrays:
Bands 7, 5, and 6

The thrust of the design effort was to optimize responsivity for each wavelength band and to minimize noise generation intrinsic to the detectors. With respect to responsivity, the approach focused on obtaining high quantum efficiency and low surface-state recombination by state-of-the-art processing procedures. Responsivity also was enhanced by application of a quarter-wavelength deposition of an index-matching silicon-monoxide antireflection coating that improved absorption of incident energy.

To minimize noise generation by the detectors, it was necessary to maximize their impedance while minimizing their capacitance. The approach taken to accomplish these goals was to choose the proper base doping of the detectors to maximize impedance and to utilize a thick silicon-monoxide insulating coating

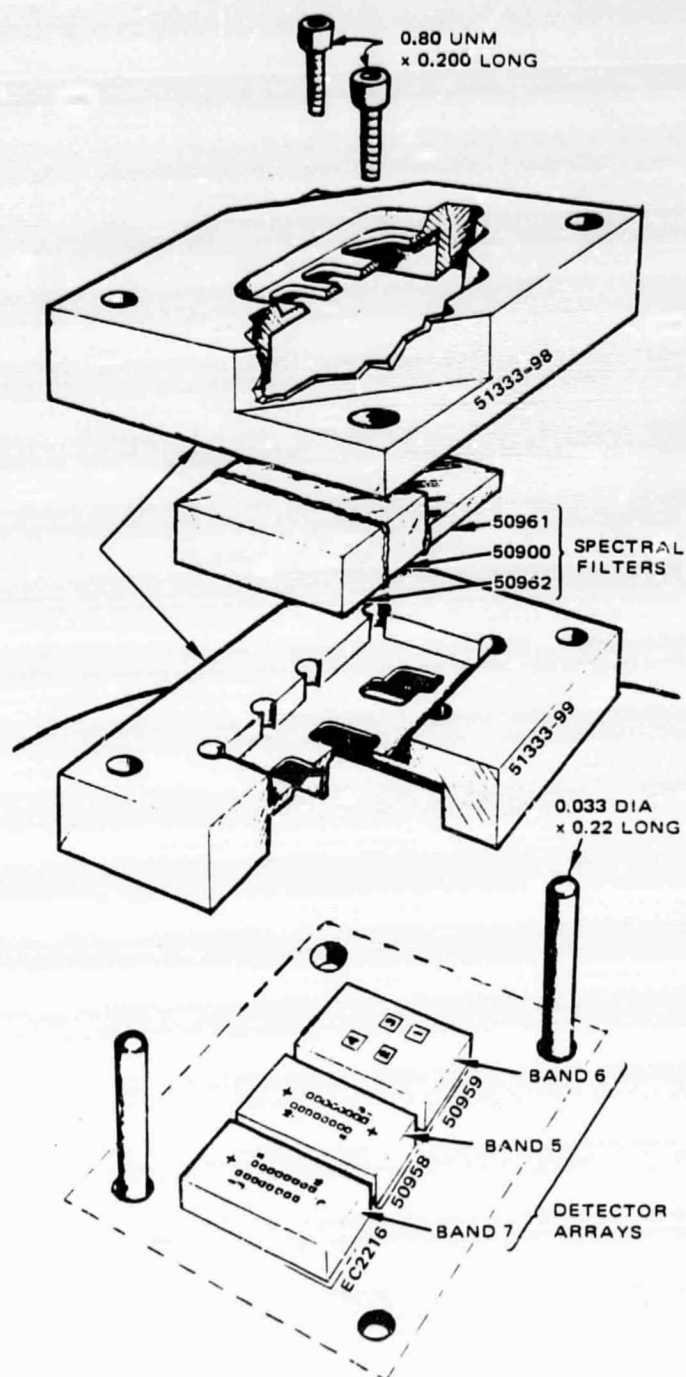


Figure 43. Spectral Filter Support Housing

under the deposited leads. Since a thin quarter-wavelength oxide coating was required over the detector's sensitive area and a thick coating under the leads, a two-step deposition process was used with the second supplemental layer adding to the thickness in the lead area. However, this resulted in a step discontinuity in the surface where the metal leads were to be deposited, making it difficult to metallize and, ultimately, causing open detector leads. The solution to this problem was to thicken the detector leads where they went over the oxide step using a second evaporation process.

In the fabrication process, the silicon-monoxide layers were being chipped and cracked when the wafer was diced into detector arrays. The chips and cracks encroached upon the detector leads and resulted in disconnected or open leads during the wire-bonding process. The solution was to remove the oxide from the immediate vicinity of the saw's kerf area so that adjacent areas of the oxide layers were no longer affected by the saw.

Cold Focal-Plane Cables

Due to the large number of conductors required on the cold focal plane (147) and the minimum impedance and heat-loss requirements, there was a critical trade-off between electrical conductance and thermal resistance of the conductor material in the design of the cold focal-plane cables. The high Lorentz constants (product of thermal conductivity and electrical resistivity divided by absolute temperature) of manganin, constantan, and other high-thermal-resistance alloys often used for cooled cable conductors prevented use of these materials. It was necessary to design cables using pure nickel or pure copper conductors with much lower Lorentz constants in order to meet the minimum electrical resistance and thermal conductivity requirements. The use of pure copper conductors required an extremely small conductor cross section (1.1×10^{-7} in²) for each Band 5 and Band 7 conductor.

The flight cables installed on the TM instrument used pure copper conductors, 8000Å thick. This was achieved by vapor-depositing the 8000Å copper conductor pattern onto a polyimide film cable base. A polyimide film cover layer was laminated over the conductors, and a 1000Å aluminum shield layer was vapor-deposited on each side. The termination pads of the conductors were electroplated with 0.005 inch of copper to facilitate solder terminations.

Since this was the first time a cable of this type had been fabricated in this manner, there was a great deal of process development effort involved in producing acceptable artwork and in fabricating the cables. These cables represent the state of the art in achievement of high electrical conductivity and low thermal conductivity.

C-2

SCAN-LINE CORRECTOR

The effectiveness of preliminary concepts for the TM was limited by an object-space scan mirror that used 40% of its motion in retrace. A scan-line corrector (SLC) mechanism was devised to allow use of a bidirectional scan and thereby improve the instrument's efficiency. The SLC, illustrated in Figure 44, utilizes two mirrors in a periscope orientation. Whenever the mirrors are rotated together about an axis through the common centerline of the mirrors, the telescope's optical axis experiences a parallel linear displacement. This configuration has the advantage of generating image displacement without any accompanying change in incident angle at the focal plane. An angular magnification in image space occurs as a result of the object-space change, which fortuitously allows a convenient working amplitude for SLC rotations.

This form of scan mechanism introduces no image rotation and insignificant focus shift. Further, the performance of the SLC does not depend on the SLC assembly's location in the telescope's optical path, except as necessary to avoid vignetting. Figure 45 illustrates the result of compensations to the scanned field by the SLC assembly.

The mechanical design is dominated by the need to minimize mass and inertia, so the mechanism can provide rapid response and to minimize the impulse transmitted to the instrument's structure. The mirrors and the mirror-support framework are made of beryllium. The moving mechanism is supported by flex pivots at the shaft ends. The spring in the pivots act in concert with the drive motor to accelerate the armature. The motor employs a moving coil and a fixed magnet to minimize its moment of inertia.

The magnetic field of the drive motor operates with an open-loop current drive. It is doubtful if a suitably accurate and compact position sensor could have been designed. Dual tachometers monitor angular rate and provide a basis for ensuring that the rotational rate is consistent with predetermined profiles.

ON-BOARD CALIBRATOR ASSEMBLY

The hardware design and development of the on-board calibration system posed one of the most intriguing and challenging problems of the Thematic Mapper. In the early evolutionary phase of the program, an internally generated calibration source and an external source, the sun, as a double-referenced, or cross-referenced approach, were considered. The sun-source calibrator scheme represented a basic, once-per-orbit check of the complete optical train of the TM. On the other hand, the internal calibrator system would provide known radiant energy inputs to the detectors during the turnaround portion of each scan. In case of failure of the internal calibration mechanism, a backup shutter would operate and provide only the dc-restoration function. Prior

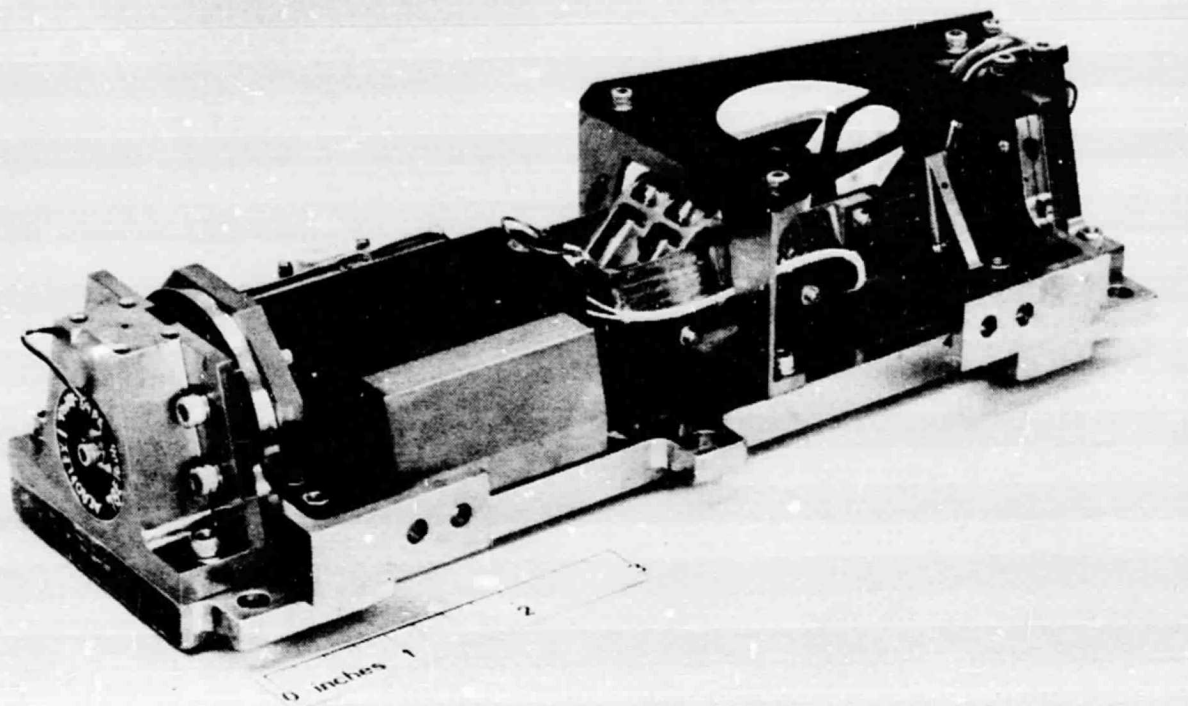


Figure 44. Scan-Line Corrector

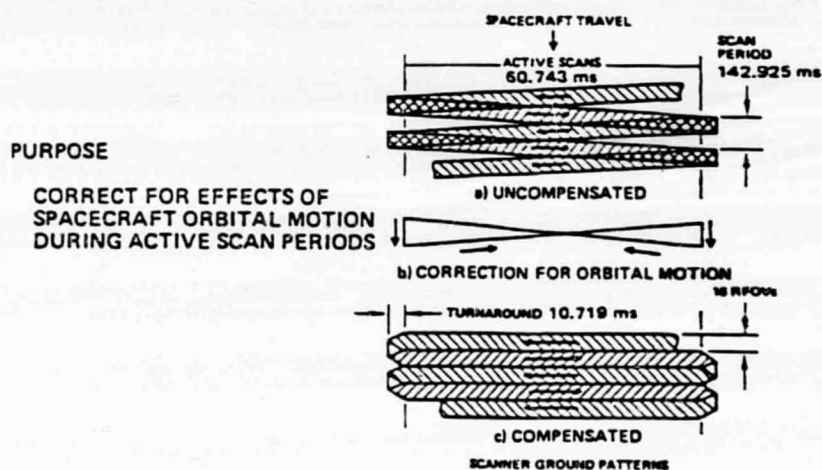


Figure 45. Scan-Line Correction Function

to the Engineering Model Preshipment Review the solar calibrator was deleted by GSFC direction because the spacecraft design would interfere with its operation.

Figure 46 is a diagram showing how the internal calibrator illumination is transmitted from the lamp sources at the base of the assembly to the projection optics at the end of the shutter, and Figure 47 shows the actual assembly. An oscillating flag passes immediately ahead of the primary focal plane each time the scan-mirror assembly is in the process of reversing its scan direction. Mounted on the head of the flag at one edge is a linear

ORIGINAL PAGE
BLACK AND WHITE PHOTOGRAPH

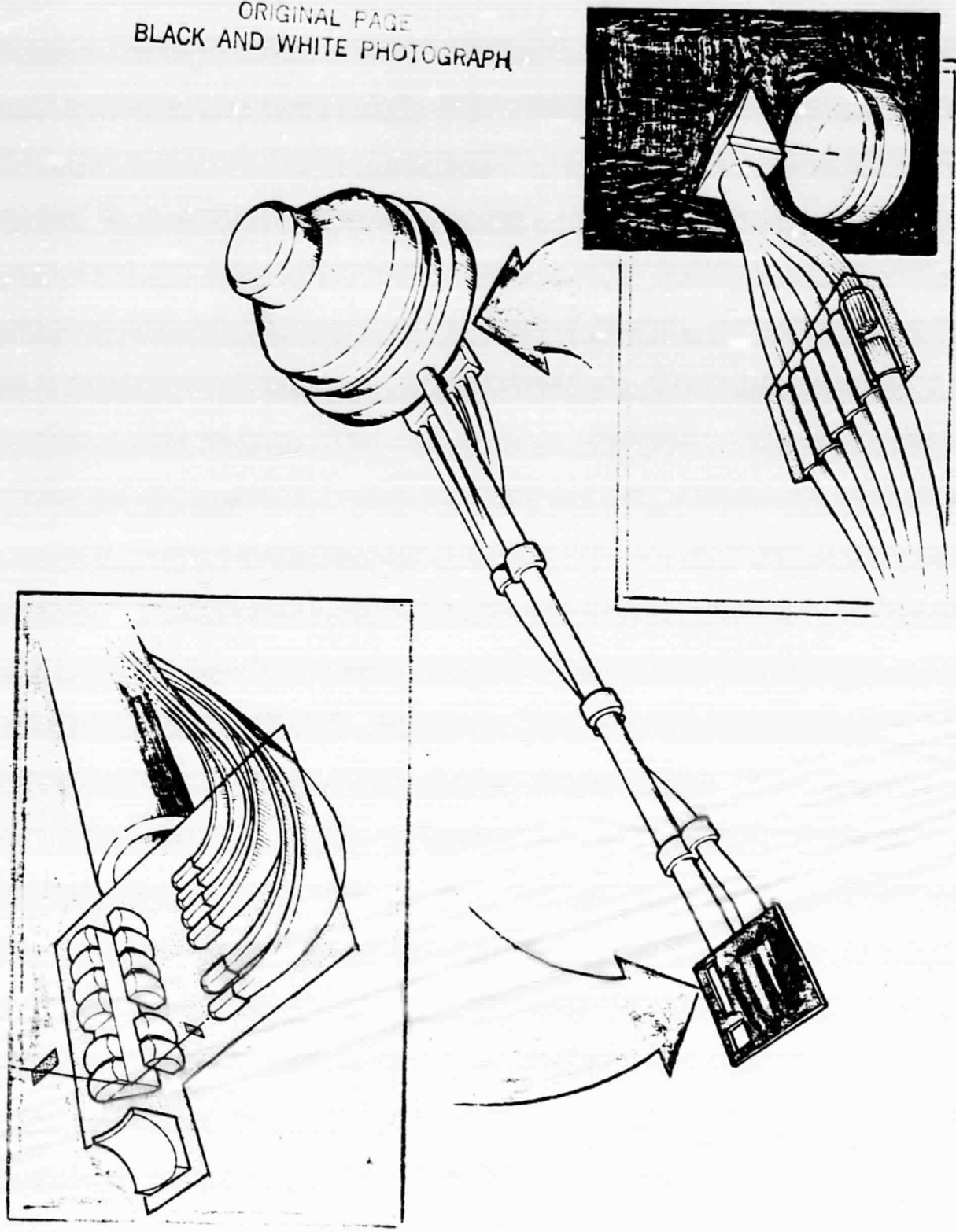


Figure 46. Internal Calibrator Flag Rotation

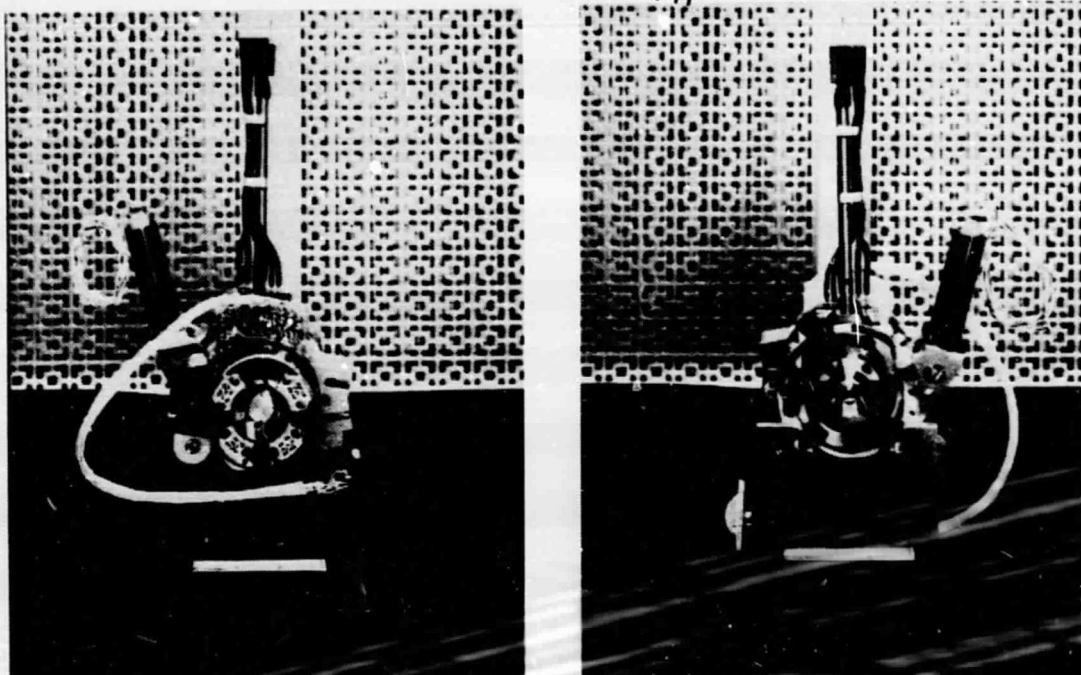
ORIGINAL PAGE
BLACK AND WHITE PHOTOGRAPH

Figure 47. Internal Calibrator Flag Mechanism

array of miniature optical elements, fed by a fiber-optics assembly and tungsten-lamp illuminators, as depicted in the more detailed drawing of Figure 48. Channels 1 through 4 cover the warm focal-plane arrays, while channels 5 and 7 are relayed to the cryogenically cooled focal plane. Channel 6, the thermal band, is calibrated by a stationary blackbody, located away from the oscillating flag shutter. The radiant energy output from the blackbody is collected by a toroidal mirror on the flag and redirected to the Band 6 detector array. The area on the flag adjacent to the linear array of optical elements is painted a flat black. Its temperature is continuously monitored, and it serves as the reference radiant energy level for dc-restoration of all bands.

Several elements of the assembly posed significant problems in development and fabrication. Foremost was the fiber-optics assembly and the challenge of providing the required levels of dynamic range and uniform, symmetric, radiance distribution to the detectors. The mechanization of the oscillating shutter represented technology previously implemented on the VISSR Atmospheric Sounder Program. Nevertheless, the several problems discussed below were specific to the TM in terms of vibration damping and assured reliability of operation over an extended lifetime.

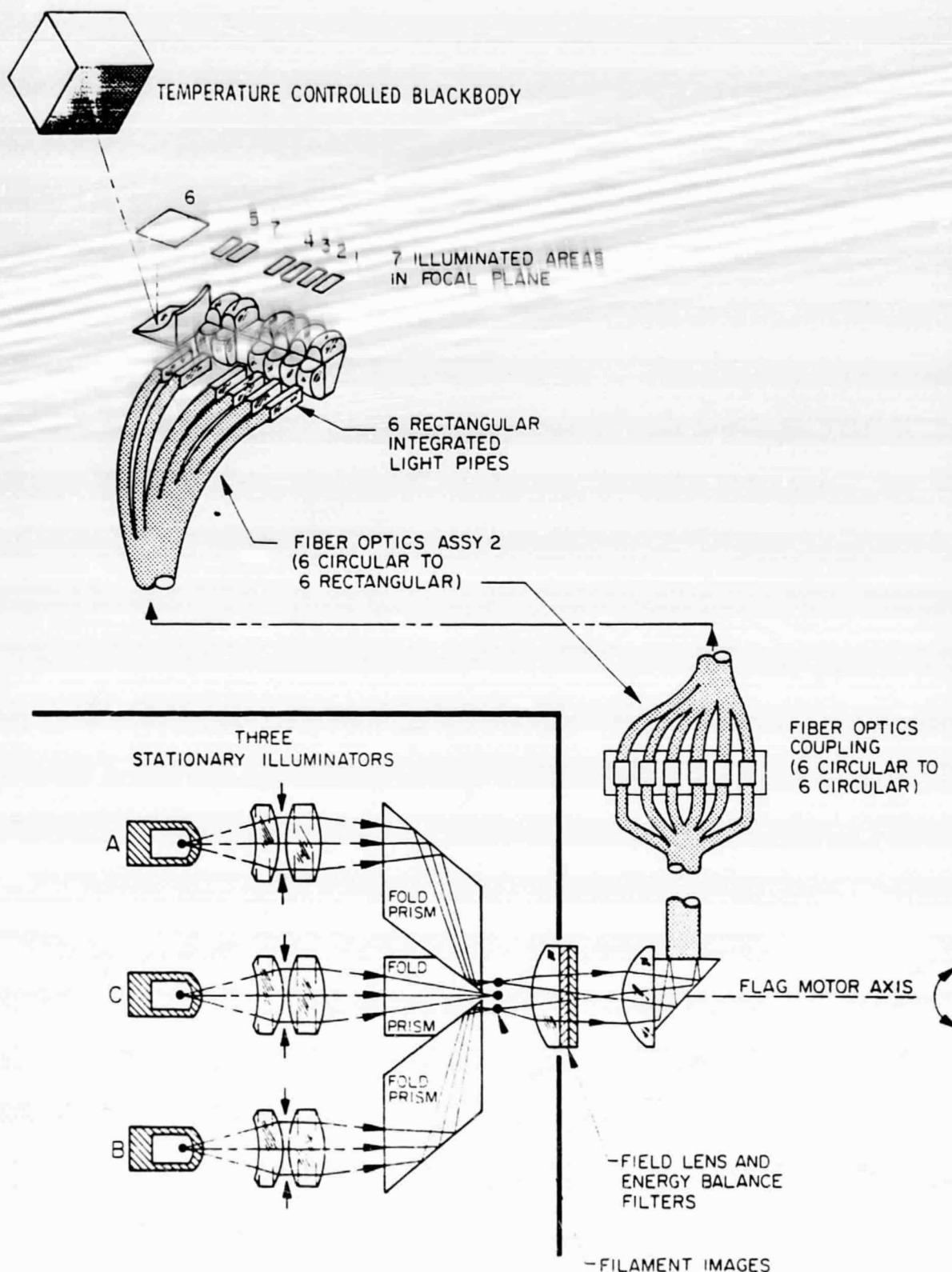


Figure 48. Internal Calibrator Scheme

Fiber-Optics Assembly

The on-board calibrator's fiber-optics system consists of the two coupled fiber-optic-bundle assemblies shown in Figure 48. The base of the input fiber-optics bundle receives energy from three tungsten lamps in the calibrator's light-source assembly via a set of relay optics. The input end of the bundle is 0.125 inch in diameter and contains approximately 3500 fibers, 0.002 inch in diameter.

This bundle is divided into six output bundles of 0.052 inch diameter. Each of the bundles must be randomized well enough that the output legs have radiometric values within $\pm 10\%$ of each other when input energy from any of the three lamps (120° apart) is passed through the fiber bundle. The output legs of the fiber-optics bundle couple to the input ferrules of the fiber-optics flag. The input end of each of the six bundles is circular, and the output, which feeds into the integrating rods, is rectangular.

The principal problem with the fiber-optics system lay in producing an assembly whose six individual radiometric outputs varied by less than 10% for any given input radiance level. The essential difficulty was in combining the individual fibers in such a way that the division of the main bundle into six separate bundles resulted in a randomized combination. This would have ensured a uniform radiance within the stated tolerance specification between the separate bundles, provided that a uniform or symmetrical distribution of irradiance existed at the input end of the main bundle.

There was a considerable expenditure of time and effort over a period of approximately 2 years by vendors who specialized in this type of fabrication. The fabrication procedure apparently introduced angular variations and asymmetry into the output-beam profile and a nonrandom distribution of individual fibers in the bundles. Notwithstanding the elaborate assembly fixtures used by the manufacturers, there were no standardized fabrication procedures developed to ensure consistency from unit to unit. Fortunately, a sufficient number of assemblies passed acceptance tests to satisfy the requirements for the three TM systems. However, if the design were to be used again, this problem area would require additional work.

Calibrator Resonant Shutter

Several problems were evident with the on-board calibrator resonant shutter. First, the damping at the interface of the resonant shutter spring and the spring bushing changed during operation, causing the shutter to stop performing per specifications. The problem was corrected by replacing the bushing with a flexure, eliminating all rubbing contact and any changes in damping.

Next, the flex pivots supporting the shutter arm fractured during qualification-level vibration. The failure was caused by excessive deflections of the pivots induced by higher-order harmonics in the pitching mode. Motion limits were added to the design to prevent the pivots from exceeding a specific deflection.

Finally, the shutter was designed to oscillate over a specified angle with a specified amount of allowable overshoot. In certain situations the electronics could momentarily lose control and drive the shutter past the allowable overshoot and into hard mechanical stops. This caused physical damage to optical components on the end of the flag. This problem was resolved in two ways. First, the electronics circuit was modified so the circuit would automatically reduce pulse amplitude if the shutter started to overshoot. (However, one or two overshoots were still possible.) Second, the hard mechanical stops were replaced with energy-absorbing bumpers. The bumpers could not be made large enough to dissipate all of the energy, but they did reduce the force transmitted to the shutter arm to a level that would allow up to three consecutive bumper impacts without damaging the shutter.

RADIATIVE COOLER

The major design challenges of the radiative cooler were to ensure that it could maintain thermal performance under severe external backloading conditions and that it could provide extreme thermal isolation while maintaining mechanical alignment of the detectors. The radiative cooler is designed to provide an environment of less than 87K for the detectors of Bands 5, 6, and 7 at the cooled focal plane. A deposited thin-film nichrome heater on the back surface of the ceramic substrate provides the capability of operating the detectors at commandable temperatures of 90, 95, and 105K. The radiative cooler's capacity is more than adequate for the 32 InSb and 4 HgCdTe detectors that comprise these bands.

The spacecraft is in a 705.3 km polar orbit. Thus, the earth's limb extends to within 25.8° of the local horizon, and the earth's albedo and thermal emittance materially affect the cooler's thermal performance. In addition to the earth's backloading, portions of the spacecraft restrict the cooler's clear field of view to less than a full hemispherical view. The cooler must operate in, and was designed to minimize, the adverse effects of this environment.

The radiative cooler thermal design [Cafferty 1982, p. 74] employs two cooling stages with open-faced honeycomb for the radiator's emitting surfaces. The radiators are shielded from direct view of the sun, earth, or spacecraft appendages. The cold-stage radiator sees only cold space and IR emissions from a

cooled radiation shield mounted on the intermediate stage. The earth's energy is shaded from the radiators of both stages by a deployable earth shield, which also serves as a door to protect and seal the cooler against contamination during launch and in-orbit service operations. Diffusely reflected solar energy and infrared emissions from the earth shield fall only on the intermediate stage radiator.

The radiative cooler assembly consists of a detector subassembly mounted in a passive radiative cooler. An exploded view of the assembly is shown in Figure 49, and a cross-sectional view is depicted in Figure 50. There are two major cooling stages: the cold-stage assembly and the intermediate-stage assembly, each with separate thermal emitters or radiators. Subassemblies include:

1. A radiator shade or shield mounted on the intermediate stage,
2. A detector subassembly, which is part of the cold stage,
3. Two electrical outgas heaters, one on each stage,
4. Temperature sensors on each stage,
5. Interstage structural supports for each stage, and
6. Stage interconnecting electrical leads.

The intermediate stage supports the cold stage and thermally decouples the latter from ambient source radiation. The cooler's mounting ring supports the intermediate stage. The fiberglass interstage support members are arranged like pretensioned spokes in a wheel. Six tension members are used to support the intermediate stage. Nine members support the cold stage to provide added rotational stiffness about the cooler's axis of symmetry. Each member is fabricated like a rigid band; i.e., it is a continuous structure wrapped around a cylindrical support at each end.

The intermediate stage shield is constructed as a bimetallic sandwich (Ni-Cu-Ni), fabricated using the "replica-optics" technique, identical to the one used on the VISSR cooler's intermediate-stage shield.

Aluminum alloy is used throughout the radiator assemblies to minimize stage masses and mass moments. The radiator's emitting surfaces are the open-faced honeycomb material used on the VISSR cooler. This material is adhesive-bonded to a honeycomb sandwich panel that provides structural support for the cold stage radiator. The honeycomb sandwich panel is a fluxless, brazed assembly

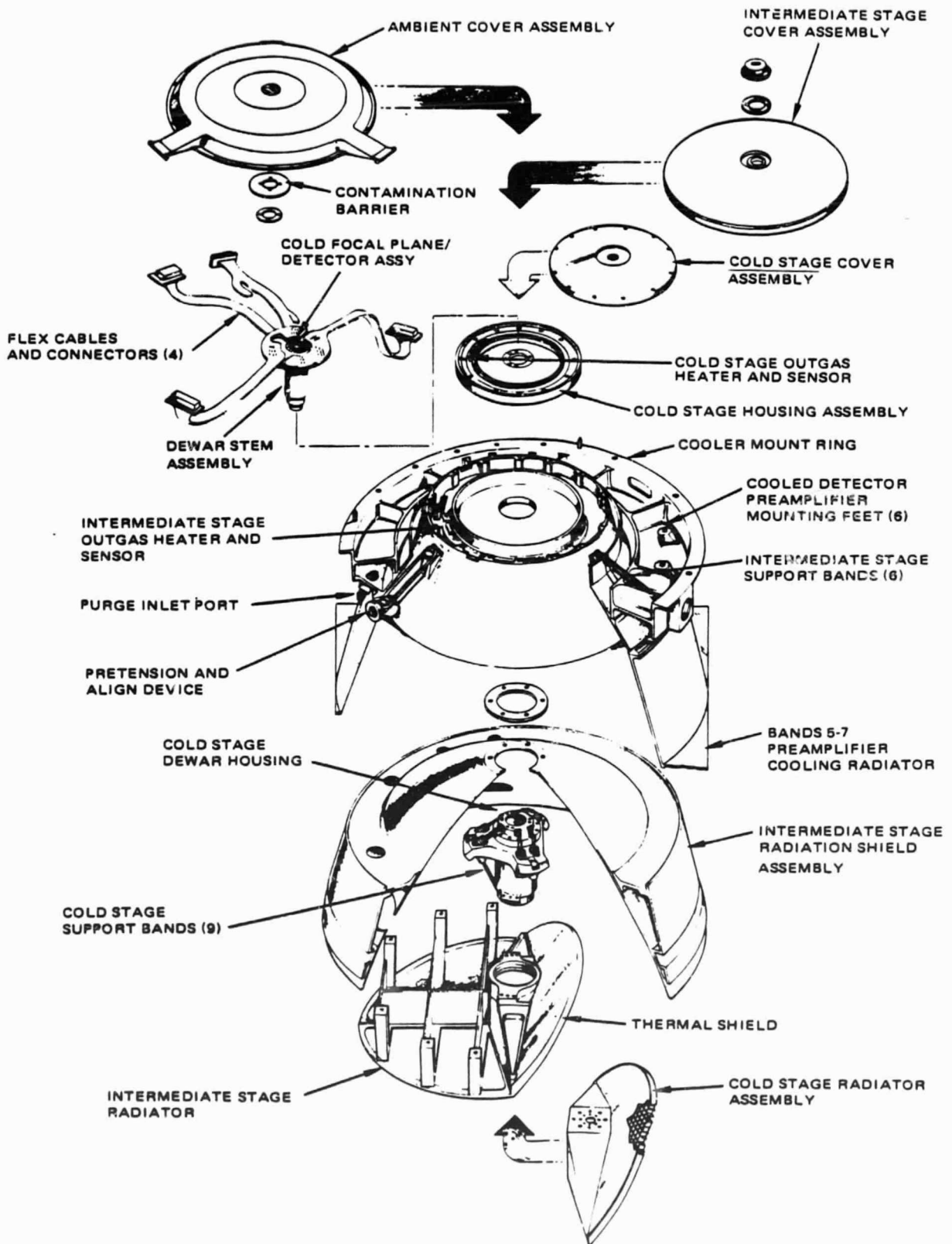


Figure 49. Radiative Cooler Exploded View

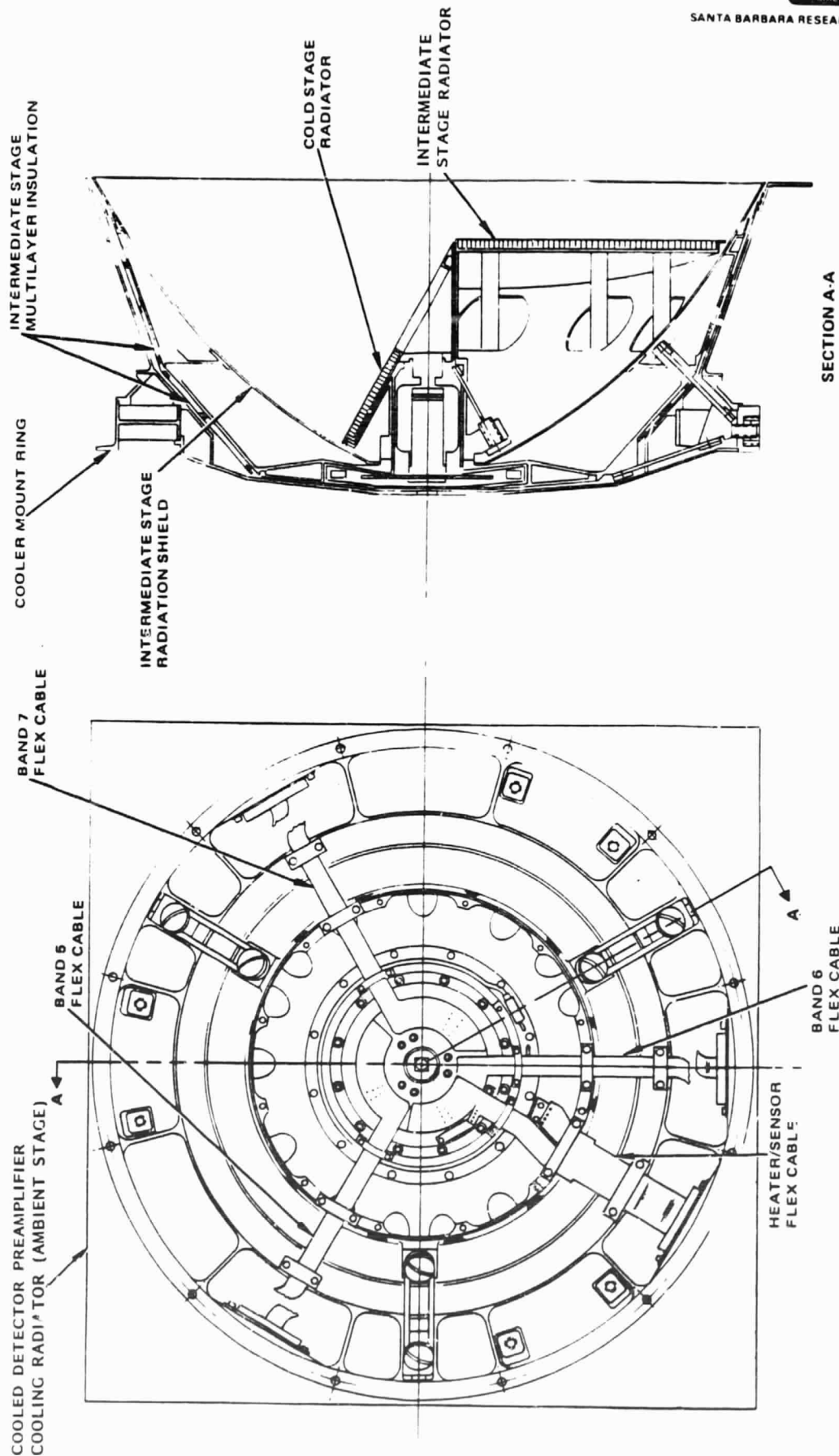


Figure 50. Radiative Cooler Layout

with intracell vents, but with complete edge closure. The cell air spaces are evacuated and the panel assembly is hermetically sealed prior to assembly in the cooler.

For the intermediate-stage radiator, the open-faced honeycomb is adhesive-bonded to a dip-brazed structural assembly with ribbed panels. Electrical flex cables are routed from the cooler's mounting ring to terminals on both stages of the cooler to provide power for outgas heaters and to carry the detector signals to the preamplifiers.

Proven technology derived from the VISSR was employed in the conceptual design of the thermal and structural elements of the radiative cooler and was further refined for the TM assembly. The successful flight performance of the TM cooler emphasized the soundness and validity of the technical approach. Significant advances were made in development of the thermal surface on the cooler's earth shield/door and also in the practical design of a "take-apart" detector/Dewar carried on the cold stage. Without this latter feature, the cost of troubleshooting during the final assembly and subsystem test phase would have been much greater.

Significant advances were also made in bench-cooling technology. The state of the art was advanced to the point where many system-level performance tests were conducted in an ambient air environment, with subsequent cost savings, where previously they had been conducted in the instrument's thermal vacuum environment.

In the following subsections, new technology developments for the TM cooler assembly are summarized in the context of the hardware problems they solved. These problems related to required thermal and structural performance, contamination control, and bench-cooling operations.

Thermal Performance

All specified thermal performance requirements were met. The specification originally contained a requirement for detector survivability in the event the spacecraft assumed a nonoperational attitude, allowing the cooler radiator to be exposed to the sun for 30 minutes. To satisfy this requirement, the open-faced honeycomb radiator surfaces of the proposed design were coated with white paint of low solar absorptance, but high emittance. Since the emittance value was critical to operational performance, a test program to measure the emittance of white-painted honeycomb was initiated. This program was cancelled when GSFC deleted the nonoperating solar exposure requirement as a cost-saving measure, and the radiators were coated instead with black paint for maximum emittance.

Heat generated in the aft-optics area and in the thermal preamplifiers in the original instrument design was to be radiated to the space/earth environment by a nadir-viewing radiator through louvers for thermal control of the instrument's temperature. However, it was subsequently determined that cost and weight could be saved by adapting the radiative-cooler housing to this use. Cold space-viewing radiators were added to the cooler's ambient housing, and heat was conducted to these radiators through the ambient housing and through "thermal feet" supporting the preamplifiers. The heat radiated to space (f10W) posed no problem for the space flight operation, but could have compromised the cooler's thermal-vacuum test results if this radiated energy had been reflected from the space-background simulator back to the cooler radiators by even a fraction of a percent.

As a result, a space-background simulator of exceptionally low reflectance was required to minimize this artificial heat load. A novel approach was used to obtain this low-reflectance surface economically. The open-faced honeycomb core material bonded on the face of the background simulator was cut on a bias, forming radiation traps over its entire surface.

The thermal surface required on the cooler's earth shield posed an opposite problem. Here, a highly reflective, low-emittance flat surface was needed to minimize solar scatter and thermal loads on the cooler's radiators while in space flight. Samples of honeycomb panels with polished face sheets obtained from vendors did not exhibit the mirror-like reflectance needed. The problem was solved by using commercially available polished aluminum foil bonded onto the earth-shield's honeycomb panels. The mirrored surface thus fabricated tolerated a temperature range of -100°C to $+60^{\circ}\text{C}$ in a vacuum. The performance characteristics were: total integrated scatter, less than 2%; surface waviness, less than 1° ; hemispherical emissivity at 25°C , less than 0.025; and solar absorptance, less than 0.15.

The other thermal-control surfaces of the cooler (a "replica-optics" aluminum-coated radiation shield, a low emissivity gold plate, and multilayer insulation blankets) posed no developmental problems, and application proceeded without incident. On the first test of the engineering-model cooler, a low temperature of 84.5K was achieved; well within the required cooling safety margin.

Structural Performance Development

The structural design of multistage radiative coolers for survival of launch vibration environments has historically posed difficult developmental problems. However, on the TM program these problems were avoided, for the most part, by careful observance of the design principles incorporated into the VISSR's cooler. By aligning the cooler-stage mass centers to the supporting structure's elastic axes, cross-coupling between the lateral, axial, and rotational modes was minimized. Modal response

of the overall system was reduced by careful control of stage mass ratios and by a vibration damper mounted on the cold stage.

A structural model cooler was used for vibration-response testing. The measured cold-stage response was less than half that of the VISSR cooler before optimizing the damper performance. However, at qualification-vibration levels, the viscoelastic rubber elements in the vibration damper failed due to excessive strain. Subsequent exploratory vibration testing indicated that the strain on the rubber could be brought to safe levels by reducing the suspended mass and optimizing damper performance. These tests also showed that the cold-stage response was within acceptable levels without the use of a vibration damper, and thus it was deleted from all flight-model coolers. The fiberglass-band interstage-support fatigue life was found to be more than adequate without the benefit of applied damping.

Another critical structural issue, vibration-induced misalignment of the cooled focal-plane array, was successfully resolved early in the program by employing elastic symmetry in structural design, by providing an interference-fit load path between assemblies without reliance on friction, and by carefully controlling the spring-rate characteristics and pretension loads of the fiberglass interstage support bands. While test-induced optical misalignment of the cooler-mounted cooled focal-plane array was never measured at the cooler subsystem level, the alignment repeatability of the cooled focal-plane array to the prime focal-plane array was held to within 12 μ r throughout the vibration and system-performance testing of the TM flight-model instruments. Focal-plane misalignments did occur during engineering model instrument vibration testing, but these were not primarily cooler-related, and the alignment integrity of the cooler did not become a development problem.

Both radiator assemblies were aluminum brazements. The cold-stage radiator assembly employed a vacuum-brazed honeycomb panel as its primary structural element. Due to the close proximity of this panel to the cooled focal-plane array and cold optics, its outgassing potential was negated by sealing the edges of the panel. The panel was evacuated through a tip-off tube, then pinched shut to retain a permanent vacuum. Little development effort was required here, and there were no final fit problems.

The intermediate-stage radiator assembly employed dip-brazing to join the complex assembly. Warpage during brazing resulted in downgrading the first assemblies to nonflight use. An intricate holding fixture, used for final machining of these assemblies after brazing, eventually solved the problem, along with some brazing process development. However, the resulting poor interstage clearance control on the engineering model caused vibration test "rattle" problems, and threatened thermal shorts during performance testing of the cooler on this model.

An electrical short problem arose within the cooler during system-level testing of the protoflight instrument. This short existed with the cooled focal-plane array at cryogenic temperature, but not at ambient temperature. An extensive troubleshooting effort discovered that the short developed between a capacitor lead and the cooler cold-stage housing when thermally induced warpage of a cantilevered distribution board caused capacitor motion. The multilayer distribution board acted like a bimetal strip, due to the anisotropic characteristics of the G-10 laminate layers. The problem was solved by providing additional clearance between the capacitors and cooler housings.

The above experience indicates that, in the future, greater safety margins in spacings within cryogenic coolers would reduce development problems and would be worth the resulting small thermal-performance penalty.

An important part of the cooler's ambient structure is a ring of I-beam cross sections, used to support the pretensioned fiberglass bands and to provide a flange for bolting the assembled cooler to the telescope structure. The engineering-model ring was machined from an LR-35 alloy forging, annealed before machining, and then stress-relieved after finish machining. Excessive ring distortion occurred during the stress-relief operation. The problem was solved by first rough machining to within 0.030 inch of final dimension, stress-relieving, and then finish machining.

Contamination Control

A "contamination barrier" was first employed on the TM cooler, separating the cavity between the cold and intermediate stages from the cavity between the intermediate stage and ambient housing. This prevented outgassing from the multilayer insulation blanket mounted on the intermediate stage from entering the cold-stage cavity where a contamination-sensitive cold window covered the detectors.

The contamination barrier was installed on the engineering-model cooler, and the cooler was subjected to test in thermal vacuum to determine if the detector signal were degraded due to contamination collecting on the cold optics. After a 48-hour vacuum bake at 60°C to accelerate the removal of contaminants, the performance of test detectors mounted at the focal plane was monitored for 300 hours. No loss in responsivity was observed over this time period.

However, both the protoflight and flight TM instruments have experienced detector performance degradation in flight, possibly due to gradual icing of the cold window. While detector performance has been regained by warming the cooler in space, thus "outgassing" the window's contamination, the contamination effect remains an open issue. The outgassing periods employed on Landsats-4 and 5 have been quite brief and it is likely that extended

outgassing periods would have significantly reduced or eliminated the problem.

ELECTRONICS MODULE

The electronics assemblies are contained in a module, as depicted in Figure 51. The major elements consist of the power supply, multiplexer, the printed circuit boards and associated cabling to the preamplifiers, and other aft optics electronics. A discussion of the multiplexer is treated separately in the following subsection. As part of the design philosophy, the power supply delivers coarsely regulated power to each circuit, with fine regulation done on each board. This provides an added level of isolation, preventing crosstalk while assuring the most practical regulation. Changes to the power supply are tabulated in Appendix B.

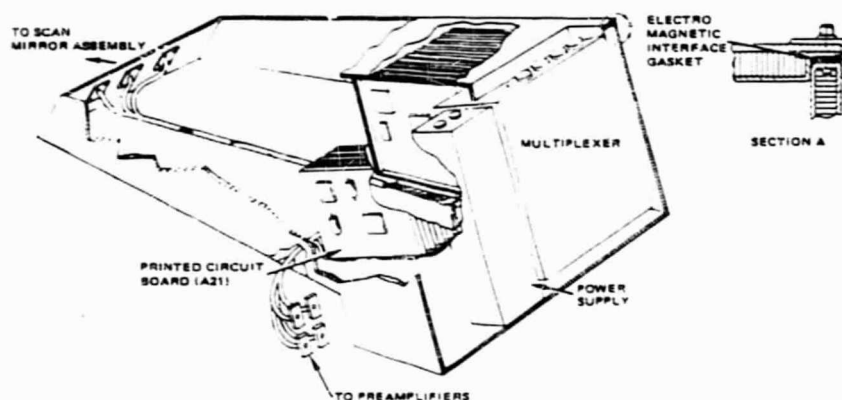


Figure 51. Electronics Module

The primary problems were in environmental temperature and heat-transfer control, minimizing weight and maximizing available volume while retaining structural integrity, and providing electrical shielding from electromagnetic interference (EMI).

Housing and Heat Sink

The primary packaging problem for the electronics was to establish reliable component operation with respect to operating temperatures. Early in the design effort, problems occurred in providing adequate cooling for the multiplexer, power supply, and the scan-line-corrector boards. The heat-transfer problems were solved by placing the power supply, multiplexer, and the scan-line-corrector boards on the radiation plate. The multiplexer was designed with a temporary bottom that could be removed so it could then be attached directly to the heat sink with screws that held the assembly to the plate.

After the development model was vibration tested, the following changes were made:

1. The heat sink was strengthened by increasing its width and providing stiffening ribs. Its material was also changed from aluminum to beryllium, primarily to reduce weight.
2. Wiring-access holes in the side were eliminated, since they were at the point of maximum stress, causing structural failure.
3. The base was changed from aluminum honeycomb to magnesium. This provided better load distribution and was easier to fabricate.
4. Doublers of aluminum were placed at all corners and at the mounting holes.

Limitations on the availability of space and the need for additional circuitry and power during the design phase caused considerable effort to be expended in redesign to fit all of the electronics within the housing space. In order to provide as much room as possible, some circuit boards were placed back to back, the output connector area was reduced in size, and four circuit boards were placed in the narrow section of the housing.

The development-model housing was made with honeycomb panels placed in a bent shell of aluminum sheet to provide an EMI barrier. This was changed to placing the honeycomb between flat aluminum sheets and closing the ends with a nickel-plated magnesium bar. This was not only structurally stronger, but also much easier to fabricate, allowed for closer tolerancing, and reduced the need for extensive fixturing at the next assembly.

Printed Wiring Boards (PWB)

Problems arose with the printed-wiring-board (PWB) harness connectors, which were not stiff enough to withstand the mating forces, and the solder pins, which were not strong enough to support the wire. To solve this, the harness connectors were stiffened by bonding them to an aluminum frame. The frame also contained a bar to which the wires were tied so their weight would not load the solder pins.

The PWB harness connectors have a common wire installed between pairs of pins. This arrangement caused the pins to become misaligned during mating. The solution was to place the connector pins in a fixture that held them while the common jumper wires were soldered. The pins then remained straight and aligned during subsequent operations.

A manufacturing problem occurred with the solder pads on the PWBs, which were lifting during the soldering operations. The lifting that occurred was found to be due to a defective lot of polyimide material. This was corrected, and additional preventive measures were taken by vacuum-baking the boards before soldering to drive out moisture.

Wire routing was a difficult design and assembly problem. In particular, it was extremely awkward to wire the connectors in place. The routing problems were solved by providing a dished cover in the bottom of the housing to provide more space, and the PWB harness connectors were wired from one side only, which allowed them to be bench-wired and removed from the housing. The entire wire harness was reconfigured to allow it to be assembled outside of the housing.

The above changes were made on all of the models. The engineering model has an aluminum heat sink instead of beryllium, and the top cover is configured to accept the multiplexer output connectors at a different angle than the flight models.

Multiplexer Assembly

Figure 52 is a simplified block diagram of the Thematic Mapper's multiplexer, illustrating its primary data-flow paths. The multiplexer's primary function is to process the scene video information from the detectors. The multiplexer also provides timing and synchronization signals to the other portions of the Thematic Mapper to synchronize the instrument's operation. Detector signals are amplified and filtered in the radiometer electronics and then provided to the multiplexer on 100 differential inputs. The multiplexer performs a dc-restoration function to compensate for offset in the previous electronics or detectors, samples the signals, and converts these samples into 8-bit digital words. These digital words are then formatted with spacecraft telemetry and synchronization bits. This results in a composite 84.9 Mbps data stream, which is processed by a pseudonoise encoder and provided to the spacecraft communications subsystem for transmission to earth.

A number of key design decisions were made early in the program to minimize the cost and risk of the multiplexer development. For instance, the multiplexer accepts its input signals in differential form to eliminate common-mode noise. This differential processing of the analog signals was carried forward throughout the electronics module and contributed to meeting the instrument's noise requirements at minimum cost.

The multiplexer also processes the information from each band in a dedicated processing module, which contains input buffers, track-and-hold and analog-multiplexer circuits, and the A/D converter. This modularity guarantees that all detectors in a particular band will be processed by the same A/D converter and, thus, will receive very similar transfer characteristics.

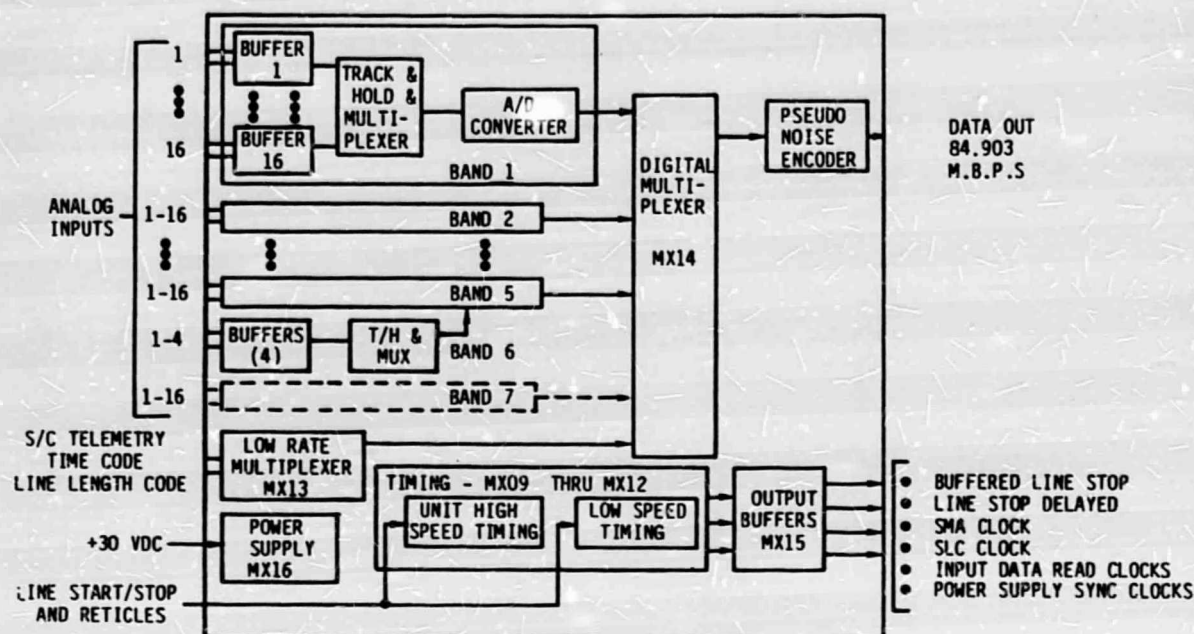


Figure 52. Multiplexer Simplified Block Diagram

It also locates all processing from the multiplexer's inputs into the digital domain on a single module, retaining excellent ground and voltage-supply integrity. The single module can also be tested independently of the entire multiplexer unit. Modularity also contributes to graceful degradation in the event of failures, since each module affects the operation of only one band.

The multiplexer accepts a regulated dc voltage from the power supply and does not regulate this voltage further before converting it to the secondary voltages utilized within the multiplexer. This approach saved approximately 20 watts of power, which would otherwise have been dissipated in a series regulator.

The multiplexer also has provisions to synchronize both its internal dc-to-dc converter and the operation of the external power supply to the multiplexer's analog-to-digital conversion process. The supplies are also capable of free-running operation. The synchronization ability was included to reduce the likelihood of coherent patterns from power-supply noise appearing in the final data.

The multiplexer development program went relatively smoothly. Only two major problems were encountered. One of these was related to the mutual interaction of the multiplexer, the power supply, and the scan-mirror assembly to maintain

instrument synchronization. The power supply powers the multiplexer and the scan mirror, while the scan mirror supplies synchronization to the multiplexer. The multiplexer, in turn, provides a clock to the scan mirror and synchronization signals to the power supply. As a result, the interaction of these three units (critical to instrument operations) is quite complex. During engineering-model checkout, a situation was discovered in which, depending upon scan-line length, the scan mirror and the multiplexer could attempt to resynchronize the power supply at a time during its operational cycle that caused the supply to shut down, thereby shutting off the instrument. This problem was ultimately resolved by making a number of changes in the power supply (documented in Appendix B).

The other major multiplexer design difficulty was related to the trimming and testing of the multiplexer's analog-to-digital converters. The converter is an 8-bit successive-approximation analog-to-digital converter, capable of operating at up to approximately 40 Mbps. The high speed and small input-signal range of the converter require that noise levels be kept extremely low, particularly on all voltage and ground-supply leads to the analog-to-digital converter hybrid. It was not possible to provide grounds of high enough quality with the converters in a test socket because of the parasitic inductance and capacitance of the socket's pins. This was true even though the converters operated excellently over their full temperature range when soldered to the final printed circuit card with its ground planes and multiple soldered voltage and ground connections. This problem was finally solved by building a test jig in which the hybrid's leads were trimmed, and the devices were clamped to a board, identical to the board used in the actual system. In addition, the critical step of trimming the current sources within the analog-to-digital converters was performed with the converters in a static rather than dynamic condition. That is, the converters were supplied dc-input signals rather than the multimegabit-per-second signals used in the actual system. This eliminated noise associated with transition of the high-speed signals, made trimming of the current sources more economical, and should have contributed to higher accuracy.

Unfortunately, due to differences in the thermal equilibrium of the converter between the static and dynamic states, the current sources behave slightly differently dynamically than in the conditions under which they were trimmed. Although the A/D converters still meet the instrument specification, this trimming difference resulted in a significant variation in the size of the multiplexer's quantization steps. In future instruments, it should be possible to reduce this nonuniformity by using data derived from the first two instruments to achieve a corrected static trim or, if necessary, by a dynamic trim of the A/D converters.

Section 7

PRELAUNCH EVALUATION

The effort involved in providing the test equipment for testing the TM prior to launch rivaled that of the TM development itself. The Bench Test and Calibration Equipment (BTCE) was the major, integrated assembly of test equipment. This equipment can only be briefly described here. A more complete description is contained in the operation and maintenance manual for the BTCE [SBRC 1982a].

The prelaunch tests performed using the BTCE are also discussed in this section. This prelaunch testing resulted in the performance parameter measurements summarized in Section 4. All the tests performed on the TM with the BTCE are listed and at least briefly described. Three tests are deemed to be so important to image quality that they are described in more detail than the others.

The first of these three tests is the measurement of the TM telescope's effective focal length (EFL). This is an important test because the focal-length value affects the detector IFOV and band-to-band registration. In fact, the EFL value had to be measured prior to performing any of the other tests because the outcome of many of the rest of the tests depended for their accuracy on exact knowledge of the EFL.

The second crucial test was the square-wave response (SWR) test. As discussed in Section 4, SWR and MTF are closely related and define the spatial resolution of the sensor. The test was required to accurately measure the SWR and to ensure that the TM was within SWR specification.

The geometric accuracy and band-to-band registration test is the third critical test for which a detailed description is presented. Image quality is depends heavily on a knowledge of the errors in band-to-band registration as well as a knowledge of errors in scan-mirror profile and other geometric errors in the system.

BENCH TEST AND CALIBRATION EQUIPMENT

The TM produces pictorial data at a rate of 85 Mbps. During testing, this data must be analyzed in near-real time to determine the effects of optical stimuli on instrument performance. Further, the complexity of tests makes it necessary to automate them in a manner that will ensure uniformity of approach from trial to trial. Review of these requirements in the early phases of the TM program led to the development of a completely machine-controlled testing philosophy that provides coordinated stimuli control and subsequent data analysis via selected algorithms.

The test equipment assembled for testing the TM is called the bench test and calibration equipment (BTCE), and its functional block diagram is shown in Figure 53. It is an interconnected system providing complete performance testing of the TM instrument from buildup and integration of the radiometer to final system performance. The system contains the equipment necessary to do the following:

1. Simulate the interface between the TM and the host spacecraft.
2. Provide the optical stimuli for performance testing and calibration.
3. Process the high-rate data stream during performance testing or recorded data playback.
4. Isolate the TM and stimuli from disturbing vibrational environments.
5. Monitor, control, and record test configurations and operational conditions.
6. Provide cooling of the cold focal plane for laboratory ambient tests.
7. Provide radiative heat sinks for thermal tests.
8. Simulate TM interfaces and signals for self-tests.
9. Provide special tools and fixtures for alignment and handling.

PDP-11/70 computer-aided testing is used to improve test accuracy (over manual-data acquisition methods) and to reduce the chance for human error by allowing a review of the computer-controlled operations prior to incorporating them into the test sequence. Additionally, the time required to configure the test article and the test equipment is reduced significantly by automated testing, and the speed of data acquisition and processing is increased significantly. The increased speed and accuracy of test operations and data processing results in decreased program costs. The increased data acquisition options available in the automated system provide the test designer and data analyst greater test flexibility, making the computer-controlled approach highly desirable.

BTCE operation is controlled by the system test computer. The man/machine interface is through three alphanumeric keyboard/display devices. The operator may initiate preestablished test sequences from this terminal or may initiate or modify individual instructions to the test system. The display devices report test status, test results, TM and ground equipment status, and state of health.

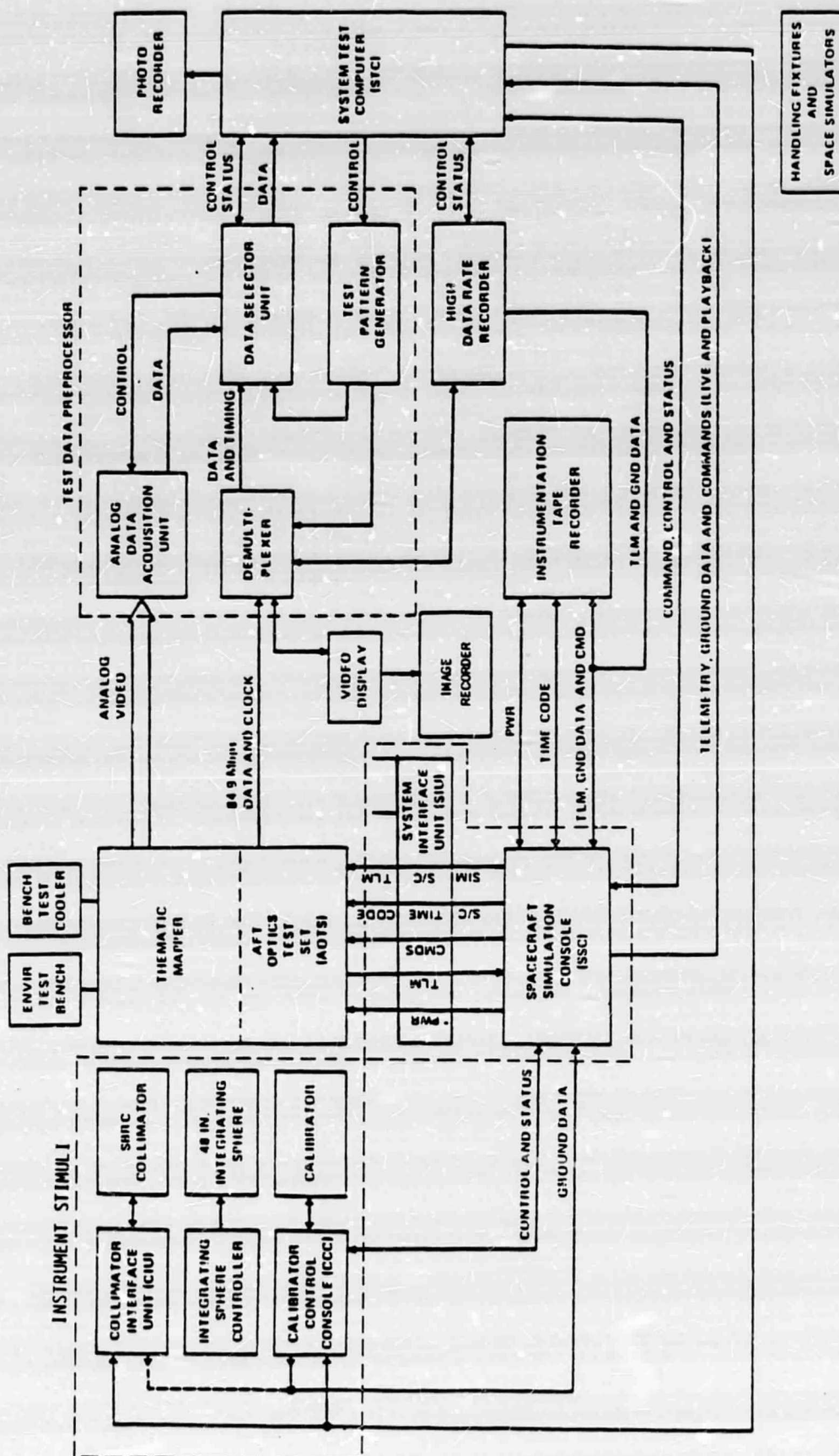


Figure 53. BTCE Functional Block Diagram

In addition to providing test control and processing test data to produce the final test results, the automated test system continuously monitors the TM and the ground equipment to detect changes within the system about which the operator should be notified. This monitoring includes testing of the TM telemetry parameters for conditions that might jeopardize the health and safety of the instrument (alarm-limit testing). The monitoring also includes testing of telemetry parameters for changes which, while not indicative of alarm conditions, should be of interest to the test conductor and test operators (suppression-limit testing).

The ability to recover and further study anomalous data is provided at the time of data acquisition by automatic recording of the high-rate raw data stream on a high-speed tape recorder and by temporary storage of the acquired raw data on a 176-Mbyte computer disk. Time code, which is used throughout the test system and is recorded on the high-speed recorder as part of the video data, allows recovery of the exact data desired.

Data evaluation of the acquired test data is automatically scheduled by the computer when the data becomes available. This provides the final results for most tests within minutes of data acquisition. The test results are presented to the test operators and to the analysts by CRT displays and on-line printer and printer/plotter printouts.

A new bench-cooling approach was used on the TM, consisting of a temporarily evacuated, take-apart Dewar combined with a temperature-controlled Joule-Thomson cryostat [Kuyper and Buller 1982, p.83]. The Dewar was evacuated only during bench test by a remote vacuum pump. After bench testing, the Dewar was allowed to return to ambient conditions, facilitating maintenance or troubleshooting operations on the cooled focal-plane assembly.

This capability to bench test and troubleshoot provided an efficient method to resolve system performance problems in the final instrument development phase. In particular, troublesome noise problems associated with electrical ground planes were resolved experimentally without extensive hardware disassembly.

Problems associated with development of the bench cooler itself were not difficult to overcome. The evacuation system was a straightforward design problem, except for the unknown conductance of the solid-particle filters that protect the detectors from dust. A test was run on the 2 μ m, nominally rated, stainless-steel sintered-mesh material. The test fixture had a conductance equivalent to a 6-inch length of 0.8-inch (diameter) tube. The conductance of the 0.7-inch (diameter) filter sample was equivalent to adding a 6-inch length of 0.8-inch (diameter) tube.

Tests on the completed bench cooler demonstrated that the pressure drop across the entire vacuum system was acceptable, even though pumping was through a 10-foot flexible line. Typical

steady-state pressure readings were 5.5×10^{-5} Torr in the detector enclosure and 1.0×10^{-6} Torr at the throat of the diffusion pump.

A thermally induced noise signal was generated in the HgCdTe detectors due to fluctuations in the level of liquid in the cryo-static reservoir during normal bench-test operation. The temperature fluctuation, typically 0.04K to 0.08K at a frequency of 1/3 Hz, introduced additional noise into the system, but the final adjustments of system gain and offset for each HgCdTe detector were accomplished. The InSb detectors were not significantly affected by this fluctuation.

All system test objectives planned for the bench cooler were accomplished. In addition to the initial radiometric calibration of the HgCdTe and InSb detectors in the TM system, the modulation-transfer function for these detectors in the system was measured. Geometric adjustments, such as band-to-band registration between detectors on the uncooled and cooled focal planes, were made using the bench cooler. Final radiometric and geometric calibration was accomplished in systems-level thermal-vacuum tests on the completed instrument.

PRELAUNCH TESTING

Prelaunch testing of the engineering, protoflight, and flight models took place over a 2-year period. The tests performed are listed in Table 15 in the sequence in which they were performed. The test sequence was determined by the level of assembly required for the test and the measurements that had to be accomplished prior to making the test.

Table 15. Prelaunch Tests Performed on the Three TM Models

DESCRIPTION	Test Name	EM	PF	FL
Effective Focal Length	EFL	*	*	*
Prime Focal Plane Assembly Focus	IA01	*	*	*
Scan Mirror/Radiometer Alignment	IA06	*	*	*
Cold Focal Plane Assembly Coarse Focus	IA03	*	*	*
Cold Focal Plane Assembly Fine Focus and Band-to-Band Registration (BBR)	IA04	*	*	*
Electronic Module Integration	IA07	*	*	*
Line-Spread Function	AC07		*	*
Radiometric and On-Board Calibrator Calibration	AC02 Bands 1-5, 7	*	*	*
Spectral Matching	AC22			*
TM Calibrator Calibration	BL07	*	*	*
Square-Wave Response	PL16/17	*	*	*
Geometric Accuracy; BBR	BL19/20	*	*	*
Radiometric Calibration	BL10 Band 6		*	*
Coherent Noise	BL12		*	*
System Readiness Test	SRT	*	*	*
Thermal Vacuum Tests	TV		*	*

Test names comprised a two-letter prefix and a two-digit number. The two-letter prefixes are IA for Integration and Alignment tests, AC for Ambient Collimator tests, and BL for Baseline tests. The two-digit numbers were at one time sequential, but because of test consolidations and deletions they are no longer sequential. Miscellaneous tests not included in this naming convention were referred to by their descriptive names. In this report the tests will be discussed using their descriptive titles, as listed in Table 15, above.

Effective-Focal-Length Measurement

Measurement of the effective focal length (EFL) of the TM telescope, the SBRC collimator, and the calibrator telescope, relates directly to satisfying the requirements for geometric accuracy (GA) and band-to-band registration (BBR). There were many problems associated with EFL measurement, the complexities being embodied in a host of instrumental, procedural, and environmental error sources. Both time-independent errors, generally connected with alignment and use of test equipment, and time-dependent errors, connected with environmental fluctuations in temperature and vibration profiles, make it difficult to achieve a measurement accuracy better than one part in 10^4 .

The definition of EFL shows the two parameters involved in EFL measurements:

$$\begin{aligned} \text{EFL} &= \frac{\Delta Y}{\Delta \phi} \\ &= \frac{\text{Lateral displacement of image at 50\% knife-edge response}}{\text{Change in field angle of source}} \end{aligned} \quad (1)$$

Table 16 lists the accuracy to which EFL was to be measured for each of the three instruments, as well as the permissible measurement uncertainties allowed in the determination of the ϕ and Y parameters. All required accuracies were met or exceeded.

Table 16. Relationship of Required EFL Accuracy to Permissible Measurement Uncertainties

Instrument	Required EFL Accuracy (inch)	Measurement Uncertainty	
		$\Delta \phi$ (μrad)	ΔY (μinch)
TM Telescope	0.030	1.76	170
TM Calibrator Telescope	0.022	0.73	120
Reticle-Pattern-Projection Collimator	0.018	0.90	100

Figure 54 shows the test setup used to measure effective focal length. The three major assemblies are indicated within dashed boxes. In the center is the TM telescope, to the right is the source and knife-edge assembly, and to the left is a Hewlett-Packard interferometer assembly that measures angular displacements of the source. A linear interferometer was used to measure y-axis offsets. In principle, one measures the angle through which the retroreflecting mirror is rotated and divides that value into the offset in Y required for the knife-edge assembly to once again center the beam on the knife-edge pattern. The test equipment was located in a clean-room environment with ambient temperature control capability and on a vibration-isolated table.

Possible sources of error include:

1. Clean-room air turbulence
2. Clean-room temperature variations
3. Vibrations in structures
4. Bending of vibration-isolation tables
5. Wobble in knife-edge stage
6. Instability of support fixtures.
7. Laser interferometer counter instability
8. Incorrect setup of interferometers
9. Alignment error in retroreflector flat's axis of rotation to knife-edge motion
10. Knife-edge motion not orthogonal to optical axis and to its own direction of motion.

Major sources of errors in EFL testing were determined to be due to thermal gradients in supports and fixtures induced by temperature variations and air turbulence within the clean room where testing was performed. An extensive set of corrective actions was initiated, including thermostatic- and turbulence-damping controls that limited temperature fluctuations to as little as 0.1°C, constructing an insulated enclosure within the clean room, insulating with foam fillers underneath the test bed and around its sides, removing heat-generating test-monitoring equipment from the immediate vicinity of test-bed fixtures, and limiting testing to the early hours of the morning when the sun had no effect on heating the building as a whole. The last approach also reduced the problem of residual low-frequency test-bed vibrations. With excellent environmental control, the laser interferometer counter proved to be a stable instrument.

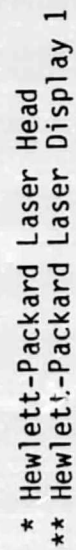


Figure 54. Test Setup Used to Measure Effective Focal Length

Deflection of the vibration-isolation table under load was monitored by strain gauges, and it proved to be no problem.

The knife-edge assembly also was a stable instrument, providing the laser was turned on several hours prior to the test procedure and allowed to temperature-stabilize and the spatial filter defining the source was configured with a slightly oversized pinhole. Angular wobble measurements, monitored by twin interferometers, showed values well within allowable limits.

Considerable work was done to provide custom-fitted interfaces between the table and fixtures. These support fixtures replaced original multilayer aluminum-block interfaces that caused errors in alignment due to thermal- and vibration-induced relative shifts.

The accuracy of angular measurements was greatly improved when the angle of the retroreflector flat was measured by reflecting off the face of the flat rather than a corner cube attached to the rear surface of the flat. Further gains in alignment accuracy were achieved by assuring perpendicularity of all test components, especially with respect to the interferometers measuring knife-edge motion and the angular motion of the retroreflector flat.

Results of these efforts were that the EFL measurement process was established with a degree of accuracy and precision that was well within required limits. For example, the average value of the EFL for the protoflight TM, determined from four measurements, was 95.904 inches with a standard deviation of 0.004; the desired value was 95.900 ± 0.030 inches.

Prime Focal-Plane Assembly Focus

The principal objective of the prime focal-plane-assembly focus test is to axially position the aft-optics support assembly relative to the telescope assembly so the prime focal-plane assembly is placed at the telescope's prime focus. The test was conducted with scan-mirror assembly, TM telescope, and aft-optics assembly mounted in the TM mainframe and oriented to align the optical axes of the TM telescope and the collimator (see Figure 55). Data was collected and optimal axial positioning of the aft-optics support was determined by maximizing the modulation transfer function (MTF) of several key detectors. See Section 4 (Performance Parameters) for a discussion of the MTF concept.

Scan-Mirror/Radiometer Alignment

This test verified the rotational alignment of the telescope housing in the TM mainframe such that the scan-mirror pivot axis is orthogonal to the detector's along-scan baseline and the rotational axis of the SLC, as shown in Figure 55.

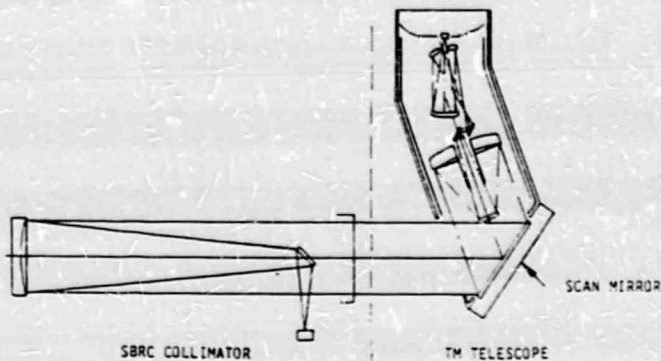


Figure 55. Optics Alignment Test Configuration

Cold Focal-Plane-Assembly Coarse Focus

This test was also performed in the same configuration as the prime focal-plane-assembly focus test. Its purpose was to axially position the radiative-cooler assembly relative to the telescope assembly, such that the cold focal-plane assembly is placed at the optimum focus location. The MTF of a Band 7 central detector was maximized to determine this location.

Cold Focal-Plane-Assembly Fine Focus and Band-to-Band Registration

This test determined fine focus of the cold focal-plane assembly and band-to-band registration of the two focal-plane assemblies. The LSF width was minimized to obtain the best focus and to assess band-to-band registration. The same configuration as used for the LSF characterization, described below, was used and is shown in Figure 55.

Electronic Module Integration

This test was performed to verify that all TM-scanner-to-electronics-module interconnected functions perform per design specifications. The test is a computer-controlled test that uses commands with telemetry verification to establish performance. The following items are tested: wiring, telemetry, heaters, blackbody, SMA control, dc-restore, fusible-link drive, cooler door, inchworm drive, calibration-lamp sequencing, calibration-shutter control, scan-line corrector (SLC), power and consumption, and IFOV interconnect.

Line-Spread Function (Optics and Detector)

The LSF is a measure of the width of the IFOV. The test configuration is shown in Figure 55. The test determined the response of selected detectors to a narrow slit source, illuminating positions on the focal plane. The distances between the illuminated positions and the detectors were varied by means of a

computer-driven x-y stepping stage in the collimator focal plane. The TM scan mirror and scan-line corrector are off and locked at midscan. The LSF is measured in the along-scan and cross-scan directions and computed by sampling the detector output as the slit is stepped across the detector. The IFOV width is defined for each detector as the angular or linear distance between the two points where the detectors' response to the slit is 50 percent of maximum.

Radiometric and On-Board Calibrator Calibration

The radiometric calibration of TM Bands 1 through 5 and 7 and the internal calibrator was performed by aligning the TM to the aperture of a 48-inch calibrating sphere, as shown in Figure 56. The calibrating sphere is part of the instrument's stimuli equipment. It is a calibrated light source containing 12 halogen lamps that can be turned on and off individually. The scan mirror is locked at midscan and the scan-line corrector is turned off. Bands 5 and 7 are cooled by the bench-test cooler. At the outset of the test, all integrating-sphere lamps are turned on. The lamps are turned off in a specified order, and data is taken at each radiance level. At the same time the sphere lamps are being sequenced, the internal-calibration-lamp sequencer is turned on and data is taken simultaneously in order to calibrate the internal, or on-board, calibrator.

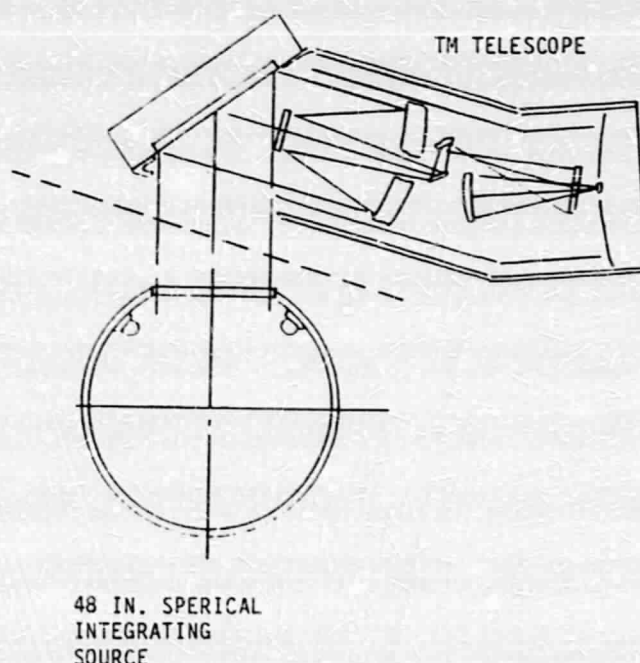


Figure 56. Radiometric Calibration Test Configuration

Data taken for each detector at each radiance level is "graphed" as signal (in MUX counts) versus input radiance, and a line is fitted to this set of data. The noise is calculated by computing the standard deviation. Average signal and noise values for each detector are computed and the SNR is calculated for a minimum and maximum scene radiance value. Figure 57 shows a typical graph of the transfer function with the line fit to the data.

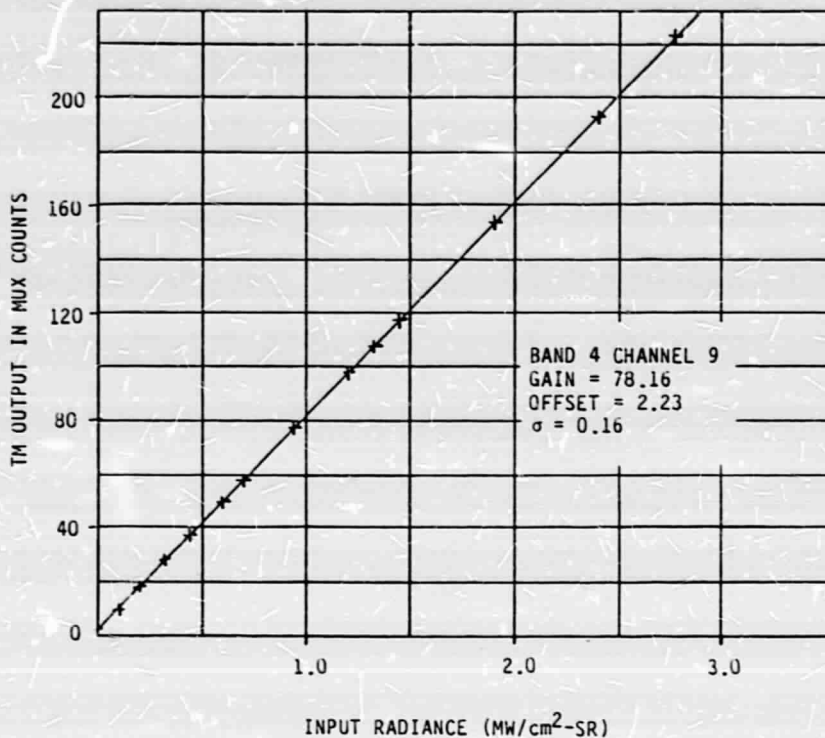


Figure 57. Typical Graph of Output Signal versus Input Radiance

Another important part of this test is the adjustment and subsequent measurement of gains and offsets for each detector. During radiometric and on-board calibrator calibration, the gains of all detector channels were first adjusted to satisfy full-scale input-radiance requirements. Then the procedure described above for obtaining data for the SNR calculation was used to obtain the value of gain and offset for each detector. This data was saved and used in the ground-based, radiometric-correction procedure for data transmitted from the orbiting TM.

Spectral Response

The TM's spectral characteristics were determined by analytically combining of the results of measurements on all pertinent subsystem components. The subassembly tests determined the spectral reflectance, transmittance, and responsivity for the mirrors, windows, filters, and detectors. The product of these

three measurements gives the system spectral response. Figure 58 shows typical graphs of these three measurements and their product. The lower and upper response edges are determined by finding the points on both sides of the curve where the response is 50% of the peak response.

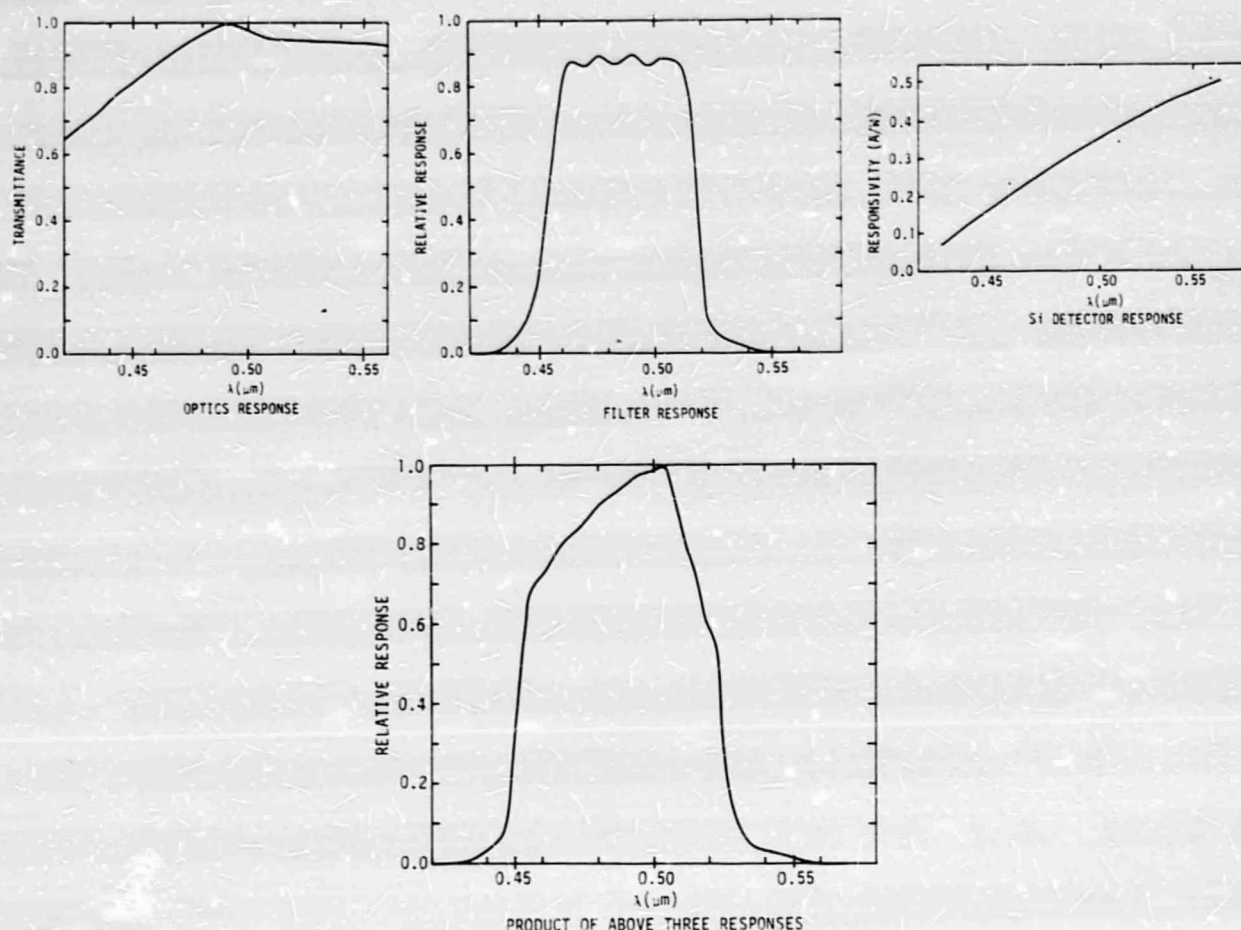


Figure 58. Spectral Response Determination

TM Calibrator Calibration

Calibration of Bands 1 through 5 and 7 of the TM calibrator (TMC) and the on-board calibrator (OBC) was performed by this test. The TM (calibrated previously) was used as the transfer standard for the TMC and the OBC. The test was performed with the TM aligned to the TMC as shown in Figure 59. Data was collected at several temperatures for the cold focal-plane array (CFPA); the prime focal-plane array (PFPA) was maintained at a constant temperature. The redundant calibration of the OBC provided a mechanism for checking the quality of the TM as a calibration source. The calibrator was subsequently used to periodically verify the stability of radiometric calibration of the TM throughout the remainder of the test program.

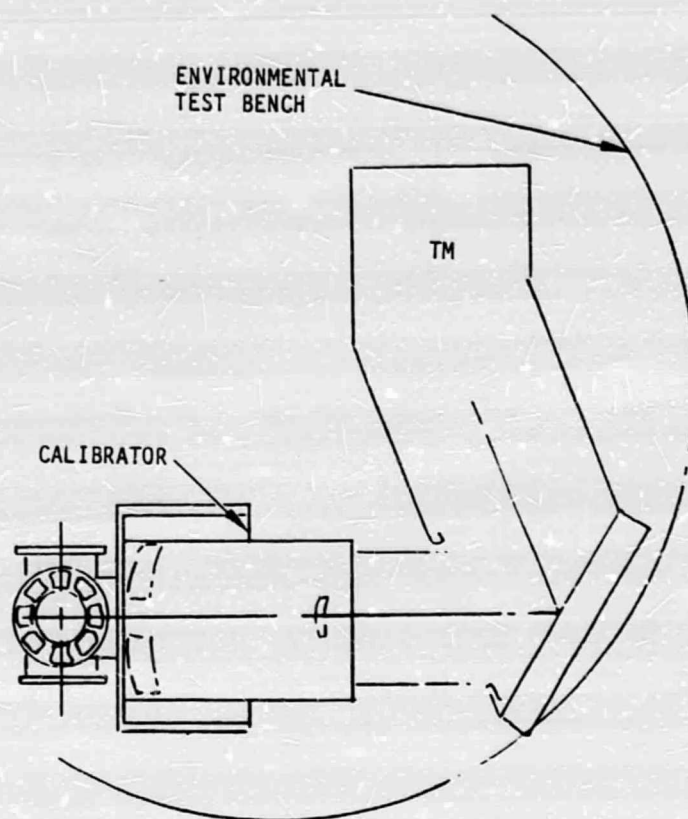


Figure 59. TM Aligned to Calibrator

Square-Wave Response

In the square-wave-response test, the system is ground-tested in full-up condition using an arrangement shown schematically in Figure 60. The ground scene is simulated using a collimator telescope with an object reticle at the focal plane focused to infinity and aimed at the scan mirror. The system presents an inherent problem in obtaining the knife-edge-response (KER) data required for calculating the square-wave response (SWR). The basis of the problem is the system sampling rate, which is one IFOV of image travel per sample. A simple edge reticle located at the collimator focal plane will be imaged at the detector array, with an image travel of one detector width between samples. This does not meet the requirement of obtaining data points at a number of edge image locations over the detector IFOV. One possible solution would be to collect edge-function data over a number of scans, each scan having a variable start delay with respect to the scan mirror's start-of-scan synchronizing pulse. This approach suffers from several sources of signal jitter, which produce "noisy" KER functions. These include scan-to-scan variations in scan velocity, vibration modes, and optical-path refractive index.

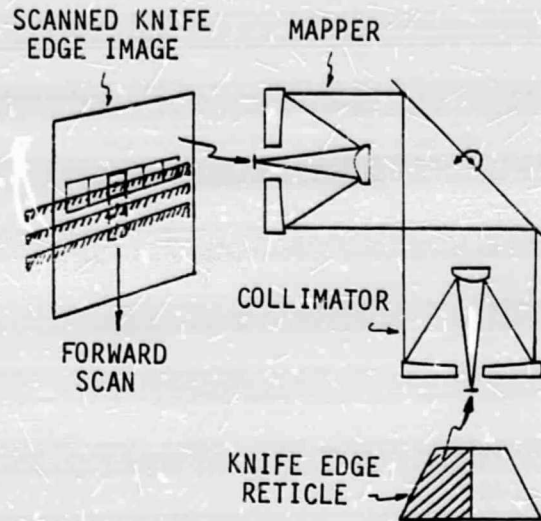


Figure 60. Full-Up Test Arrangement (Top View)

A preferred method was developed for obtaining KER data on a single scan, referred to as the "phased knife-edge approach". A special "phased edge" reticle was developed for use in the test set-up of Figure 60. Operation of the phased-edge reticle can be visualized by first considering a conventional bar reticle, located at the collimator focal plane and imaged at the focal plane as shown in Figure 61.

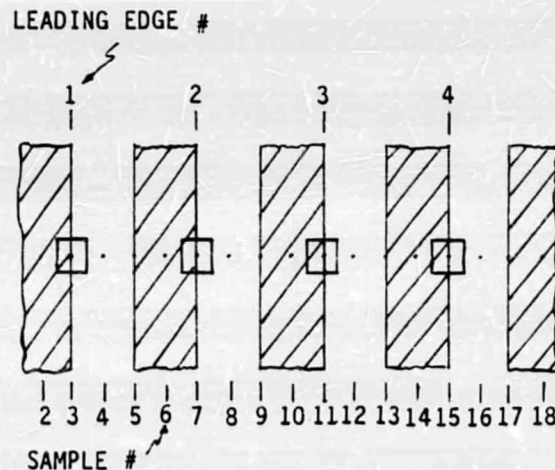


Figure 61. Conventional Bar Reticle

This reticle has a number of bars and spaces of equal width. The bar width is constant and images an integral number of detector IFOVs at the focal plane. The reticle image passes across an individual detector at a rate of one detector IFOV per sample. Relative motion of the detector IFOV with respect to the

reticle bars is shown with a dot indicating timing of successive signal samples, in this case two samples per bar or space. It is apparent that the relative phase between edges and IFOV is unchanged from bar to bar, producing constant fractional IFOV obscurations and constant signal levels from bar to bar. In the illustration, signal level is a constant 50% at samples No. 3, 7, 11, and 15 on leading edges 1, 2, 3, and 4, respectively.

A comparable phased-edge reticle, shown in Figure 62, has image spaces 2 IFOVs wide and bars 2.25 IFOVs wide. Over the same range of samples, fractional obscurations of $1/4$, $1/2$, $3/4$, 1, and 0 IFOV are produced by leading edges at sample No. 3, 7, 11, 15, and 16, respectively. Use of a fifth bar and space would produce signal No. 20 as a repetition of signal No. 3 and, therefore, would be redundant. Using this principle, a number of KER points can be obtained on a single scan, the density of points being determined by the size of incremental IFOV per bar width. In practice, a 10-bar reticle is used with a 5.1 IFOV bar width and a 5.0 IFOV space width. This produces an edge-phase shift of 0.1 IFOV plus a number of points outside the IFOV. Overall reticle size in the along-scan direction is on the order of 100 IFOVs or about ± 2.1 mrad field angle, referred to the system's optical axis. Total sampling time on a single scan is about 0.95 ms, which effectively nullifies vibration effects below a few hundred hertz.

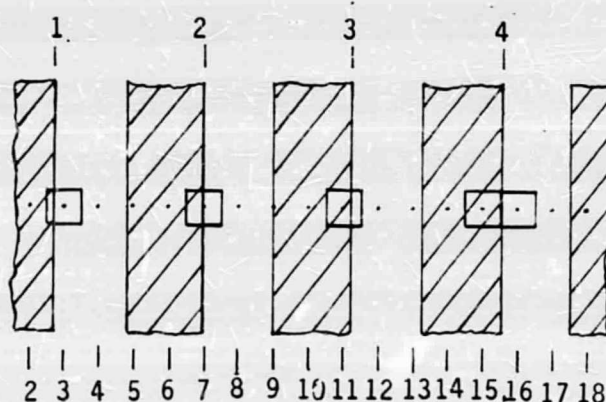


Figure 62. Phased-Edge Reticle

Computer algorithms are used to selectively retrieve and reassemble the KER data from the detector data stream. The reassembly algorithm first finds maximum and minimum (clear and opaque) signal levels, then locates the bar edge to which the signal is closest $(s_{\max} + s_{\min})/2$. In the 4-bar reticle case, shown in Figure 56, the signal closest to 50% occurs at sample No. 7, leading edge No. 2. The computer then consults a look-up table, stored for edge No. 2 and finds a set of relative sample numbers prearranged in a sequence that generates a KER function with 50% point at edge No. 2. Part of such a table for edge No. 2 is shown in Figure 63. This data would be translated into the KER function shown in Figure 64.

RELATIVE SAMPLE #	COMPUTED ABSOLUTE SAMPLE #
N + 8	15 (0% OPEN)
N + 4	11 (25% OPEN)
N	7 (50% OPEN)
N - 4	3 (75% OPEN)
N + 9	16 (100% OPEN)

Figure 63. Look-Up Table at Edge No. 2 = 50% Signal

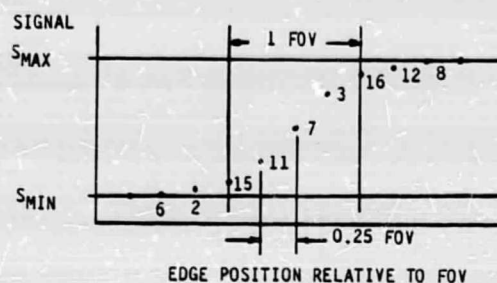


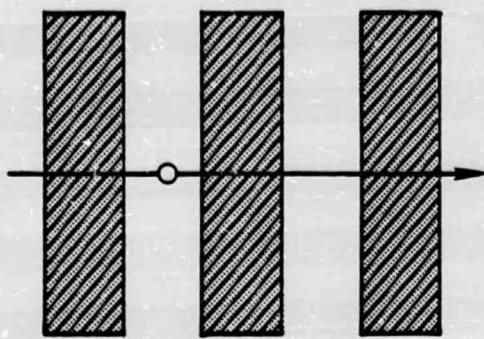
Figure 64. Reassembled KER Data

The first derivative of this function yields the line-spread function (LSF). The LSF is then analytically moved across each of the four specification input-bar patterns, as shown in Figure 65;a,b. Each bar pattern represents illuminated and nonilluminated areas. As the LSF is moved across the bar patterns the maximum and minimum illuminated areas are computed (Figure 65;d,e). These maximums and minimums are then used as the peaks and valleys of a square wave (Figure 65;f). The modulation response is computed by obtaining the ratio of the difference between the high- and low-amplitude values to twice the mean of the computed square wave. The MTF was also computed by Fourier transforming the LSF, but this was not required by NASA. Therefore, the MTF calculation was only done for a few cases and has not been included in formal program documentation.

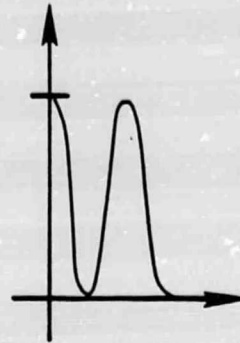
Geometric Accuracy and Band-to-Band Registration

This performance test is the principal test that permits the performance of the TM to be defined as a precision scanning multispectral mapping system. Performance specifications covered by this test are:

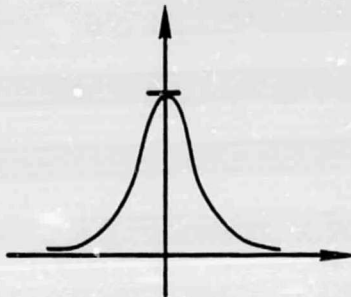
- Band-to-band registration - The band-to-band registration (BBR) is an assessment of the spatial alignment (registration) of all bands/channels in both along- and cross-scan directions. BBR can be considered a local specification of any place along the scan line.



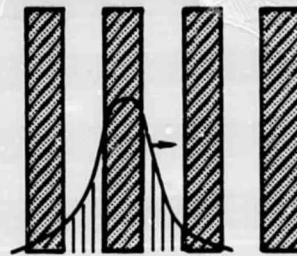
(a)



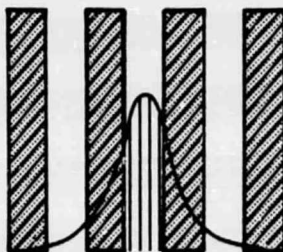
(b)



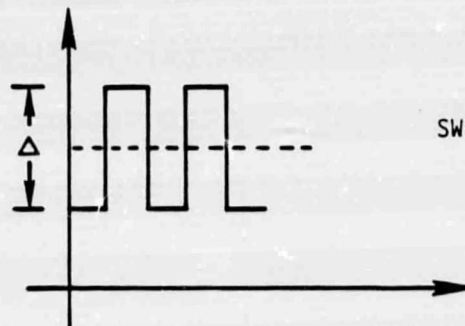
(c)



(d)



(e)



(f)

$$SWR = \frac{\Delta}{2(\text{mean})}$$

Figure 65. Square-Wave-Response Test Sequence

- Scan rate - Scan rate is the first derivative of the scan profile.
- Overlap/underlap - This parameter is the alignment between adjacent scan lines.
- Scan-line length - This is the angular distance across the scan line.
- Self-induced vibration (SIV) - SIV, if any, is the result of vibration generated by the oscillating scan mirror.

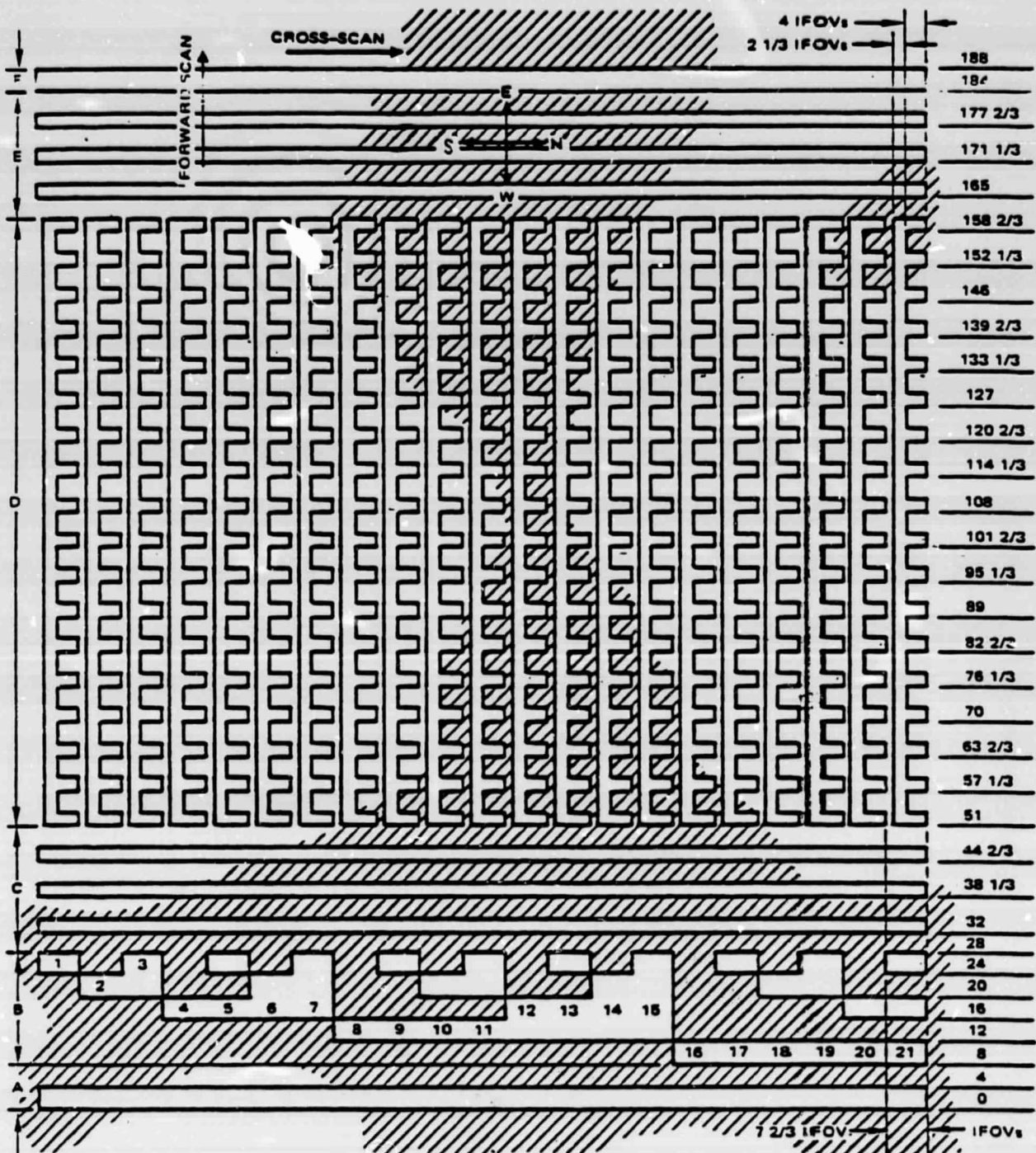
The above performance parameters are measured by projecting a complex illumination pattern that is encoded with spatial information onto the TM focal plane. Figure 66 illustrates one of the reticle patterns used. Several discrete functions are built into the pattern:

1. Regions A and F are initiation knife edges (radiance steps), used to initialize selection rules for forward and reverse scans, respectively.
2. Region B is a binary code that provides coarse cross-scan angular positional data.
3. Regions C and E are sets of three knife edges with $1/3$ IFOV phase difference between adjacent edges. These regions permit along-scan angular positions to be computed for all bands/channels.
4. Region D consists of a phased-knife edge, such that along-scan and cross-scan angular positional data can be computed for selected channels of all bands.

The data collected during this test includes:

- Index A, which is used to align the TM to the TM calibrator.
- Index B measures beam uniformity. The maximum and minimum TM signals for all bands/channels are measured.
- Index C collects data that is used to calibrated cross scan sensitivity.
- Index D collects the prime data required to determine the TM's GA/BBR performance.

All aspects of the TM's BBR/GA performance are obtained via analysis of data collected by Indexes B, C, and D. The data analysis is accomplished with computer software having the major subprograms listed below.



ORIGINAL PAGE
BLACK AND WHITE PHOTOGRAPH

Figure 66. GA/BBR Reticle Battlements

- VII-1: Selection of Data for Use Along Scan, Cross Scan, and Determination of Associated Binary Code Data: ASCS/BINCOD
- VII-2: Cross-Scan Sensitivity Parameter, $(\partial\phi/\partial S)_{CS}$
- VII-3: Along-Scan Angular-Phase Position Alignment, $\Delta\phi_{AS}$
- VII-4: Boresight Drift Correction Along Scan $\Delta\phi_{AS}(CORR)$
- VII-5: Boresight Drift Correction Cross Scan $\Delta\phi_{CS}(CORR)$
- VII-6: Dynamic Band-to-Band Registration Along Scan
- VII-7: Dynamic Band-to-Band Registration Cross Scan
- VII-8: Geometric Accuracy - Scan Profile (Along Scan) and Self-Induced Vibration (Along Scan)
- VII-9: Geometric Accuracy - Scan Profile (Cross Scan) and Self-Induced Vibration (Cross Scan)

Radiometric Calibration - Band 6

Radiometric calibration of Band 6 was accomplished by configuring the TM as in the radiometric calibration of Bands 1 through 5 and 7, except that alignment is to the TM calibrator (TMC), mounted on the environmental test bench as shown in Figure 59. The TMC (also known as the external calibrator) contains two blackbodies, one stabilized at 320K and the other at several temperatures between 260K and 320K. At each stabilized temperature, data is taken from all four Band 6 channels. The TM's internal calibration blackbody is also stabilized at several temperatures to obtain calibration data from the blackbody. This test is designed to be performed in a thermal-vacuum environment.

NEAT is calculated at two scene temperatures: 300K and 320K. First, the response (MUX counts) versus radiance is computed, then the Band 6 noise level is converted from MUX counts to radiance to apparent blackbody temperature variation at each temperature, and this value is the NEAT.

Coherent Noise

The coherent noise test of all TM bands is performed by aligning the TMC to the TM (see Figure 59), turning on the floodlamp of the TMC, and collecting data from Bands 1 through 5 and 7. The flooding lamp presents a source of illumination which varies monotonically as a function of scan angle. This results in TM output signals that ramp up (or down, depending on scan direction) from a very low level to approximately half scale. An attempt was made to color-correct the lamp illumination to provide similar signal levels in each band. A similar procedure is followed for Band 6, except that the TMC blackbody is used for

the radiance source. Data output can be photographs or in the form of power-spectral-density plots.

System-Readiness Test

A special test, the system readiness test, was used to determine the overall systems readiness of the TM at any time during the test program to verify that no gross malfunctions had occurred. The test configuration is shown in Figure 59. The calibration of all the bands is checked using both the OBC and the TMC. The scan mirror, line length, and electronics are also checked, as well as all commands and telemetry channels.

Thermal-Vacuum Tests

The tests described above were all performed in the ambient environment. The following tests were also conducted in thermal vacuum: system readiness, square-wave response, geometric accuracy and band-to-band registration, and coherent noise. The test configuration for the thermal-vacuum tests is shown in Figure 59.

Section 8

LANDSAT-4 IMAGE DATA QUALITY ANALYSIS

INTRODUCTION

Landsat-4 was launched in July 1982 and carried the TM instrument, described in this report, as well as the fourth MSS. Immediately after launch, a 2-year-long series of detailed investigations commenced, sponsored by NASA at the Goddard Space Flight Center (GSFC). Research plans for these investigations, the Landsat Image Data Quality Analysis (LIDQA), had been specified before launch so that the performance of the TM could be immediately assessed. The LIDQA investigations have demonstrated the high quality of the TM as a spaceborne multispectral radiometer and have shown that the instrument met or exceeded most of its design goals.

TM's new short-wave infrared (SWIR) spectral capability yielded improved mineral and plant discrimination compared to the MSS, as anticipated by ground-based and airborne TM simulations. Moreover, the improved spatial resolution and geometric accuracy of Landsat-4 and the TM have resulted in satellite image maps exceeding 1:100,000 U.S. map accuracy standards. Finally, based on an information entropy measure, principal component analysis, and classification results, the data acquired has been shown to approach theoretical limits in information content per pixel, exceeding the MSS by at least a factor of two.

LANDSAT-4 LIDQA OBJECTIVES

The LIDQA program sought to characterize the TM sensors on board Landsats 4 and 5 relative to design specifications and to evaluate image quality relative to user needs [GSFC 1981]. This section addresses the Landsat-4 sensors and is an expansion of a paper presented at the 1984 meeting of the Committee on Space Research [Schueler and Salomonson 1984]. Section 9 presents an analysis of Landsat-5 data conducted at SBRC.

Sensor evaluation includes radiometric accuracy, spatial blur and geometric fidelity, and spectral performance. Image evaluation relative to user needs includes cartography and land-use mapping, agricultural and botanical applications, hydrology, and geological applications, including petroleum and mineral exploration as well as land-form characterization. Each of these evaluation areas of the LIDQA program was supplemented by investigations conducted as part of the normal NASA research effort.

The Landsat 4/5 ground-based data-processing systems have provided the data products that enabled scientists to evaluate sensor performance and image quality. Between July 1982 and July 1983 a set of systems, collectively called the "Scrounge" system, was used to provide data products for analyses. From July 1983

to the present, the TM Image Processing System (TIPS) has provided the data products. Aside from minor formatting differences, the products from both of the systems, discussed in Appendix A, are the same.

Three digital image products are provided by the ground-processing system. The first is the raw data, which is not generally available. The other two products are readily available and include archival (A) tapes and product (P) tapes. The A tape consists of data that has been corrected radiometrically, but not geometrically. The P tape provides both radiometrically and geometrically corrected data. Color composite or black-and-white film transparencies in 241 x 241 mm format or paper prints are also available.

SENSOR EVALUATION

As discussed in Section 4, three fundamental sets of sensor parameters characterize TM performance, i.e., radiometric, spatial, and spectral performance characteristics. Instrument sensitivity is one of three fundamental radiometric characteristics and is often characterized by the user in terms of the noise equivalent ground reflectance, or $NE\Delta\rho$. A second radiometric parameter is dynamic range, which establishes the sensor's saturation radiance above which the sensor will no longer respond. A third radiometric quality is the calibration accuracy that gives the user confidence that a digital number (DN) from the sensor corresponds to a specific radiance that entered the sensor aperture.

The second set of characteristics involves the sensor's spatial resolution, coverage, and geometric accuracy. The sensor's instantaneous field of view (IFOV), modulation-transfer function (MTF), and swath width are the spatial resolution and coverage parameters. The IFOV is the projection of the detector aperture on the ground, and the MTF defines the total allowable system blur. The swath for Landsat 4 and 5 matches Landsats 1-3 at 185 km across track, for a repeat cycle of 16 days in a 705-km polar, sun-synchronous orbit.

The third and final set of characteristics involves spectral resolution and coverage, including spectral band locations and bandpass limits for each, as well as spectral bandpass uniformity from detector to detector. Each of these classes of sensor characteristics is discussed below in terms of the LIDQA program results.

Radiometry

Sensitivity

The TM was designed to meet NASA-specified $NE\Delta\rho$ requirements of 0.5% in Bands 2 through 4, 0.8% in Band 1, and 1.0% and 2.4%

in Bands 5 and 7, respectively. A noise-equivalent temperature difference (NE Δ T) requirement of 0.5K was imposed on the thermal Band 6. The dynamic-range requirements for each band accounted for anticipated high-reflectance ground features and, in conjunction with the NE Δ ρ requirements, dictated the use of eight-bit quantization to both cover the dynamic range and provide fine quantization within the noise levels desired.

All reflective bands provide better-than-specified NE Δ ρ for both the Landsat 4 and 5 TMs [Engel and Weinstein 1983], as indicated in Table 5, Section 4. The measurements for the thermal band show that the TM NE Δ T is about four times better than specified as a result of better-than-anticipated detector performance. This indicates that a smaller thermal IFOV (60 meters versus 120 meters) could be achieved in a TM instrument, while probably still meeting the 0.5K NE Δ T requirement.

Dynamic Range

Specifications on maximum radiance response were exceeded in every reflective band, and the specified temperature dynamic range was also exceeded in the thermal band. However, the TIPS provides processed image products whose dynamic range is approximately as specified. That is, selected dynamic range cutoffs are applied to the data in ground processing, and the data is then linearly stretched to a full 0 to 255 DN.

The satellite-radiance-to-image digital number (DN) relationship has been shown to be linear over the entire dynamic range in both the reflective and thermal bands, so that linear conversion from DN to aperture radiance is accurate. Moreover, Dozier [1984] has computed the saturation radiance in each band, and the calculated saturation reflectance outside the atmosphere. These latter percentages range from about 25% in the blue Band 1 to about 70% in the near-IR Band 4.

The relationship between sensor DN and aperture radiance, L , is given by the following expression:

$$L = \left(\frac{R_{\max} - R_{\min}}{255} \right) \text{DN} + R_{\min}, \quad (2)$$

where estimates of R_{\max} and R_{\min} are listed in Table 17, based upon average values from prelaunch aperture radiance calculations. Furthermore, assuming a linear relationship between ground reflectance and sensor radiance, the following expression can be derived [Colwell 1983, chap. 12]:

$$L = \left(\frac{H_0}{\pi} T^{(1+\sec z)} \cos z + 0.72 L_a \right) \rho + L_a, \quad (3)$$

where,

$$H_o/\pi = \frac{\sum H(\lambda) r_{TM}(\lambda) \Delta\lambda}{\pi \sum r_{TM}(\lambda) \Delta\lambda}, \quad (4)$$

is the effective radiance of a perfect Lambertian scatterer normal to the sun outside the atmosphere, z is the solar zenith angle, T is the atmospheric transmittance, and L_a is atmosphere scattering radiance. $H(\lambda)$ is the solar spectral irradiance, and $r_{TM}(\lambda)$ is the Thematic Mapper spectral response. H_o/π for Landsat 4 and 5 TMs are listed in Table 17. The resulting R_{max} and R_{min} values are averages for both sensors. The difference between Landsat 4 and 5 values is small.

Table 17. Reflective Band Radiance Parameters

Band (nm)	H_o/π (mW/cm ² -sr-μm)		R_{max}	R_{min}	L_o	$\frac{R_{max}-R_{min}}{255}$ ($\times 10^{-2}$)	T	ρ_{SAT}
	Landsat 4	Landsat 5						
1. 0.485; blue	61.6	61.6	15.2	-0.15	5.77	6.02	0.69	0.28
2. 0.56; green	57.8	57.9	29.7	-0.28	3.5	11.75	0.74	0.77
3. 0.66; red	49.6	49.5	20.4	-0.12	2.25	8.06	0.79	0.56
4. 0.83; near IR	33.2	33.3	20.6	-0.15	0.66	8.15	0.83	0.85
5. 1.65; SWIR 1	6.7	6.9	2.7	-0.037	0	1.08	0.89	0.50
7. 2.22; SWIR 2	2.6	2.6	1.4	-0.015	0	0.57	0.91	0.65

Equation (3) can be inverted and combined with Eq. (2) to yield ground reflectance in terms of sensor DN. To simplify the results, it is generally assumed that $L_a = L_o \cos z$, where L_o is the value of L_a at $z = 0$. This is a close approximation up to about $z = 50^\circ$. In this case, the result is:

$$\rho = \frac{\frac{R_{max} - R_{min}}{255} DN + R_{min} - L_o \cos z}{\left(\frac{H_o}{\pi} T^{1+\sec z} + 0.72 L_o \right) \cos z}. \quad (5)$$

Using Eq. 5, one can estimate ground reflectance using TM data, although it is helpful to have an estimate of T . This can be obtained using radiosonde data and LOWTRAN 5, as discussed by Lansing and Barker [1984]. Better atmospheric correction can perhaps be obtained using more complicated atmospheric models, as discussed by Dozier [1984], but the error in estimates of T may not allow more accurate models to do a significantly better job of correcting atmospheric degradation.

Using Eq. (5), the saturation reflectance (ρ_{SAT}) was computed, and the results also appear in Table 17. These results are not identical to those of Dozier, but are close. Discrepancies may be attributed to differences in the way the results were computed. First, Dozier used solar spectral data from Thekaekara [1970], and the Table 17 results were calculated using Neckel and Labs data [1981], which does not agree exactly with Thekaekara's data. Secondly, Dozier used a different atmospheric model than Eq. (3) that takes into account multiple reflections of scattered radiance and, therefore, is more exact, but not amenable to closed-form analysis.

The low saturation reflectance in TM Band 1 causes saturation in snow images [Dozier 1984]. However, in general, many agricultural and geologic features of interest have low reflectance, and saturation is not a problem [DeGloria 1984; Dykstra, Everett, and Sheffield 1984]. Features that have low reflectance fill only the low-order bits of the TM's dynamic range, and radiometric sensitivity for these features would be improved had the sensors been designed with a lower saturation reflectance. However, the TM dynamic range was tailored in each band to produce a sensor that would provide a reasonable compromise between the conflicting needs of users at the two ends of the dynamic range. Moreover, the TM actually exceeded its specifications on both ends of the dynamic range.

Ground Temperature Estimation from TM Band 6

TM Band 6 has yielded estimates of surface temperature to approximately $\pm 1K$ [Engel, et al. 1983; Anuta, et al. 1984]. Although the TM NEAT is $0.1K$, as measured by Lansing and Barker [1984], atmospheric effects and, to a smaller extent, calibration errors degrade the temperature measurements. Engel, et al. [1983], Anuta, et al. [1984], and Wukelic, et al. [1984], each performed calculations of water-body temperature using Band 6 data and compared the estimates to the best water-temperature estimates available at test sites.

Engel, et al. [1983], assumed a linear relationship between sensor radiance and surface radiance including atmospheric transmittance and scattering. Thermal data from the TIPS has a dynamic range from $260K$ to $320K$, and the nonlinear-radiance-to-temperature conversion provided by the Planck equation yields a nonlinear relationship between surface temperature and the DN of TM Band 6, which can be approximated within $0.2K$ by a cubic fit. Engel, et al., provide a procedure to calculate ground temperature from sensor DN, given atmospheric transmission and scattering, which can be obtained from radiosonde data (See Section 9).

Moreover, a rough approximation to ground temperature from the DN of TM Band 6 can be attained using a "nominal" atmosphere with $T = 0.82$ and $L_a = 0.09$, in which case ground temperature is given by:

$$\text{Temperature} = -13.6 + 0.38 \text{ DN} - 6.1 \times 10^{-4} \text{ DN}^2 + 7.8 \times 10^{-7} \text{ DN}^3. \quad (6)$$

This equation will be in error when T and L_a diverge from the assumed values, but will usually give good enough results to be used as a rough approximation. For example, the temperature error for a scene over Los Angeles for which $T = 0.75$ and $L_a = 0.14$ ranged from 0.1 to 3.8°C.

As pointed out at the close of Section 6, the quantizer steps, or bin sizes, are unequally spaced in the TM, i.e., for each unit change in input analog signal, the corresponding quantizer step is not the same as other quantizer steps. A method of correcting for unequal bin sizes was developed and used, and the before and after results of a corrected histogram are shown in Figure 67. Using the corrected histograms for all channels, fairly precise calculations of relative gain and offset were made. Table 18, reproduced from Lansing [1983], shows the relative gains and offsets for three scenes. Corrected scene counts are obtained by substituting these values into the following equation:

$$Q_{\text{corrected}} = \frac{Q_{\text{scene}} - Q_{\text{shutter}}}{G_{\text{relative}} - Q_{\text{offset}} + Q_{\text{reference}}}, \quad (7)$$

where Q represents quantized output in DN, and G is gain in DN per $\text{mw}/\text{cm}^2\text{-sr-}\mu\text{m}$.

Temperature estimates were made for specific locations in several of the scenes studied. Table 19 shows the estimates from the TM and surface records. The noise-equivalent temperature difference (NE Δ T) was calculated to be 0.11K at 300K for a uniform area of Lake Erie from the Buffalo scene.

Table 18. Relative Gain and Offsets in Counts

Scene	Quantity	Channel			
		1	2	3	4
Buffalo	G_{rel}	0.998	1.011	0.975	1.017
	Q_{of}	-1.2	1.6	-0.7	1.5
	Q_{ref}	← 78 →			
Los Angeles	G_{rel}	1.002	1.015	0.968	1.015
	Q_{of}	-1.0	0.9	-0.7	0.7
	Q_{ref}	← 83 →			
New York	G_{rel}	0.980	1.024	0.972	1.024
	Q_{of}	-1.1	1.2	-0.7	0.9
	Q_{ref}	← 80 →			

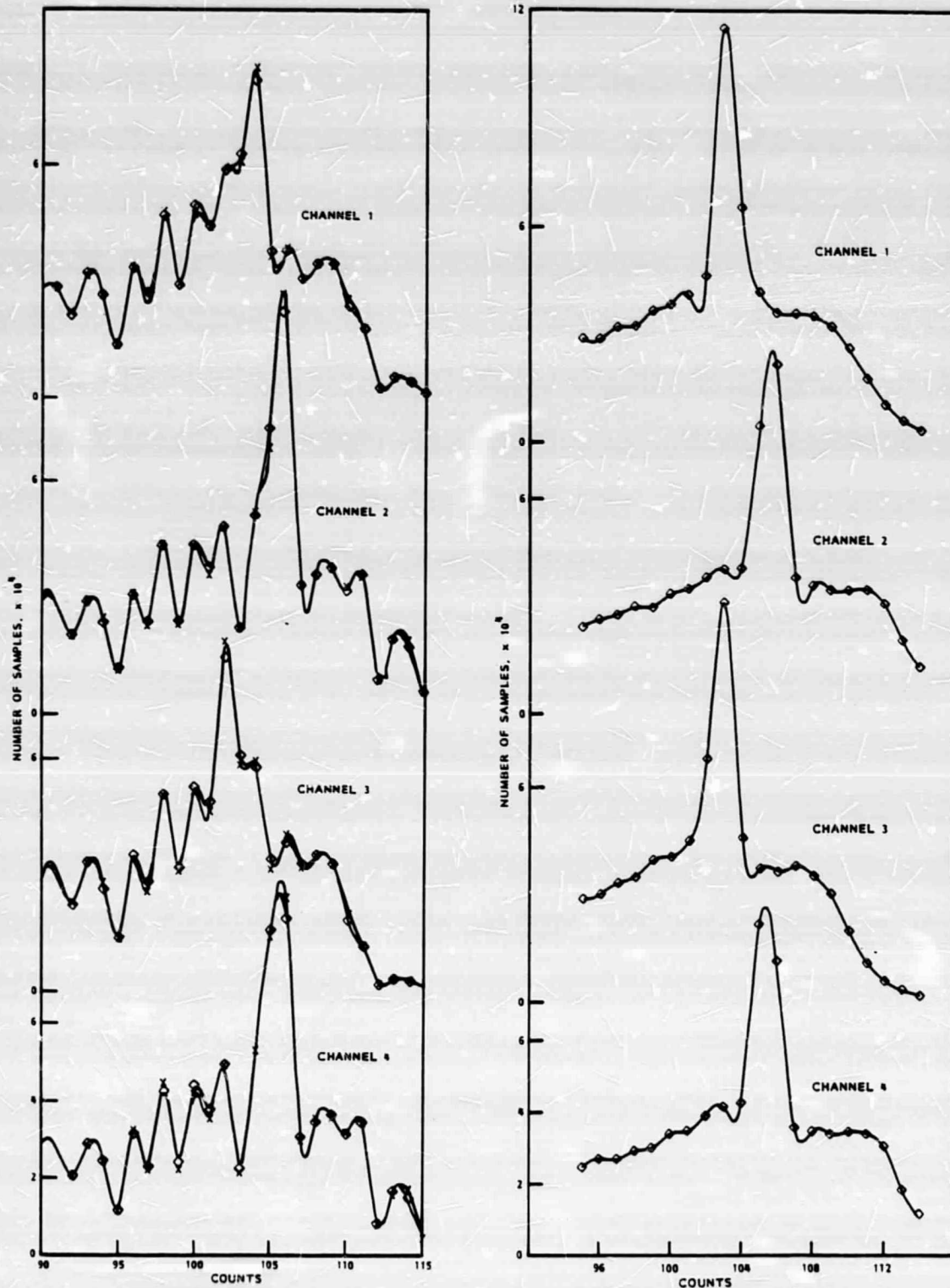


Figure 67. Comparison of Histograms Before and After Corrections for Unequal Bin Sizes (Los Angeles Scene)

Table 19. Average Temperature Data (°C)

Location	Ocean Santa Monica, CA	Casitas Lake, CA	Battery Park Bay, NY	Lake Erie, NY
Calculated Temperature	19.5	19.8	10.5	24
Surface Records Temperature	16.7	17.2	10.6	21

Reflective-Band Calibration

Measurements at SBRC prior to launch provided detector gain and offset coefficients for all detectors on the TM to meet the calibration requirements. Estimated absolute calibration accuracy was $\pm 5\%$, or twice as good as was specified [Barker 1984]. Castle, et al. [1984], performed direct ground measurements coincident with TM overflights to produce in-orbit calibration checks on the Landsat 4 Thematic Mapper. They transferred ground-radiance measurements to space with an estimated rms accuracy of $\pm 5\%$ and compared the results to estimates derived from the TM. Selected detectors in Bands 2, 3, and 4 were in agreement with ground-based estimates to within 6.6%, 2.4%, and 12.9%, respectively, for an average agreement of 7.3%.

Sensor Radiometric Stability and Anomalous Behavior

Relative to TM internal calibration data, Barker, et al. [1984], noted cyclic gain variations in the cold focal plane array (CFPA) with periods of 2 months and peak-to-peak variations of 5 to 7%. However, Engel, et al. [1983], show that relative changes in the gain of all detectors on the TM were within about 1% over a 4-month period following launch. Since then, additional data has been gathered for more than a year since launch on the 12 scenes listed in Table 20, and this data is displayed in Figure 68.* As shown in Table 21, even the peak-to-peak variation was within 1% for all but Band 7. The apparent inconsistency of Barker's absolute measurements and the relative gain results of Engel, et al., has not yet been resolved. If a reasonable mechanism could be isolated that would cause Bands 5 and 7 to

*A comparison of Figure 68 and the same data from Engel [1983] shows that the relative gain of corresponding channels varies in opposite directions in the graphs. The gain is actually the same. However, the method of graphing was changed. In Engel [1983] the positions of the points on the graphs were computed by subtracting the relative gain for each scene from the relative gain of a base scene (the first one). For Figure 68 the subtraction was performed in the opposite order.

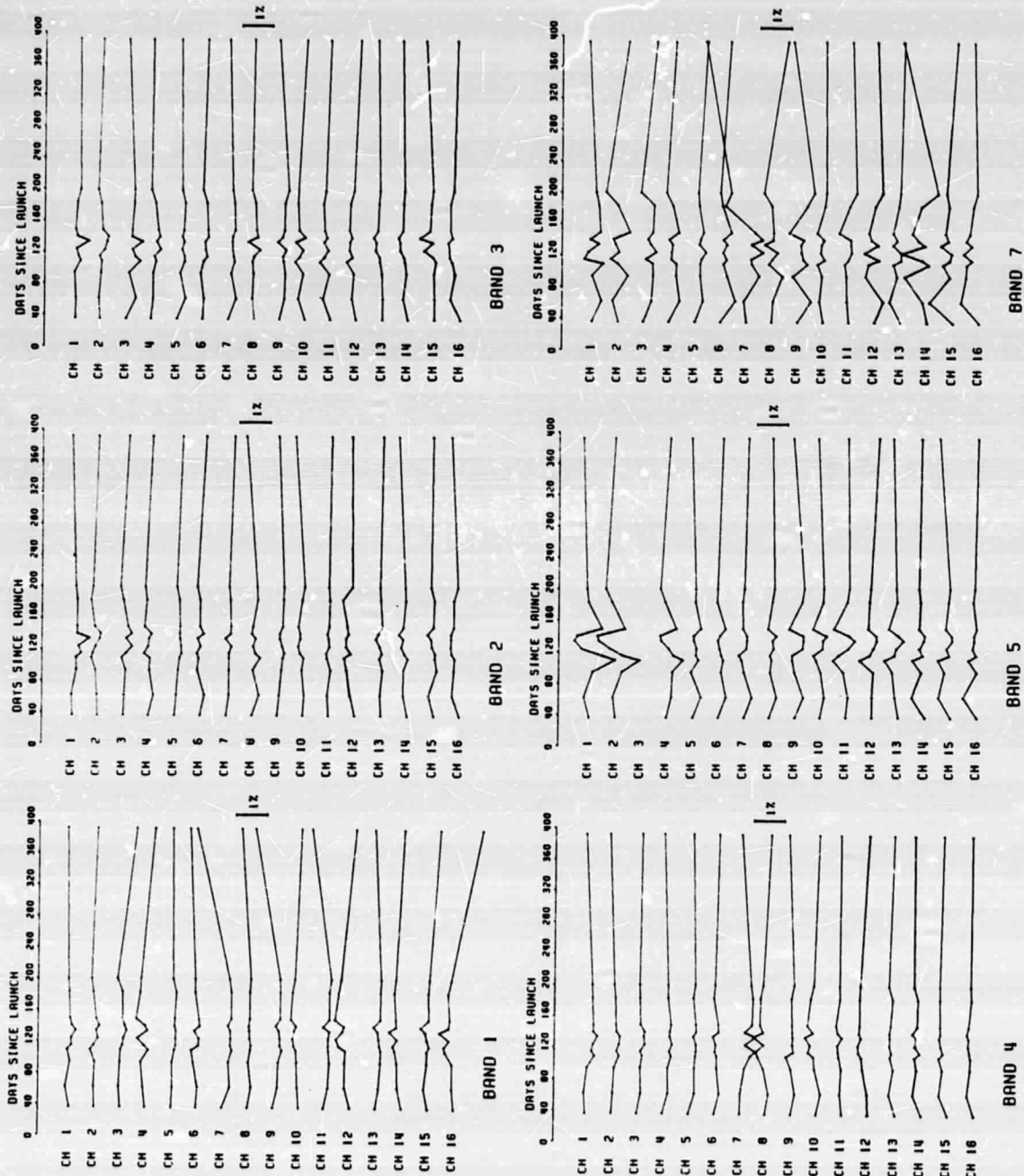


Figure 68. Relative Radiometric Stability; Bands 1 through 5 and 7

Table 20. Scenes Used to Measure Relative Gains for Bands 1 through 5 and 7.

Title	Date	Path-Row	Days Since Launch
Central Florida	21 Aug 82	16-40	36
New Orleans	16 Sep 82	22-30	62
Western Indiana	18 Oct 82	22-32	94
Baltimore/Washington	2 Nov 82	15-33	109
Lethbridge	8 Nov 82	41-25	115
Death Valley	17 Nov 82	40-35	124
Bald Mountain	17 Nov 82	40-34	124
New York/Philadelphia	27 Nov 82	14-32	134
Salton Sea	10 Dec 82	39-32	149
Clarksdale	15 Jan 83	37-36	183
Sacramento	1 Feb 83	44-33	200
TDRSS San Francisco	12 Aug 83	44-34	392

Table 21. TM Protoflight Model (Landsat 4) Reflective Band Radiometric Stability Summary

TM Band (μm)	ΔRMS (%)	ΔPEAK (%)
1. 0.485 (blue)	0.42	0.89
2. 0.56 (green)	0.18	0.33
3. 0.66 (red)	0.12	0.55
4. 0.83 (near IR)	0.11	0.49
5. 1.65 (SWIR 1)	0.15	0.82
7. 2.22 (SWIR 2)	0.47	1.33

vary cyclically in gain in such a way that all detectors vary together, then relative changes would be expected to be small, despite absolute calibration drift.

One other instability, of much higher frequency than bi-monthly, is characterized by a scan-to-scan (7 Hz or slower), and somewhat random dc-offset-level shift that has been described by Malila, et al. [1984]. Although these offset-level shifts are noticeable in low-radiance scene data (e.g., nighttime data) by averaging entire scans, the shifts are generally less than half a DN, and are well within the allowable sensor performance limits. Moreover, the shifts are systematic enough that they may be correctable by means of an algorithm suggested by Malila. This algorithm exploits the correlation of calibration shutter data with the offset-level shift, and subtracts one from the other to correct the anomaly. No cause for scan-correlated offset shift has yet been determined.

Other anomalies have been studied, including band nonuniformities that cause striping in low-level imagery such as water

[Anuta, et al., 1984; Malila, et al., 1984; Bernstein, et al., 1984]. Efforts by several teams of investigators have resulted in a thorough characterization of the striping effects in all spectral bands, and methods of striping removal have been suggested [Murphy, et al., 1984; Bernstein, et al., 1984; Fischel 1984]. Three kinds of striping have been noted in TM imagery, including detector-detector striping, scan-to-scan striping, and multiscan banding [Fischel 1984].

The most obvious striping effect is detector-to-detector striping. It is noticeable even after radiometric correction. Bernstein, et al. [1984], show that the detector gain-offset corrections do not fully correct detector-detector striping because of rounding errors in the eight-bit quantization process. They also demonstrate an interesting destriping algorithm they call "probabilistic" destriping that performs well in correcting the striping that would normally remain in radiometrically corrected TM imagery.

Scan-to-scan differences have also been studied. Malila, et al. [1984], report that a west-east variation in overall scene brightness, attributable partly to sun angle and reflectance effects, is different in forward and reverse scans. Fischel [1984] noted a bright-target saturation effect, which also causes scan-to-scan banding to occur. Murphy, et al. [1984], included a striping removal algorithm in the Canadian ground-processing procedures that accounts for some scan-direction dependencies, including an exponential "droop" effect [Murphy, et al., 1984; Kieffer, Eliason, and Chavez 1984] with a decay time of about 1,000 pixels. This time period is extremely short compared to the dc-restoration time constant associated with the TM system and has not yet been explained. Finally, Bernstein, et al. [1984], have reported a multiscan banding effect, consisting of random changes in brightness over several scans. The frequency of this effect is very low, and there is, as yet, no good explanation of the effect, although it may be related to the scan-correlated shift reported by Malila.

Coherent noise, which is correlated in frequency, or coherent with specific electronic or mechanical oscillations in the system, also has been studied [Anuta, et al., 1984; Kieffer, Eliason, and Chavez 1984; Bernstein, et al., 1984; Wrigley, et al., 1984]. Investigators mentioned several frequencies but, in particular, they emphasized a small image degradation at 0.3 cycle/pixel, purportedly caused by a spacecraft 32-kHz switching power supply [Bernstein, et al., 1984]. Wrigley, et al. [1984], removed this noise from the image by notch filtering in the spatial frequency domain, and Bernstein, et al. [1984], demonstrated an interesting spatial domain filtering technique based on measuring the phase of the noise pattern.

One detector in the Landsat-4 TM system failed prior to launch, and the corresponding pixels are replaced with those of a neighboring detector to produce image products. Bernstein, et

al. [1984] and Fusco, et al. [1984], both examined alternate algorithms for failed detector replacement. In general, both teams found that an algorithm based on replacement of a failed detector output with that of the same detector from a different band yielded superior results, compared to the standard algorithm that uses a neighboring detector in the same band. Fusco, et al., are examining the possibility of implementing their algorithm in the Italian ground-processing system.

The thermal-band calibration has been verified by Lansing and Barker [1984]. The key result of the verification shows there has been correctable thermal-band gain variation over time as shown in Figure 69. Most of this variation can be traced to suspected water condensation on a radiative cooler window. The average blackbody reference value also decreased by about 15% over the same period, and relative internal gains among the four Band 6 channels varied by 5% over the 9 months after launch. However, an outgassing cycle in January 1983 was shown to return the thermal-band gain to its original value, as indicated by the arrow in Figure 69, validating the reliability of the calibration reference.

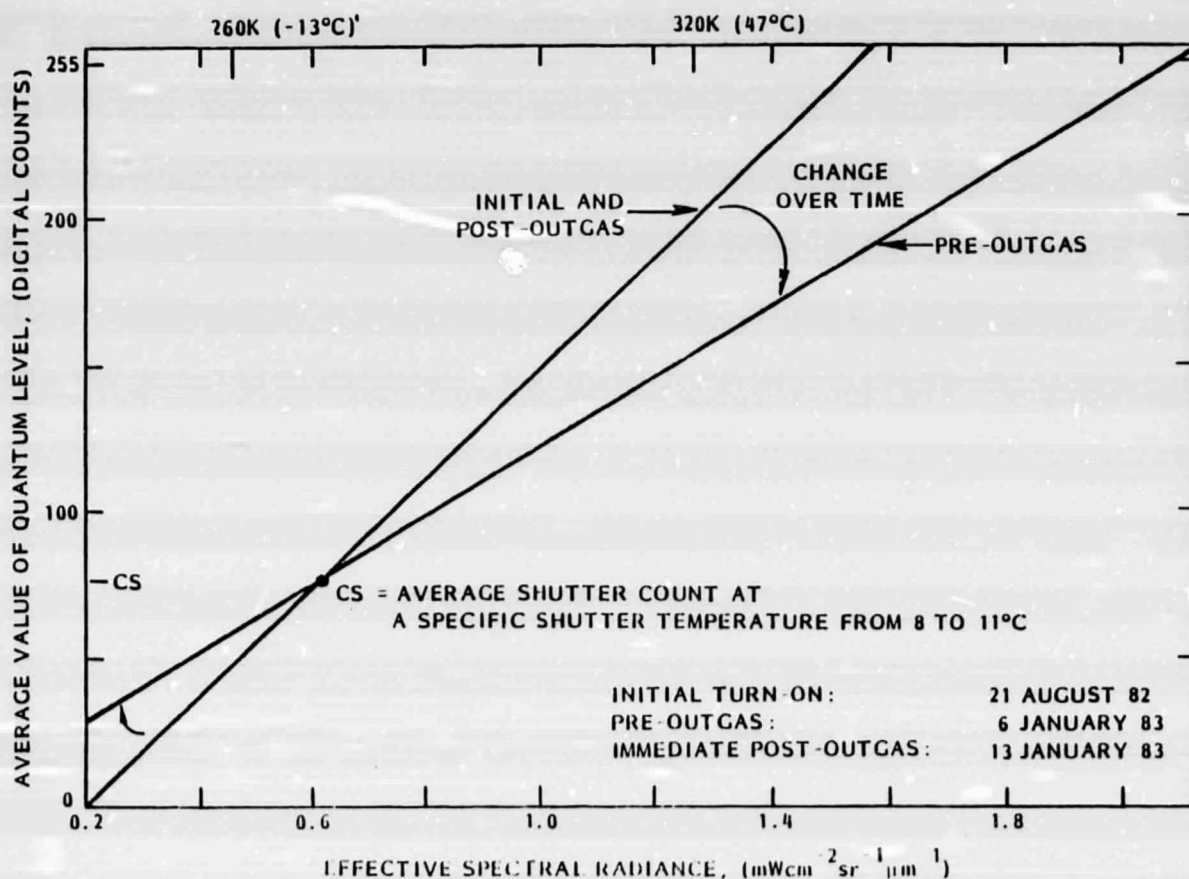


Figure 69. Initial Calibration Unchanged After Outgassing
 (Decreasing Slope Indicates Increasing Gain)

Resolution; Instantaneous Field of View (IFOV) and Blur

Landsat's spatial resolution performance is generally characterized by two parameters. One is the IFOV, which is just the geometrical projection of a detector onto the ground and is measured in meters on a side on the ground. However, the MTF is more important because it accounts for all system blur, including the optical system, the detector IFOV, and the electronics response. Therefore, the MTF completely characterizes sensor image quality, aside from sampling artifacts, in a spatial-sharpness sense. The equivalent spatial-blur characteristic is the sensor line spread function (LSF), which defines how a linear input radiance (a road is a practical example) is blurred by the sensor. The sensor MTF and LSF were both characterized accurately on the ground prior to launch by SBRC [Schueler 1983] and approximately on-orbit by several investigators [Anuta, et al., 1984; Wrigley, et al., 1984; Markham 1984a].

Because the LSF and MTF are essentially equivalent measures of spatial resolution performance, and because MTF is conveniently specified at a single spatial frequency (the Nyquist frequency, with a period equal to twice the center-to-center spacing of adjacent detectors on the focal plane), only MTF was specified, and both the Landsats 4 and 5 TM exceeded the MTF specification. Independent computations [Schueler 1983; Markham 1984a] of Landsat-4 LSFs were performed, based on available prelaunch TM frequency response measurements made at SBRC. Comparison of these results, with an LSF width at half-maximum of 1.2 to 1.3 IFOVs, to on-orbit data, suggests a degradation of on-orbit LSF of 10 to 20% (1.4 to 1.6 IFOVs) in Markham's work [1984a] as well as that of Anuta, et al. [1984] and Schowengerdt [Wrigley, et al., 1984]. These degradations seem small enough to be attributed to a combination of atmospheric blur and uncertainties as well as degradations resulting from the coarse TM sampling rate on orbit. The tentative conclusion to be drawn from these efforts is that the TM's spatial-imaging performance appears to be consistent with prelaunch measurements.

Sampling and Resampling Effects

The spatial performance of the Landsat sensors, both the MSS and the TM, are limited not only by the image blur characterized by the MTF or LSF, but also by discrete sampling, at approximately one IFOV intervals, of the terrain below the spacecraft. Recent studies of the specific sampling artifacts pertinent to MSS and TM have been performed [Park and Schowengerdt 1982a], and show that spatial errors in the TM data can be attributed to image blur, errors in the nonideal image resampling used to correct geometric errors, and aliasing (moiré) errors due to scene under-sampling by the sensor. A key result is that the cubic convolution resampling algorithm employed by the original Scrounge geometric processing system at GSFC produced errors in early scenes which could be reduced by modifying the parameters in the algorithm. This "parametric" cubic convolution algorithm [Park and

Schowengerdt 1982b] was used to correct later scenes [Fischel 1984].

Geometric Quality

The appearance, as well as the fundamental accuracy and utility of TM data, is founded on a cornerstone of pixel-level data registration to standard maps (geodetic accuracy) and between successive scenes (temporal registration accuracy), as well as pixel-to-pixel registration between bands [Beyer 1983]. The key to attaining the required accuracies in each of these three areas involves three steps. First, the system, including the sensor and the spacecraft, must be of the highest quality to reduce errors to a minimum. Second, equipment must be available to continuously monitor the errors that exist and to provide that information in conjunction with the scene data. Third, a software system must be provided to implement the necessary corrections, based on the measured errors.

Geodetic errors were restricted to less than half a pixel after correction processing, and temporal registration errors were restricted to less than 0.3 pixel. Earth topographic effects were excluded from these error specifications, due to the fact that spacecraft ephemeris variation between successive overflights will cause uncontrollable distortion between different images of the same geographic area. Band-to-band registration error was restricted to 0.2 pixel between bands on the same focal plane and to 0.3 pixel between bands on different focal planes.

Early analysis suggested that the TM scan-mirror repeatability errors might be the chief error source contributing to problems in all three of the registration-performance areas mentioned above. As a result, 0.23 pixel error was allowed to estimate the probable data quality. In fact, performance was about seven times better than predicted, with only 0.033 pixel error being attributed to scan-mirror repeatability. Moreover, spacecraft attitude deviation errors are limited to 0.015 pixel, and the combination of both of these error sources is about a sixth of the allowable temporal registration error. The result of this high-quality system performance has been an overall geodetic performance good enough that successive scenes that are matched to ground control points, rather than to each other, still are registered to one another to within the temporal registration specifications [Brooks, et al., 1984]. Finally, band-to-band registration, after geometric corrections, has been obtained to within 0.1 pixel, or half the requirement.

The necessary error-monitoring-and-correction system to achieve this performance requires a complicated set of interactive measurement, recording, and transmission devices connected to the sensor and to the spacecraft. The geometric correction system is illustrated in Figure 70. The mirror-scan motion is monitored and included in payload-correction processing, along with angular-displacement information. These critical pieces of

information, combined with spacecraft attitude and ephemeris information, allow the TIPS to compute the actual point on the ground at which the TM was looking at several points throughout each mirror scan cycle. As a result, geodetic errors can be corrected to the accuracy of the measurements in the payload-correction data stream. A feedback loop to continuously reduce the measured spacecraft errors is provided through gyroscopes, star trackers, attitude-control reaction wheels, and an on-board computer. Finally, the overall ground-correction process, involving control-point processing and resampling, uses the measured errors to correct the image data.

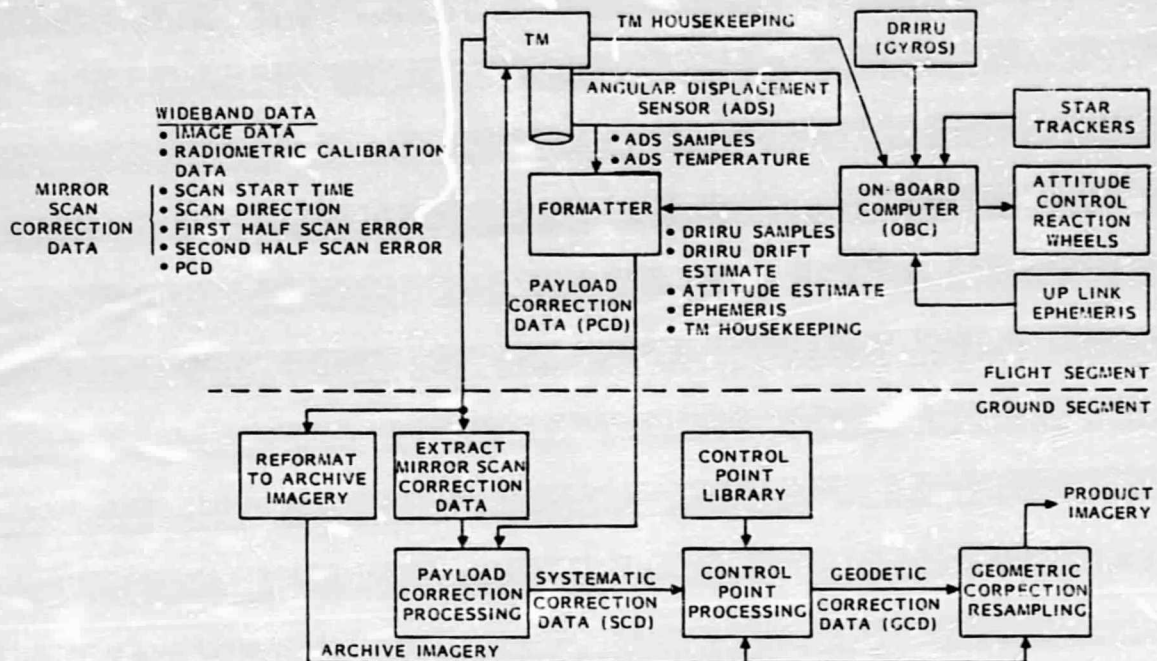


Figure 70. Landsat-4 Thematic Mapper Geometric Correction System (after Beyer [1983])

Key factors contributing to geodetic error are spacecraft attitude and ephemeris error, as well as pointing errors. Temporal registration accuracy is limited to primarily the same errors that affect geodetic accuracy, plus spacecraft jitter and scan-mirror-profile errors, nonlinearity, and repeatability. Finally, band-to-band registration accuracy is limited only by TM sensor errors, especially scan-mirror nonlinearity and detector-electronics time-delay variations. These latter effects were measured prior to launch [Schueler 1983], and are part of the ground-processing system. Additional band-to-band errors can occur if the telescope focal length changes or the focal planes shift on orbit. In spite of the many error sources, Colvocoresses [1984] found that 1:100,000 maps can be made with TM data as accurately as standard map products. In fact, a Thematic Mapper image map of Washington, D.C., is available from the United States Geological Survey (USGS).

Spectral Characteristics

The final set of parameters that characterize the Landsat sensor's performance are the spectral bands, including location, bandpass, and detector-to-detector bandpass uniformity. These specifications represent only the general characteristics, and detailed measurements of all components that affect sensor response as a function of wavelength were combined to produce end-to-end characteristics for each channel.

A common technique used to approximate the irregular bandpass data is to assume that each spectral band can be characterized by a perfect rectangular bandpass with area equal to the area under the actual bandpass and cutoffs given by the specified band cutoffs. Palmer and Tomasko [1980] show that this approximation works best if the long and short equivalent bandpass cutoffs are selected to be equal to the mean wavelength in the band, plus or minus the spectral-response-shape standard deviation multiplied by the square root of 3. This result has proved to be very close to the "50% cutoffs" used to specify the TM bands [Palmer and Tomaski 1980], which are located at the points where the spectral response equals half its maximum value.

Qualitative conclusions concerning on-orbit detector-to-detector spectral bandpass uniformity can be drawn from Figure 68, which show that the detector-to-detector relative response time variation was less than 1% over a year, using twelve TM scenes (Table 20) with entirely different spectral characteristics. Spectral nonuniformities among detectors would have contributed to relative changes in radiometric response because of the spectral variation in the TM scenes used. Therefore, at least in a qualitative sense, these results give evidence of good spectral uniformity.

IMAGE QUALITY

Information Content

A key aspect of TM performance that has emerged from the LIDQA studies (beyond the fact that the sensor has substantially met its basic engineering performance requirements) has been the discovery that the raw information content of the TM data appears to exceed that of the MSS sensor by at least a factor of 2 per pixel for the reflective bands.

The LIDQA results were for typical United States scenes. Price [1984] used an information entropy (pixel-to-pixel variability) measure to find that the ratio of TM information content per pixel to that of MSS for a specific set of scenes was about 1.8 to 1. TM's increased pixel-to-pixel variability also led to a factor of 2 improvement in its classification performance over the MSS. Anuta, et al. [1984], and Haas and Waltz [1984] found a doubling of the number of classes separated by an unsupervised

clustering algorithm for coincident TM versus MSS data. Bernstein, et al. [1984], Anuta, et al. [1984], Malila, et al. [1984], and Crist and Cicone [1984] found that TM has twice as many principal spectral components as MSS does. A physically based example of TM's increased spectral information content is the "wetness" component reported by Crist and Cicone, which has no counterpart in MSS data. Finally, Welch and Userly [1984], Walker, et al. [1984], and Colvocoresses [1984] all found that TM's spatial resolution and geometric accuracy were within 1:100,000 USGS map accuracy standards, while MSS offers 1:200,000 accuracy. Again, these results appear consistent with a factor of 2 improvement in information content of TM over MSS.

The LIDQA results summarized above can be better appreciated in the context of a theoretical upper bound to the TM's information capacity. Huck, et al. [1981], showed that the upper bound on information transmission capacity of a line-scanning sensor in bits per unit area is given approximately by the ratio of the number of bits of quantization (eight for TM versus six for MSS) to the area of the IFOV (900 m^2 for TM versus 6400 m^2 for MSS). Therefore, if the TM has twice as many orthogonal spectral components as the MSS, the ratio of the TM upper-bound information capacity in bits per unit area to that of the MSS is approximately 19. Conversion from a ratio of bits per unit area to bits per pixel eliminates the sensor IFOV area ratio and results in an upper bound of 2.6 for the ratio of TM information content in bits per pixel to that of MSS.

The LIDQA results (factor of about 2) compared to the upper limit of 2.6 can be understood by noting that the upper bound pertains to the ratio of information capacity of two information channels (the TM and the MSS) and not to the information content of any specific data sets. How much actual information gain is achieved is scene-dependent, as demonstrated by Hyde, Spencer, and Vesper [1983]. Using simulated data sets, they showed that MSS and TM classification performance should be essentially the same for fields greater than 40 acres in area. When area per field dropped to a range of 10 to 40 acres, then TM accuracy was about 10 to 15% better than MSS, comparable to LIDQA results on actual data. Finally, for fields smaller than 10 acres, simulated TM data offered twice the classification accuracy of simulated MSS data.

Image Utility Relative to MSS

The TM was initially designed with radiometric, spatial, and spectral requirements intended to provide some specific improvements in performance relative to MSS for land-use discrimination, crop and mineral identification, and overall land classification accuracy. Specifically, the finer quantization was expected to improve classification accuracy by providing more accurate ground reflectance estimates. The finer spatial resolution was motivated by studies that showed that smaller acreage fields than those in the United States would be classified more accurately by

a sensor with a smaller IFOV than MSS, principally due to the reduced number of "mixed" boundary pixels that would otherwise confuse the classifiers. The extra and narrower spectral bands were intended to yield improved discrimination of both minerals and plants due to the spectral differences that exist in ground features in the short-wave infrared that do not exist in the visible and near infrared.

Williams, et al. [1984], sequentially degraded TM data to MSS quality so they could determine what aspects of TM data quality contributed most to its improved classification performance. They found that the radiometric effect was strongest, followed by the improvement in spectral performance, in conformance with findings by Toll [1984]. Notably, they found that the TM's spatial-resolution improvement actually degrades classification of fields. This is attributed to the fact that the TM's smaller IFOV measures within-field variability that is ignored by the MSS, and this variability tends to confuse the classifier. They suggest that the classifiers be improved in such a way as to efficiently use the smaller TM IFOV. Until then, better results can often be obtained by aggregating TM pixels prior to running a field classifier that has been optimized for MSS data, except for fields that are so small as to show little within-field variability even in TM data.

Several investigators have verified Williams' overall finding that TM exceeds MSS in land-use classification accuracy, with TM providing an average of about 85%, versus MSS performance of 75%, relative to ground truth. Specifically, Toll found that TM yielded 85% accuracy and Quattrochi [1984] about 90%, compared to MSS performance of 75%. Middleton, et al. [1984], found that TM generally exceeded MSS by 11 to 13% in land-use classification accuracy.

The expected TM capacity to classify small fields more accurately than MSS has not been adequately verified, but available evidence is encouraging. In a study comparing TM data and MSS data, Markham [1984b] found that TM can detect objects as small as 16 meters as compared to 40 meters for MSS. Witt, Blodgett, and Marcell [1984] looked for surface mines in Appalachia using TM and MSS data. They found that TM offered great improvements over MSS in map registration accuracy and in its ability to delineate small irregular surface features, such as narrow contour-strip mines. The average improvement in classification accuracy for mine categories was 25%. DeGloria [1984] found that the TM resolution allows improved detection and identification of fields less than about 12 acres in area. However, there appears to be a paucity of specific investigations into the improved ability of TM to classify smaller fields than MSS, such as those in China.

Crop identification within agricultural areas depends largely on the sensor's spectral discrimination capability, and TM outperformed MSS quite dramatically, as was anticipated. Key examples show that the addition of short-wave infrared (SWIR) TM

Bands 5 and 7 was the principal reason for the performance improvement, although the narrower visible and near-infrared Bands 2, 3, and 4 also contributed. Specifically, DeGloria [1984] found that the SWIR bands provide critical leaf moisture-content discrimination that leads to the capability to separate crops such as alfalfa and sugar beets, which are not easily separable with MSS data.

Figure 71 illustrates the TM SWIR crop discrimination capability. Alfalfa and sugar beets have very similar reflectance profiles throughout the visible and near IR, but show a significant dissimilarity in the SWIR spectral range. In particular, a maximum difference in reflectance occurs in TM Band 5, at $1.65 \mu\text{m}$. It is not surprising that discrimination of alfalfa and sugar beets is enhanced in Band 5 TM images. This is illustrated in Figure 72, which shows a portion of the Imperial Valley in California just south of the Salton Sea imaged by TM on 12 December 1982. Figure 72(a) illustrates that Band 4 yields essentially no discrimination among four fields indicated by a bracket and an arrow. On the other hand, Figure 72(b), demonstrates a dramatic difference in Band 5 reflectance between the fields on the left and those on the right. The two dark fields in the Band 5 image have been verified as sugar-beet fields with reduced SWIR reflectance due to high leaf-moisture content, and the bright fields were planted with alfalfa.

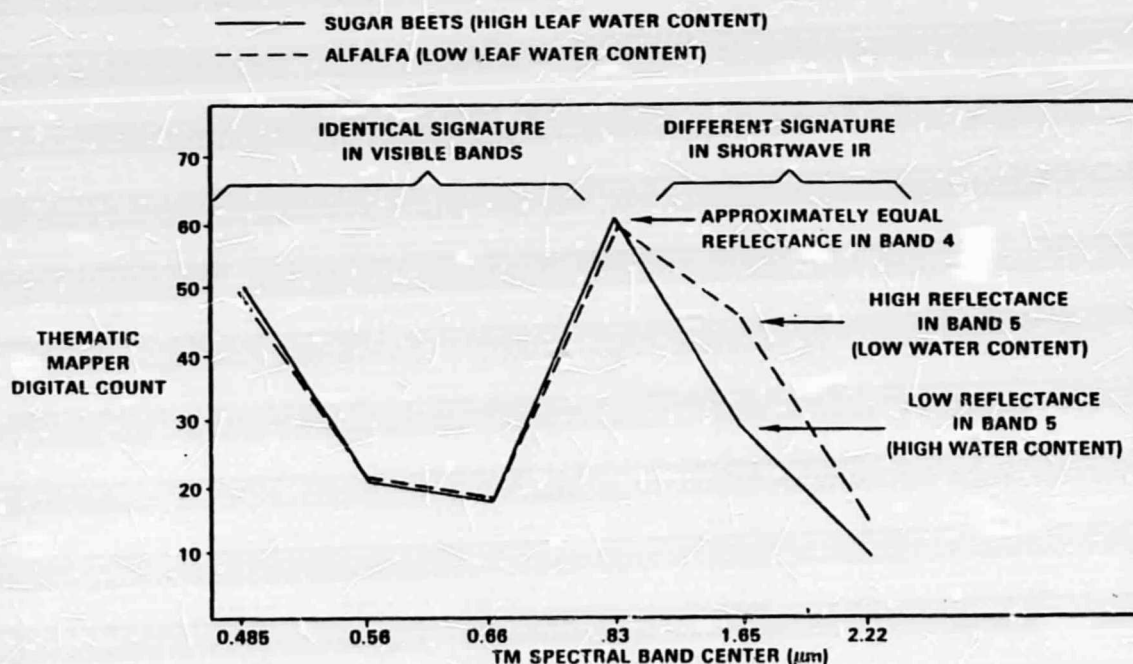


Figure 71. Spectral Signatures Reveal Differences Among Crops

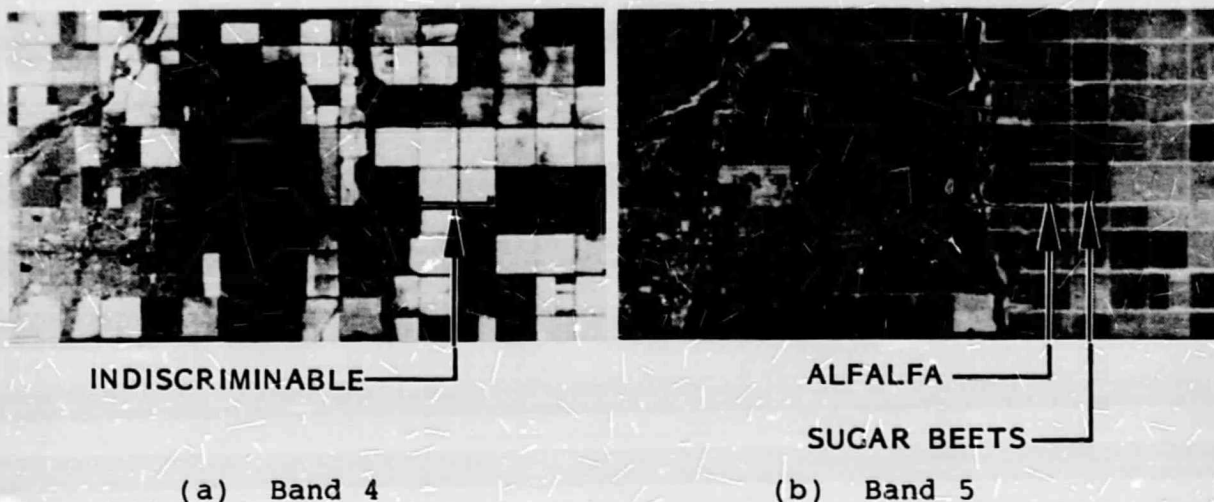


Figure 72. TM SWIR Capability Enhances Crop Discrimination

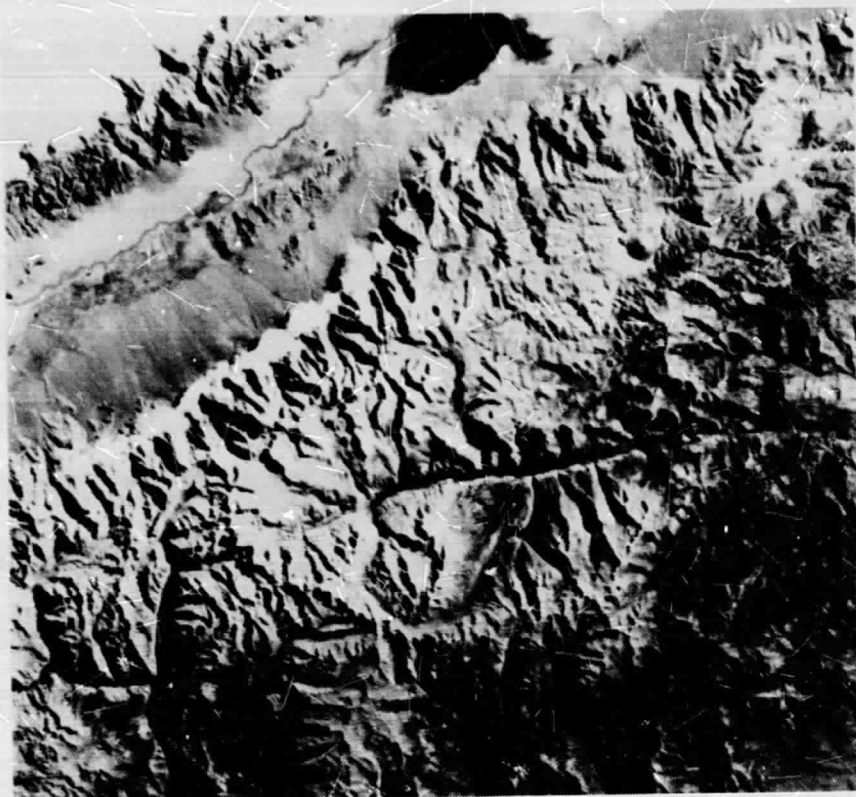
Pitts, et al. [1984], showed that the SWIR bands also enhanced corn and soybean separability, allowing these crops to be identified up to a month earlier in the year than is possible with MSS. TM Band 5 also enhanced separation of meadow and hardwood, as well as soil classification [Thompson and Henderson 1984]. Even the TM's thermal Band 6 has been found useful in renewable resource classification, enhancing tree identification in forests [DeGloria 1984], and improving soybean and sorghum discrimination [MacDonald 1984].

Water-resources planning is also included in TM user requirements. Dozier [1983] found that a critical component in water resources planning that MSS has been unable to supply is readily available with TM. Especially in California, but also in many other locations, much of the agricultural water supply is derived from snow runoff. The ability to estimate snowpack is critical to estimating snowmelt and subsequent water supplies. Unfortunately, MSS confuses clouds with snow, and extensive estimation has been necessary in the past to distinguish the two in MSS data. Moreover, Dozier showed that TM has a generally higher saturation level than MSS, making TM data more useful than MSS for snow-hydrology studies.

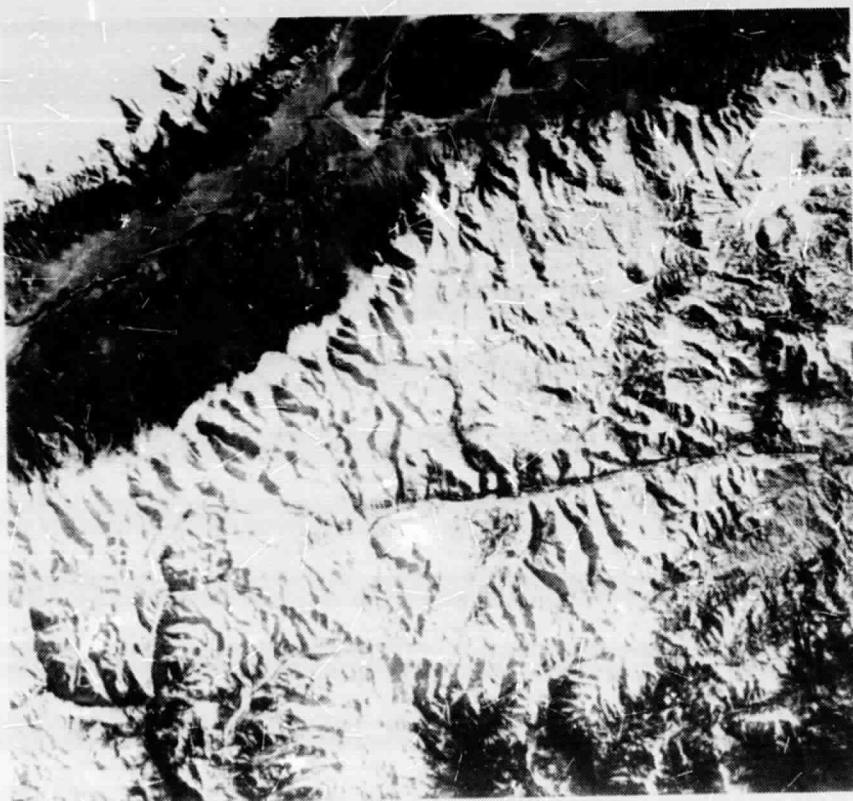
Figure 73 and Plate 2 illustrate the TM snow/cloud discrimination capability. As Figure 73 illustrates, the reflectance of snow and clouds is quite different in the SWIR. Therefore, TM Bands 5 and 7 discriminate between snow and cloud easily. To visualize this discrimination capability even more clearly, Plate 2 shows two renditions of Sierra-Nevada mountains data, acquired on February 16, 1983. The image on the left in Plate 2 was made using TM Bands 2, 3, and 4 to spectrally approximate MSS Bands 1, 2, and 4. Because snow and clouds both have high reflectance throughout the visible and near IR, both snow and clouds appear white in this image. On the other hand, the image on the right



SANTA BARBARA RESEARCH CENTER
a subsidiary



TM Bands
2,5,7



TM Bands
2,3,4

Plate 2. Sierra Nevada Snow and Cloud Discrimination

ORIGINAL PAGE
BLACK AND WHITE PHOTOGRAPH

in Plate 2 was made using TM Bands 2, 5, and 7. Because clouds have high reflectance over the entire spectral range, they again appear white. However, snow is dark in Bands 5 and 7 so that snow appears blue in this image and is very easily distinguishable from clouds.

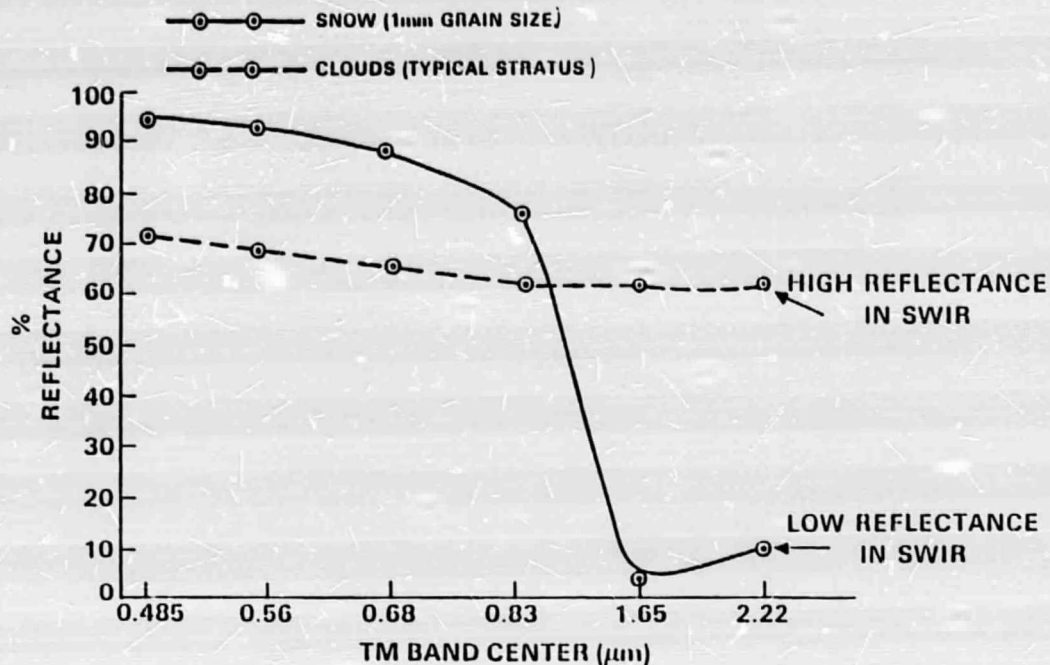


Figure 73. Snow and Clouds: Similar in Visible Band, Separable in Shortwave Infrared

The TM's earth-resource-distinguishing capability extends into the aquatic vegetation regions, as well. Specifically, Ackleson and Klemas [1984] found that TM is effective in discriminating submerged plants from sand in water depths of up to 2 meters, and Hardisky and Klemas [1984] showed that TM Bands 3, 4, and 5 can provide biomass estimates in coastal marshes. Schiebe [1984] found that TM Band 3 can help monitor suspended sediments in lakes. A major ecological concern is the effect of electrical-power-plant cooling-water effluent on the temperature of large water bodies, and both Anuta, et al. [1984], and Wukelic, et al. [1984], studied the application of TM Band 6 to temperature measurement of power-plant effluents with encouraging results.

An example of the use of Band 6 to create a ground temperature map is shown in Plate 3. This color image is a density slice of a night scene over Buffalo, New York, taken on August 22, 1982. The large water body in the middle of the image is Lake Erie. Warm areas are red (21°C) and cold areas are blue (6°C). Water-temperature information obtained from Lake Erie at the time verified the TM temperature estimates to within about 1°C [Engel, et al., 1983].

Mineral identification by spectral discrimination has been assessed by several geologists as one of the most useful improvements provided to the geology community by the TM. The new SWIR Bands 5 and 7 are the key components in this success, due to the significant spectral signature structure possessed by clay minerals in the SWIR spectral region. Specifically, Borengasser, Brandshaft, and Taranik [1984] and Podwysocki and Bender [1984] have found that clays and iron oxides are easily discriminable for the first time with TM data using Bands 5 and 7. Iron oxides provide a unique signature in the visible green and red, and clays in the SWIR, so that spectral band ratio products allow relatively easy visual identification of clays and iron oxides in color-coded TM imagery.

Plate 4 illustrates TM's capability to delineate mineral information by means of a hue, intensity, saturation (HIS) algorithm applied to data. Spectral Bands 2, 3, 4, 5 and 7 of the Thematic Mapper sensor were all used to create the picture.

Hue is manifested by a Band 5/7 ratio, which is coded red, and by a Band 3/2 ratio, coded green. Clay carbonates do not reflect light well in Band 7, so the ratio of Band 5 to Band 7 will peak in areas of the scene containing clay. By coloring the Band 5 and 7 ratio with red light, clay will have a red hue in the image. Iron oxides are also of interest to the geologist, and those minerals have low reflectivity in Band 2, so that a Band 3 to 2 ratio will peak in areas where iron oxides appear. The Band 3 to 2 ratio is coded with green light so that iron oxide has a green hue in the image. Mixtures of red and green light produce yellow, so that particularly promising areas for mineral exploration that contain both clay and iron oxides have a yellowish tone in this image.

Intensity is manifested in Plate 4 using Band 4 as a mask to suppress shadow areas. Because Band 4 has relatively uniform reflectance for many types of ground cover, Band 4 was used to indicate areas of shadow to provide topographical relief to the image.

Finally, where neither iron oxides nor clay exist, and both the 3/2 and 5/7 band ratios are very small in value, a nearly equal mix of saturated red, green and blue light is automatically provided to obtain a white image, indicating an area of little geological interest.

Borengasser, Brandshaft, and Taranik, as well as Abrams [1984] and Dykstra, Everett, and Sheffield [1984], agree that geological maps made with TM data provide high correlation with existing maps that were painfully produced by man-years of field geology. Dykstra found that TM provided detection of phenomena related to hydrocarbon seepage, which may be useful in petroleum exploration. Finally, these research workers and Short [1984] report that TM's enhanced spatial resolution provides direct visual identification of likely prospecting sites to an extent significantly better than MSS.



Plate 3. Density Slice of a Night Scene over Buffalo, NY.

ORIGINAL PAGE
BLACK AND WHITE PHOTOGRAPH

15210



Plate 4. Hue Intensity Saturation Transformation —
Death Valley, CA.

ORIGINAL PAGE
BLACK AND WHITE PHOTOGRAPH

152B

CONCLUSION

The LIDQA studies have not only shown that the Thematic Mapper has met its original specifications, but have characterized its performance radiometrically, spatially, and spectrally. The sensor has been shown to have a sensitivity performance better than 0.5% $NE\Delta\rho$ in the reflective bands, and an $NE\Delta T$ of 0.11K. Although raw TM data also exceeds its dynamic range specifications, the TIPS sets the dynamic range approximately equal to specification. Several minor instabilities and anomalous radiometric effects have been reported, but the overall radiometric performance has been rated excellent by all LIDQA investigators. TM's spatial performance has exceeded specification both in terms of image sharpness and geometric accuracy, yielding mapping at least twice as accurate as MSS. Spectral performance is within specification.

The LIDQA studies have also shown that the TM's image utility is at least a factor of 2 higher than MSS. TM has the capability to separate twice as many land-use classes as MSS and has demonstrated a 10 to 15% improvement in land-use classification accuracy in United States scenes. Finally, TM's spectral capability in the SWIR has been shown to provide the enhanced plant and mineral discrimination capability that was anticipated as well as other improvements, such as snow/cloud discrimination. These results are consistent with the finding that TM's raw information capacity is at least twice as great as MSS on a per pixel basis, and is close to the upper theoretical limit.

Section 9

LANDSAT-5 DATA ANALYSIS AT SANTA BARBARA RESEARCH CENTER

Evaluation of the performance of the Landsat-5 TM, launched in March 1984, is an ongoing effort. The results of the two studies summarized in this section represent only those investigations performed at SBRC since August 1984 when adequate data became available. The first study analyzes the response of the reflective levels to scenes that tend to saturate the detectors. The second study evaluated the performance of the thermal band.

BRIGHT-TARGET RECOVERY

One area of data analysis that has not been emphasized in previous TM studies is bright-target recovery (BTR); i.e., the rapidity with which a detector recovers from saturation caused by a bright object. According to the GSFC specification to which the TM was designed, the reflective channels must recover from radiance levels defined in the specification in four IFOVs or less. In the analysis presented here, Band 1 was used as the test case because Band 1 saturates more frequently than other bands. The reason is that the Band 1 saturation level was set to a value ($1.00 \text{ mW/cm}^2\text{-sr}$) much lower than the other bands relative to solar radiance.

Since clouds and snow have very high reflectance, Band 1 frequently saturates over clouds and snow and would also be expected to provide a more severe test of bright-target recovery than other bands. Note also that the cloud or snow radiance is likely to be twice as high as the $1.00 \text{ mW/cm}^2\text{-sr}$ saturation value above. Therefore, we define areas of the picture where bright-target recovery requires more than four IFOVs as "bright-target delays."

Two types of BTR delays have been observed: (1) a single detector fails to recover as rapidly as its neighbors, and (2) a scan-to-scan effect occurs, known as "banding." The first of these two types of delays is observed as a light "finger" extending into a darker area. This type of delay is discussed here. The second is seen as alternating "light" and "dark" stripes corresponding to forward and reverse scans. This effect is described by Fischel [1984].

Techniques for Detecting BTR Delays

The type of scene to be analyzed must contain objects that cause saturation, have a relatively well-defined sharp edge or rapid dropoff extending for more than approximately three pixels in the cross-scan direction (vertically, or nearly so), and a uniform background.

W. J. ... SANTA BARBARA RESEARCH CENTER

A sharp edge in the scene enables one to determine if recovery has actually occurred. The edge must extend for several pixels so that detector response for adjacent detectors can be compared. A uniform background is required, because variations in the terrain would tend to hide the delays. One of the best scenes for BTR delay detection is a scene containing bright clouds over water, since water is so uniform. However, the difficulty in using clouds as the cause of saturation is that they are such irregular objects that they do not often exhibit a sharp edge extending in the cross-scan direction for several pixels.

Visual Detection of Simulated BTR Delays

Before Landsat-5 data was available, tests were made to determine whether the eye was sensitive enough to detect BTR delays. To test the eye's sensitivity, a "perfect" cloud with "perfect" water background was computer-generated by modifying cloud and water pixels in a cloud-over-water scene from Landsat-4. (The purpose of this simulated scene was to approximate bright target rolloff and was not intended as an exact model of detector and electronics performance.) The simulated cloud was characterized by a 200-pixel, straight, vertical edge and by a rolloff that fit an exponential curve, similar to the type of rolloff expected from a detector viewing a natural cloud edge. Figure 74 shows natural cloud rolloff of several detectors compared to the rolloff from the "perfect" cloud. The rolloff from the natural clouds is more gradual at the first pixel after saturation because, on the average, only half a pixel will contain cloud data at the cloud edge, and, in addition, a cloud is not normally bright all the way to its edge; i.e., the cloud would tend to be less dense at the edges. Thus, the "perfect" cloud will have a more clearly defined edge than would normally be expected in natural clouds.

Using the "perfect" cloud, artificial BTR delays were generated by extending a detector's recovery to one, two, and three pixels beyond the four-pixel successful-recovery point. The number of delays created and their locations along the edge of the cloud were randomly selected to make the test as objective as possible. The maximum number of delays allowed was 100. The test was conducted several times at each delay level; i.e., one, two, and three pixels beyond specified recovery location. Figure 75 shows the artificial delays and the "perfect" cloud rolloff used in this test. The resulting 512 x 512 pixel image was displayed on an AED 512 Color Graphics Terminal. With this terminal a 512 x 512 image is displayed on an 8 x 8 inch screen, which is much larger than the area in which Landsat scenes are normally displayed, making detection of small features easier.

When viewing this data, the human eye was able to detect very small BTR delays. In all cases, successful detection was better than 95%, and usually was 100%. The results for the three-pixel delay, shown below, were typical:

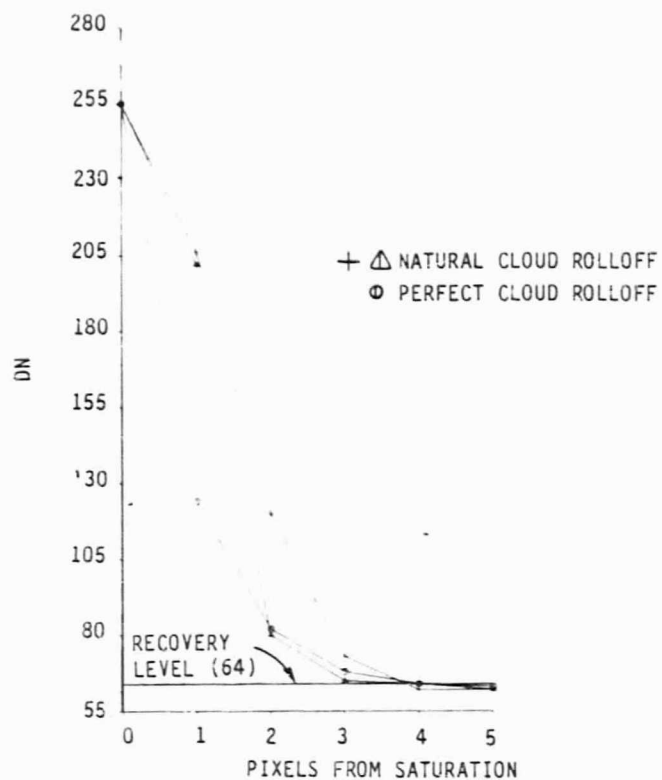


Figure 74. Cloud Rolloff, Simulated and Actual

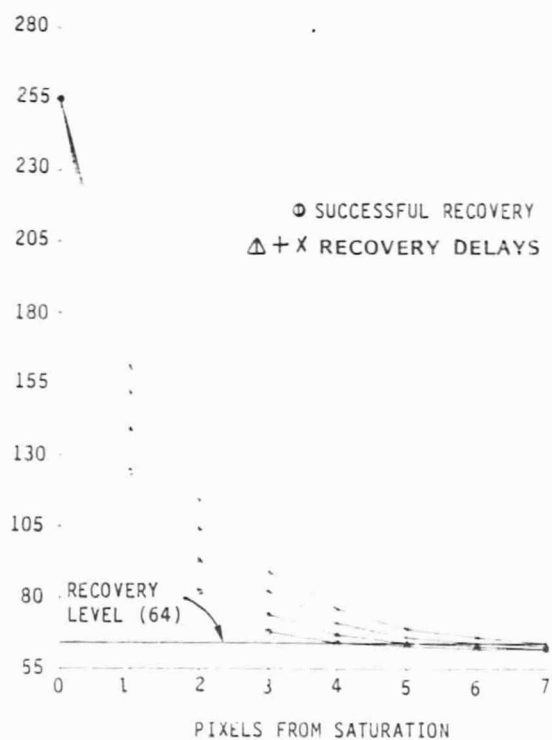


Figure 75. Simulated Detector Rolloff, Including Delays

Number of Delays

<u>Counted</u>	<u>Actual</u>	<u>%</u>
8	8	100
21	21	100
75	76	98.7

Results from these tests showed that the larger the number of delays the greater the chance of missing one, with only a small change in detection capability caused by less extensive delays. The worst case was the one-pixel delay level where 95.2%, 40 delays out of 42, were detected.

In the above simulation, noise was ignored. However, in reality, noise will make a difference in the ability to detect BTR delays. If the sensor noise is large in relation to the signal level of a BTR delay, the delay would be indistinguishable from the noise. Thus, the ability to measure the severity (extent of affected pixels) of a BTR delay will always be limited by sensor noise.

In addition to the assumption of a noiseless sensor, the test was biased in favor of detection by the eye inasmuch as the approximate location of the BTR delays was known. In an actual TM scene there would be no way of knowing if BTR delays even existed, let alone where they were.

Detection of Actual BTR Delays

Having established the feasibility of BTR delay-detection by eye using simulated TM data, the test was extended to a real TM scene. Scenes containing bright clouds were examined to find those with the requisite edge and background characteristics. Since no cloud-over-water scenes were available, an image of clouds located over southern New Mexico, near Alamogordo (scene 50129-17075, path 33, row 37) was chosen. While not the most ideal scene for BTR delay detection, it was found to be adequate since the cloud shadow provided a relatively uniform area in which to search.

To facilitate locating BTR delays in examining Landsat-5 data, a program (EDGEFIND) was written to search for sharp edges in a full TM scene. EDGEFIND narrows the search by providing 512 x 512 pixel images of locations of possible BTR recovery delays. The 512 x 512 subscenes generated by EDGEFIND were then scanned by eye on the AED 512 graphics terminal to locate any delays.

Results and Discussion

Using the methods described, it was possible to detect BTR delays by eye. The only subscenes found in the real data that exhibited BTR delays were from Band 1. This is not an unexpected result since, as mentioned earlier, Band 1 is most prone to

saturation. However, the delays occurred in a slightly different manner than expected. Rather than an isolated detector recovering just a few pixels more slowly than its neighbors, the delays were as many as 140 pixels in extent and occurred in several detectors simultaneously. Detectors 16, 14, 12, and 2 consistently exhibited BTR delay, although the delay of detector 2 was not as severe as the others.

The delays were apparent only after close examination of the scene; however, they became much more apparent after a linear "stretch" was performed on the data. Plate 5 shows a raw 512 x 512 A-tape image in which more delays occur than in any of the other subscenes examined and the same subscene with a linear "stretch" to highlight the delays, which appear as barely discernible, fine white streaks emanating into the blue areas. The blue areas represent saturated pixels. Since the data used here has not been radiometrically and geometrically corrected, some anomalies can be observed, especially scan nonlinearities. The jagged edges are an artifact of the A-tape data having each alternating scan shifted about 46 pixels from normal. These edges were left in the picture since they differentiate the forward and reverse scans so well, with the forward scans shifted to the right.

Measurement of the Severity of BTR Delays

BTR delays can also be detected by examining the digital numbers (DN) or actual pixel values. Table 22 shows the DN levels of all 16 detectors for a portion of a reverse scan (read from right to left) from the above scene during a bright target recovery. There are two clouds in this scene whose edges are outlined in boldface numbers in Table 22. Saturation from the first cloud extends across all detectors and from Pixel 0 to Pixel 5 for Detector 6. The northernmost edge of the second cloud commences at Pixel 22 and extends through Pixel 28.

The DN levels of Detectors 16, 14, 12, and 2 are several counts higher than those of the neighboring detectors 15, 13, 11, and 1, showing that they do not recover as rapidly as their neighbors. It should be noted that this data is scene-dependent. For example, Detectors 1 and 2 show the northernmost edge of a cloud from approximately Pixels 22 to 28. Because of this cloud, Detector 1 has higher values than Detector 2 for a short distance, which masks the BTR delay effect. Also, the cloud saturation does not completely end until approximately Pixel 29, at which point the delays are easily seen.

In order to more clearly show the severity of these delays an attempt was made to smooth out the natural variability of the ground data by averaging. Using data from the same subscene and scan as in Table 22 averages by pixel of detector groups 16-14-12 and 15-13-11 were computed and are shown in Figure 76. The 16-14-12 group is clearly higher than the 15-13-11 group. This delay does not exist for all even detectors in the same location in the scan, even though they all "see" the same cloud. Figure 77

Table 22. Pixels from Saturation (Reverse Scan)

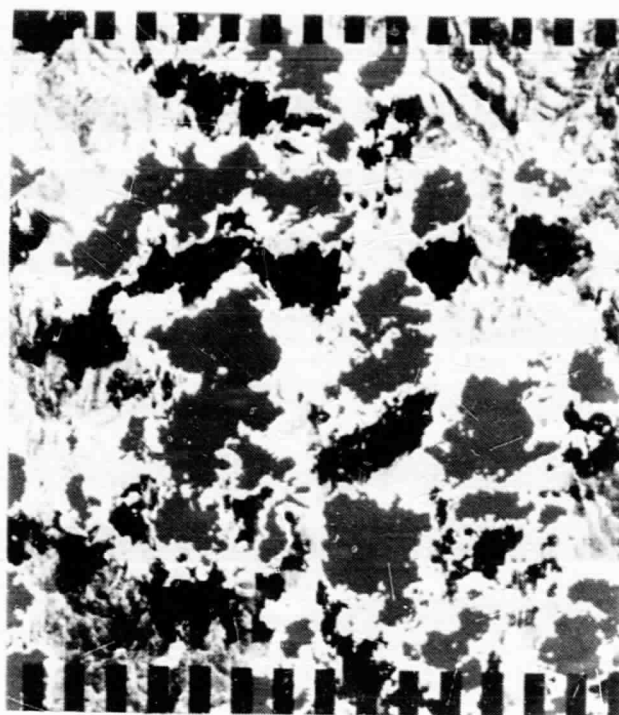
30	29	28	27	26	25	24	23	22	21	20	19	18	17	16	15	14	13	12	11	10	9	8	7	6	5	4	3	2	1	0		
16	59	56	57	59	55	61	58	58	60	69	62	66	77	89	91	90	92	79	80	77	85	102	121	134	141	145	163	173	255	255	255	
15	51	55	55	55	56	58	54	53	53	55	53	54	55	61	59	63	64	73	77	86	90	104	117	139	178	169	172	178	226	255	255	
14	55	55	58	57	61	70	66	59	58	55	56	61	58	57	59	63	64	73	77	86	90	104	117	139	178	194	177	174	205	255	255	
13	52	53	56	54	55	59	58	54	55	55	54	54	57	58	59	61	65	66	73	75	90	129	141	123	122	144	171	161	174	255	255	
12	53	53	58	59	57	61	60	58	58	59	57	64	65	62	68	66	66	66	70	74	90	134	135	159	142	165	130	141	162	210	255	
11	52	54	51	54	57	53	52	53	54	53	55	52	54	56	60	65	62	60	63	68	85	136	132	188	185	189	177	226	230	224	255	
10	52	51	50	55	53	54	53	54	53	55	51	53	53	53	64	63	58	53	57	59	74	166	175	180	212	189	221	255	255	255	255	
9	52	54	51	51	54	52	54	52	55	54	55	55	54	54	57	59	55	55	57	59	59	146	229	181	202	197	247	255	255	255	255	
8	52	53	53	53	53	53	53	50	56	55	55	54	54	57	55	55	51	53	55	54	57	74	156	189	203	204	251	255	255	255	255	
7	54	54	55	53	53	53	55	55	57	55	56	58	59	57	57	57	54	58	59	55	65	74	88	152	218	245	253	255	255	255	255	
6	56	54	58	53	56	53	51	55	57	55	57	55	58	58	57	55	60	53	53	55	64	78	117	179	255	255	255	255	255	255	255	
5	55	54	56	57	55	50	54	54	54	53	54	53	53	54	55	52	54	55	49	52	53	58	73	83	138	238	255	255	255	255	255	
4	54	55	57	61	57	52	55	54	55	57	55	55	55	61	58	54	61	57	53	54	53	50	59	85	123	228	255	255	255	255	255	
3	57	57	57	59	58	54	54	55	57	55	57	54	54	57	58	58	63	54	54	55	53	55	59	82	117	221	255	255	255	255	255	
2	59	61	73	74	61	54	70	66	62	59	59	61	61	60	61	66	61	60	55	55	57	55	77	100	134	230	255	255	255	255	255	
1	54	61	70	77	69	64	82	129	94	58	57	57	55	54	59	59	54	54	54	53	51	52	54	62	74	70	101	229	255	255	255	255

D E T E C T O R S

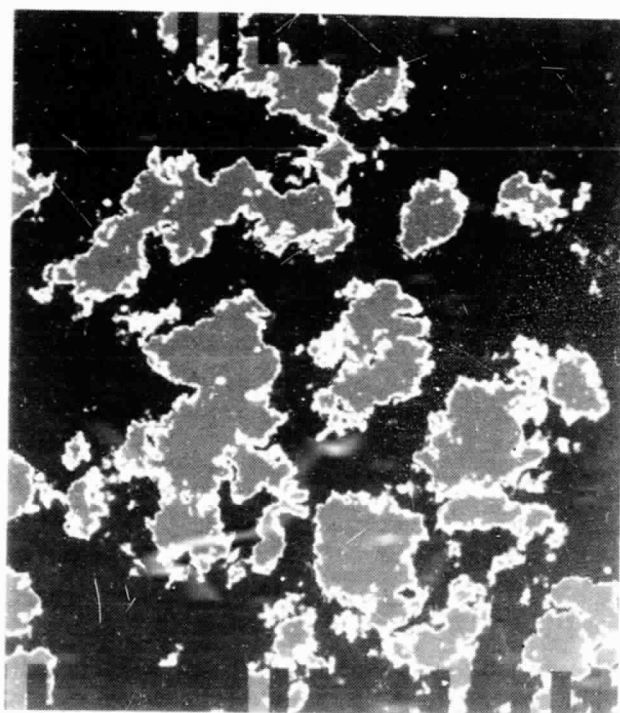
84-10-347



SANTA BARBARA RESEARCH CENTER
a subsidiary



Stretched



Unstretched

ORIGINAL PAGE
BLACK AND WHITE PHOTOGRAPH

Plate 5. Bright Cloud Image.

160a

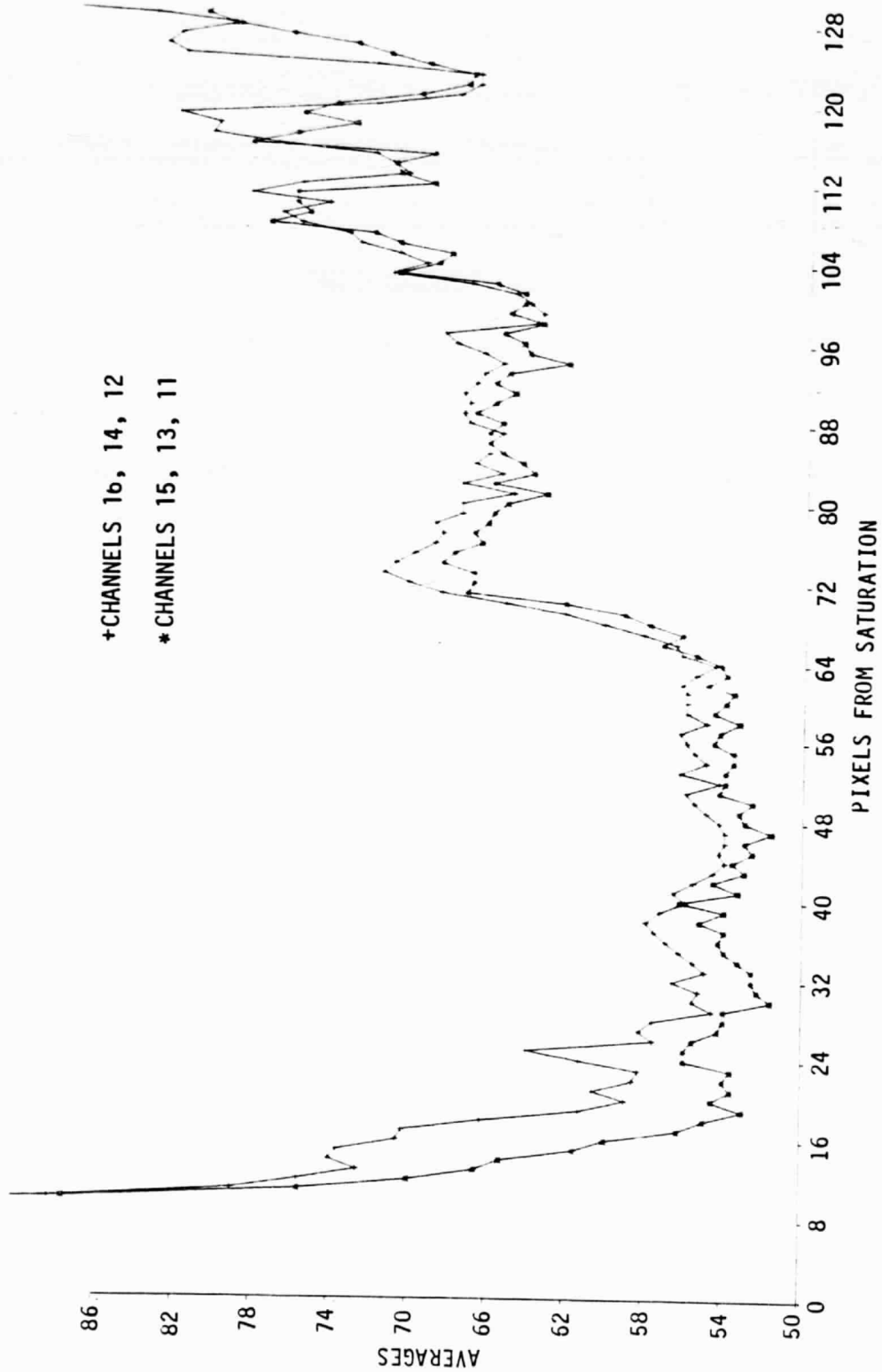


Figure 76. Detector Averages after Saturation (Delays)

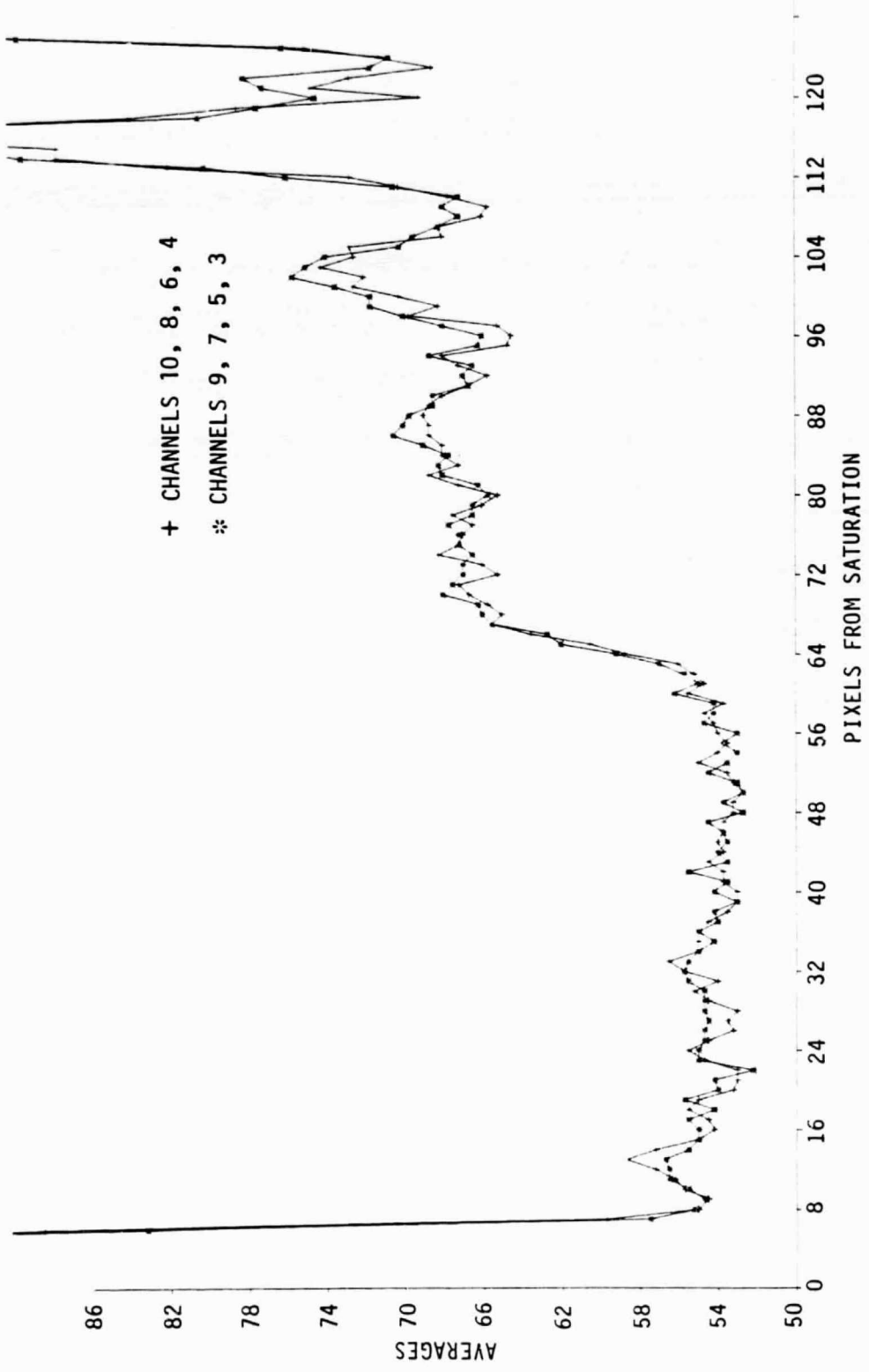


Figure 77. Detector Averages after Saturation (Successful Recoveries)

shows the output for detector groups 10-8-6-4 compared to 9-7-5-3 in the same area as that of Figure 76. The averages of these two groups are similar, showing no saturation effect.

When there is no saturation effect, detectors 16, 14, and 12 behave in a manner similar to their neighbors. Figure 78 shows detectors 16, 14, 12 and 15, 13, 11 averaged over an area (from another subscene) not affected by a bright target. As in Figure 77, the two averages are basically the same. Figure 79 shows the difference between the two sets of averages of Figure 78: even detectors minus odd detectors. (At about pixel 56, scene variability masks the BTR delays in both Figures 78 and 79.) The presentation in Figure 79 clearly shows that even detectors and odd detectors track closely in response to scene radiance.

The data presented up to this point shows that BTR delays exist, but they do not indicate the duration of the delays. The reason for this is that the subscenes examined up to this point contain numerous clouds within close proximity of one another and also contain variable background data. The delay is hidden by adjacent clouds and/or scene variability. Plate 5 shows this phenomenon quite well. The maximum delay in the subscene of Plate 5 is only about 60 pixels. Figure 80 is a graph of the maximum delay in an area of a subscene containing very few clouds and a relatively smooth background. This graph shows the differences in averages, as does Figure 79, for detector groups 16-14-12 and 15-13-11. The first 36 pixels after saturation are greatly affected by the variability of the scene, and the delays are masked. The remainder of the graph, up until approximately pixel 140 after saturation, shows the delays quite well.

Besides the length of the delays, the magnitude of the delays, i.e., the number of DN levels above normal, is of interest. However, the exact magnitude was difficult to determine since the "normal" level or background of the scene was so variable. Even the cloud shadow contained more variability than is acceptable for accurate determination of the background. Nonvariability is necessary to determine noise level and to distinguish between a BTR delay and noise. The above graphs only approximate the magnitude of the delays. The largest differences in averages occur shortly after saturation and seldom exceed 8 DNs. The mean seems to be about 3 DNs.

Cause of BTR Delays

The reason for the BTR delays has not been determined. One possibility is that, since this data has not been radiometrically corrected, the different gains and offsets for each detector are causing the problem. Normal radiometric corrections applied to the data would correct for the apparent gain and/or offset differences. However, this cannot be the case since the effect disappears after a relatively short distance and also because the apparent gain/offset differences do not occur in data that has not been affected by a bright target.

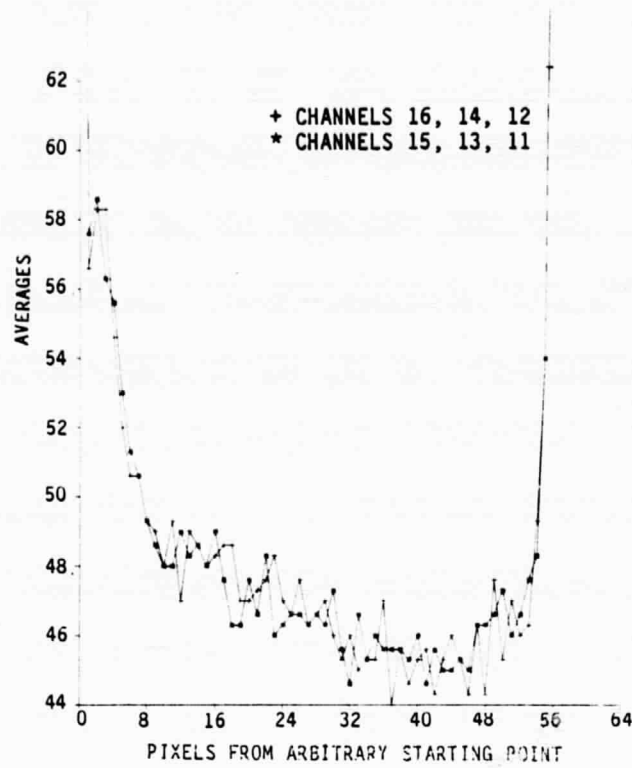


Figure 78. Detector Averages, No Saturation

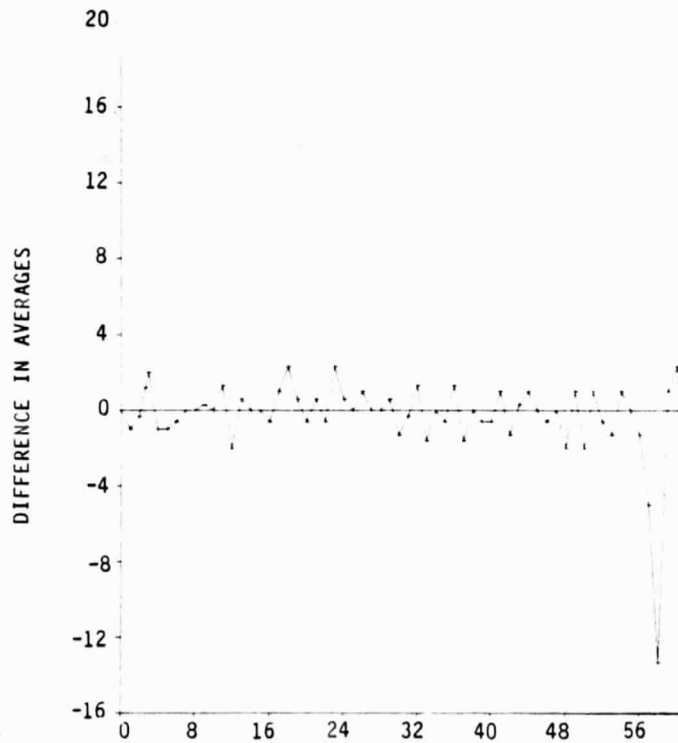


Figure 79. Detector Differences (16,14,12 vs 15,13,11)

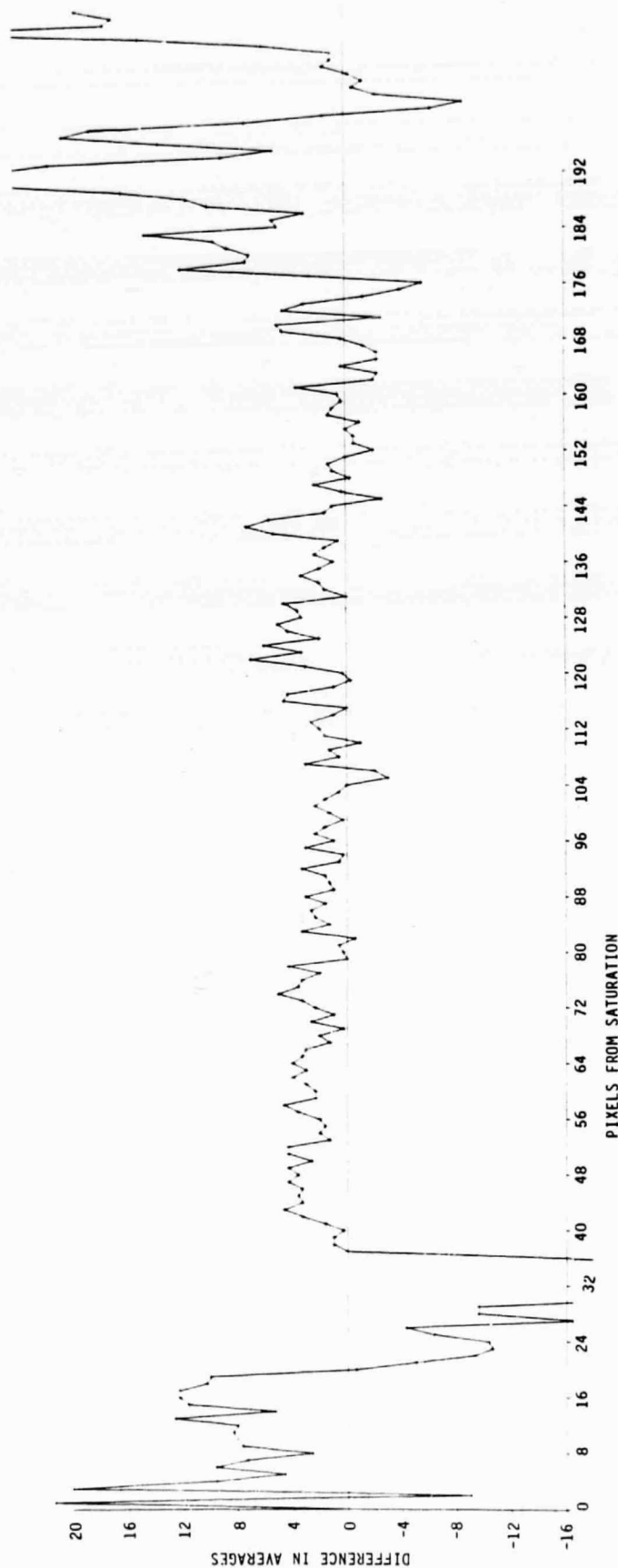


Figure 80. Detector Differences after Saturation, Maximum Duration
(Detectors 16,14,12 vs 15,13,11)

The other possibilities are that saturation has affected the TM preamplifier or the physical characteristics of the detectors themselves, requiring 140 or so pixels to recover. Indeed, pre-launch evaluation demonstrated that deep preamplifier saturation would create a long recovery delay.

Conclusions

Detection of BTR delays using the eye to examine TM data has been shown to be feasible on simulated "perfect" scenes. However, as can be observed from Plate 5, the delays are difficult to detect in real data unless the data has been artificially modified to enhance the delays or unless one knows where to look. The delays are actually more difficult to detect than Plate 5 indicates, since this 512 x 512 pixel subscene is a very small portion of a full scene, which is approximately 6000 x 7000 pixels. As a result, special computer search routines are required to identify those areas in which BTR delays might occur. Thus, even though the delays exist, if they are never seen, or at worst rarely seen, they cannot have a significant effect on the visual appearance of the data. However, these effects could affect fine-scale radiometry.

Ideally, ground processing would compensate for this effect, and the final product would not contain any evidence of the delays. To do this accurately, more research is necessary in order to fully explain and characterize the delays. Also, a scene containing saturated clouds over a uniform background, like water, is required to achieve these goals, rather than the New Mexico scene used in this study. The explanation of why these delays occur would require more research into the effects of saturation on the electronic components in TM.

THEMATIC MAPPER THERMAL-BAND PERFORMANCE

The thermal-band performance of the TM instrument on the Landsat-4 satellite, evaluated with respect to the stability of the gain over time, was presented in a paper by Engel [1983]. These findings were summarized in Section 8. A similar evaluation of Landsat-5 data, completed recently at SBRC, is presented here in more detail.

Landsat-5 Thermal Band

Effective Radiance

The effective radiance at the TM aperture is defined as:

$$L(T) = \int_0^{\infty} L_b(\lambda, T) R(\lambda, T_f) d\lambda / \left[\int_0^{\infty} R(\lambda, T_f) d\lambda \right], \quad (8)$$

where $L_p(\lambda, T)$ is the spectral radiance of an ideal blackbody at temperature T , and $R(\lambda, T_f)$ is the spectral response of the TM at cold-focal-plane temperature, T_f . This expression was evaluated for several blackbody temperatures at each of the three T_f control points. The following equations in power-series form, which are convenient for rapid computation of L for any T and T for any L^* , were fitted to these results using the coefficients shown in Table 23.

$$L = a' + b'T + c'T^2, \quad (9)$$

$$T = a'' + b''L + c''L^2 + d''L^3. \quad (10)$$

The following relationships (simplified from the Planck function), which use fewer constants and are more convenient for hand calculators where the computation time difference is not as noticeable, can also be used with the coefficients of Table 23:

$$L = K_1 / (e^{K_2/T} - 1), \quad (11)$$

$$T = K_2 / [\ln(K_1/L + 1)]. \quad (12)$$

The results using these equations agree with Equation (8) to within about 0.2%.

Table 23. Coefficients for Evaluating Effective-Radiance Equations

Coefficient	Protoflight Focal Plane Temperature			Flight, All Temperatures
	90K	95K	105K	
a'	1.771	1.827	1.950	1.6023
b'	-1.916×10^{-2}	-1.965×10^{-2}	-2.071×10^{-2}	-1.765×10^{-2}
c'	5.4656×10^{-5}	5.5708×10^{-5}	5.798×10^{-5}	5.1292×10^{-5}
a''	194.06	194.89	195.39	193.30
b''	169.25	168.08	165.56	173.55
c''	-77.99	-79.21	-75.84	-82.44
d''	18.927	20.050	18.150	21.25
K_1	67.162	69.527	74.571	60.776
K_2	1284.3	1293.1	1311.1	1260.56

The coefficients for the protoflight TM in Table 23 vary with focal-plane temperature because the spectral response of these detectors changes. This response was measured at 95K. Responses at the other temperatures were estimated using typical data for the detector material. The longwave 50% response points

*L. Linstrom, NASA GSFC: Personal Communication.

for the protoflight TM, including optics, are 11.95 μm , 11.75 μm , and 11.3 μm for 90K, 95K, and 105K focal-plane temperatures. The shortwave 50% response point remains at 10.42 μm over the temperature range. The longwave 50% response point for the flight TM remains at 12.42 μm and the shortwave at 10.45 μm over the temperature range.

Calibration

Equations (13) through (17) represent the calibration installed at launch. Coefficients for evaluating these equations are listed in Table 24. Notice that the calibration is in terms of radiance at the TM aperture and, thus, does not include atmospheric effects, which are discussed below.

$$L = (Q_{sc} - Q_{sh} + k_c)/G_c, \text{ and} \quad (13)$$

$$k_c = (aL_{sh} - b)G_i. \quad (14)$$

$$G_i = (Q_{cb} - Q_s)/(L_{cb} - L_{sh}), \quad (15)$$

$$L_{sh} = 0.53 + 0.0025 Q_{sh}, \text{ and} \quad (16)$$

$$G_c = F_{rv}G_i. \quad (17)$$

Table 24. Coefficients for Evaluating Thermal-Band Calibration at Launch

Coefficients	Channel			
	1	2	3	4
a	0.841	0.841	0.831	0.829
b	0.1702	0.2050	0.1646	0.2030
f_{rv}	0.69	0.65	0.69	0.64

More complete reduction of thermal vacuum data after calibration produced additional useful information, summarized below [Equations (18) through (21)] with the evaluation coefficients of Table 25. Equation (19) is a fit to the TM thermal-vacuum test data, where two blackbodies were used as scene sources so that the time between data points could be minimized, allowing accurate determination of the shutter radiance in scene terms.

- Effective spectral radiance at TM ($\text{mW cm}^{-2} \text{ sr}^{-1} \mu\text{m}^{-1}$)

$$L = (Q_{sc} - Q_{sh})/G_c + L_{esh} \quad (18)$$

- Shutter scene-equivalent radiance

$$L_{esh} = a + bT'_{sh} \quad (19)$$

- Ratio of external gain to internal gain

$$f_{rv} = \frac{1}{c + dT'_{sh}} \quad (20)$$

- Shutter counts as a function of shutter temperature ($^{\circ}\text{C}$)

$$Q_{sh} = e + 4.612 T'_{sh} \quad (21)$$

The variability of f_{rv} (Equation 20), the ratio of external gain to internal gain, may be due to slight shifts in the internal shutter position. If this is the case, greater stability would be expected in orbit, and it should be possible to estimate the relative value of f_{rv} from ground-truth data.

Table 25. Evaluation Coefficients for Later Calibration Items

Coefficients	Channel			
	1	2	3	4
a	0.490	0.466	0.489	0.465
b	0.0139	0.0148	0.0137	0.0148
c	1.41	1.45	1.42	1.47
d	0.003	0.010	0.002	0.010
e	29.19	29.29	29.34	29.24

Orbital Data Studies

GSFC has furnished tapes for these studies for one scene: a raw data CCTA tape with unity RLUT and a tape of telemetry information. The scene is in Alabama, ID No. 50014-15463, path 20, row 38. A digital image of the raw data had a striped appearance (as expected) because there is some difference in channel gains.

Histogram Studies

Frequency histograms of the number of pixels versus quantum level counts were made of the scene. The raw scene and the corrected imagery are shown in Figure 81.

Partial histograms for each channel of the scene, appear in Figure 82 (page 173). The histograms have been fitted with cubic spline curves since they facilitate perceiving the pattern of the data points.



(a) Raw Data Image (Image data amplitude is stretched to 17 counts)



(b) Corrected Image (Stretched to 15 Counts)

Figure 81. Alabama Scene: Raw Data Image and Corrected Image

Two effects were apparent after reviewing the histograms:

1. There is a ripple from count to count. This is attributed to the fact that the switch points between levels in the quantizer are not equally spaced with regard to input analog signal level. Wider spacing between two switch points will produce a greater number of samples per count than will a narrow spacing.
2. Channel 1 tends toward higher quantum levels than the others because of differences in gain and/or offset.

Empirical scene-correction estimates were made, discussed below, of the magnitudes of differences in quantum levels between channels and between forward and reverse scans in the various regions. The forward-reverse differences were negligible. The channel-difference values were applied as gain and offset corrections to each pixel of the raw data, as shown in Equation 22, below. A digital image of the corrected data is shown in Figure 81.

Corrected scene counts:

$$Q_{scc} = (Q_{sc} - Q_{sh})/G_{rel} - Q_{of} + Q_{ref}, \quad (22)$$

where Q_{ref} = approximate mean shutter counts = 81.5, and the evaluation coefficients are as given in Table 26.

Table 26. Coefficients for Evaluating Empirical Corrections

Coefficients	Channel			
	1	2	3	4
G_{rel}	1.078	0.940	1.038	0.944
Q_{of}	-0.14	0.66	-0.59	0.06
Q_{sh}	81.48	81.58	81.63	81.53

Quantizer Step Size Correction

Attempting to find channel relative gains from the histograms of these scenes is difficult because of the interaction between the quantizer irregularities and the particular scene content. Quantizer step-size data from unit tests of the multiplexer, which contains the quantizer, was used in a trial correction of the histograms, but was not very effective. The differing gains of the four channels and the fact that the channels use the same quantizer allow a bootstrap method of further step-size correction to be partially successful. In this approach, channel histograms are overlaid and shifted to bring histogram high or low quantity regions, which are apparently from the same feature,

into approximate registration. If the quantizer counts are not in alignment, a trial smooth curve is drawn through the overlaid histograms. Correction factors to form the smooth curve are tabulated for each count and each channel. The factors at each count should be near the same value for all channels. This condition occurs after a few iterations of the process.

An example of the results of this process is shown starting with Figure 82 where raw data histograms (partial count range only) of the four channels appear and have an obvious peak. The partially effective step-size correction from multiplexer unit tests is shown in Figure 83. After three iterations, the correction factors at each count are averaged across the four channels and each average used to correct the raw data, giving the histograms shown in Figure 84. The three sets of data from Figures 82 through 84 are overlaid in Figures 85 through 87 to show the validity of the method. Note the low scatter in Figure 87. The correction factors can be compared to multiplexer-unit-level test data in Table 27. These factors are the ratios of ideal (constant) step size to measured step size.

Table 27. Quantizer Step-Size Corrections from Histogram Overlay Method and from Multiplexer Unit-Test Data

MUX Counts	Correction Factor	
	Overlay Method	Unit-Test Data
75	0.60	0.70
76	1.47	1.31
77	0.96	1.21
78	0.75	0.93
79	0.97	0.59
80	0.81	0.93
81	1.21	1.13
82	1.20	1.12
83	0.51	0.66
84	1.50	1.20
85	1.12	1.12
101	1.03	0.93
102	1.37	1.16
103	0.78	0.68
104	0.90	1.01
105	1.14	1.08
106	0.95	1.02
107	0.73	0.66
108	1.15	1.28

Note: The 75-85 count region bin sizes are based on hundreds of samples versus the tens of thousands of samples for all the other bin sizes and produce rougher looking overlays.

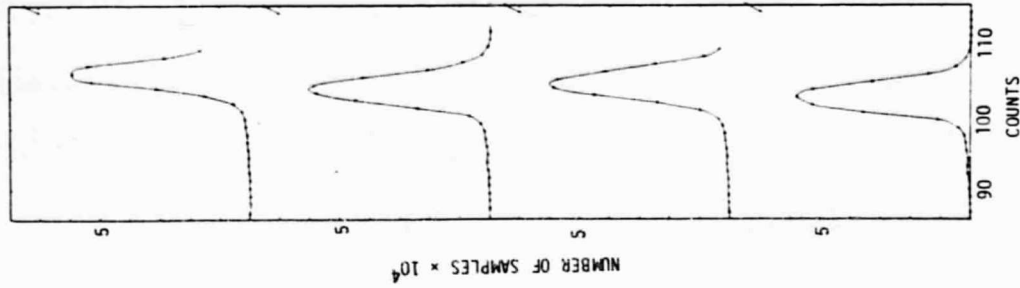


Figure 82. Alabama Scene:
Raw Data Frequency
Histograms

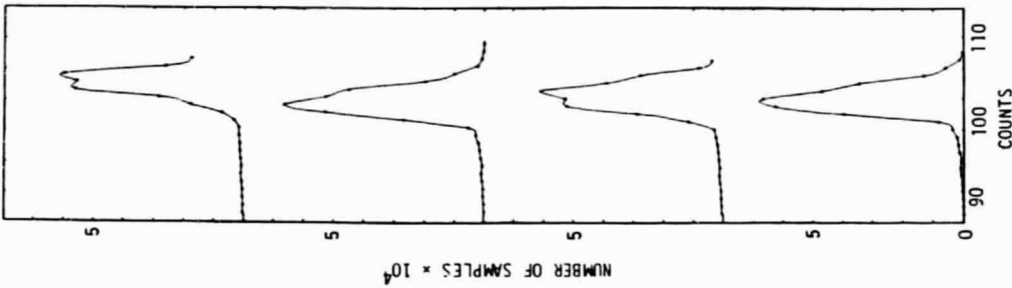


Figure 83: Alabama Scene:
Step-Size Correction from
Multiplexer Unit Tests

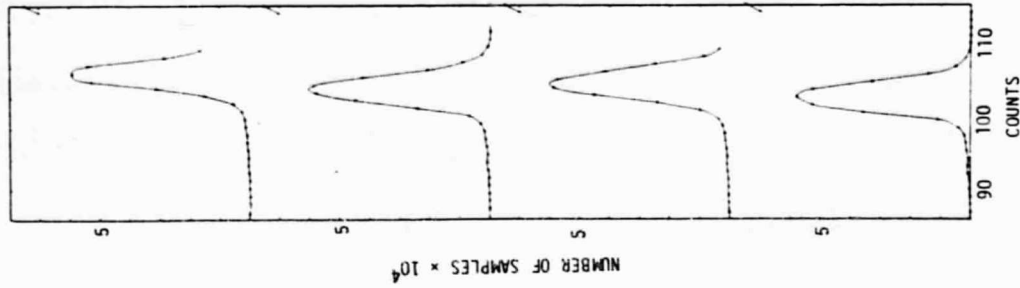


Figure 84: Alabama Scene
Frequency Histograms,
Hand-Adjusted for
Quantizer Levels

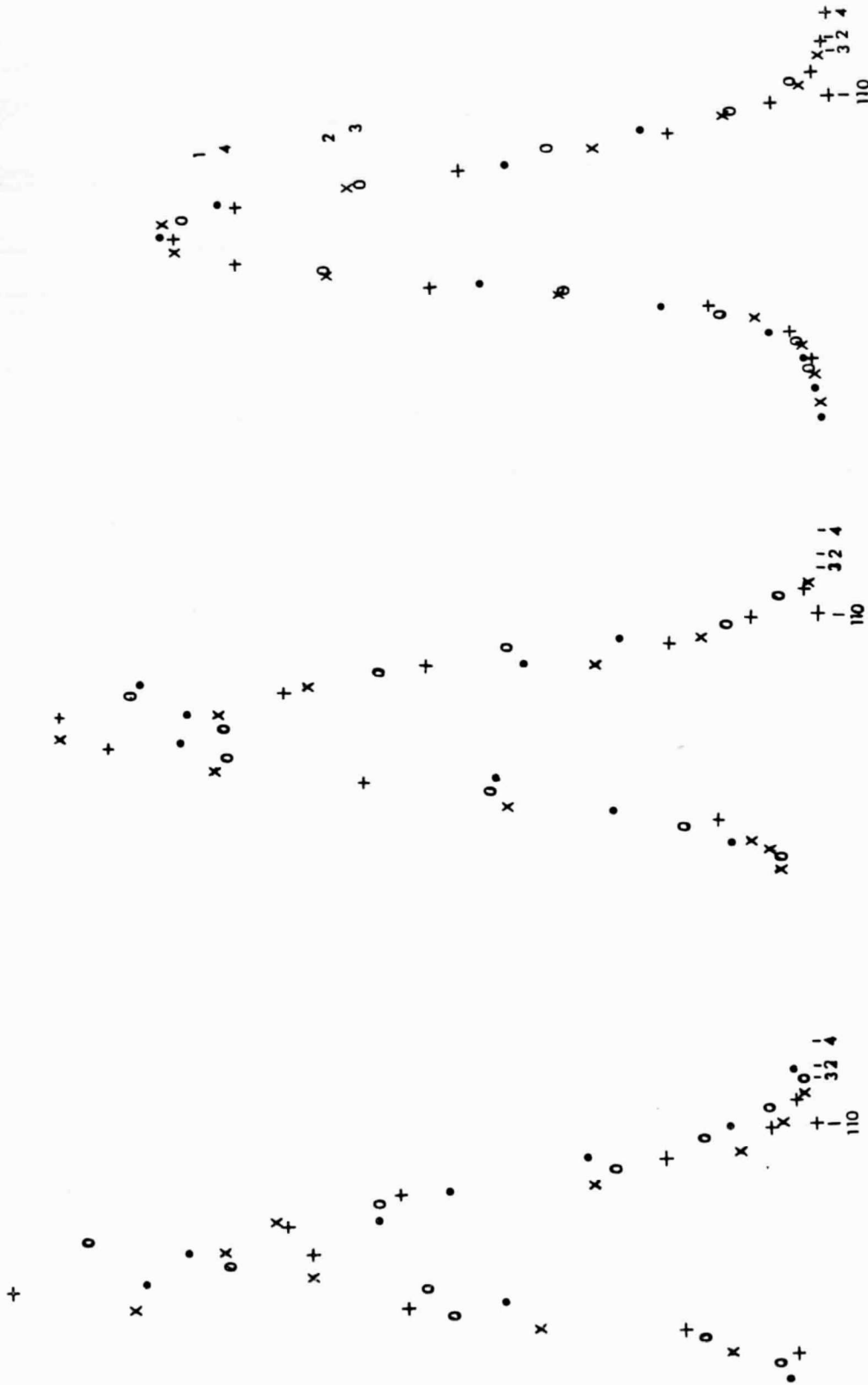


Figure 85. Alabama Scene:
Same Data as Figure 82;
Channels Shifted Horizontally on Raw Data

Figure 86. Alabama Scene:
Same Data as Figure 83;
Channels Shifted Horizontally

Figure 87. Alabama Scene:
Same Data as Figure 84;
Channels Shifted Horizontally after Hand Adjustment for Quantizer Levels

The above process was also used on a low-quantity region from the histograms of the Alabama scene, between pixels 65 and 90. No peak was available for overlaying purposes, so a transition point was chosen for matching the channels. Figures 88 and 89 show the curves for the four channels. Figure 88 shows the channels corrected using the multiplexer unit-test data. Again, this method was only partially effective. Figure 89 shows the data further corrected by the hand method. The transition points used for matching the channels are marked on the graphs. It should be noted that this "transition" data is taken from a low-quantity region of the scene histogram and, thus, is not statistically as good as if there had been more samples. However, it gives reasonably good results as can be observed from Figure 81.

Gain and Offset

The gain of the channels was calculated using Equations (15) and (17), and the results are shown in Table 28. The average of gain G_c over the four channels from thermal-vacuum test was multiplied by relative gain G_{rel} as determined from the Alabama scene [Equation (22)] to obtain the renormalized gain G_c' . The ratio of this value to G_i is the renormalized f_{rv}' .

The offset was calculated by first calculating the scene-equivalent effective spectral radiance of the shutter L_{esh} from Equation (19). Then the offset in counts, estimated from the Alabama scene, was divided by the renormalized gain G_c' to put the offset in radiance units, which was then added to L_{esh} and averaged over the channels to give renormalized L_{esh}' .

Notations and Subscripts Used

Notations

L	Effective spectral radiance, $\text{mW cm}^{-2} \text{ sr}^{-1} \mu\text{m}^{-1}$
T	Temperature, K
T'	Temperature, °C
λ	Wavelength, μm
R	Responsivity
Q	Quantized output, counts (ct)
G	Gain, $\text{ct}/(\text{mW cm}^{-2} \text{ sr}^{-1} \mu\text{m}^{-1})$
f_{rv}	Gain factor G_c/G_i
k	A constant

Subscripts

b	Ideal blackbody	i	Internal
cb	Internal calibrator	e	Scene equivalent
sh	Calibrating shutter blackbody	rel	Relative
sc	Scene	ref	Reference
f	Cold focal plane	of	Offset
c	Channel or corrected	a	Atmosphere

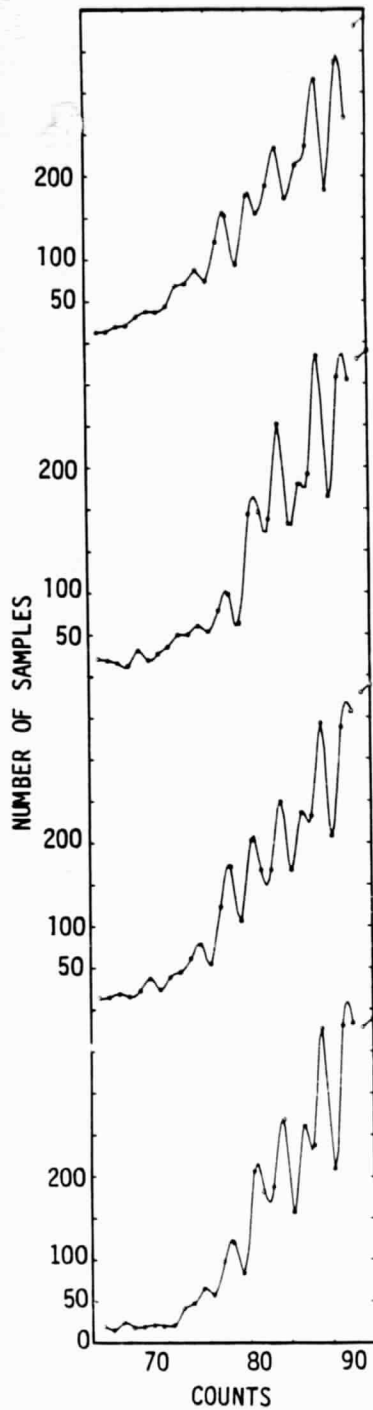


Figure 88. Alabama Scene
Low-Level Frequency
Histograms Adjusted by
Multiplexer Unit-Test
Data for Quantizer Levels

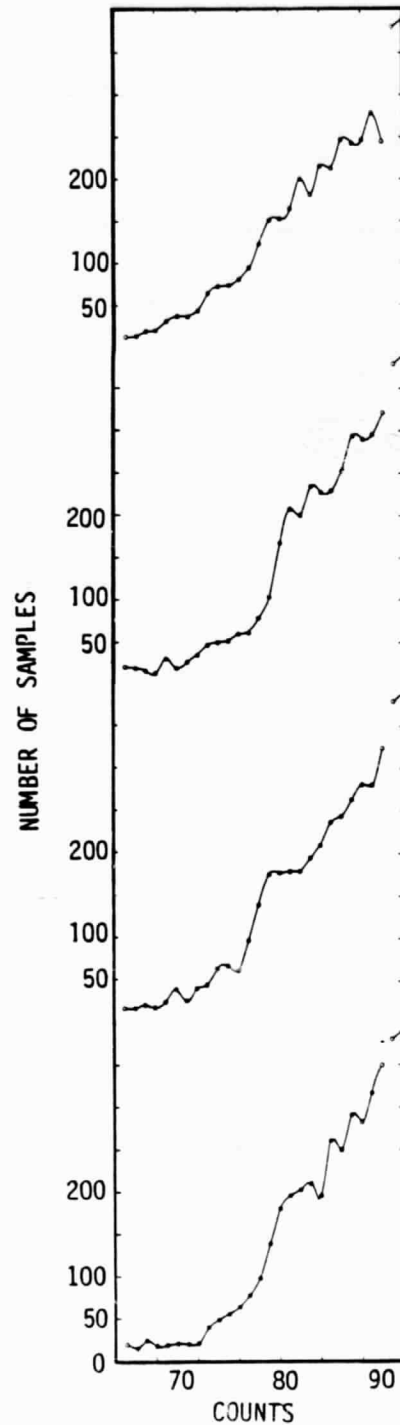


Figure 89. Alabama Scene
Low-Level Frequency
Histograms Hand-Adjusted
for Quantizer Levels

Table 28. Gain and Offset Calculations for Alabama Scene
 (Q in counts, L in $\text{mW cm}^{-2} \text{sr}^{-1} \mu\text{m}^{-1}$)

Channel	1	2	3	4
$Q_{cb} - Q_{sh}$	50.3	45.2	46.4	44.5
L_{cb} (34.39°C)	← 1.025 →			
L_{sh} (11.2°C)	← 0.731 →			
G_i	170.41	153.12	157.19	150.92
f_{rv}	0.693	0.640	0.693	0.632
G_c	117.9	98.1	108.8	95.3
G_{rel}	1.078	0.940	1.038	0.944
<u>Renormalized</u>				
G_c'	113.2	98.7	109.0	99.1
f_{rv}'	0.662	0.645	0.694	0.658
L_{esh}	0.646	0.631	0.643	0.630
$-Q_{of}/G_c'$	0.001	-0.007	0.005	-0.001
L_{esh}'	0.639	0.631	0.643	0.637



SANTA BARBARA RESEARCH CENTER
a subsidiary

APPENDICES

Appendix A

HARD-COPY PRODUCTION

Generation of Thematic Mapper hard-copy images starts with computer-compatible "P" (processed) tapes containing 8-bit (256 levels) scene data that has been geometrically and radiometrically corrected. A full TM scene consists of 6967 pixels per line and 5965 image lines (approximately 185 by 185 km). TM data has been processed in two different tape formats: "scrounge" and the Thematic Mapper Image Processing System (TIPS). The "scrounge" system was an interim (scrounged together) process developed by NASA for use until the General Electric TIPS facility became operational. All Landsat-4 data was processed using this format. In "scrounge" format, three tapes at 6250 bpi contain all seven bands of image data for one full scene. Tape 1 contains full scene data for TM Bands 1 and 2, tape 2 contains full scene data for Bands 3 and 4, and tape 3 contains data for Bands 5, 7, and 6. The TIPS system is now on line and all Landsat-5 Thematic Mapper data is currently processed by this facility. In the TIPS format, a full TM scene is divided into four quadrants and data for each quadrant is put on a separate tape at 6250 bpi. This procedure permits users to purchase smaller than full-scene images at a reduced price (quadrants are sold separately). Each tape contains data for all seven bands of a particular quadrant. Therefore, in order to make a full-scene picture, image data from the four quadrants must be pieced back together.

The first step in producing a hard-copy image is to generate a histogram for each band in the area of interest (either the entire scene, or part of it). As shown by the histogram in Figure 90, image data is generally clustered in some portion of the 0 to 255 grey-level range. Histogram data is used to determine a minimum and maximum grey-level value over which to linearly "stretch" the data. By expanding, or "stretching," the clustered portion of the data out over the full 256 grey levels, contrast is improved and more detail is brought out. All data is lost outside the selected minimum/maximum range. A linear stretch produces good results and is the stretch most often applied to image data. However, other types of stretches can be performed: logarithmic, histogram equalization, or histogram normalization.

The next processing step is to apply a correction factor, which, in effect, restretches the image data to compensate for the nonlinear contrast index (H&D curve) of the Kodak Laser Recording Film. The linear stretch and film-correction stretch are actually done in one step as the data is being written to the film.

An Optronics L5500 Laser Photowriter is used to make black-and-white negatives of each input image by translating pixel values to 25 μm squares with the correct density on the Laser

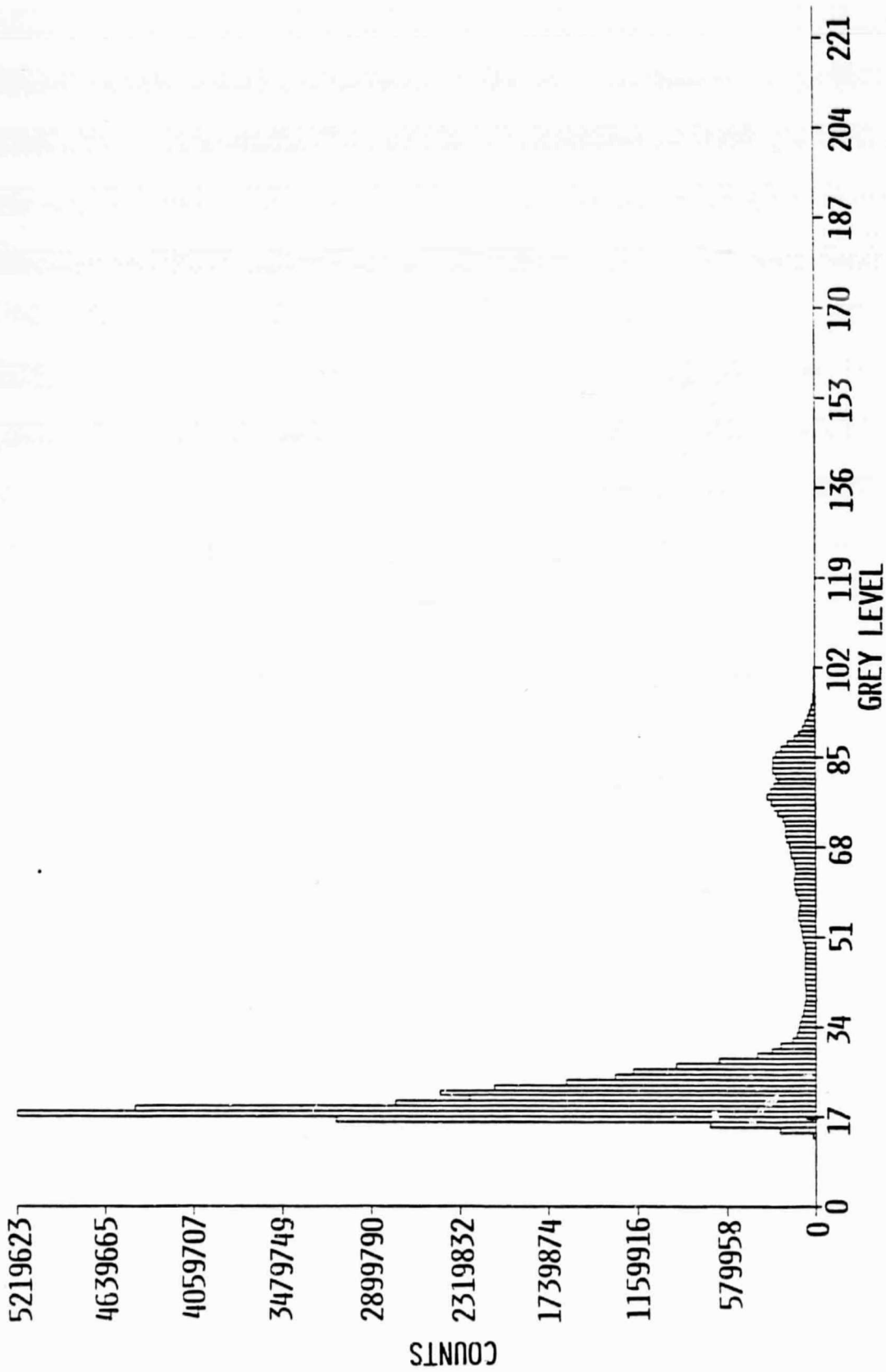


Figure 90. Histogram from TM Band 2 Data of San Francisco, California.
Image Data is Clustered Between Grey Levels 16 and 90.

Recording Film. Grey scales and registration marks (crosshairs) are also written to the film. The Laser Recording Film is then developed by an automatic processor. Plate 6 shows black-and-white positives of all seven Thematic Mapper bands of San Francisco, California, after processing.

If a color picture is desired, black-and-white negatives from any three bands are needed. The crosshairs on each negative are used to coregister the negatives. Once perfect coregistration is achieved, holes are punched in the film so that each negative can be perfectly aligned in the dark. A color composite is generated by exposing a black-and-white negative of one band through a red filter, a black-and-white negative of another band through a green filter, and a third band through a blue filter. (Filters used are a No. 47 blue tricolor, No. 58 green tricolor, and No. 25 red tricolor.) Exposure time is adjusted by monitoring the "grey" scale on the color composite.

Plate 7 illustrates the color film-generation process. Note that the dark (dense) areas in the green negative of San Francisco appear green in the color composite. These same areas are very light (clear) on the red and blue negatives. This means that no light will reach the film through the green filter, only through the red and blue filters. Light passed through a blue filter produces yellow, the complement of blue, on the film while light passed through a red filter will appear cyan, the complement of red on the film. Cyan added to yellow produces the color green on the color composite.

Areas that are clear on the green, Band 4 image, but dense on the red, Band 7 and blue, Band 3 images, will appear magenta (the complement of green) on the film. This is because only light passed through the green filter will reach the film. Urban areas in the San Francisco scene appear magenta in this color composite. Blue areas in the color composite can be explained in the same way. The blue areas are dense on the blue, Band 3 negative, and light on the green, Band 4 and red, Band 7 negative. Thus, only red and green light will reach the film. This will produce cyan (complement of red) and magenta (complement of green) on the film. Cyan mixed with magenta yields blue on the color composite.

Plates 8 through 11 are examples of different Thematic Mapper color composites. Plate 8 is a full-scene image of Las Vegas, Nevada, acquired December 12, 1982. Band 7 (2.22 μm) was passed through a blue filter, Band 3 (0.66 μm) was passed through a green filter, and Band 2 (0.57 μm) through a red filter.

Plate 9 shows a portion of the California coastline near Santa Barbara. This image covers an area approximately 100 by 130 km and was acquired November 19, 1983. A blue filter was used for Band 2 (0.57 μm), green for Band 3 (0.66 μm), and red for Band 4 (0.83 μm). Green vegetation has a strong reflectance in Band 4 and thus appears red in this color composite.

Plate 10 is a full-scene image of the area around the Salton Sea, California, acquired December 12, 1982. A blue filter was used for Band 3 (0.66 μm), green for Band 4 (0.83 μm), and red for Band 7 (2.22 μm). Green vegetation, with its strong reflectance in Band 4, appears green in this color composite.

Plate 11 is a subimage of the Washington, D.C., area. This image covers an area approximately 48 by 48 km and was acquired November 2, 1982. Band 1 (0.485 μm), centered in the blue region of the electromagnetic spectrum, was passed through a blue filter, Band 2 (0.56 μm), in the green region, through a green filter, and Band 3 (0.66 μm), in the red region, through a red filter. This color composite combination simulates a "true color" image, or what you might expect to see if you looked down on the Washington, D.C., area from above.



ORIGINAL PAGE
BLACK AND WHITE PHOTOGRAPH

Plate 6. Linearly Stretched Images of San Francisco, CA.

C-3

87 a

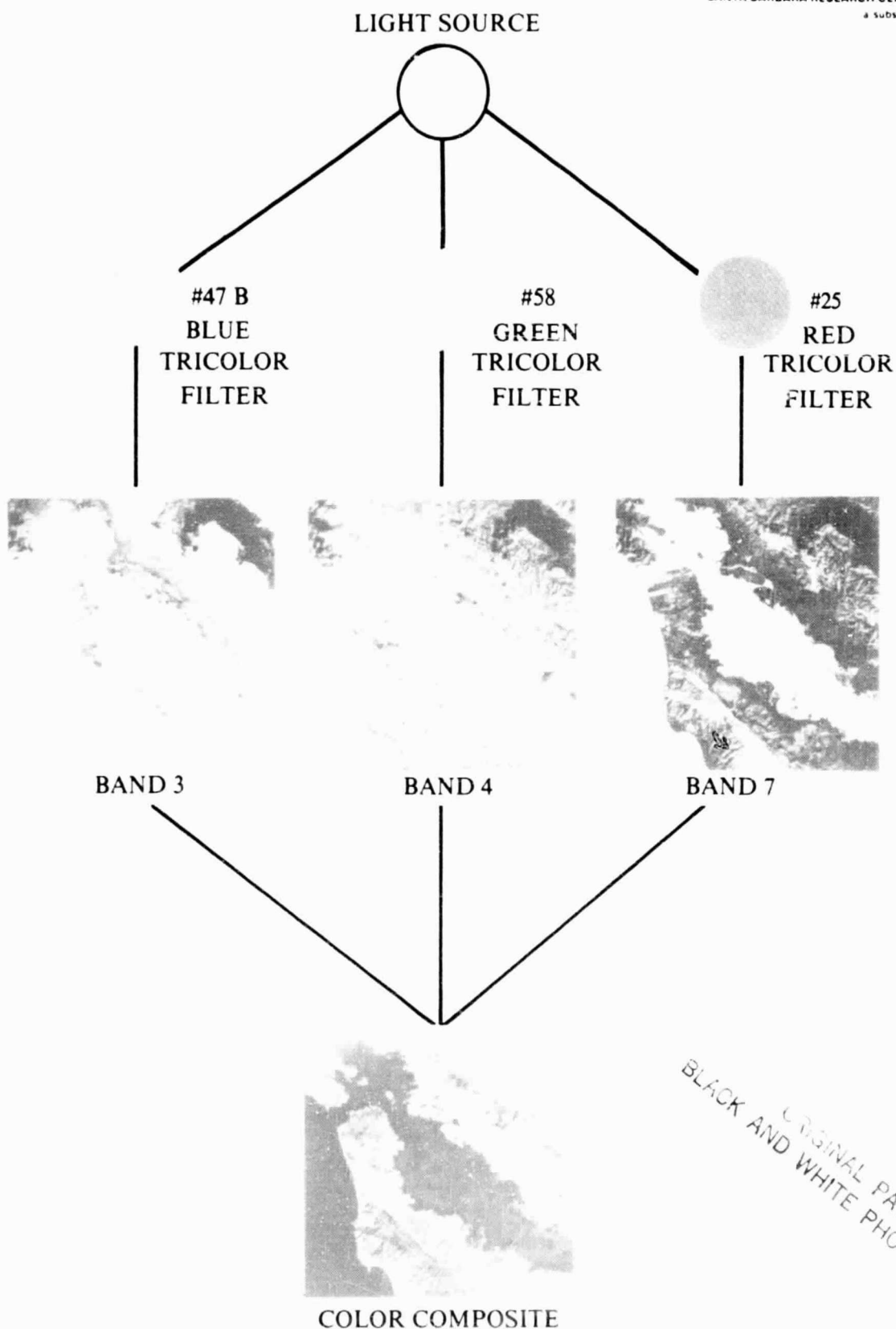


Plate 7. Color Film Generation Process



Plate 8. Full Scene Image of Las Vegas, NV.

ORIGINAL PAGE
BLACK AND WHITE PHOTOGRAPH

187C

84-10-343

HUGHES
SANTA BARBARA

SANTA BARBARA RESEARCH CENTER

a subsidiary



Plate 9. California Coastline — Point Conception to Santa Barbara

ORIGINAL PAGE
BLACK AND WHITE PHOTOGRAPH

11812



ORIGINAL PAGE
BLACK AND WHITE PHOTOGRAPH

Plate 10. Full Scene Image of Salton Sea, CA.

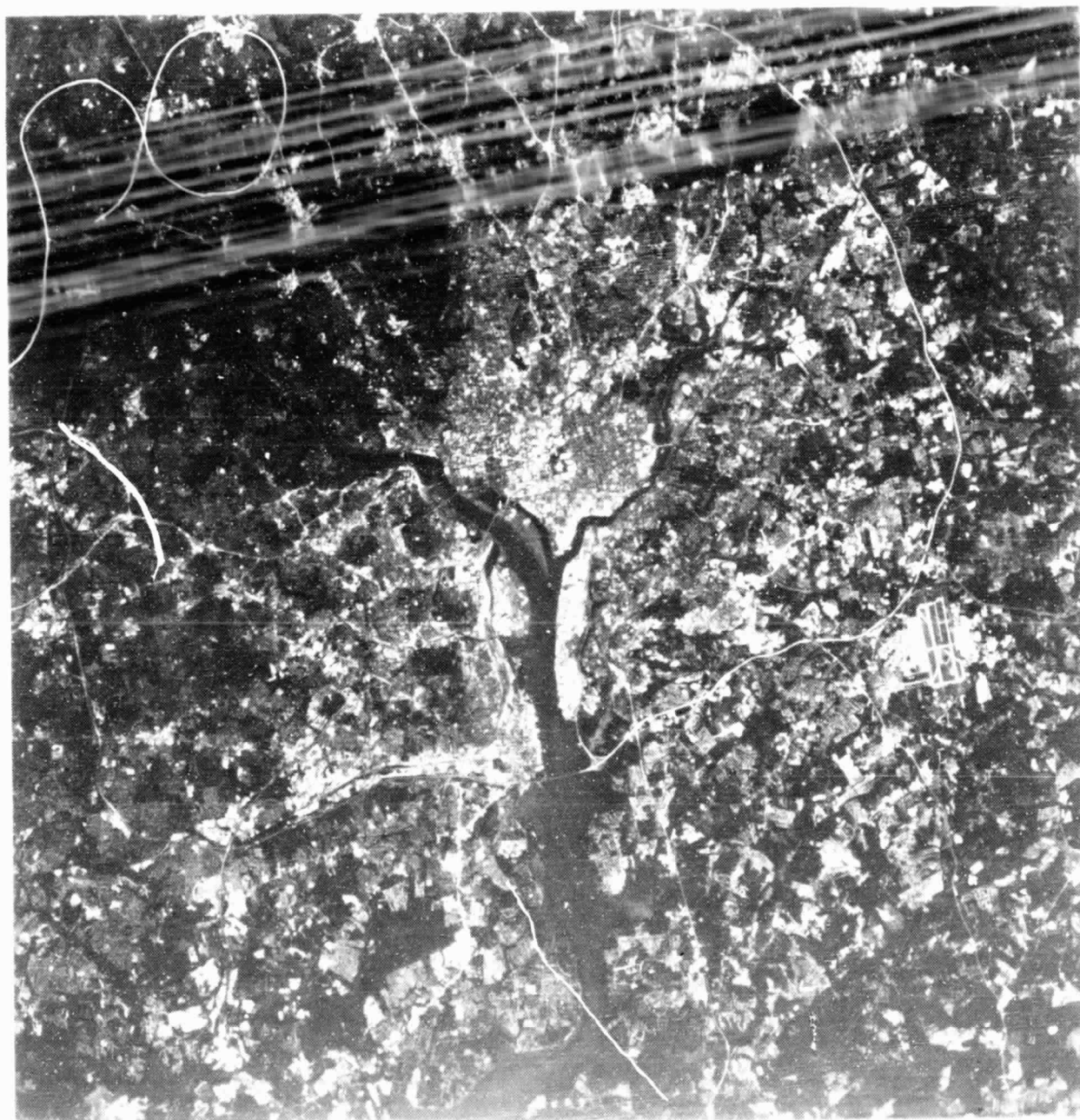


Plate 11. Subimage of Washington, DC (48 x 48 km)

ORIGINAL PAGE
BLACK AND WHITE PHOTOGRAPH

Appendix B

DESIGN CHANGES DURING HARDWARE DEVELOPMENT

Figure 1 (Section 2) shows the chronology of hardware development. From the time of the breadboard development program through the flight-model preshipment review numerous design changes were made. These changes are summarized below.

TM CRITICAL ELEMENT BREADBOARD PROGRAM

The 18-month breadboard development program was conducted between June 19, 1974 and January 31, 1976 to demonstrate the feasibility and performance of three critical elements of the TM design that had not been proven on either the MSS or the VISSR. These elements were a 40.6-cm bidirectional scan-mirror assembly, a scan-line corrector (image motion compensator), and a silicon photodiode array with integral preamplifier input stages. These three assemblies were designed, fabricated, and tested to demonstrate performance consistent with the requirements of the TM system. The measured performance met or exceeded the original design goals in all cases except for deficiencies in the design of the photodiode array package. These deficiencies were well-defined and understood and corrections prescribed.

The following features were developed during the breadboard program:

1. The scan-mirror assembly.
 - a. Torquer drive logic and circuits were designed to operate during turnaround, rather than during backscan as in the MSS design.
 - b. Leaf-spring mirror bumpers were developed to reduce bumper mass compared to the MSS, because this mass had caused significant cross-axis motion.
 - c. Brazed beryllium eggcrate mirror construction was designed.
 - d. A magnetic compensator for nonlinearity caused by the restoring force of the mirror flex pivots was developed.
2. Scan-line corrector breadboard model mechanism, logic, and circuits.
 - a. A single-axis scan-line corrector was developed after changing the basic arrangement of mirrors many times during the paper design.
 - b. The frame design required added stiffening.

- c. Opening the feedback loop for a part of the flyback (at scan mirror turnaround) gave nearly ideal performance.
3. Silicon photodiode array assembly.
- a. The first attempts were made to fabricate arrays. Tests showed the need for integral light shielding to avoid response to stray signals.
 - b. Test results with these arrays and initial preamplifier and boost amplifier designs showed very uneven frequency response, suggesting a change in circuit layout to improve response.
 - c. Dielectric-loss noise was recognized as a significant noise contributor; low-loss materials were selected whenever they affected capacitance.

CONCEPTUAL DESIGN REVIEW

The contract to build the TM started in April 1977. By the time of the Conceptual Design Review (CDR) in July 1977, development efforts had caused a number of changes to be made in the design described in the proposal including the following:

- 1. Scan-mirror assembly.
 - a. The torquer was changed from a location behind the scan mirror to a pancake configuration in a central opening in the mirror, reducing flex pivot forces and increasing efficiency and speed of response.
 - b. The scan-mirror fabrication method was changed from an eggcrate with face sheets brazed on both sides to two half-mirror slabs with eggcrates machined on one side of each half and subsequently brazed together.
- 2. The main-frame assembly was changed from an aluminum casting to aluminum honeycomb for greater stiffness and less weight.
- 3. The multiplexer design was changed from two 43 Mbps outputs to one 85 Mbps output to fit the TDRSS data system.

DETAIL DESIGN REVIEW

By the time of the Detail Design Review (DDR), June 1978, the following additional changes had been made:

- 1. Scan-mirror assembly (SMA).
 - a. The scan-angle monitor (SAM) was redesigned to improve mirror startup.

- b. The frame material was changed from aluminum to beryllium to increase rigidity so that the relative motion between the SAM and the mirror pivots would not cause variations in the active scan amplitude.
 - c. A controlled heater was added at the SMA interface to provide constant temperature so that thermal expansion would not affect scan amplitude.
 - d. Redundancy was increased in the electronics to improve reliability.
2. Multiplexer. Pseudonoise encoding was added to improve synchronization and to reduce unwanted spectral components.
3. Radiometer.
- a. The sun-calibrator design, as presented in the proposal, would not function as expected. The design was then modified to use an increased aperture area, thus reducing sensitivity to tiny flaws in the optical path.
 - b. Self-protective shutdowns, including thermal, were added to the power supply.
 - c. Electronics redundancy was increased.
 - d. A nadir-viewing louver assembly was removed as unnecessary.
 - e. The instrument mounting to the spacecraft was changed from a three-point to a four-point mounting.
 - f. The bulkheads were changed from aluminum to beryllium to provide added frame stiffness and necessary weight reduction.
 - g. The calibrator was changed, replacing a moving neutral density filter with a set of switched lamps that could be operated by an automatic sequencer.
 - h. The radiator plate for the electronics module was changed from aluminum to beryllium to reduce weight.
 - i. The seventh spectral band was added to the cold focal plane. In the original requirement the seventh band was optional, and its spectral location was undefined. The design proposed had allowed space for the seventh band at either focal plane.

TM ENGINEERING MODEL PRESHIPMENT REVIEW

The Engineering Model Review was held in November 1980. Changes described at that review were [SBRC 1980]:

1. The sun calibrator was deleted by GSFC direction. The sun calibrator had been designed before the spacecraft and was removed when the spacecraft design interfered with its necessary field of view. Unfortunately, this was the only in-orbit calibration provision for the complete optical path.
2. Provisions were made for adding an angular displacement sensor to be mounted on the TM to furnish high-frequency (jitter) attitude information. The sensors were provided by the spacecraft contractor and installed during spacecraft integration.
3. Scan-mirror assembly.
 - a. The SAM was redesigned for two, instead of four, bounces of the optical path at the back of the scan mirror in order to reduce cross-axis sensitivity.
 - b. A nickel coating was added to the scan mirror between the beryllium and the silver to reduce optical scatter.
 - c. The magnetic compensator was redesigned to enable position adjustment.
 - d. A vibration absorber was added to the scan mirror, minimizing mirror distortion near scan start.
 - e. A backup control mode, using pickoffs on the bumpers, was recommended.
 - f. A ground correction to the scan profile, based on the location of the midscan pulse from the SAM, was recommended.
4. The main-frame changes were:
 - a. Increased torsional stiffness of the SMA bulkhead to improve scan geometry.
 - b. Increased stiffness of the thermal feet connecting TM to the spacecraft.
5. The secondary mirror support was redesigned for higher natural frequency and reduced weight.
6. Radiative cooler door/shroud.
 - a. Stronger magnetic latches were incorporated.

- b. A kinematic hinge replaced the diaphragm.
 - c. The fail-safe heater was redesigned for improved reliability.
7. Onboard calibration shutter.
- a. The extension spring size was increased to reduce operating stress.
 - b. The fiber optics sleeving was overcoated to eliminate possible outgassing.
8. Four support struts were added to the relay optics structure to raise the natural frequency and reduce amplification at the folding mirror.
9. Operability of the alignment and focus mechanism was improved by cutting the shaft between the brake and the drive and reconnecting it with a flexible coupler.
10. The vibration damper on the cold stage of the radiative cooler was removed after it failed in vibration test and was found to be unnecessary after further testing and analysis.
11. Prime focal-plane assembly.
- a. Optical shields were added over the bond pad areas of the detector, which had been found to be sensitive to photons.
 - b. The detector fabrication method was changed to give a stable, low-resistance contact at the common junction of the array.
 - c. Metallization and shielding were used in the input circuits to reduce crosstalk. Some of the shielding was adjusted by bending to fine tune the transient response during FPA acceptance testing.
12. Cold focal-plane assembly.
- a. Shields were added to reduce crosstalk.
 - b. Jumper wires to the distribution board were changed from a platinum alloy, which fatigued, to gold, with a resultant increase in heat load during bench cooling.
 - c. The high-value feedback resistors' stray capacitance caused poor frequency response. This was improved by placing the resistors on sapphire standoffs, thus reducing capacitance to ground, and by adding a parallel capacitor to swamp out the stray capacitance of the resistors.

13. Changes in the signal amplifiers served to augment stability, improve frequency response, and reduce noise.
14. The amplifier circuit values of Band 6 were changed to reduce sag and improve stability.
15. Additional adjustments were added to the postamplifiers for Bands 1 through 5 and 7 to improve control of gain and frequency response.
16. Numerous changes were made in the power supply. These are listed in Table 29.
17. Multiplexer changes requested by GSFC were:
 - a. Replacement of triaxial output cables by twin axial output cables.
 - b. Spacecraft interface connectors were tilted to provide better access on the spacecraft.

PROTOFLIGHT PRESHPMENT REVIEW

Several changes were announced at the Protoflight Preshipment Review [SBRC 1981]:

1. Several changes and adjustments were made in the electronics module to correct problems, including shutter control, which allowed the oscillating shutter to tap against its bumper stops.
2. The onboard calibration shutter changes included:
 - a. Adding extension springs to decrease the natural period of oscillation, bringing it closer to the scan rate.
 - b. Adding bumpers to positively limit shutter excursions.
 - c. Shifting the encoder timing to provide a backup dc-restore.

FLIGHT MODEL PRESHPMENT REVIEW

At the time of the Flight-Model Preshipment Review more changes were announced [SBRC 1982c]:

1. The synchronization lines to the power supply were opened to cure a self-shutdown problem that had occurred in this model. These lines had been opened to PS-1 in the proto-flight model during spacecraft integration.

Table 29. TM Power Supply Changes Documented at the Engineering Model Preshipment Review

INPUT DESIGN

Eliminate Common-Mode Choke

- Weight and Power Savings
- Redesigned Current Shunt

Redesigned Input-Command Board

- New Component Layout
- Removed 6.4V Regulator from Input-Command Board
- Redesigned Pulse-Stretch Circuitry
- Redesigned Filter Circuitry

MINISWITCHER DESIGN

Modified Sync Circuit

- Changed Phasing or Sync Signal
- Added Comparator for Sync-Signal Threshold Control
- Added Noise Filters
- Changed Supply Power for Sync and Overcurrent Circuits from 5V, Generated by Mini PWM Chip, to 6.4V Regulator
- Increased Response Time of Slow-Start Circuit
- Redesigned Overtemperature Circuitry
- Moved Overtemperature Control to Slow-Start Circuitry
- Added Hysteresis and Noise Filters
- Added Third Connector
- Revised Interconnect Between Boards

Maxi Switcher Design

- Added Phase-Lock Comparator to Sync-Control Circuitry
- Modified Current-Limit Circuitry
Current-Limit Control Connected to Slow-Start Circuitry
- Modified Multiplexer Control Loop
Added Zero for Increased Stability
- Modified Input Telemetry Circuitry
Added Noise Filters
Relocated Decoupling Resistors
Added New Current Shunt

Output Circuitry

- Combined 8.5V (Radiometer) and $\pm 29V$ (SMA) Output Boards Into One Subassembly
- Power Transformer Design
Added Taps for Bands
Added Turns for Increased Output Voltage
- Modified CDVU Switching Current Limit Circuit
- Modified Limit-Cycle Circuit for Radiometer
- Revised Telemetry Scaling
- Revised Component Types and Values as Required by Stress Derating

2. Resistors were added during spacecraft integration in the return lines of Band 1 to reduce coherent noise, which was higher than specified.
3. Band 6 occasionally failed to turn on in test. The wiring of a voltage regulator was corrected to resolve the problem.
4. The frames holding PFPA quartz substrates were changed from Invar to beryllium to reduce stress on the quartz.
5. To correct a problem found during thermal-vacuum testing of the protoflight model, some interstage spacings in the radiative cooler were increased to ensure clearance during cool-down. This problem was discovered during thermal-vacuum testing of the protoflight TM.
6. A redundant closed-position switch was added to the radiative cooler door/shroud assembly.

Appendix C

REFERENCES

- Abrams, M. 1984. Geologic Utility of Landsat-4 TM Data, In *Landsat Early Results Symposium Proceedings*, ed. J.L. Barker. Greenbelt, MD: NASA (GSFC).
- Ackleson S., and Klemas, V. 1984. Assessing Landsat TM and MSS Data for Detecting Submerged Mast Communities. In *Landsat Early Results Symposium Proceedings*, ed. J.L. Barker. Greenbelt, MD: NASA (GSFC).
- Anuta, P., et al. 1984. Landsat-4 MSS and TM Data Quality and Information Content Analysis. In *IEEE Transactions: Geoscience and Remote Sensing*, vol. GE-22, no. 3, pp. 222-236. New York, NY: IEEE.
- Barbe, D., and S. Campana. 1977. Imaging Arrays and the Charge-Coupled Concept. In *Advances in Image Pickup and Display*, pp. 241-255, B. Kazan, ed. New York, NY: Academic Press.
- Barker, J. 1984. Prelaunch Absolute Radiometric Calibration of the Reflective Bands on the Landsat-4 Protoflight Thematic Mapper. In *Landsat Early Results Symposium Proceedings*, ed. J.L. Barker. Greenbelt, MD: NASA (GSFC).
- Barker, J., et al. 1984. Characterization of Radiometric Calibration of Landsat-4 TM Reflective Bands. In *Landsat Early Results Symposium Proceedings*, ed. J.L. Barker. Greenbelt, MD: NASA (GSFC).
- Bernstein, R., et al. 1984. Analysis and Processing of Landsat-4 Sensor Data Using Advanced Image Processing Techniques and Technologies. In *IEEE Transactions: Geoscience and Remote Sensing*, vol. GE-22, no. 3, pp. 192-221. New York, NY: IEEE.
- Beyer, E. 1983. Thematic Mapper Geometric Correction Processing. In *Proceedings of the 17th International Symposium on Remote Sensing of Environment*. Ann Arbor, MI: Environmental Research Institute of Michigan.
- Borengasser, M.; Brandshaft, D.; and Taranik, J. 1984. *Geological Applications of Enhanced Landsat 4 TM Imagery of South-Central Nevada*. Paper read at Third Thematic Conference, Remote Sensing for Exploration Geology, April 1984, at Colorado Springs, CO.

- Brooks, J., et al. 1984. TM Geometric Correction Performance and Evaluation. In *Proceedings of the 10th International Symposium on Machine Processing of Remotely Sensed Data*, pp. 22-28. West Lafayette, IN: Purdue University (Laboratory for Applications of Remote Sensing).
- Cafferty T.T., and Kuyper, D.J. 1982. Radiative Cryogenic Cooler for Thematic Mapper. In *SPIE Proceedings*, vol. 364, p. 74. Bellingham, WA: SPIE.
- Castle, K.R., et al. 1984. In-Flight Absolute Radiometric Calibration of the TM. In *IEEE Transactions: Geoscience and Remote Sensing*, vol. GE-22, no. 3, pp. 251-255. New York, NY: IEEE.
- Cocoa Beach Working Group. 1973. *Advanced Scanners and Imaging Systems for Earth Observation*. NASA SP-335. Washington, DC: NASA.
- Colvocoresses, A. 1984. Mapping of Washington, D.C. and Vicinity with the Landsat-4 TM. In *Proceedings of the 50th Meeting of the American Society of Photogrammetry*, pp. 757-764. Falls Church, VA: Photogrammetry Society.
- Colwell, R.N., ed. 1983. *Manual of Remote Sensing*. 2nd ed. 2 vols., chap. 12. Falls Church, VA: American Society of Photogrammetry.
- Crist, E., and Cicone, R. 1984. A Physically-Based Transformation of TM Data: The TM Tasseled Cap. In *IEEE Transactions: Geoscience and Remote Sensing*, vol. GE-22, no. 3, pp. 256-262. New York, NY: IEEE.
- DeGloria, S. 1984. Spectral Variability of Landsat-4 TM and MSS. In *IEEE Transactions: Geoscience and Remote Sensing*, vol. GE-22, no. 3, pp. 303-311. New York, NY: IEEE.
- Dozier, J. 1983. Snow Hydrology (Lecture 13). *Landsat Sensor Design and Operation: A Short Course for Users*, C. Schueler, ed. Goleta, CA: Santa Barbara Research Center.
- _____. 1984. Snow Reflectance from Landsat-4 Thematic Mapper. In *IEEE Transactions: Geoscience and Remote Sensing*, vol. GE-22, no. 3, pp. 323-328. New York, NY: IEEE.
- Dykstra, J.; Everett, J.; and C. Sheffield. 1984. Evaluation of Landsat-D TM Performance as Applied to Hydrocarbon Exploration. In *Landsat Early Results Symposium Proceedings*, ed. J.L. Barker. Greenbelt, MD: NASA (GSFC).

- Earth Observatory Satellite Mission Review Group (EOSMRG). 1971. *Final Report*. Greenbelt, MD: Goddard Space Flight Center.
- Engel, J.L., and Weinstein, O. 1983. Thematic Mapper: An Overview. In *IEEE Transactions: Geoscience and Remote Sensing*, vol. GE-21, no. 3, pp. 258-65. New York, NY: IEEE.
- Engel, J., et al. 1983. Radiometric Performance of the Thematic Mapper. In *Proceedings of the Seventeenth Symposium on Remote Sensing of Environment*. Ann Arbor, MI: Environmental Research Institute of Michigan.
- Fischel, D. 1984. Validation of the TM Radiometric and Geometric Correction Algorithms. In *IEEE Transactions: Geoscience and Remote Sensing*, vol. GE-22, no. 3, pp. 237-242. New York, NY: IEEE.
- Fusco, L., and Treverse, P. 1984. TM Failed Detector Replacement. In *Landsat Early Results Symposium Proceedings*, ed. J.L. Barker. Greenbelt, MD: NASA (GSFC).
- Goddard Space Flight Center (GSFC). 1973. *Advanced Scanners and Imaging Systems for Earth Observation*. Greenbelt, MD: NASA.
- _____. 1981. *Application Notice for Participation in the Landsat-D Image Data Quality Analysis Program*. Greenbelt, MD: NASA.
- Haas R., and Waltz, F. 1984. Evaluation of TM Data for Natural Resource Assessment. In *PECORA VIII Proceedings*, pp. 122-133. Sioux Falls, SD: Augustana Research Institute.
- Hardisky M., and Klemas, V. 1984. Remote Sensing of Coastal Wetlands Biomass Using TM Wavebands. In *Landsat Early Results Symposium Proceedings*, ed. J.L. Barker. Greenbelt, MD: NASA (GSFC).
- Harnege, J., and Landgrebe, D. 1975. *Landsat-D Thematic Mapper Technical Working Group Final Report*. JSC-09797. Houston, TX: NASA.
- Huck, F., et al. 1981. Application of Information Theory to the Design of Line-Scan Imaging Systems. *NASA Tech. Paper No. 1897*. Greenbelt, MD: NASA.
- Hughes Aircraft Company (HAC). 1970. *Final Report for the Multi-spectral Scanner Study*. Contract No. NAS5-11624; HAC B6872-550-0038R. El Segundo, CA: HAC.

- _____. 1976. (Space and Communications Group) *Proposal for a Thematic Mapper Instrument System*. RFP No. S-79160/229; HAC Ref. 76(44)-11728/B4596-SCG60347P. El Segundo, CA: HAC.
- Hyde, R.; Spencer, M.; and Vesper, N. 1983. *An Estimate of Cost Effectiveness of Machine Processing Increased Spatial Resolution MSS Data*. (Holcomb Research Institute; Butler University; National Oceanic and Atmospheric Administration, P.O. No. NA83AAA02079). Indianapolis, IN: Butler University.
- Kieffer, H.; Eliason, E.; and Chavez, P. 1984. Thematic Mapper Intraband and Radiometric Performance. In *Landsat Early Results Symposium Proceedings*, ed. J.L. Barker. Greenbelt, MD: NASA (GSFC).
- Kuyper, D.J., and Buller, J.S. 1982. Bench Cooling the Thematic Mapper. In *SPIE Proceedings*, vol. 364, p. 83. Bellingham, WA: SPIE.
- Lansing, J. 1983. *Thematic Mapper Thermal Band Destriping and Ground Truth Comparison*. Internal Memorandum. Goleta, CA: SBRC.
- Lansing, J., and Barker, J. 1984. Thermal Band Characterization of TM. In *Landsat Early Results Symposium Proceedings*, ed. J.L. Barker. Greenbelt, MD: NASA (GSFC).
- MacDonald, R. 1984. Preliminary Evaluation of TM Image Data Quality. In *Landsat Early Results Symposium Proceedings*, ed. J.L. Barker. Greenbelt, MD: NASA (GSFC).
- Malila, W.A., et al. 1984. Characterization of Landsat-4 MSS and TM Digital Image Data. In *IEEE Transactions: Geoscience and Remote Sensing*, vol. GE-22, no. 3, pp. 177-191. New York, NY: IEEE.
- Markham, B. 1984a. Characterization of the Landsat Sensor's Spatial Response. In *Landsat Early Results Symposium Proceedings*, ed. J.L. Barker. Greenbelt, MD: NASA (GSFC).
- _____. 1984b. Preliminary Comparisons of the Information Content and Utility of TM Versus MSS Data. In *Landsat Early Results Symposium Proceedings*, ed. J.L. Barker. Greenbelt, MD: NASA (GSFC).
- Middleton, E., et al. 1984. Relative Accuracy Assessment of Landsat-4 MSS and TM Data for Level I Land Cover Inventory. In *Landsat Early Results Symposium Proceedings*, ed. J.L. Barker. Greenbelt, MD: NASA (GSFC).

- Murphy, J., et al. 1984. Revised Radiometric Calibration Technique for Landsat-4 TM Data. In *IEEE Transactions: Geoscience and Remote Sensing*, vol. GE-22, no. 3, pp. 243-250. New York, NY: IEEE.
- Neckel, H., and Labs, D. 1981. Improved Data of Solar Spectral Irradiance from 0.33 to 1.25 μm . *Solar Physics* 74:231-249.
- Palmer, J. 1984. Effective Bandwidths for Landsat-4 MSS and TM Subsystems. In *IEEE Transactions: Geoscience and Remote Sensing*, vol. GE-22, no. 3, pp. 336-338. New York, NY: IEEE.
- Palmer J., and Tomasko, M. 1980. Broadband Radiometry with Spectrally Selective Detectors. *Optics Letters* 5(5):208-210.
- Park, S., and Schowengerdt, R. 1982a. Image Sampling, Reconstruction, and the Effect of Sample-Scene Phasing. *Applied Optics*, 21(17):3142-3151.
- _____. 1982b. Image Reconstruction by Parametric Cubic Convolution. In *Computer Vision, Graphics, and Image Proceedings*, vol. 23, pp. 258-272. New York, NY: Academic Press.
- Pitts, D., et al. 1984. Evaluation of Corn/Soybean Separability Using TM Data and TM Simulator Data. In *IEEE Transactions: Geoscience and Remote Sensing*, vol. GE-22, no. 3, pp. 312-318. New York, NY: IEEE.
- Podwysocki, M., and Bender, L. 1984. A Preliminary Evaluation of Landsat-4 TM Data for Geometric and Radiometric Performance, In *Landsat Early Results Symposium Proceedings*, ed. J.L. Barker. Greenbelt, MD: NASA (GSFC).
- Price, J. 1984. Comparison of the Information Content of Data from the Landsat-4 TM and MSS. In *IEEE Transactions: Geoscience and Remote Sensing*, vol. GE-22, no. 3, pp. 272-280. New York, NY: IEEE.
- Quattrochi, D. 1984. An Initial Analysis of Landsat-4 TM Data for the Discrimination of Agricultural, Forested Wetland, and Urban Land Cover. In *Landsat Early Results Symposium Proceedings*, ed. J.L. Barker. Greenbelt, MD: NASA (GSFC).
- Salomonson, V.V., and Mannheimer, H. 1984. An Overview of the Evolution of Landsat-4. In *Proceedings of the PECORA VIII Symposium*, pp. 32-44. Sioux Falls, SD: Augustana Research Institute.

Santa Barbara Research Center (SBRC). 1980. *TM Engineering Model Preshipment Review*. Goleta, CA: SBRC.

_____. 1981. *TM Protoflight Model Preshipment Review*. Goleta, CA: SBRC.

_____. 1982a. *Thematic Mapper System Operation and Maintenance Manual for the Thematic Mapper Assembly*. (HS236-8131) Goleta, CA: SBRC.

_____. 1982b. *Thematic Mapper System Operation and Maintenance Manual for Bench Test and Calibration Equipment* (4 vols.). (HS236-8132) Goleta, CA: SBRC.

_____. 1982c. *TM Flight Model Preshipment Review*. Goleta, CA: SBRC.

Schiebe, F. 1984. A First Evaluation of TM Data to Monitor Suspended Sediments in Lakes. In *Landsat Early Results Symposium Proceedings*, ed. J.L. Barker. Greenbelt, MD: NASA (GSFC).

Schueler, C. 1983a. TM Protoflight Model Line Spread Function. In *Proceedings of the 17th International Symposium on Remote Sensing of Environment*. Ann Arbor, MI: Environmental Research Institute of Michigan.

Schueler, ed. 1983b. *Landsat Sensor Design and Operation: A Short Course for Users*. Goleta, CA: SBRC.

Schueler, C., and V. Salomonson. 1984. Landsat Image Data Quality Studies. In *Advances in Space Research*. Committee on Space Research. New York, NY: Pergamon Press.

Seyrafi, K. 1973. *Electro-Optical Systems Analysis*. Los Angeles, CA: Electro-Optical Research Company.

Short, N. 1982. *The Landsat Tutorial Handbook: Basics of Satellite Remote Sensing*. NASA No. 1078. Greenbelt, MD: NASA (GSFC).

Short, N. 1984. Assessment of Computer-Based Geologic Mapping of Rock Units in the Landsat-4 Scene of Northern Death Valley, CA. In *Landsat Early Results Symposium Proceedings*, ed. J.L. Barker. Greenbelt, MD: NASA (GSFC).

Thekaekara, M.P. 1970. *The Solar Constant and the Solar Spectrum Measured from a Research Aircraft*. NASA TR-R-35. Greenbelt, MD: NASA.

- Thompson D., and Henderson, K. 1984. Evaluation of TM for Detecting Soil Properties under Grassland Vegetation. In *IEEE Transactions: Geoscience and Remote Sensing*, vol. GE-22, no. 3, pp. 319-322. New York, NY: IEEE.
- Toll, D. 1984. Preliminary Study of Information Extraction of TM Data for a Suburban/Regional Test Site. In *Landsat Early Results Symposium Proceedings*, ed. J.L. Barker. Greenbelt, MD: NASA (GSFC).
- Walker, R., et al. 1984. An Analysis of Landsat-4 TM Geometric Properties. In *IEEE Transactions: Geoscience and Remote Sensing*, vol. GE-22, no. 3, pp. 288-293. New York, NY: IEEE.
- Welch R., and Usery, E. 1984. Cartographic Accuracy of Landsat-4, MSS and TM Image Data. In *IEEE Transactions: Geoscience and Remote Sensing*, vol. GE-22, no. 3, pp. 281-287. New York, NY: IEEE.
- Williams, D., et al. 1984. A Statistical Evaluation of the Advantages of Landsat TM Data in Comparison to MSS Data. In *IEEE Transactions: Geoscience and Remote Sensing*, vol. GE-22, no. 3, pp. 294-302. New York, NY: IEEE.
- Witt, R.; Blodget, H.; and Marcell, R. 1984. Final Comparison of TM and MSS for Surface Mine Assessment in Logan County, West Virginia. In *Landsat Early Results Symposium Proceedings*, ed. J.L. Barker. Greenbelt, MD: NASA (GSFC).
- Wrigley, R., et al. 1984. TM Image Quality: Registration, Noise, and Resolution, In *IEEE Transactions: Geoscience and Remote Sensing*, vol. GE-22, no. 3, pp. 263-271. New York, NY: IEEE.
- Wukelic, G., et al. 1984. Landsat-4 Image Data Quality Analysis for Energy Related Applications. In *Landsat Early Results Symposium Proceedings*, ed. J.L. Barker. Greenbelt, MD: NASA (GSFC).

INDEX

Aft-optics assembly 68, 73, 75, 117
Aliasing 33, 36-37, 56, 60-61, 143
Applications 2, 6, 131
Atmospheric Effects 143, 168
 Scattering 134, 135
 Transmittance 6, 134, 135
Baffles 70, 77
Bandwidth 55-56, 60-61
Bench test and calibration equipment (BTCE) 109-113
 Alarm-limit testing 112
 Suppression-limit testing 113
Bonding 70, 71, 85, 105
Bright-target recovery 155-166
Calibration 2, 31, 33
 Accuracy 132, 138
 Amplitude modulation 43
 Calibrating sphere 119
 Data 22
 Errors 28, 135
 Lamp sequencing 118, 119
 Reflective band 136
 Shutter 75, 95, 118, 140, 187, 188
 Sources 18, 119
 Tests 113, 118, 119, 121
 Thermal band 142, 168
Coherent noise 113, 129, 130, 141
Coefficient of thermal expansion 71
Color composite 2, 132, 181, 182
Compression amplifier 58
Crosstalk 60, 79, 83, 85, 104, 187
Cubic convolution 143
Data transmission 28, 58, 106, 147
Detectors
 Charge-coupled devices (CCD) 53, 60
 Indium antimonide (InSb) 12, 21, 53, 87
 Mercury cadmium telluride (HgCdTe) 12, 21, 53
 Monolithic 12, 20-21, 53, 60
 Silicon photodiode array 7, 183-184
Digital
 Image 132, 169, 171
 Number (DN) 9, 12, 14, 22-23, 58, 106, 132-135, 159, 164
 Word 9, 12, 22-23, 106

Distributed capacitance 79

Dynamic range 93, 132-133, 135, 153

Effective focal length (EFL) 17, 38, 109, 113-117

Electromechanical scanner 5, 9-11, 17

Electrical filtering
 Bessel 56
 Butterworth 56, 57
 Goldberg 56

Electronics 20, 22, 23, 25, 33, 35-36, 90, 104-106

Electronics module
 Heat sink 104-106, 110
 Multiplexer (MUX) 12, 20, 22-23, 58, 61, 106-108, 173-174, 185
 Power supply 104, 107-108, 185, 188-189
 Printed wiring boards (PWB) 104-106, 108

Engineering model (EM) 101-103, 106, 108, 113, 183, 186, 189

False color 12

Fiber-optics assembly 93, 95, 187
 Calibrator flag 92,93
 Tungsten lamps 18,95

Field of view
 Instantaneous field of view (IFOV) 25, 27, 43, 60, 122-123, 143, 147-148
 Swath 14, 25, 27, 132

Flight model (F) 12, 38, 70, 73, 106, 113, 140, 188, 190

Focal-plane assemblies
 Cold focal plane (CFPA) 9, 12, 21, 78-79, 83, 85, 87, 89, 102, 110, 113, 138, 178, 185, 187
 Cables 89
 Heaters 97
 Coarse/fine focus 118,121
 Prime focal plane (PFPA) 9, 12, 20, 31, 78-80, 83-84, 102, 113, 118, 187

Gain-offset correction 141

Geometric errors
 Band-to-band registration 41, 113-114, 125-128, 144-145
 Ephemeris 144-145
 Distortion 144
 Pointing 145
 Temporal registration 144-145

Goddard Space Flight Center (GSFC) 1,5,131

Ground-temperature estimation 135

Inchworm 20, 50, 52, 77-78, 118

Knife-edge response (KER) 122-125

Lambertian scatterer 134

Landsat-D Image Data Quality Analysis (LIDQA) Program 131-132, 146-147, 153

Line-spread function (LSF) 33, 38-39, 118-119, 125, 143

LOWTRAN 134

Manual of Remote Sensing 31

Materials

- Graphite-epoxy 17, 20, 46, 50, 68-69, 71, 75, 77
- Hygroscopic 44
- Telescope 71

Modulation transfer function (MTF) 33-38, 56, 60, 63, 109, 113, 117-118, 125 132, 143,

National Aeronautics and Space Administration (NASA) 1-2, 5, 28 125, 131-132, 179

Noise-equivalent reflectance ($NE\Delta\rho$) 6, 12, 31, 38, 40, 132-133, 135-136, 153

Noise-equivalent temperature ($NE\Delta T$) 6, 12, 31, 37-38, 40, 129, 133, 135-136, 153

Nyquist frequency 36, 40, 143

On-board calibrator assembly 90-95, 113, 119-121

Optical finishing 44, 72

- Chipping 72
- Contamination 21, 73, 97, 100, 103
- Durability 73

Optical-metering structure (OMS) 68-69, 77

Outgassing 21, 102-103, 142, 187

Overlap/underlap 18, 20, 41, 56, 127

Phased-knife edge 127

Prelaunch evaluation 2, 109, 166

Primary mirror 17, 44, 69-72

Print through 63

Protoflight model (PF) 1, 2, 37 39-41, 113, 140, 188, 190

Pushbroom sensor 25,27

Radiative cooler 9, 21, 23, 50, 68, 96-101, 118, 186, 190

- Bimetallic sandwich 97
- Cooling stages 96, 97
- Earth albedo 96
- Earth shield 96-97, 100-101
- Heat transfer 55
- Honeycomb structure 96, 100-105, 184
- Louvers 23, 101, 185
- Thermal control 101
- Thermal emittance 55, 96

Vibration response 97
Visible and Infrared Spin-Scan Radiometer (VISSR) 1, 43, 53,
55, 60, 93, 97, 100-102, 183
Radiosonde data 134-135
Relay optics 9, 20-21, 50, 73, 77, 95, 187
Resampling 143, 145
Resolution 131
 Radiometric 12, 25-28, 30-31
 Spatial 5, 12, 25-28, 30, 33-37, 143
 Spectral 5, 25-28, 30-33, 147
Reticle patterns 127-128
Sampling rate 6, 55-56, 122, 143
Saturation reflectance 133, 135
Scan-line corrector (SLC) 7, 13, 18-19, 52, 60, 73, 90, 104,
118-119, 183
Scan-mirror assembly (SMA) 7, 9, 14, 17-18, 44-46, 63-66, 73,
91, 107, 113, 117-119, 121-122, 183, 184, 189
 Bumpers 14, 46, 96, 183, 186, 188
 Eggcrate construction 17, 46, 59, 63, 65, 71, 183, 184
 Distortion 46, 186
 Drive 46, 59
 Scan-angle monitor (SAM) 63, 65, 67, 184
Scan-profile 113
Scrounge system 131, 143, 179
Secondary mirror 17, 44, 46, 59, 70, 71, 186
Signal-to-noise ratio (SNR) 27, 31, 38, 40, 53, 58
Solar zenith angle 134
Spectral bandpass 28, 30-33, 132, 146
Spectral cutoffs 31, 146
Spectral uniformity 146
Square-wave response (SWR) 33, 35, 38, 40, 109, 122
Striping 140-141
 Multiscan banding 141
Sun calibrator 90, 186
Sun-synchronous 7, 132
System-readiness test 130
Tapes
 Archival (A) 132
 Product (P) 132
Telemetry 106, 112, 118, 130, 169

Telescope
 Reflective 44
 Refractive 44
 Ritchey-Chretien 17, 44, 45, 59
User needs 5, 30, 38, 131
Whiskbroom sensor 25, 27